Mechanical Characterisation, Processing and Microstructure of Wheat Flour Dough

Mohd Afandi P Mohammed

August 2012

Mechanics of Materials

Department of Mechanical Engineering

Imperial College London

A thesis submitted for the degree of Doctor of Philosophy of

Imperial College London and the Diploma of Imperial College

Declaration of Originality

I hereby declare that all material in this thesis is my own work except where clearly stated otherwise, in which case references are always provided.

Abstract

The mechanical behaviour of dough, gluten and starch was studied in an effort to investigate whether bread dough can be treated as a two phase (starch and gluten) composite material. Mechanical loading tests revealed rate dependent behaviour for both the starch and gluten constituents of dough. There is evidence from Cryogenic Scanning Electron Microscopy (Cryo-SEM) that damage in the form of debonding between starch and gluten occurs when the sample is stretched. In addition, the Lodge material model was found to deviate from the tension and shear stress-strain test data by a considerably larger amount than from the compression test data. This could indicate that 'damage' is dominant along the gluten-starch interface, causing debonding; the latter occurs less under compression loading, but is more prevalent in tension and shear loading. A single-particle finite element model was developed using starch as a filler contained in a gluten matrix. The interface between starch and gluten was modelled using cohesive zone elements with damage/debonding occurring under opening/tension and sliding/shear modes. The numerical results are compared to experimental stress-strain data obtained at various loading conditions. A comparison of stress-strain curves obtained from 2D and 3D single-particle models and a multi-particle model led to good agreement, indicating that the single-particle model can be used to adequately represent the microstructure of the dough studied here. Finally, the simulation of extrusion was performed using the finite element method, where demonstration of the predictive capability of a continuum numerical model with small scale experimental results was performed.

Acknowledgements

I would like to take this opportunity to thank several people who have assisted me with this project over the last few years. Firstly, I wish to thank my supervisors, Dr Maria Charalambides and Professor Gordon Williams for their continuous support and guidance throughout this project. I am thankful for financial support provided by Malaysian Ministry of Higher Education and Universiti Putra Malaysia. I would like to show my appreciation to all members of Mechanics of Materials section, especially Dr Idris Mohammed, Dr Hari Arora, Dr Edmund Tarleton, Miss Shamsiah Awang Ngah, Dr Ioannis Giannakopoulos, Dr Ruth Brooker, Mr Diego Alvarez Feito, Dr Jibumon Babu and Mr Soratos Tantideeravit. Finally, on a more personal level, I would like to thank my friends and family for their continuous support and encouragement.

Table of Contents

List of Figures

List of Tables

Nomenclature

T_0	Onset temperature (starch gelatinisation)
T_p	Peak temperature (starch gelatinisation)
T_c	Conclusion temperature (starch gelatinisation)
a_w	Water activity (GAB model)
M	Equilibrium water content (GAB model)
M_o, C and k	Model parameters (GAB model)
ε	True strain
l	Current gauge length (uniaxial tension)
l_0	Original gauge length (uniaxial tension)
δ	Gauge displacement (uniaxial tension)
σ	True stress
D	Original specimen diameter (uniaxial tension)
F	Applied force
A	Instantaneous cross-sectional area (uniaxial compression)
h	Instantaneous sample height (uniaxial compression)
H	Initial sample height (uniaxial compression)
r	Instantaneous sample radius (uniaxial compression)
R	Initial sample radius (uniaxial compression)
ε_r	Recoverable strain
$\dot{\gamma}$	Shear strain rate
r	Radius of rotating plate (cone-plate geometry)

θ	Cone angle (cone-plate geometry)
ω	Rotational speed (cone-plate geometry)
R	Edge radius of rotating plate (parallel plate geometry)
H	Gap between the upper and lower rheometer plates (parallel plate geometry)
$\dot{\gamma}_E$	Shear strain rate at the edge of a parallel plate geometry
τ_R	Apparent shear stress (parallel plate geometry)
τ_E	Corrected shear stress
$\Gamma(t)$	Measured torque at time, t
γ_0	Amplitude of shear strain (shear strain sweep)
L	Displacement of the upper plate (shear strain sweep)
H	Gap between plates (shear strain sweep)
σ_0	Amplitude of shear stress (shear strain sweep)
δ	Phase lag relative to the strain (shear strain sweep)
G'	Shear storage modulus
G''	Shear loss modulus
$G(t)$	Relaxation constant
S	Gel stiffness
n	Power law constant
$G'(1)$	Storage modulus constant
$G''(1)$	Loss modulus constant
G	Relaxation constant (linear viscoelastic model)

$G(1)$	Stress relaxation constant (Lodge rubberlike model)
$\mathbf{C}$	Right Cauchy-Green tensor
$\mathbf{C}^{-1}$	Inverse of the right Cauchy-Green tensor
t	Present time
t'	Reference time
$\mathbf{B}$	Left Cauchy-Green tensor
$\mathbf{F}$	Deformation gradient
$\mathbf{F}^{\mathrm{T}}$	Transpose of matrix of the deformation gradient $\mathbf{F}$
$\mathrm{d}\mathbf{x}'$	Original distance
$\mathrm{d}\mathbf{x}$	Deformed distance
$\lvert\mathbf{C}\rvert$	Determinant of tensor $\mathbf{C}$
$\mathrm{adj}[\mathbf{C}]$	Adjoint of tensor $\mathbf{C}$
x_1', x_2' and x_3'	Coordinates of unstretched block
x_1, x_2 and x_3	Coordinates of stretched block
$\Delta x_1', \Delta x_2'$ and $\Delta x_3'$	Dimensions of unstretched block
$\Delta x_1, \Delta x_2$ and Δx_3	Dimensions of stretched block
α_1, α_2 and α_3	Ratio of x_i and x_i', where $i = 1,\ 2$ or 3
λ	Stretch ratio
$\Gamma(a)$	Gamma function
$\Gamma(a,s)$	Incomplete Gamma function
f	Damage function (Lodge rubberlike model)

σ_D	Damaged true stress (Lodge rubberlike model)
τ_D	Damaged shear stress (Lodge rubberlike model)
$g(t)$	Prony series time function
ξ_i	Relaxation time constant (Prony series)
g_i	Dimensionless time constant (Prony series)
g_∞	Infinite dimensionless time constant (Prony series)
G_i	Modulus of the i^{th} spring (Prony series)
G_∞	Modulus of the infinite lone spring (Prony series)
G_0	Instantaneous modulus (Prony series)
σ_0	Instantaneous true stress (visco-hyperelastic model)
P_0	Instantaneous nominal stress (visco-hyperelastic model)
dW	Work performed on the system by the surroundings (First law of thermodynamics)
dU	Differential change in internal energy (First law of thermodynamics)
dQ	Differential change in heat (First law of thermodynamics)
W	Strain energy function
I_1, I_2 and I_3	First, second and third strain invariants (hyperelastic model)
λ_1, λ_2 and λ_3	Stretch ratios in the three principal axes (hyperelastic model)
μ	Instantaneous initial shear modulus (van der Waals hyperelastic model)
λ_m	Locking stretch constant (van der Waals hyperelastic model)

a	Global interaction parameter (van der Waals hyperelastic model)
$\varepsilon^n_{plastic}$	Plastic true strain (Viscoplastic model)
$\varepsilon^n_{elastic}$	Elastic true strain (Viscoplastic model)
ε^n_{total}	Total true strain (Viscoplastic model)
$\mathbf{t}$	Nominal traction stress vector (traction-separation law)
$\mathbf{K}$	Coefficient tensor (traction-separation law)
$\boldsymbol{\delta}$	Separation vector (traction-separation law)
t_n^o	Critical normal stress (traction-separation law)
G_c	Energy release rate (traction-separation law)
δ_c	Critical separation (traction-separation law)
$\boldsymbol{\sigma}_E$	Hyperelastic stress tensor (PTT model)
$\boldsymbol{\sigma}_v$	Viscoelastic stress tensor (PTT model)
$G^*(\omega)$	Complex modulus (PTT model)
$\eta^*(\omega)$	Shear viscosity (PTT model)
γ_s	Strain at which shear thinning occurs (PTT model)
m	Exponent (PTT model)
γ_p	Strain at which “rupture” occurs under shear (PTT model)
$\boldsymbol{\sigma}$	Stress tensor (Pom-Pom model)
$\mathbf{S}$	Orientation tensor (Pom-Pom model)
ϕ	Backbone stretching parameter (Pom-Pom model)

$\mathbf{A}_{(1)}$	Evolution of orientation tensor (Pom-Pom model)
$\mathbf{I}$	Identity tensor (Pom-Pom model)
∇v	Tube deformation rate vector (Pom-Pom model)
λ_s	Characteristic stretch relaxation time scale (Pom-Pom model)
q	Stretch limit (Pom-Pom model)
x_d	Experimental data point (RMSPE Equation)
x_m	Model data point (RMSPE Equation)
n	Total data points (RMSPE Equation)
r	Ratio of two successive relaxation time constant
σ_{Mises}	Von Mises stress
τ_{crit}	Critical shear stress (Coulomb friction model)
μ	Coefficient of friction (Coulomb friction model)
τ_{max}	Critical shear stress limit (Coulomb friction model)
$\bar{\dot{\varepsilon}}$	Average strain rate for extrusion test
S	Extrusion speed
D_b	Die entry diameter
D_a	Die exit diameter
α	Half of entry angle
R	Extrusion ratio
A_b	Cross-sectional area of billet
A_a	Area of the extrudate at die exit

Abbreviation

CSSR	Constant Shear Strain Rate
LAOS	Large Amplitude Oscillatory Shear
Cryo-SEM	Cryogenic Scanning Electron Microscopy
USDA	United States Department of Agriculture
NABIM	National Association of British and Irish Millers
HMW	High Molecular Weight
LMW	Low Molecular Weight
TEM	Transmission Electron Microscopy
GAB	Guggenheim-Anderson-de-Boer
FiSER	Filament Stretching Rheometer
CFE	Cylindrical Flared End
PTFE	Polytetrafluoroethylene
LVR	Linear Viscoelastic Region
SAOS	Small Amplitude Oscillatory Shear
PTT	Phan-Thien Tanner
PMMA	Polymethylmethacrylate
FE	Finite Element
CTSR	Constant True Strain Rate
CCS	Constant Crosshead Speed
ALE	Arbitrary Lagrangian-Eulerian

Chapter 1. Introduction

1.1 Overview of Bread-Making Process

Bread-making is the process of producing bread using wheat flour and water. It is considered as one of the oldest food manufacturing techniques, dating back from the period of ancient Egypt, as shown in Figure 1.1(a). A systematic procedure of bread-making by ancient Egyptians in Figure 1.1(a) shows the complexity of the procedure, starting from pounding the grain, mixing and kneading the dough, and baking (from top left to top right in Figure 1.1(a)). The middle left image in Figure 1.1(a) shows the workers making the bread into different shapes, and containers of water used for dough mixing are shown in the middle right image. The bottom images in Figure 1.1(a) show the workers milling the grain into flour using a grindstone equipment before making the bread (from bottom right to bottom left in Figure 1.1(a)) An example of bread produced by ancient Egypt is shown in Figure 1.1(b), dating back to 1500 BC. Meanwhile, the bread-making history in Europe started as early as the Pompeii era, as shown in the painting of “House of Baker” in Figure 1.1(c).

(a)

(b)

(c)

Figure 1.1. (a) Ancient Egypt bread-making process [Touregypt 2010]; (b) bread produced by ancient Egypt, dating back to 1500 BC [British Museum 2010]; and (c) the painting of “House of Baker” [BBC 2010].

In modern day bread-making, an automated bread-making process has been employed to cope with the increasing demands on bread production volume. An example of an automated dough-making manufacturing line which consists of mixer, extruder, sheeter and cutter is shown in Figure 1.2.

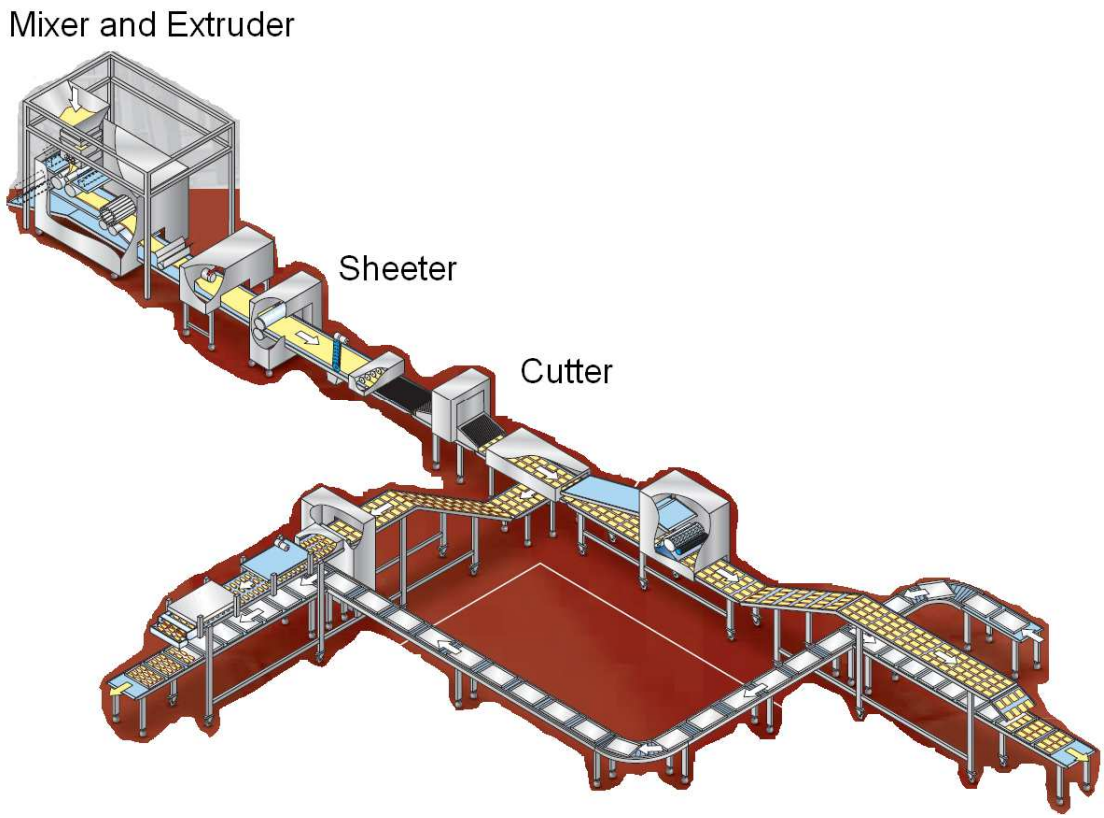

Figure 1.2. Modern dough production line [Rondodoge 2010] from mixing to cutting processes.

Even though the dough-making process has become automated, information about the mechanical/ rheological behaviour of wheat flour dough and its influence towards the process is less understood. Since a modern manufacturing line produces a large volume of dough at a time, a detailed understanding of the rheological behaviour of dough is important to produce a consistent dough quality. In addition, a non-uniform shape of bread causes difficulties in packaging and could be less appealing to consumers.

In a large scale mixing process, food technologists need to spend a large amount of dough to find the optimum mixing parameters using trial and error methods. This is

because under-mixed or over-mixed dough has less elasticity than ‘optimum-mixed’ dough produced with ‘optimum’ mixing parameters. The under-mixed or over-mixed dough may not rise properly during proofing and baking [Dobraszczyk and Morgenstern 2003], which would produce bread that crumbles when consumed by humans or stales quickly.

Bread-making is still being seen as an art or craft rather than a scientific approach [Hicks and See 2010], where most of the process relies on the experience of the bread-maker. Therefore research into dough rheology is needed to replace current empirical and ‘trial and error’ approaches.

1.2 Project Aims and Objectives

1.2.1 Previous Studies on Wheat Flour Dough at Imperial College

Studies on wheat flour dough comprising of experimental, analytical and numerical analyses have been conducted at Imperial College for several years. The results from this work are summarised in the following publications: “The biaxial deformation of dough using bubble inflation technique” [Charalambides *et al.* 2002a; Charalambides *et al.* 2002b], “Effect of friction on uniaxial compression of bread dough” [Charalambides *et al.* 2005] and “Large deformation extensional rheology of bread dough” [Charalambides *et al.* 2006]. The information from the mechanical characterisation was used to predict the behaviour of wheat flour dough during sheeting [Xiao *et al.* 2007] and extrusion [Wanigasooriya 2006]. This thesis will investigate the mechanical behaviour of wheat flour dough using experimental work described in all these publications, followed by a suitable constitutive model which will be developed based on the microstructure theory of wheat flour dough [Amemiya

and Menjivar 1992; Dobraszczyk and Motgenstern 2003]. A continuum material model will then be developed for a processing study of dough, specifically the extrusion process.

1.2.2 Problem Statements

Wheat flour dough is a viscoelastic, i.e. a time dependent behaviour material which is subjected to large deformation during processing. To obtain an accurate material model for dough is complicated due to factors like the highly non-linear stress strain relationship at large deformations, time dependent behaviour and the possible change in microstructure at large deformation. These have caused difficulties in achieving a consistently high quality in the final baked product. Many rheological tests of dough reported in the literature are inappropriate in predicting the end use quality since the tests do not measure the system under appropriate deformation conditions (i.e. compression tests in laboratory at <10 mm/s [Kouassi-Koffi *et al.* 2010] compared to industrial dough sheeting rate at >500 mm/s [Rondo 2012]) and do not account for the microstructure of dough responsible for the baking quality [Dobraszczyk and Motgenstern 2003].

In addition, the rheological properties of dough cannot be determined accurately with one of the simpler suggested constitutive models, namely the Lodge rubberlike model [Tanner *et al.* 2008] or the Phan-Thien-Tanner (PTT) model [Phan-Thien *et al.* 1997]. These models as well as others currently available, only focus on the dough behaviour in terms of time and deformation without taking into consideration the microstructure of dough. This in turn causes incomplete understanding of the behaviour of dough during the processing. It is suspected that the differences in the

stress-strain results at low and large deformation of dough [Uthayakumaran *et al.* 2002] are due to the interaction among different components of dough microstructure, i.e. starch and gluten.

1.2.3 Research Objectives

The aim of this research project is to investigate the mechanical behaviour of wheat flour dough using mechanical loading tests. The effect of deformation on the microstructure of dough, i.e. starch and gluten, will be investigated. This includes the mechanical properties of dough, gluten and starch under various deformation modes, namely under uniaxial compression, uniaxial tension and simple shear. Microstructure studies using Cryogenic Scanning Electron Microscopy (Cryo-SEM) will be conducted to investigate the effect of deformation on the microstructure of wheat flour dough.

The information from the mechanical tests and Cryo-SEM results are then used to establish constitutive laws which capture the non-linear response of the material. This includes rheological and micromechanical models, which can be employed in the finite element method. The micromechanics model will take into consideration the non-linear response of dough constituents, i.e. starch and gluten, and the interface between the constituents. Finally, the simulation of extrusion is performed using the finite element method, where demonstration of the predictive capability of a continuum numerical model with small scale experimental results is performed.

1.3 Project Outline

The thesis is separated into seven chapters. Chapter 1 discusses an overview of the bread-making process and description of the project. Chapter 2 summarises microstructure and mechanical testing studies of dough from previous literature. This is followed by Chapter 3 which describes in detail various material models that have been suggested for dough and were also investigated in the current work. This includes the Lodge rubberlike, visco-hyperelastic, viscoplastic and micromechanics models. Chapter 4 then explains the sample preparation for dough, gluten and starch, and experimental methods under uniaxial compression, uniaxial tension and simple shear. Cryo-SEM test procedures are also explained in this chapter. The experimental results for gluten, starch, and dough are shown and discussed in the same chapter. Information from the experimental results is used in Chapter 5 for constitutive modelling using different material models, namely the Lodge rubberlike and the micromechanics models. In particular, the micromechanics model will take into account the interface between starch and gluten. Chapter 6 focuses on the numerical study of ram extrusion of dough, where comparisons are performed between continuum models and experimental results by Wanigasooriya [2006] and Lim [2007]. Finally Chapter 7 concludes the thesis and describes possible future investigations.

Chapter 2. Mechanical Characterisation and Microstructure of Wheat Flour Dough

2.1 Introduction

The stress-strain relationship describes the amount of deformation in a material which is subjected to an external force or vice versa. Accurate stress-strain measurements are important to ensure the stress-strain results obtained represent the mechanical behaviour of a material. To obtain this, careful sample preparation and mechanical test procedures are needed, especially for soft solid materials like wheat flour dough [Dus and Kokini 1990].

An investigation on the mechanical behaviour of wheat flour dough is performed to understand the behaviour of dough during processing and baking. It is important to be able to measure the mechanical properties so that constitutive models can be developed that can predict dough behaviour under different loading conditions. The model can then be used to simulate processes of wheat dough, i.e. sheeting and extrusion. For example, a method of using rubber elasticity and viscoelasticity has been employed to represent the mechanical behaviour of dough [Charalambides *et al.* 2006], which was then applied in a simulation of dough sheeting using the finite element method [Xiao *et al.* 2007].

The mechanical behaviour of dough can be characterised using extensional and shear tests. Extensional tests are performed under uniaxial compression, uniaxial tension and bubble inflation modes. Shear tests on the other hand are performed using rheometers under strain sweep and frequency sweep modes at small deformation

[Phan-Thien and Safari Ardi 1998; Ng and McKinley 2008; Lefebvre 2009] and constant shear strain rate (CSSR) mode at large deformation. Shear tests at oscillatory large deformation, i.e. Large Amplitude Oscillatory Shear (LAOS) were performed by Phan Thien *et al.* [2000] and Ng *et al.* [2011]. The advantage of readily available equipment like the rheometers attracts researchers to include shear properties in dough studies.

The stress-strain relationship of dough is studied under small and large deformations. Uthayakumaran *et al.* [2002] observed differences in the stress-strain results at low and large deformation, which are believed to be due to the interaction among different components of dough microstructure, i.e. starch and gluten. Amemiya and Menjivar [1992] on the other hand believe that the stress-strain relationship of dough can be described using a microstructure based theory. Therefore in this chapter, the microstructure of wheat flour dough is discussed first, with dough being a composite of two main constituents, namely starch and gluten. This is followed by a discussion on the water distribution between gluten and starch during mixing from literature. Mechanical tests on dough are described next, namely under uniaxial compression, uniaxial tension and shear rheometry modes. Finally Cryogenic Scanning Electron Microscopy (Cryo-SEM), a technique to observe the microstructure of dough is discussed.

2.2 Microstructure of Wheat Flour Dough

2.2.1 Wheat Flour

Before discussing the microstructure of wheat flour dough, it is worth mentioning wheat, a cereal grain used to make wheat flour. The United States Department of

Agriculture (USDA) classifies six classes of wheat, namely Hard Red Spring, Hard Red Winter, Hard White, Soft White, Soft Red Winter and Durum [USDA 2011]. The classes of wheat in the USA depend on where the wheat is grown, i.e. Hard Red Winter is primarily grown in Texas, whereas Hard White and Soft White in Washington, Oregon, Idaho and Michigan.

The National Association of British and Irish Millers (NABIM) on the other hand, classify wheat into four different groups consisting of thirty wheat varieties in total [NABIM 2011]. Examples of the wheat varieties include Solstice and Hereward in Group 1, and Cordiale and Einstein in Group 2. The wheat varieties are assessed based on the wheat growing conditions and feedback from milling companies in the UK. The classification is performed to guide the milling companies. There are thirty companies associated with NABIM in 2011 [NABIM 2011]. The milling companies select specific wheat varieties and process them for commercial markets. The most commonly available wheat flour types in the commercial market are, for example strong wheat, plain and self-raising flour. These types of flour are normally used for different products, i.e. the strong wheat flour is used to make bread, plain flour for biscuits and pastry, and self-raising flour for cakes.

The main components in wheat flour are starch (68-76 % w/w), gluten (6-18 % w/w), and lipids, ash and gum (3-4 % w/w) [Figoni 2011]. The actual percentage of flour components depends on the type of the flour, i.e. Uthayakumaran [2002] measured the gluten content of Australian Strong and Bakers flour type as 13.9 % and 12 % respectively. Most of the rheological work on wheat flour dough has been focussed on starch and gluten, since these are the largest constituents of wheat flour

[Uthayakumaran 2002; Ng 2007]. A detailed explanation of the microstructure of gluten and starch will be provided in Sections 2.2.3 and 2.2.4 respectively.

2.2.2 Dough Mixing

Wheat flour dough produced in industry normally consists of wheat flour, water, salt, yeast, emulsifier and sweetener. To provide a simpler mechanical/rheological study, only a simple mixture of wheat flour, salt (sodium chloride) and water are considered in this study. Mixing is often performed in laboratories using a mixer which has the capability to record the torque response over mixing time in order to determine the optimum mixing time. The mixing time and hence energy provided during mixing of dough is important because undermixed or overmixed dough will influence the mechanical behaviour of dough. This is because the main dough components, i.e. starch and gluten get hydrated and develop interactions [Amemiya and Menjivar 1992; Goesart *et al.* 2005] during the mixing process. An example of mixing torque versus time plot for a sample of dough is shown in Figure 2.1(a) [Wanigasooriya 2006]. The dough was mixed at a constant speed of 118 rpm using a planetary pin mixer. The mixer consists of four planetary pins on the head revolving around two stationary pins at the bottom of the mixing bowl, as shown in Figure 2.1(b).

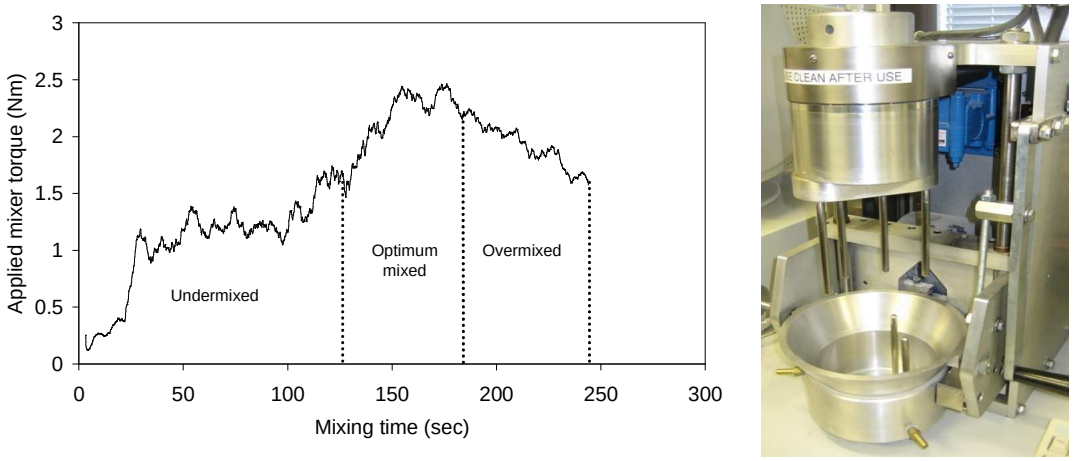

(a) (b)

Figure 2.1. (a) Mixograph output of flour dough by Wanigasooriya [2006] at a constant speed of 118 rpm; and (b) the planetary pin mixer used by Wanigasooriya [2006]. A mixture of 62 % w/w, 37.5 % w/w and 0.5 % w/w of wheat flour, water and salt respectively was used to make the dough for graph in (a).

The graph in Figure 2.1(a) can be separated into three regions: undermixed, optimum mixed and overmixed. At the beginning of the mixing stage, the resistance towards deformation of dough is low, as indicated by the low torque values in the undermixed region. In this stage, hydration of starch and gluten occurs, followed by a mechanical development of the gluten network and starch [Zheng *et al.* 2000; Dobraszczyk and Mortgenstern 2003]. The mechanical development results in an increase in dough resistance to deformation, as shown by the increasing torque at increasing mixing time (>100 seconds mixing time) in Figure 2.1(a). The torque then peaks at the optimum mixed region, a region also known as peak dough development [Zheng *et al.* 2000]. This occurs at a mixing time range of 150-170 seconds in Figure 2.1(a). Further mixing causes a reduction in the torque value, which is believed to be caused by the large gluten network being broken into smaller networks due to mechanical force [Zheng *et al.* 2000], and possibly damage of the starch and gluten interface.

2.2.3 Gluten

Gluten is a major protein in wheat flour dough, which consists of two major subcomponents, glutenin and gliadin. Glutenin is a protein consisting of 20 % high molecular weight (HMW) subunits and 80 % low molecular weight (LMW) subunits [Edwards *et al.* 2003]. Glutenin is responsible for the firmness of dough in bread making because it increases the stability of dough through a three dimensional network that forms between the protein molecules during the kneading process [Pfluger 2009]. Gliadin is a glycoprotein present in wheat and it is around 60 % soluble in ethanol. These proteins are essential in giving breads the ability to rise properly and fix their shapes on cooking [Pfluger 2009]. Schematic images of glutenin and gliadin structures are shown in Figure 2.2. Glutenin consists of long fibers (Figure 2.2(a)), whereas gliadin is the short twisted fibers located between the long glutenin fibers (Figure 2.2(b)).

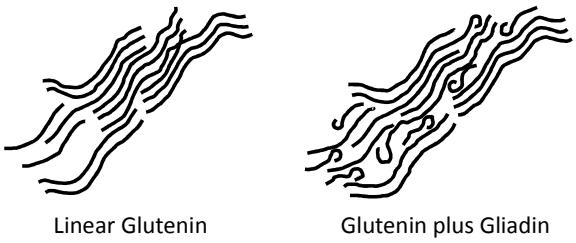

Figure 2.2. Images of: (a) glutenin; and (b) glutenin and gliadin (reproduced from Edwards *et al.* [2003]).

The mechanical behaviour of wheat gluten has been investigated by previous researchers [Singh and MacRitchie 2001; Ng and McKinley 2008; Uthayakumaran *et al.* 2002]. Singh and MacRitchie [2001] described the extension of large glutenin molecules in terms of rubber elasticity by describing the entanglement of glutenin

chains. Dobraszczyk and Mortgenstern [2003] on the other hand described how the presence of chain branches gives rise to strain hardening, which is a necessary property for the stability of polymers that undergo large deformation. These studies suggest that gluten can be treated as a rubber-like material. However it should be noted that gluten is different than some conventional rubbers (i.e. natural or synthetic rubber) since gluten absorbs water for hydration during mixing of dough, as well as having glutenin and gliadin structures.

Gluten can be prepared in either wet (also called “native”) or dry (also called “vital”) form. The extraction of gluten from wheat flour dough was first performed almost 300 years ago by an Italian named Beccari. His water-washing technique is still employed in the commercial process today. An example of the preparation of gluten in wet form is provided by Abang Zaidel *et al.* [2008], following the Standard AACC [1976] procedure. They obtained gluten from dough by washing and massaging the dough under running tap water to remove the starch. They assumed the starch was absent when cloudiness did not appear in a container of clear water after the gluten was squeezed into it. The sample obtained using this method is known as wet/native gluten. Alternatively, the wet gluten can be cut into small pieces and allowed to dry for ~24 hours at room temperature. The dried gluten can then be crushed with mortar and pestle to become powdered gluten. The powder is later mixed again with water to produce reconstituted wet gluten, also known as vital gluten.

Ng and McKinley [2008] for example mixed dry gluten with water for 12 minutes to produce vital gluten. They have found that the moisture weight content of gluten is between 60-65 % based on the observation of excess water in the mixing bowl during the gluten mixing process. When the moisture content is too low (i.e. < 60 %), the

gluten appears to be too dry, whereas when the content is too high (i.e. > 65 %), the gluten appears wet, with unincorporated water pooled at the bottom of the bowl. The mixograph output of the gluten-water mixture performed by Ng and McKinley [2008] is shown in Figure 2.3. It shows that once the mixture is fully developed, the peak to peak fluctuations remain approximately constant with no noticeable change after approximately 800 seconds. In comparison, the mixograph of flour dough in Figure 2.1(a) [Wanigasooriya 2006] shows that the peak torque drops after 200 seconds once optimum mixing is achieved. This suggests that no damage occurs in gluten compared to dough during the mixing process.

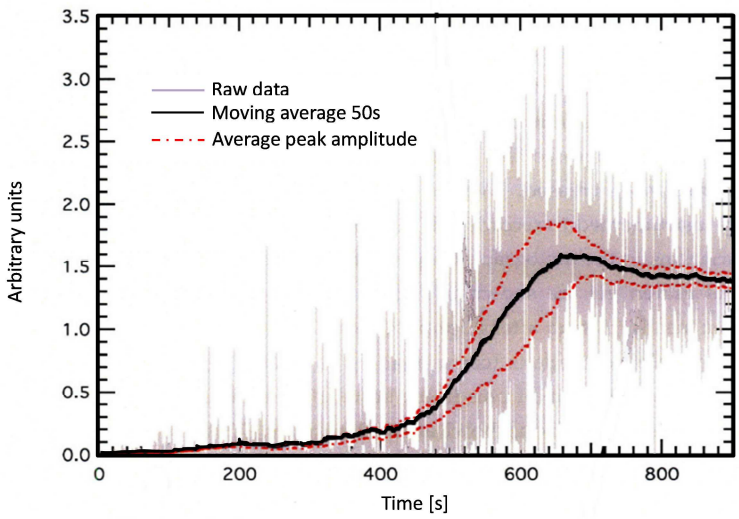

Figure 2.3. Mixograph output of the gluten-water mixture by Ng and McKinley [2008].

Native and vital gluten each have distinctive advantages and disadvantages. As a result, there is considerable debate about which is the best to represent the gluten in mixed dough. Table 2.1 provides a list of pros and cons of the wet and dry gluten sample preparation [Ng 2007]:

Table 2.1. Pros and cons of vital and native glutens.

	Vital Gluten	Native Gluten
Pros	Dry gluten can be mixed with sufficient amount of water and the mechanical work input can be recorded during the mixing process.	The network formed during mixing of dough is still retained, which enables the measurement of the properties of the gluten constituent of dough. These can be used in a composite model of dough.
Cons	Production involves drying and milling, which may irreversibly damage or alter the network of gluten that is formed upon hydration.	Difficult to maintain consistent mechanical work input and ultimate water content during manual washing and massaging the dough under running water.

Vital gluten can be prepared with a prescribed amount of water and the mechanical work input can be recorded during the mixing process. However, the disadvantage of vital gluten is that the production of dry gluten involves drying and crushing, which may irreversibly damage or alter the network of gluten that is formed upon hydration. Native gluten on the other hand still retains the gluten network formed during mixing of dough, which makes it possible to determine the properties of the gluten as it appears in the actual dough material, as indicated in Table 2.1. Therefore, in order to obtain gluten which represents the dough constituent in a real system, native gluten is preferred over vital gluten.

2.2.4 Wheat Starch

Wheat starch consists of two types [Tanner *et al.* 2011b], type A and type B. Type A is oblate in shape, while type B is circular in shape. A good review on starch is provided by Goesaert *et al.* [2005]. Starch represents the largest portion of flour [Stauffer 2007], where it comprises of amylose and amylopectin. Dry starch granules absorb water for hydration during dough mixing. The phases of starch-water at different temperatures are shown in Figure 2.4.

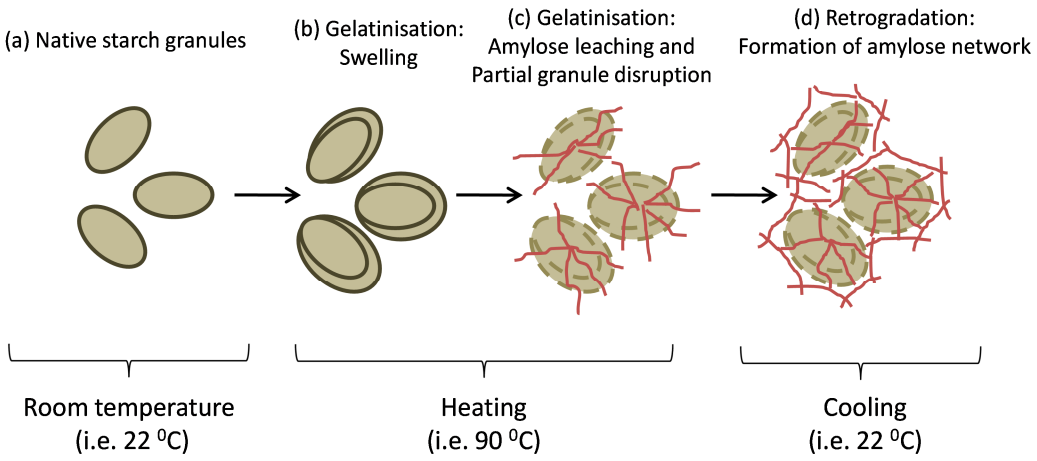

Figure 2.4. The phases of starch-water at different temperature (reproduced from Goesaert *et al.* [2005]).

Below a characteristic temperature, also known as gelatinisation temperature, the hydration process of starch is reversible, as shown in Figure 2.4(a). Gelatinisation first occurs when the starch swells, as shown in Figure 2.4(b). The gelatinisation temperature is determined using Differential Scanning Calorimetry (DSC). In Figure 2.5, the starch swelling factor investigated by Tester and Morrison [1990] is defined as: swelling factor = (swollen volume)/(initial volume of air-dried starch). The

procedure to measure the starch swelling factor is described by Tester and Morrison [1990].

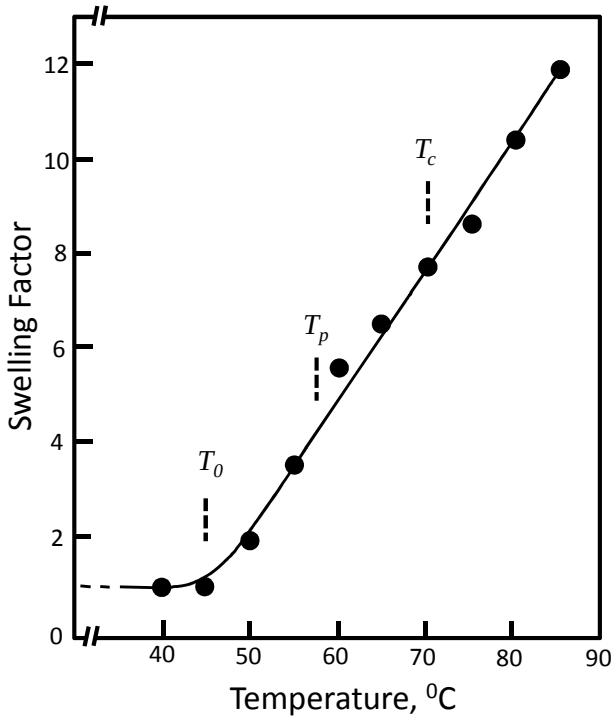

Figure 2.5. Gelatinisation in terms of swelling factor versus temperature of wheat starch (reproduced from Tester and Morrison [1990]).

In Figure 2.5, T_o , T_p and T_c represent the onset (initiation of gelatinisation), peak (mid point gelatinisation) and conclusion (complete gelatinisation) temperatures at approximately 45 ^{0}C , 60 ^{0}C and 70 ^{0}C respectively. It is observed in Figure 2.5 that starch continues to swell after the conclusion temperature. However, once starch is heated higher than 85-90 ^{0}C , it undergoes a series of changes which leads to irreversible destruction of the starch granule. This irreversible destruction is observed in amylose, a component of starch which is in crystalline form at low temperatures [Stauffer 2007]. When starch is heated, the crystalline amylose solubilises, or starts to

flow out of the starch granules [Hermansson and Svegmark 1996], as shown in Figures 2.4(c) and 2.6.

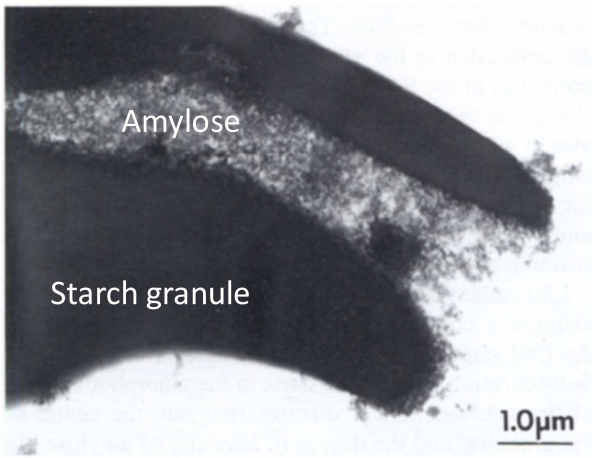

Figure 2.6. Transmission Electron Microscope (TEM) image of wheat starch granule heated at $75\ ^{0}C$ [Hermansson and Svegmark 1996]. Amylose is shown to start leaching out of through the opening of the starch granule.

If the heated starch is cooled back to room temperature, i.e. $22\ ^{0}C$, it will form an amylose network in crystalline state known as retrogradation, as shown in Figure 2.4(d). Retrogradation is also believed to cause the staling process of bread during storage [Hermansson and Svegmark 1996]. Staling is a phenomenon of bread which leads to tough crusts, with a firm and a less elastic crumb. This causes the bread to lose its moisture, flavour and texture when consumed.

2.2.5 Water Distribution between Wheat Flour Components

The water distribution between flour components, i.e. starch and gluten, needs to be known to ensure the amount of water added to flour constituents (e.g. for vital gluten) represents those in the mixed dough. A few methods are available to measure this, namely the simple liquid addition method and the water vapour absorption method

[Roman-Gutierrez *et al.* 2002a; 2002b]. To select between these methods requires information on the hydration properties of the flour components, where Roman-Gutierrez *et al.* [2002b] discussed that this depends on two factors:

1. ability of the flour components to interact with water molecules;

2. their ability to trap a large amount of water inside macromolecular complexes formed by the swollen flour components.

These factors are difficult to quantify due to the flour components (i.e. starch and gluten) competing for water during the hydration process [Ng 2007]. This in turn makes it almost impossible to determine directly the water distribution for each flour component when water is added during mixing.

Therefore assumptions are made in the methods to determine the water distribution between flour components. In the simple liquid addition method, the gluten is assumed to take the water first for hydration before the remaining water is then taken by starch. In the water vapour absorption method on the other hand, Roman-Gutierrez *et al.* [2002b] measure only the ability of the individual flour components to trap water molecules without considering any competing effects for water between the flour components.

Roman-Gutierrez *et al.* [2002b] measured the ability of the individual flour components to trap water molecules by measuring the mass of an initially dry sample (i.e. starch) placed on an atmospheric microbalance in a continuous flow of air at controlled relative humidity. The mass of water absorbed at different humidities, which is known as the water activity, a_w, was then used to determine the theoretical

distribution of water in dough through the Guggenheim-Anderson-de-Boer (GAB) model. The GAB model is described as:

$$M = \frac{\left(M_o C k a_w\right)}{\left(1 - k a_w\right)\left(1 - k a_w + C k a_w\right)} \tag{2.1}$$

where M is the equilibrium water content (% dry basis), and M_o, C and k are model parameters used to fit the experimental data. The theoretical water distribution among flour components for a strong wheat flour type was found to be approximately 88 % for starch and 12 % for gluten/others at 60 % relative humidity and 25 ^{0}C .

2.2.6 Effect of Microstructure on Stress-Strain Behaviour of Wheat Flour Dough

Two major components of wheat flour dough that are believed to influence the mechanical properties of dough are starch and gluten. On applying mechanical action during mixing, hydrated gluten aggregates partially dissociate, unfold, and stretch to form a gluten phase throughout the dough [Amemiya and Menjivar 1992]. The starch granules and gluten phase then interact by forming starch-starch, starch-gluten and gluten-gluten interactions, as shown in Figure 2.7. Starch-starch and starch-gluten interactions are an important source of elasticity in the dough based on the starch concentration present. The interactions store potential energy upon deformation and thus contribute to the elastic behaviour of dough.

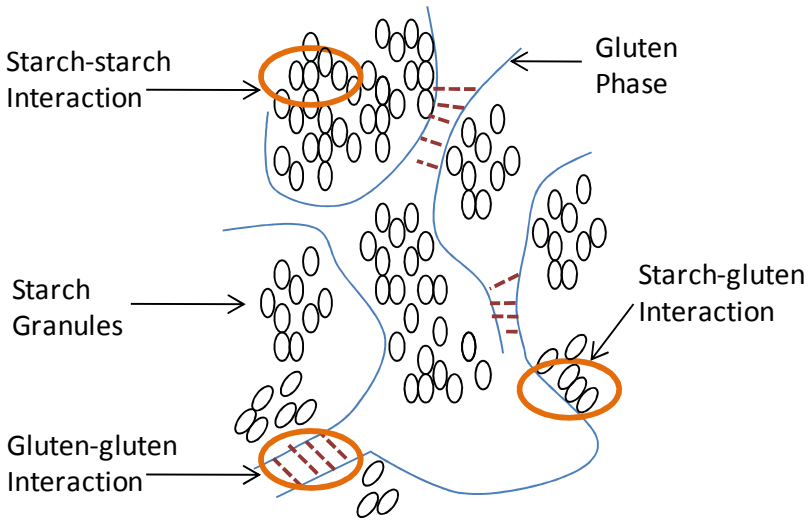

Figure 2.7. Microstructure interactions in wheat flour dough (reproduced from Amemiya and Menjivar [1992]).

The stress-strain relationship for dough can be interpreted using these interactions, as illustrated in Figure 2.8 for the simplest mode of deformation, uniaxial tension. The curve shown is one that was measured in the current work at a strain rate of 5/min. The influence of starch and gluten interactions (1, 2 and 3 in Figure 2.8(b)) on the stress-strain behaviour is discussed below. The stress-strain curve is divided into four regions; pre-yield, plateau, strain-hardening and post fracture corresponding to regions i to iv in Figure 2.8(a) respectively.

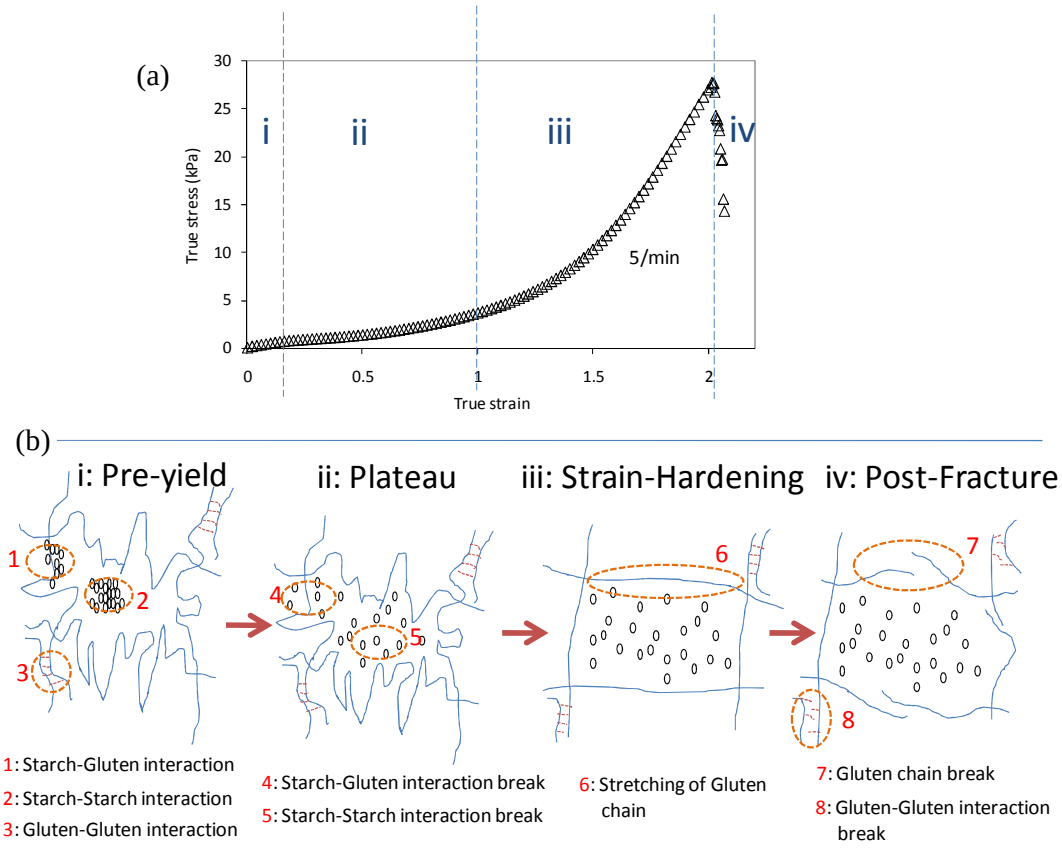

Figure 2.8. (a) Different regions of the stress-strain curve of wheat flour dough under uniaxial tension; and (b) starch and gluten interactions in the different regions ((b)i is reproduced from Amemiya and Menjivar [1992] and (b)iii from Dobraszczyk and Morgenstern [2003]). Stress and strain in Figure 2.8(a) are calculated through Equations (2.2) and (2.3) in Section 2.3.

In the pre-yield region (region i in Figure 2.8(a)), short range starch-starch and starch-gluten interactions are likely to dominate the response measured (1 and 2 in Figure 2.8(b)) whilst gluten-gluten interactions (3) have a minor effect. In the plateau region (region ii in Figure 2.8(a)), the starch-starch and starch-gluten interactions start to break down due to deformation (4 and 5 in Figure 2.8(b)). It is likely [Dobraszczyk and Morgenstern 2003], based on the theory of polymer melts, that disentanglement in gluten-gluten interactions at some point may permit the gluten chain to move about

freely and act as a viscous liquid. When the dough enters the strain hardening region (region iii in Figure 2.8(a)), the microstructure is determined by two processes: further break down of short-range interactions which cause flow, and resistance by longer-range gluten-gluten interactions (6 in Figure 2.8(b)) [Amemiya and Menjivar 1992]. When a continuous gluten phase is present, gluten-gluten interactions dominate the region and the continuous network gives rise to the strain hardening effect. This phenomenon is also known as elastomeric behaviour [Ferry 1980].

In the strain hardening region (6 in Figure 2.8(b)), the presence of chain branches is important in giving rise to strain hardening, which is a necessary property for the stability of polymers that undergo large deformation [Dobraszczyk and Morgenstern 2003]. Strain hardening in dough is thought to arise mainly from entanglement coupling of the larger gluten molecules which gives rise to the high stress observed under high strain [Singh and MacRithie 2001]. Entanglement can be viewed as one of the physical constraints between segments of the polymer chain, rather like knots, where the polymer chains lock and are not free to move past each other. This is shown in Figure 2.9.

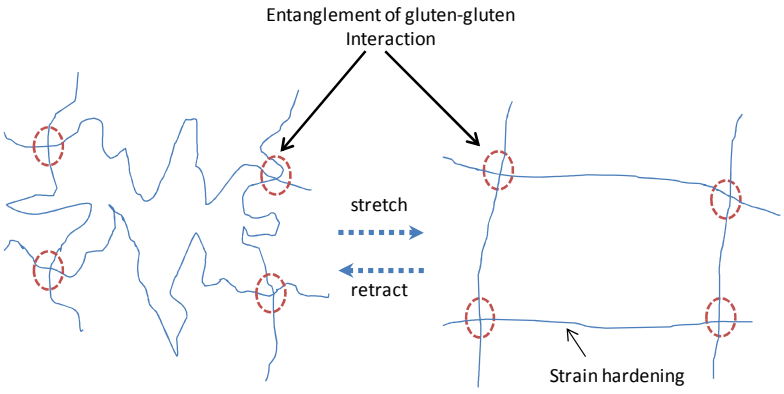

Figure 2.9. Strain hardening which is believed to be caused by entanglement of gluten-gluten interaction (reproduced from Dobraszczyk and Mortgenstern [2003]).

Strain hardening is different under extensional and shear deformation. During extensional flow, strain hardening is attributed to entanglement of long-chain molecules, whereas in simple shear the chains remain coiled and can slip past each other, giving rise to shear thinning at higher strains. Dobraszczyk and Morgenstern [2003] showed that shear and extensional viscosities are quite comparable at low deformation. However, as the deformation increases, shear and extensional viscosities deviate from each other, as shown in Figure 2.10 for biaxial extension and shear rheometry test results of wheat flour dough performed at a constant strain rate (0.1/s). In short, shear tests show shear thinning while tensile tests show work hardening. Finally, in the post fracture region (region iv in Figure 2.8(a)), the stress reaches a peak and the gluten chain and gluten-gluten interaction begin to break down (7 and 8 in Figure 2.8(b)).

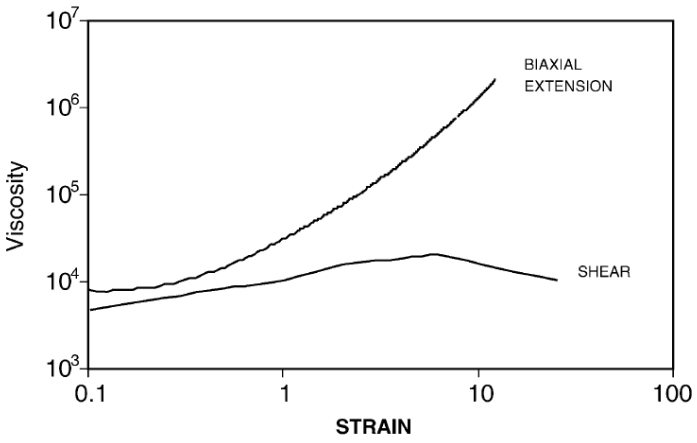

Figure 2.10. Large deformation biaxial extension and shear rheometry tests results of wheat flour dough performed at constant strain rate (0.1/s) [Dobraszczyk 2004].

2.3 Mechanical Loading Tests

2.3.1 Uniaxial Tension

The uniaxial tension tests are performed by clamping both ends of a sample and pulling them in opposite directions at a fixed rate using a testing machine. The load direction in a tensile test is opposite to the load direction in a compression test. Various methods have been employed to measure the tensile properties of dough. The challenge in uniaxial tension tests is to properly clamp the ends of a sample, especially for soft solid samples. A non-properly clamped sample causes flow at the ends, causing inconsistent strain-strain results. For example, in the "Hook design" tensile test by Toh [2000], both ends of the dough strip were clamped and extended upwards at the centre by a hook to form a V-shape, as shown in Figure 2.11(a). This technique is not accurate due to the effect of material flow at the clamped region when the strip is extended, which in turn caused inconsistent results. Ng and McKinley [2008] on the other hand used the Filament Stretching Rheometer (FiSER) for the transient tensile tests of dough. FiSER is designed to monitor in real-time the evolution of the mid-plane diameter during the experiment, as shown in Figure 2.11(b). An example of the sample deformation observed with FiSER is shown in Figure 2.11(c).

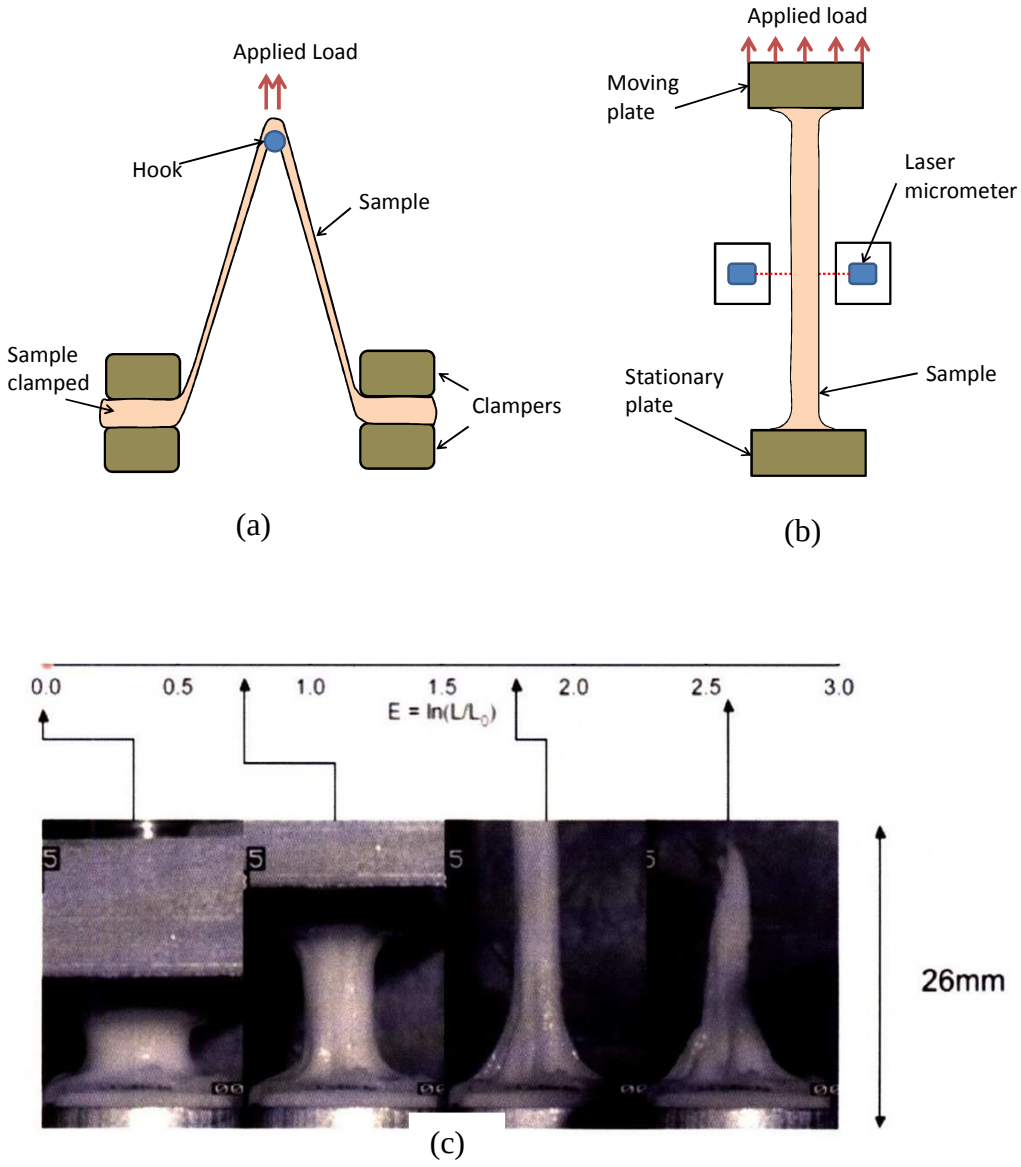

Figure 2.11. (a) “Hook design" tensile test; (b) FiSER test; and (c) observation of tensile test using FiSER [Ng 2007].

To obtain uniform deformation in dough tensile tests, Charalambides *et al.* [2006] and Wanigasooriya [2006] performed uniaxial tension tests using samples made from a dumbbell shaped mould, a cylindrical flared end (CFE) mould and an “I” shaped mould, as shown in Figure 2.12.

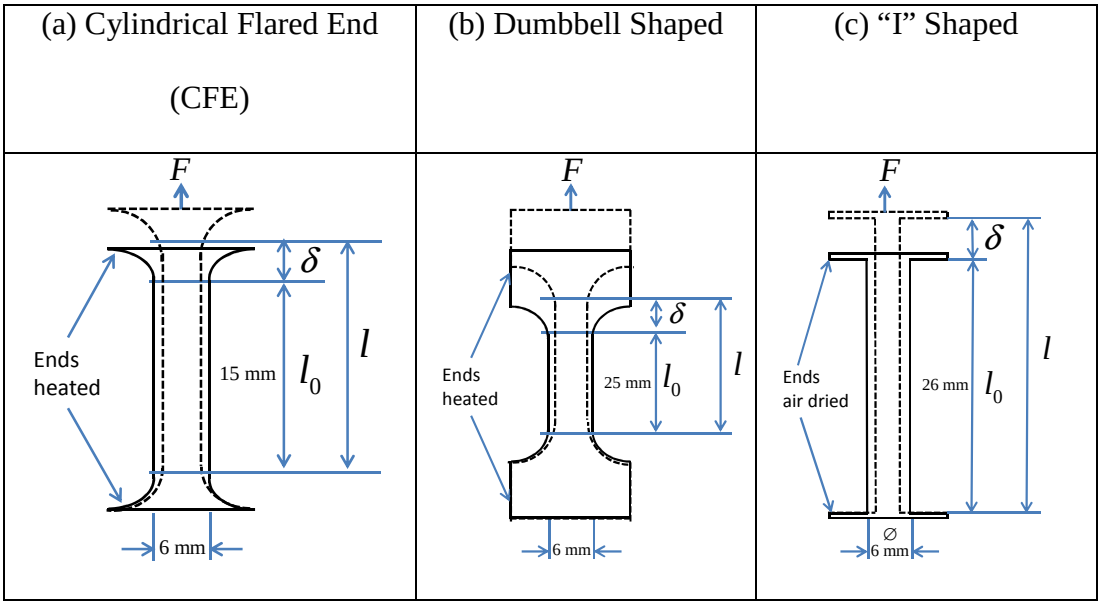

Figure 2.12. (a) Cylindrical Flared End (CFE); (b) dumbbell; and (c) "I" shaped moulds [Wanigasooriya 2006].

The tensile tests procedure is as follows. A sample of dough is placed into a mould (dumbbell, CFE or "I" shaped moulds) before the excess dough is cut off according to the shape of the mould. The sample ends are then heated (CFE and dumbbell shaped mould) or air dried ("I" shaped mould), so that the end sections harden and can be glued to the test platens. This will also ensure no flow from the sample's end during the tests. Consistent results were obtained using dumbbell shaped, CFE and "I" shaped moulds, indicating the importance of drying the ends of the sample. However, it was found that "I" shaped mould sample preparation is the fastest from the rest of the other designs and the results of the tests obtained using this geometry are comparable to the other two designs. This is because the end sections of the "I" shaped mould is thinner and quickly air dries, whereas the end sections of the other moulds require a longer time to harden from heating. An example of experimental results using "I" shaped mould is shown in Figure 2.13. A uniform deformation is

observed across the sample, as indicated by the lines marked on the sample in Figure 2.13.

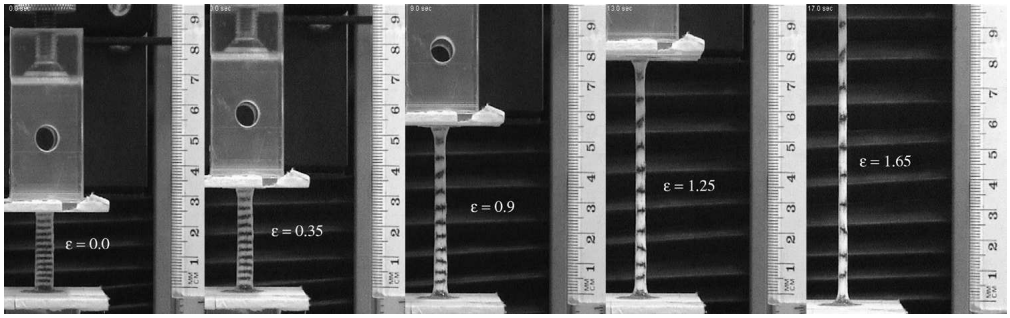

Figure 2.13. Observation of tensile test using "I" shape mould [Wanigasooriya 2006].

As shown in Figure 2.12(c), the strain, ε during uniaxial tension test for the "I" shaped geometry is described as:

$$\varepsilon = \ln \frac{l}{l_0}. \tag{2.2}$$

l_0 is the original gauge length, and l is the current length $\left(l = l_0 + \delta\right)$, with δ being the displacement. The true stress, σ is calculated as:

$$\sigma = \frac{4F}{\pi D^2} \frac{l}{l_0} \tag{2.3}$$

where D is the original specimen diameter and F is the applied load.

2.3.2 Uniaxial Compression

The main objective of compression tests is to provide a true uniaxial stress without any shear deformation taking place. It is a popular uniaxial test because it is relatively easy and simple to prepare appropriate samples for the test. There is no need to clamp

the end of the sample as in uniaxial tension tests, and only a PTFE (Polytetrafluoroethylene) ring shape mould is needed to produce a cylindrical shaped sample, as well as PTFE platens for the tests. However, the main challenge in compression tests is friction between the sample and the loading platen interface, which causes inhomogeneous uniaxial stress. This effect is also known as the "friction hill" that causes barelling of the tested specimen. For a cylindrical sample in compression, barelling is a phemonenon where the diameter half way through the length of the compressed sample being larger than the diameter at the top and bottom edges [Charalambides and Dean 1997], as shown in Figure 2.14(b). Charalambides *et al.* [2006] showed that the severity of the frictional locking (localised deformation within the specimen which causes barelling) will become less pronounced when the height of the sample is increased. For a taller sample, the frictional locking is negligible as the overall sample volume is larger than a shorter sample of the same diameter. Lubricant is used to eliminate the friction effect between the sample and the platen surface. Charalambides *et al.* [2005] for instance used 500 centistokes silicone lubricant to achieve a near frictionless compression test. They found out that no barelling is observed on the sample when the lubricant is used, as shown in the comparison of images between lubricated and non-lubricated compression tests on dough samples in Figures 2.14(a) and 2.14(b) respectively.

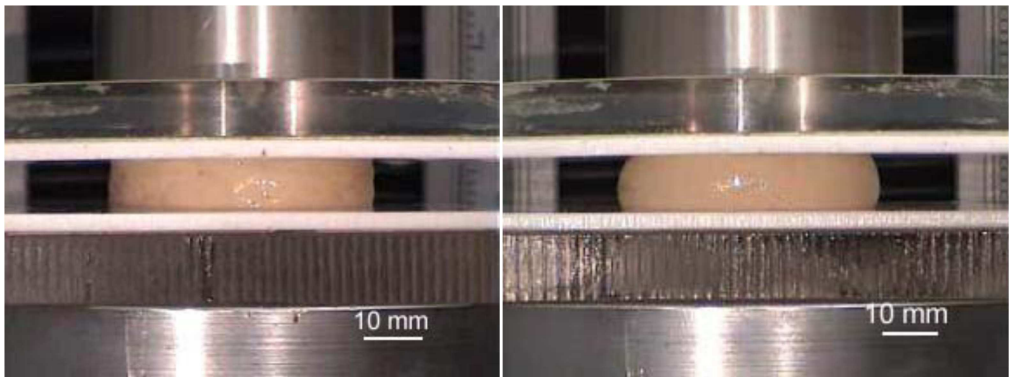

(a) (b)

Figure 2.14. Compression tests on dough samples [Charalambides *et al.* 2005] for: (a) lubricated compression; and (b) non-lubricated compression.

However, it should be noted that due to the frictional effect, compression tests can only be used to obtain stress results up to a true strain of -0.85 to -1 [Macosko 1994; Charalambides *et al.* 2006].

In a uniaxial compression test, the nominal stress, σ , can be described as:

$$\sigma = \frac{F}{A} \tag{2.4}$$

where A is the instantaneous cross-sectional area corresponding to F , the instantaneous load. The true strain ε is given by:

$$\varepsilon = \ln\left(\frac{h}{H}\right) \tag{2.5}$$

where h and H are the instantaneous and initial sample height respectively, related by $(h = H - \delta)$, with δ being the displacement. By assuming incompressibility and a homogeneous deformation of the material, the volume of a cylindrical sample remains constant during the deformation with $\pi r^2 h = \pi R^2 H$, where r and R are

instantaneous radius and initial radius of the sample respectively. The true stress can then be calculated as:

$$\sigma = \frac{F}{\pi R^2}\left(\frac{h}{H}\right) \tag{2.6}$$

Charalambides *et al.* [2005] and Wanigasooriya [2006] performed lubricated compression tests on dough samples with heights ranging from 6 mm to 20 mm, and consistent results were obtained from all the heights tested.

2.3.2.1 Compression Relaxation

Stress relaxation tests are performed to investigate the time dependent behaviour of dough. A stress relaxation test can be conducted in compression mode, where a specimen is compressed to a required strain and held fixed for a period of time while the stress decay is measured. Forces incurred during loading of dough will generate stress. Upon holding at the required strain, the stress in dough will decay over a long period of time. If the rest time is too short, a significant amount of stress inside the dough will be present, which in turn influences the stress-strain measurements. Stress relaxation can be described using phenomenological mechanical models consisting of springs and dashpots. In this work, the Prony series is used. The 1D equivalent of the Prony Series in tension consists of a series of Maxwell elements connected in parallel with a spring. This will be discussed later in Section 3.3 in the next chapter.

2.3.2.2 Compression Loading-Unloading and Recovery Tests

Loading-unloading tests are performed by applying and subsequently removing a load at a constant strain rate. In this test, a PTFE film is placed between the surface of the sample and the top loading platen. This is to prevent the top platen to stick to the surface of the sample during the unloading stage. Loading-unloading tests are very relevant to dough processing, particularly for sheeting [Xiao 2005] and extrusion processes [Wanigasooriya 2006]. In both processes, dough is subjected to loading and unloading due to mechanical contact with the processing rigs.

To determine the recovery strain on dough and gluten after loading-unloading tests, recovery tests on dough and gluten can be performed to determine the plastic strain and elastic recovery. Tanner *et al.* [2007] for example performed recovery tests on dough in tension mode by cutting the samples at the middle of the specimen under a specific strain and measured the recovery strain using a video camera. This is shown in Figure 2.15.

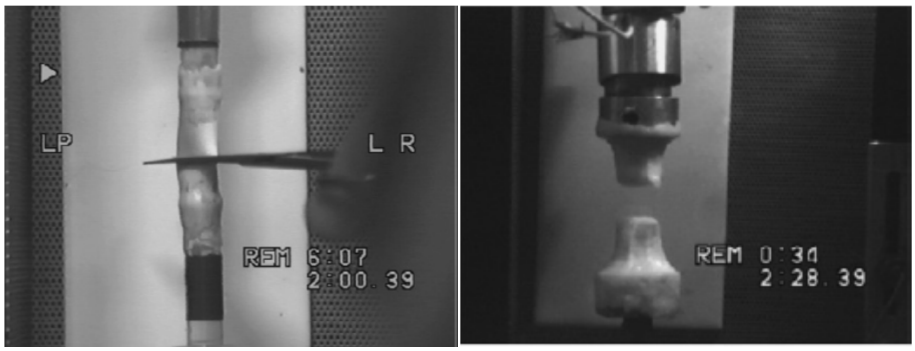

(a) (b)

Figure 2.15. Recovery test under tension mode performed by Tanner *et al.* [2007]: (a) during cutting; and (b) after cutting.

From the experimental results, Tanner *et al.* [2007] measured the recoverable strain, ε_r, which is defined as:

$$\varepsilon_r = \ln\left[\frac{\text{length after cutting}}{\text{length before cutting}}\right] \tag{2.7}$$

Equation (2.7) was then compared with the Lodge rubberlike model fitted with a damage function [Tanner *et al.* 2007], which will be discussed later in the next chapter. It is worth mentioning that the recovery test shown in Figure 2.15 does not consider the effect of gravity, which may influence the recovery strain of dough on the top and bottom portions of the specimen cut during the measurement.

2.3.2.3 Cyclic Compression and Cyclic Tension

Cyclic compression or tension tests are often performed by loading and unloading a sample under tension or compression mode at the same strain rate. The reloading curve is activated once the stress in the unloading curve becomes zero. An interesting phenomenon in cyclic test stress-strain curve is the Mullins effect. The Mullins effect [Mullins 1947] is a phenomenon of stress softening, which is commonly observed in filled elastomers as a result of damage associated with strain. An idealized response of the Mullins effect is shown in Figure 2.16.

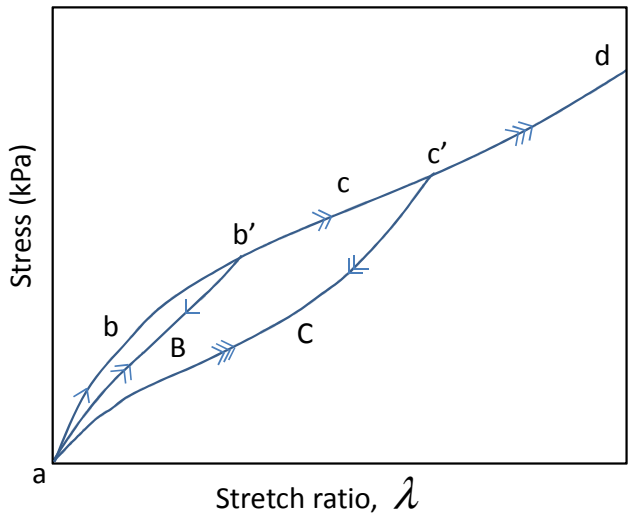

Figure 2.16. The Mullins effect for a tension test (reproduced from Ogden and Roxburgh [1999]).

Figure 2.16 shows stress versus stretch ratio, λ of the Mullins effect in simple tension. The loading paths are discussed as follows [Ogden and Roxburgh 1999]. Consider first the primary loading path (abb') during the tension test. The material will follow the $(b'Ba)$ path back to the original state. As the same material is unloaded again with higher strain, notice that the path now follows $(aBb'cc')$ as indicated from the arrow sign from (a) to (c') in Figure 2.16. If the loading is unloaded at (c'), then the new unloading path will be $(c'Ca)$. Further loading will cause the same pattern of path.

There exist several patterns of unloading and reloading curves of the Mullins effect, as shown in Figure 2.17. Figure 2.17(a) shows the Mullins effect where the reloading response coincides with the unloading response, whereas Figure 2.17(b) shows a different reloading and unloading response. A possible reason why the unloading-

reloading curve differs is because of viscoelasticity, i.e. time dependent behaviour [Kaliske *et al.* 2001]. The time-dependent behaviour can be described using a combination of serial and parallel elastic and viscous elements, or springs and dampers respectively. Details on the viscoelastic model will be described in Chapter 3.

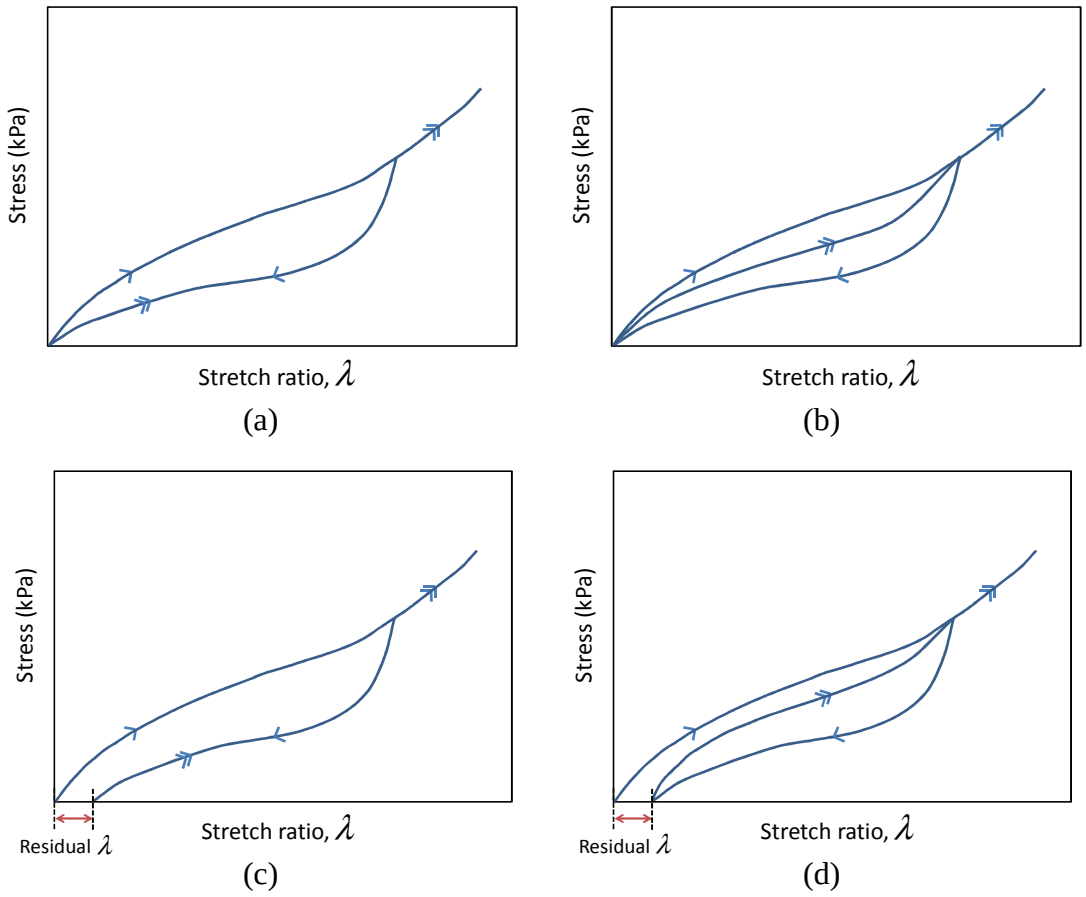

Figure 2.17. Four types of Mullins effect ((c) and (d) are reproduced from Diani *et al.* [2009]) for rubberlike materials.

Figures 2.17(c) and 2.17(d) on the other hand have similar patterns to Figure 2.17(a) and 2.17(b) respectively but they are now exhibiting a permanent set, as discussed by Diani *et al.* [2009]. The permanent set refers to the residual extension remaining after a sample is stretched and released, which is referred as the residual stretch ratio, λ, in

Figures 2.17(c) and 2.17(d). The residual stretch ratio can be measured using recovery tests discussed in Section 2.3.2.2. Diani *et al.* [2009] suggested that the reason for the permanent set is due to microstructural damage in the material. However it should be noted that permanent set for a material exhibiting the Mullins effect is very complex, since microstructure damage in a material can occur in various forms. In a filled material for example, damage can occur as debonding between filler and matrix or cracks in the matrix or filler [Mishnaevsky Jr. 2007]. This highlights the need to study the Mullins effect using a micromechanics model, which will be discussed in the next chapter (Section 3.5).

The Mullins effect has been investigated for filled rubbers [Bergström and Boyce 1998; Dorfmann and Ogden 2004] and biological material which behave like rubber, such as soft biological tissues [Bergström and Boyce 2001].

2.3.3 Shear Rheometry

Shear properties can be determined from the response of materials during angular displacement using a rheometer. The rheometer has the capabilities to control the stress and strain in either continuous or sinusoidal rotation. Two types of commercially available rheometers are the strain controlled rheometer and the stress controlled rheometer, as shown in Figure 2.18. On a strain controlled rheometer, a shear strain or shear strain rate is applied to the sample and the resulting shear stress is measured. The sample geometry in the rheometer is controlled by a strain detector attached to a motor and a strain transducer at the base. Both detector and transducer are controlled by a computer. Unfortunately, the minimum strain resolution in some instruments may not be adequately accurate to be useful and the frequency range may

also be limited [Kavanagh and Ross-Murphy 1998]. On a stress controlled rheometer, a shear stress is applied to the sample and the shear strain or shear strain rate is measured. However, the fast electronic feedback for a modern stress-controlled rheometer allows the rheometer to be used in strain-controlled mode too. This is possible when the measurements of the position and rotation rate of the spindle are precisely measured using an optical encoder and radial position transducer. The encoder and transducer are connected to a sophisticated electrical control system and data logging facilities which provide real time electronic feedback system. The electronic feedback system then allows the controlled strain mode to be performed [Barnes 2003].

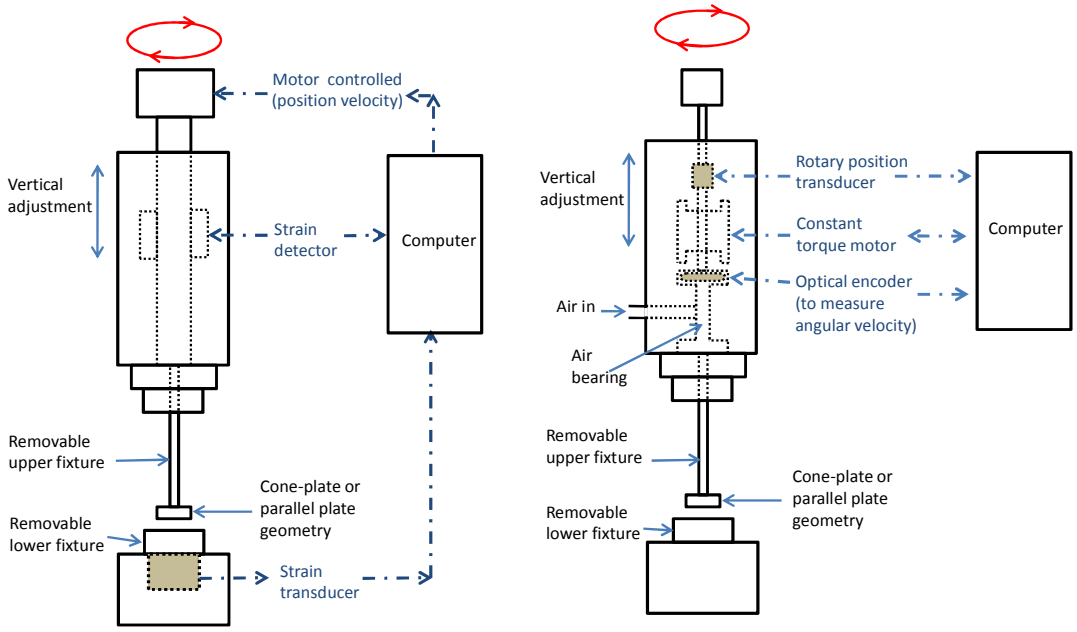

Figure 2.18. (a) Strain controlled rheometer; and (b) stress controlled rheometer (reproduced from Kavanagh and Ross-Murphy [1998]).

The most common shear tests performed on dough are frequency sweep, strain sweep and constant shear strain rate (CSSR) tests [Phan-Thien *et al.* 1997; Tanner *et al.*

2008; Ng and McKinley 2008]. Frequency sweep and strain sweep tests are performed in oscillatory mode, whereas CSSR tests are conducted under a continuous increase in shear strain. Frequency sweep tests imply monitoring the frequency response over time at a constant strain, while strain sweep tests imply monitoring the strain response over time at a constant frequency. In CSSR tests, the transient changes in shear stress are monitored as the sample is deformed over time. The configuration of all the shear tests is illustrated in Figure 2.19.

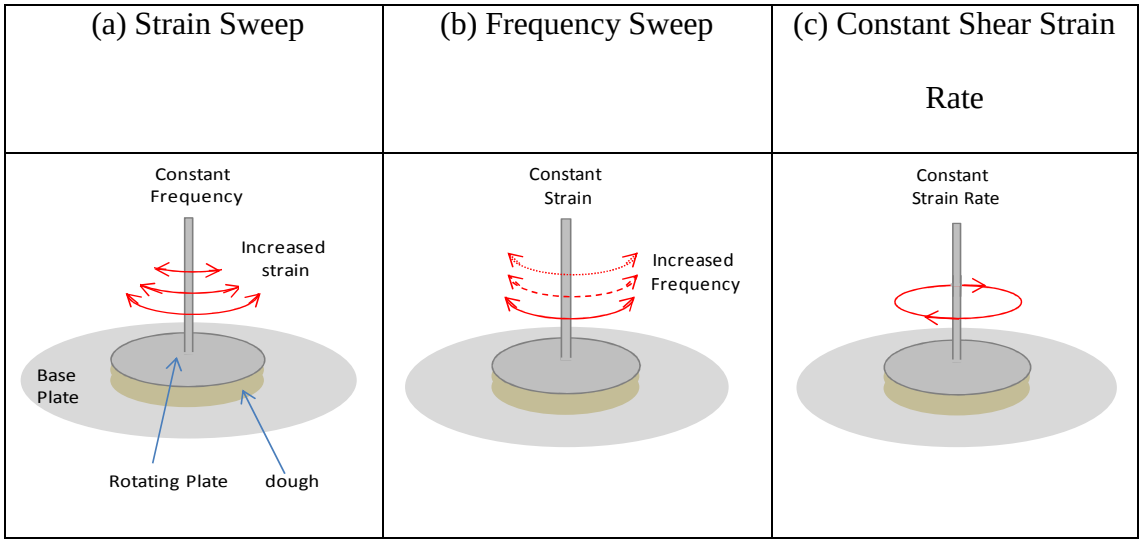

Figure 2.19. Configurations for shear tests.

Shear rheometry tests can be performed either by using cone-plate or parallel plate geometry, as shown in Figure 2.20. The difference between these two geometries will be discussed in Section 2.3.3.1. A main challenge in shear rheometry is the unwanted slippage at the edge of the sample during shear tests. Two types of forces are thought to be responsible for the slippage, the gravitational and the frictional forces. Gravitational forces cause slippage if the sample viscosity is too low [Laun 2006], whereas frictional forces cause sample slippage at high rotation speeds due to insufficient grip or friction during rotational motion. For soft solid materials, lack of

sufficient friction also causes slippage of the sample between the plates of rheometer especially when performed at high shear rates. To overcome this problem, Ng and McKinley [2008] and Tanner *et al.* [2008] used sandpapers attached on the plates of the rheometer. Another challenge is the dynamic vibration during high frequency tests. An example of this phenomenon is the effect of motor inertia during the frequency sweep tests performed at high frequency, when the inertia effect becomes dominant and influences the rheological properties of the sample tested. A study by Klemuk and Titze [2009] showed that the inertial response becomes more dominant than the material response at 62 Hz for a non-Newtonian material, i.e. Polyisobutylene solution. However, based on previous work, dough is usually tested by only up to a frequency of 30 Hz [Tanner *et al.* 2008], therefore the effect of motor inertia can be ignored.

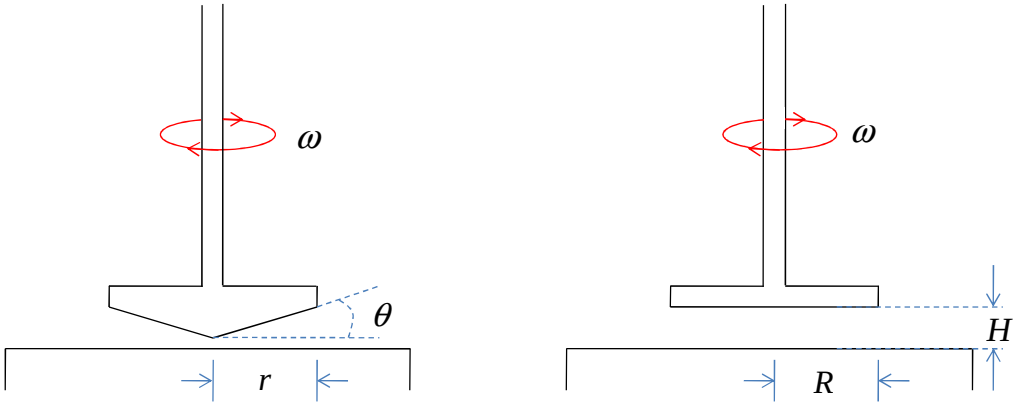

(a) (b)

Figure 2.20. Geometries of: (a) cone-plate; and (b) parallel plate rheometer.

2.3.3.1 Constant Shear Strain Rate

Constant shear strain rate (CSSR) tests are performed to measure the stress response by continuously increasing the shear strain at a constant rate. The configuration of the

tests is depicted in Figure 2.20. For cone-plate geometry (Figure 2.20(a)), the shear rate, $\dot{\gamma}$ can be calculated as:

$$\dot{\gamma} = \frac{r\omega}{r \tan\theta} = \frac{\omega}{\tan\theta} \tag{2.8}$$

where ω is the rotational speed, θ is the cone angle and r is the radius of the rotating plate. The shear strain in the cone-plate geometry is therefore uniform throughout the gap.

In parallel plate geometry, the shear strain is a function of the radius, varying from zero at the centre of the sample, to a maximum at the edge of the rotating plate, *R*. The shear rate, $\dot{\gamma}$, at the edge of a parallel plate geometry (Figure 2.20(b)) is defined as:

$$\dot{\gamma} = \frac{R\omega}{H} \tag{2.9}$$

where H is the constant gap between the upper and lower rheometer plates. Keentok and Tanner [1982] investigated shear stress using parallel plate and cone-plate geometries with different gap, H, values. They proposed a minimum gap size of 1 mm and $(H/R) \sim 0.05$, beyond which the shear stress and normal stress in the parallel plate geometry is unaffected by the gap, and a good agreement is seen between the shear stress data from cone-plate and parallel plate geometries. However, it should be noted that since measurements of shear stress in the parallel plate geometry is taken at the edge of the plate, R, edge fracture of the sample should be

avoided. Tanner *et al.* [2008] have shown that edge fracture occurs at shear strain of 20 for a dough sample.

A last note regarding the shear data is the correction needed for the apparent rim shear stress calculated by the rheometer at large shear deformations as outlined by Phan-Thien *et al.* [2000] and Ng *et al*. [2011]. The motivation for this correction is that at large strain, the material is non-linear and this might affect the accuracy of the rheometer calculations which assume a linear stress-strain relationship. The apparent shear stress for a parallel plate rheometer, τ_R calculated at the edge of the plate, R, is described as:

$$\tau_R(t) = \frac{2\Gamma(t)}{\pi R^3} \tag{2.10}$$

where $\Gamma(t)$ is the measured torque at time, t. The apparent rim shear stress is calculated by the rheometer software using the measured torque, $\Gamma(t)$, with an assumption that stress is linearly proportional to strain and its time derivative [Steffe 1996; Ng *et al.* 2011]. A corrected shear stress, τ_E is proposed by Phan-Thien *et al.* [2000] described as:

$$\tau_E = \frac{3\Gamma}{2\pi R^3} + \gamma_E \frac{\mathrm{d}}{\mathrm{d}\gamma_E}\left(\frac{\Gamma}{2\pi R^3}\right) \tag{2.11}$$

whereas Ng *et al.* [2011] proposed the following form:

$$\tau_E = \tau_R \left[\frac{3}{4} + \frac{1}{4} \frac{\gamma_E}{\tau_R} \frac{\partial \tau_R}{\partial \gamma_E} \right]. \quad (2.12)$$

Tanner *et al.* [2008; 2011a] and Macosko [1994] on the other hand proposed a simple correction, where the value of τ_E is taken to be equal to τ_R at a 3/4 radius in a parallel plate test:

$$\tau_E = \tau_R \left[\frac{3}{4} \right] \quad (2.13)$$

which means that the second term in the bracket of Equation (2.12) is neglected. By substituting Equation (2.10) into Equation (2.13), τ_E becomes:

$$\tau_E(t) = \frac{3\Gamma(t)}{2\pi R^3} \quad (2.14)$$

which is equal to the cone-plate shear stress equation [Steffe 1996]. To show the difference between the equations above (Equations 2.10 to 2.14), a constant shear strain rate (CSSR) test at 5/min was performed on a dough sample in this work. The experimental procedure of the CSSR tests is discussed in Section 4.3.3. The rheometer output shear stress-shear strain results are shown in Figure 2.21. Equations (2.10) to (2.14) are then calculated using the test data and the results are shown in Figure 2.21. It can be seen that the results using Equation (2.10) is the same as the rheometer output. Equations (2.11) and (2.12) on the other hand give a lower stress-strain curve than the rheometer output curve. Finally, the lowest stress-strain curve is obtained using Equations (2.13) and (2.14).

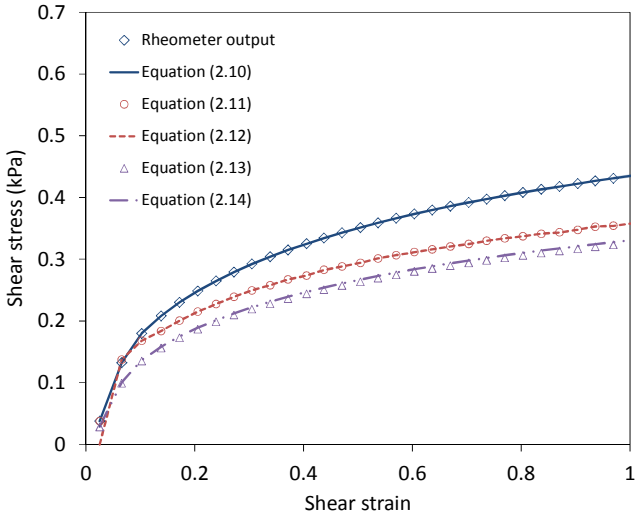

Figure 2.21. Differences of shear stress for parallel plate rheometer obtained using Equations (2.10) to (2.14).

The difference in the results obtained using Equations (2.10) to (2.14) in Figure 2.21 causes difficulties in choosing an accurate equation to measure the shear stress for the parallel plate geometry. The assumptions made by Macosko [1994] and Tanner *et al.* [2008; 2011], where the cone-plate shear stress is equal to parallel plate stress (Equation (2.14)), is not suitable since the shear strain for a parallel plate geometry is a function of the radius of the plate. Ideally, Equation (2.14) is accurate if the cone-plate geometry is used since the shear strain is constant throughout the gap (Equation (2.8)). However, if sandpapers are needed on the plate surface to prevent slippage of the sample during the tests, the parallel plate geometry is more practical [Phan-Thien *et al.* 1997; Tanner *et al.* 2008; Ng and McKinley 2008]. On the other hand, Equation (2.10) is only valid for Newtonian materials, as shown by Steffe [1996]. It is therefore concluded that the correction by Phan-Thien *et al.* [2000] and Ng *et al.* [2011] (Equations (2.11) and (2.12)) will be used on all samples tested using the parallel plate geometry.

2.3.3.2 Shear Strain Sweep

Strain sweep tests are conducted by increasing the strain in logarithmic scale at a constant frequency. Assuming a sample is located between the plates of a rotational rheometer, the strain in the material between the plates is a function of time [Steffe 1996]:

$$\gamma = \gamma_0 \sin(\omega t) \tag{2.15}$$

where γ_0 is the amplitude of the strain, which is equal to L/H when the motion of the upper plate is $L\ sin(\omega t)$. L is the displacement of the upper plate, H is the gap between the plates and ω is the frequency expressed in rad/s. The shear strain rate, $\dot{\gamma}$, then becomes:

$$\frac{d\gamma}{dt} = \dot{\gamma} = \frac{d\left(\gamma_0 \sin(\omega t)\right)}{dt} \tag{2.16}$$

which can be evaluated as $\dot{\gamma} = \gamma_0 \omega \cos(\omega t)$. In the linear viscoelastic region, the shear stress produced by the shear strain input is:

$$\sigma = \sigma_0 \sin(\omega t + \delta). \tag{2.17}$$

σ_0 is the amplitude of the shear stress and δ is the phase lag relative to the strain. Dividing both sides by γ_0 gives $\frac{\sigma}{\gamma_0} = \left(\frac{\sigma_0}{\gamma_0}\right)\sin(\omega t + \delta)$. Using trigonometry and simplifying the equation yields:

$$\sigma = G^{'}\gamma + \left(G^{"}/\omega\right)\dot{\gamma}. \tag{2.18}$$

$G^{'}$ is the shear storage modulus and $G^{"}$ is shear loss modulus expressed as:

$$G^{'} = \frac{\sigma_0}{\gamma_0}\cos(\delta) \;\; ; \;\; G^{"} = \frac{\sigma_0}{\gamma_0}\sin(\delta). \tag{2.19}$$

The linear viscoelastic region (LVR) can be defined from the graphs of $G^{'}$ and $G^{"}$ versus applied shear strain. Constant values of $G^{'}$ and $G^{"}$ over a range of shear strain indicate the LVR, i.e. as shown in Figure 2.22 for strains approximately $< 10^{-3}$.

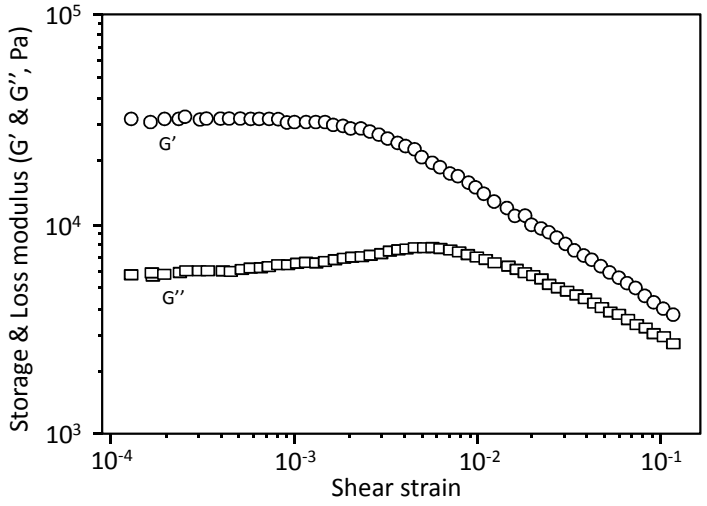

Figure 2.22. Linear viscoelastic region of dough obtained by Phan-Thien *et al.* [1997].

It should be noted that Equations (2.15) to (2.19) are not applicable beyond LVR. The study beyond LVR is known as Large Amplitude Oscillatory Shear (LAOS). Readers can refer to Ewoldt [2009] and Ng *et al.* [2011] for details of the LAOS tests and analysis.

2.3.3.3 Shear Frequency Sweep

Before describing the shear frequency sweep test, it is worth mentioning the critical gel behaviour of materials, based on the study by Winter and Mours [1997]. Consider Figure 2.23 for a material microstructure consisting of monomers. The monomers are randomly distributed without any crosslink. The monomers would flow like a liquid if diluted in a solvent. However, when the monomers are subjected to polymerisation, in which the monomers crosslink and start to form polymer networks (Figure 2.23(b)), the material would not behave as a liquid anymore but not yet as a solid. The material at this stage is known as critical gel. The relaxation modes of the material at this stage can be represented through a power law mode as [Winter and Mours 1997]: $G(t) = St^{-n}$, where $G(t)$ is the relaxation constant, S is the gel stiffness, t is time and n is the power law constant. Further crosslinks caused the monomer networks to span across the entire material, where the material now would behave like a solid, as shown in Figure 2.23(c). Dough has been shown to behave like a critical gel material, based on the work by Gabriele *et al.* [2001], Ng *et al.* [2006], Lefebvre [2009], Tanner *et al.* [2008] and Migliori and Gabriele [2010]. The critical gel behaviour of dough is caused by gluten, as shown by Ng and McKinley [2008] and Ng *et al.* [2011]. A strain value within the plateau region in the strain sweep tests (linear viscoelastic region in Figure 2.22) can then be used to perform frequency sweep tests, where the power law representation by Winter and Mours [1997] can be used to define the rheology of the critical gel material. The frequency sweep test will be discussed in detail below.

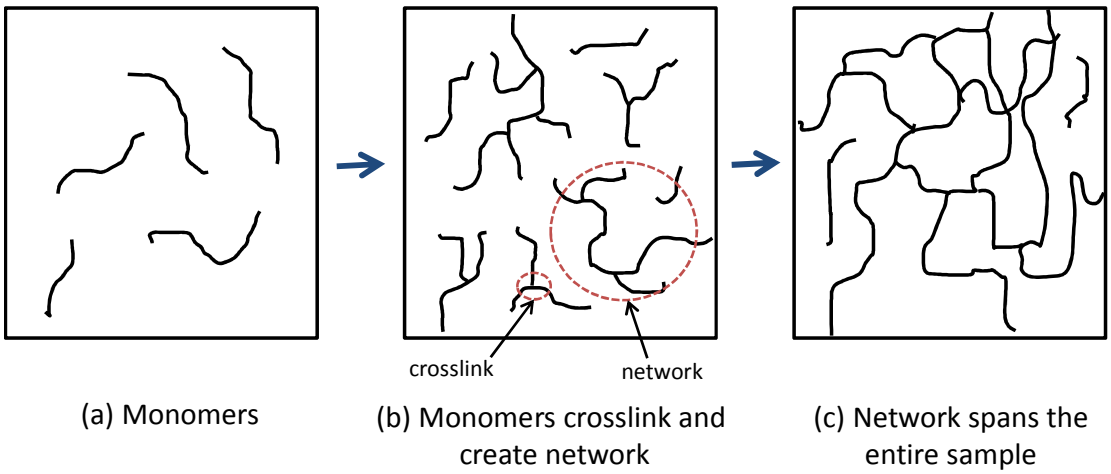

Figure 2.23. Critical gel material illustration (reproduced from Winter and Mours [1997]).

Frequency sweep tests are performed by setting a constant value of strain while frequency increases in a logarithmic scale and the stress response is measured. The strain used for the tests has to be in the linear viscoelastic region, as defined from the strain sweep tests discussed previous subsection. Frequency sweep tests for dough in the linear viscoelastic region can be described using the following function:

$$G'(t) = G'(1)\omega^n, \qquad G''(t) = G''(1)\omega^n \tag{2.20}$$

where $G'(t)$ and $G''(t)$ are the storage and loss moduli respectively, $G'(1)$ and $G''(1)$ are the storage and loss moduli constants respectively, ω is frequency and n is the power law constant. A power law can also be fitted to stress relaxation data in the form of $G(t) = G(1)t^{-n}$. The stress relaxation constant $G(1)$ is related to $G'(1)$ through [Tanner *et al.* 2008]:

$$G(1) = G^{'}(1)\frac{2(n!)}{n\pi}\sin\frac{n\pi}{2} \tag{2.21}$$

where $G(1)$ has the unit of $\left(\text{Pa}\cdot\text{s}^{n}\right)$. The relationship between phase angle δ, $G^{'}$, $G^{''}$ and n is as follows [Tanner *et al.* 2008]:

$$\tan\delta = \frac{G^{''}(\omega)}{G'(\omega)} = \tan\frac{n\pi}{2}. \tag{2.22}$$

The stress relaxation constant $G(1)$ and power law constant n can be used in the Lodge rubberlike model, which will be discussed later in the next chapter. An example of frequency sweep test results of dough performed at 0.1 % strain is shown in Figure 2.24.

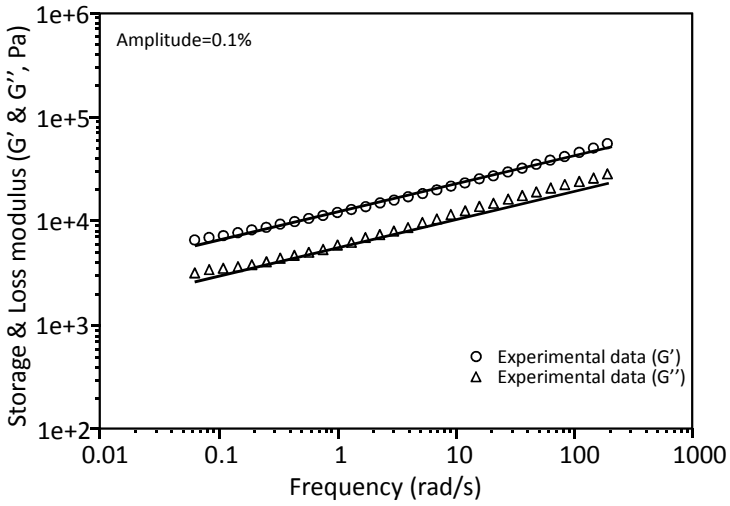

Figure 2.24. Frequency sweep test results obtained by Tanner *et al.* [2008], where $G^{'}(1) = 12.2$ kPa , $G^{''}(1) = 5.5$ kPa and $n = 0.27$ are used to fit the tests.

2.4 Cryogenic Scanning Electron Microscopy (Cryo-SEM) of Wheat Flour Dough

Cryogenic Scanning Electron Microscopy (Cryo-SEM) tests are usually performed to observe the microstructure of hydrated/soft samples. A “cold stage” is used to allow the sample to undergo rapid freezing in liquid nitrogen to avoid dehydration from the alternative chemical drying technique [James 2009]. Without dehydration, a similar structure to that observed in fresh samples can be examined [Freeman *et al.* 1991]. Images with higher magnifications than optical light microscopy can be observed using Cryo-SEM, which allow a closer inspection of the sample’s microstructure [Kontogiorgos and Goff 2006].

However, a disadvantage of the Cryo-SEM technique is the formation of ice crystals on the sample surface during rapid freezing. The ice crystals may obscure the sample’s microstructure in the Cryo-SEM chamber. To remove the layer of ice crystals from the surface, a procedure called sublimation is performed, by transferring a sample from the colder temperature stage after the rapid freezing process, to a higher reference temperature in the Cryo-SEM chamber. The sublimation process is discussed in detail in the next section.

2.4.1 Effect of Sublimation

The sublimation process can be described using the pressure-temperature diagram of water shown in Figure 2.25 [Robards and Sleytr 1985]. The diagram shows the phases of water (solid, liquid or vapour phase) at different pressures and temperatures, with the triple point and the critical point of water also being shown. The lines in the diagram indicate the boundaries between the different phases. The

triple point of water is the point that separates water from the solid, liquid and vapour phases, where these three phases coexist in thermodynamic equilibrium. The critical point of water is the point at which no phase equilibrium exist between the liquid and vapour phases. It should be noted that the triple point of water is 274.16 ^{0}C at 0.0061 bar, whereas the critical point of water is 374 ^{0}C at 218 bar.

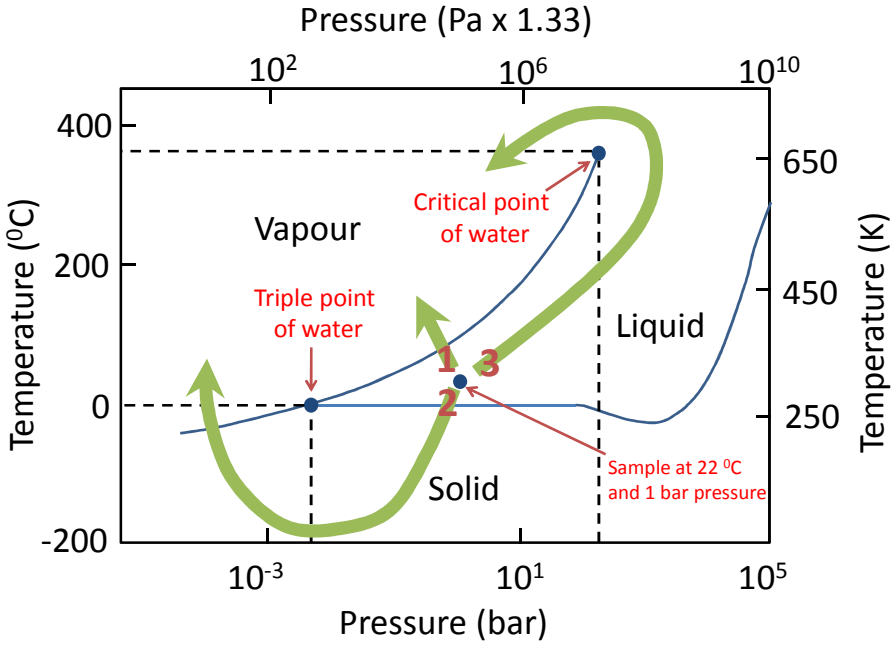

Figure 2.25. The temperature-pressure diagram for water (reproduced from Robards and Sleytr [1985]). The arrows show the possible ways of moving from the liquid phase to the vapour phase. Arrows indicate: Route 1 (air drying), Route 2 (freeze drying) and Route 3 (critical point drying) respectively. The triple point and the critical point of water are also shown.

The diagram also shows three possible routes by which water in a specimen can be removed. Route 1 involves passing through the boundary between liquid and vapour phase; this is also known as air drying. Route 2, also known as freeze-drying, involves a procedure where the liquid in the specimen is first converted into solid by

freezing, i.e. exposure to liquid nitrogen (liquid nitrogen temperature is -196 ^{0}C at atmospheric pressure). The surrounding pressure on the freezed specimen is subsequently reduced to a value much lower than atmospheric pressure, i.e. high vacuum conditions [Dunlap and Adaskaveg 1997]. When the temperature of the surrounding freezed specimen is increased under high vacuum conditions, the frozen water on the specimen surface will change from the solid to the vapour phase [Robards and Sleytr 1985] (as shown by Route 2 crossing the solid-vapour line in Figure 2.24). This procedure is known as sublimation. Note that the vacuum conditions are defined using the following standard [National Physical Laboratory 2011]: low vacuum (1×10^{5} Pa (1 bar) to 3×10^{3} Pa (0.03 bar)), medium vacuum (3×10^{3} Pa (0.03 bar) to 1×10^{-1} Pa (1×10^{-6} bar)), and high vacuum (1×10^{-1} Pa (1×10^{-6} bar) to 1×10^{-4} Pa (1×10^{-9} bar)).

Route 3 on the other hand involves replacing water in the sample with a liquid that has a lower critical point than water. When the temperature and pressure are increased above the critical point temperature, the liquid changes to vapour without overheating the specimen. This will cause a minimal effect to the surface tension of the specimen. An example of liquid used is Freon or liquid CO_2 (CO_2 critical point is 31.04 ^{0}C at 72.8 bar), which was used to examine biological specimens [Smith and Finke 1972]. Route 3 is also known as critical point drying.

For a semi-liquid specimen, the disadvantage of Route 1 is that the specimen cannot be dried directly with the liquid phase present since this can cause a very high surface tension, which in turn causes shrinkage to the specimen. Route 3 on the other hand requires the water in the specimen to be removed first. If the specimen is directly

subjected to Route 3 without removal of water, the specimen will be damaged because it needs to be heated at a very high temperature and pressure [Robards and Sleytr 1985] (critical point of water is 374 ^{0}C at 218 atm). Route 2 therefore provides an advantage where there is no need to remove water from the specimen compared to Route 3. By solidifying the specimen at a very low temperature, Route 2 provides a minimal effect of surface tension compared to Route 1. This makes it possible to observe the microstructure of a hydrated specimen, i.e. food and living cells.

Various studies on Cryo-SEM of dough were performed using different sublimation conditions. For example, Freeman *et al.* [1991] performed the Cryo-SEM using sublimation setting at -70 ^{0}C for 9 minutes, Zounis *et al.* [2002] used -65 ^{0}C for 6 minutes, Kontogiorgos *et al.* [2008] used -80 ^{0}C for 30 minutes and Yi and Kerr [2009] used -70 ^{0}C for 10 minutes. The images from these mentioned studies are shown in Figure 2.26.

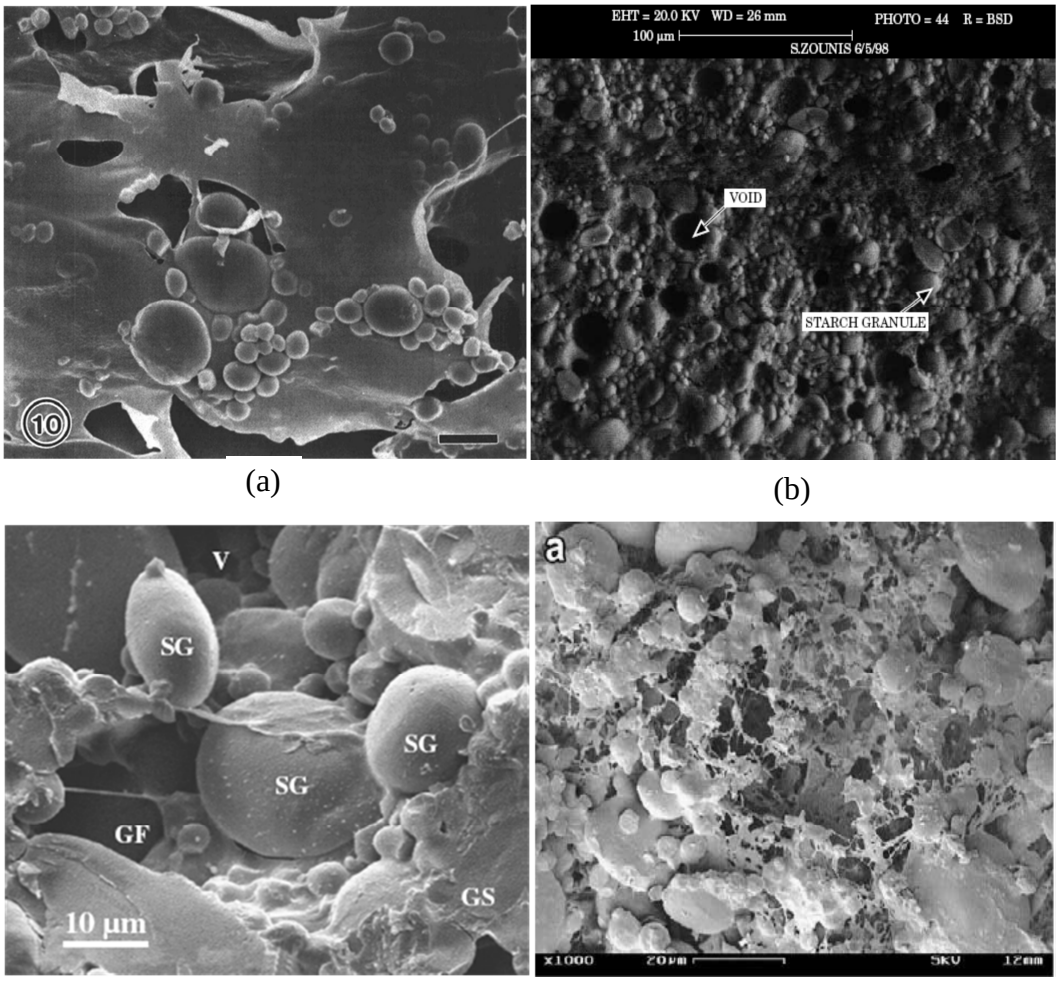

(a) (b)

(c) (d)

Figure 2.26. Images of dough observed by: (a) Freeman *et al.* [1991]; (b) Zounis *et al.* [2002]; (c) Kontogiorgos *et al.* [2008]; and (d) Yi and Kerr [2009].

It can be seen in Figure 2.26 that different sublimation settings give different results in terms of the appearance of the starch and gluten interface. In Figures 2.26(a) and 2.26(c) for example, the starch appears to be embedded in the gluten network, whereas the starch and gluten interface are not as clearly observed in Figures 2.26(b) and 2.26(d). This indicates a need to determine the best sublimation settings on a reference image, before any effect of, for example deformation, can be studied on the microstructure of dough. To the author's knowledge, no Cryo-SEM studies have been

reported focussing on the starch and gluten interface when dough samples are deformed, i.e. stretched or compressed.

2.5 Conclusion

The microstructure of wheat flour dough was discussed, which consists of starch and gluten as the main constituents. In order to obtain gluten which represents the dough in a real system, native gluten would be the best option, since the gluten network formed during the mixing of dough is still retained. This enables determination of the properties of gluten as it appears in the actual dough material. Wet starch obtained by washing of dough needs to be dried at room temperature before it can be mixed with water again to produce reconstituted wet starch. The water distribution between flour components, i.e. starch and gluten, needs to be known to ensure that the amount of water added to starch represents the constituent's water content in dough. The relationship between microstructure and stress-strain of wheat flour dough is summarised based on previous reported studies by Amemiya and Menjivar [1992] and Dobraszczyk and Motgenstern [2003].

Mechanical loading tests under uniaxial tension, uniaxial compression, and shear rheometry were also reviewed. The various possible tensile sample geometries were considered as well as the possible barelling effect under uniaxial compression, and the rheometer plate's geometry under shear rheometry tests. This is followed by a discussion on the correction needed for the apparent rim shear stress calculated by the rheometer at large shear deformations. Finally, previous studies on Cryogenic Scanning Electron Microscopy (Cryo-SEM) on dough were discussed as well as the effect of sublimation on the dough samples.

Chapter 3. Material Models for Wheat Flour Dough

3.1 Introduction

Systematic mechanical characterisation studies on wheat flour dough were first performed by Schofield and Scott-Blair in a series of publications [Schofield and Scott-Blair 1932; 1933a; 1933b; 1937]. They used a simple Maxwell fluid model to characterise the dough by considering a situation in which the relaxation time is not constant but varies with stress. However, since these studies were performed in 1930's, mathematical software like MATLAB [MATLAB 2009] and commercial finite element software like Abaqus [Abaqus 2009] were not readily available at that time. This initially made it difficult to model the Maxwell model numerically.

The idea of using the finite element method to simulate deformation of dough and processes in the dough manufacturing line is to replace a long series of large scale tests and usage of materials that would be costly and time consuming. Development of simple, quick and practical schemes to characterise the complex behaviour of dough are performed using some of the constitutive models available in commercially available finite element software packages.

This chapter reviews a few material models suitable for soft solid materials. Firstly the Lodge-rubberlike model suggested by Tanner *et al.* [2008] and Ng and McKinley [2008] is presented. This is followed by the visco-hyperelastic model [Charalambides *et al.* 2006] and the viscoplastic model. Micromechanics models are discussed next and finally the Phan-Thien Tanner [Phan-Thien *et al.* 2000] and Pom-Pom polymer [McLeish and Larson 1998] models are reviewed.

3.2 Lodge Rubberlike Model

The basic rheological model is the power law fluid, which describes stress, σ and constant strain rate, $\dot{\gamma}$, as:

$$\sigma = k\dot{\gamma}^n \tag{3.1}$$

where n is the power law constant, and k is the consistency index. This model is very simple and as a result it is widely used to model the behaviour of dough. However, the terms k and n in the model do not provide any physical meaning, and the model cannot be used to characterise complex viscoelastic behaviour. The terms only represent empirical values of the material tested.

To overcome this, the linear viscoelastic model is introduced, which can be described using the following:

$$\boldsymbol{\sigma} + p\mathbf{I} = \sigma = \int_{-\infty}^{t} G\left(t - t'\right)\dot{\gamma}dt' \tag{3.2}$$

where $\boldsymbol{\sigma}$ is stress tensor, p is the pressure, $\mathbf{I}$ is the unit tensor. For simplicity, the term $\boldsymbol{\sigma} + p\mathbf{I}$ normally used in the field of rheology is described as simply σ, which is the stress term normally used in solid mechanics. G is the relaxation function described in the range of reference time t' and time t.

Tanner *et al.* [2008] and Ng and McKinley [2008], in independent studies, included finite strain elasticity in the linear viscoelastic model, which is based on the approach by Winter and Mours [1997]. The Lodge rubberlike model is first considered in the linear viscoelastic region [Macosko 1994] using the following:

$$\sigma = \int_{-\infty}^{t} \frac{d}{dt'} G\left(t - t'\right) \varepsilon\left(t'\right) dt' \tag{3.3}$$

where σ is the stress and $\varepsilon\left(t'\right)$ is the strain as a function of time t'. Finite strain is then included in the strain function, $\varepsilon\left(t'\right)$, in Equation (3.3), which can be described as [Winter and Mours 1997]:

$$\sigma = \int_{-\infty}^{t} \frac{d}{dt'} G\left(t - t'\right) \mathbf{C}^{-1}\left(t, t'\right) dt' \tag{3.4}$$

where $\mathbf{C}^{-1}\left(t, t'\right)$ represents the inverse of the right Cauchy-Green tensor [Holzapfel 2000], which is also known as the Finger tensor [Tanner *et al.* 2008]. The strain tensor is described as relative to the present time t and reference time t' [Tanner *et al.* 2008].

The power law can be included into Equation (3.4) to yield:

$$\sigma = \int_{-\infty}^{t} \frac{d}{dt'} \left[G(1)\left(t - t'\right)^{-n} \right] \mathbf{C}^{-1}\left(t, t'\right) dt' \tag{3.5}$$

where $G\left(t\right) = G(1)t^{-n}$ [Gabriele *et al.* 2001; Ng *et al.* 2006; Lefebvre 2006; Migliori and Gabriele 2010; Tanner *et al.* 2008; 2011a]. Equation (3.5) therefore becomes:

$$\sigma = \int_{-\infty}^{t} nG(1)\left(t - t'\right)^{-(n+1)} \mathbf{C}^{-1}\left(t, t'\right) dt'. \tag{3.6}$$

The relaxation modulus, $G(1)$ and power law exponent, n, can be determined from Small Amplitude Oscillatory Shear (SAOS) tests, i.e. in the linear viscoelastic region, as described in Sections 2.3.3.2 and 2.3.3.3.

It is worth noting that Macosko [1994] described the Lodge model in Equation (3.4) using the left Cauchy-Green tensor, $\mathbf{B}$ instead of $\mathbf{C}^{-1}$. The different forms of strain tensors used by previous authors [Macosko 1994; Ng and McKinley 2008; Tanner *et al.* 2008] cause some confusion about which type of tensor should be used to describe the Lodge rubberlike model.

To clarify this, the deformation gradient tensor, $\mathbf{F}$, which is used to obtain $\mathbf{B}$ and $\mathbf{C}^{-1}$ is discussed first. Consider a block with point P embedded in the body and point Q, a neighbouring point separated by a small distance $d\mathbf{x}'$, as shown in Figure 3.1.

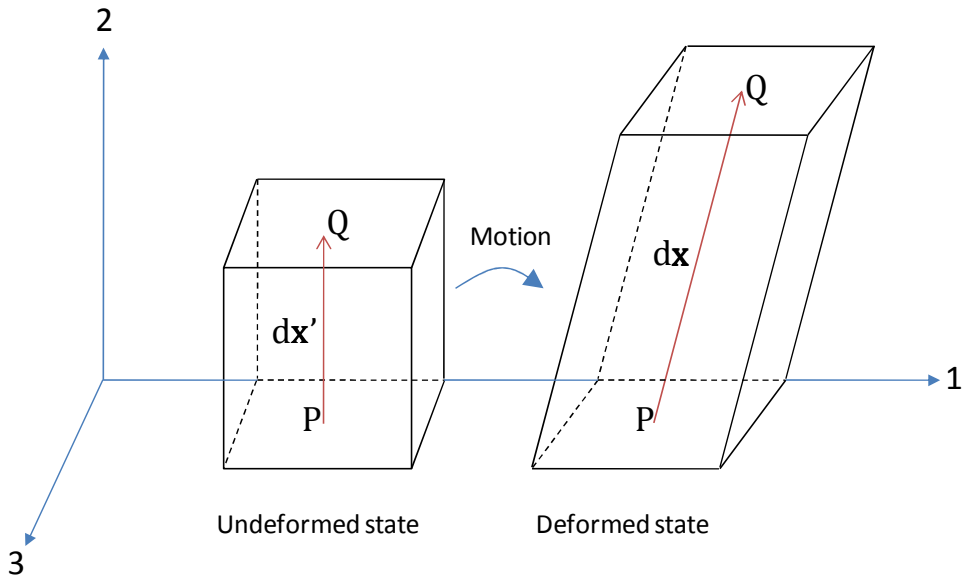

Figure 3.1. Representation of deformation gradient using a block (reproduced from Macosko [1994]).

The block is deformed to a new state. Point P and Q will move with the material, and the small displacement between them will stretch and rotate as indicated by the direction and magnitude of the new distance d**x.** The change in d**x** with respect to $d\mathbf{x}'$ is called the deformation gradient, or simply $\mathbf{F}$ [Macosko 1994]:

$$\mathbf{F} = \frac{d\mathbf{x}}{d\mathbf{x}'}. \tag{3.7}$$

The deformation gradient is used to define the left Cauchy-Green tensor, $\mathbf{B}$, using the following equation [Holzapfel 2000]:

$$\mathbf{B} = \mathbf{F} \cdot \mathbf{F}^{\mathrm{T}} \tag{3.8}$$

where $\mathbf{F}^{\mathrm{T}}$ is the transpose of the deformation gradient matrix $\mathbf{F}$.

Tanner *et al.* [2011a] on the other hand used the following deformation gradient:

$$\mathbf{F} = \frac{d\mathbf{x}'}{d\mathbf{x}}. \tag{3.9}$$

Notice the difference between the deformation gradients in Equations (3.7) and (3.9). Equation (3.9) can be used to obtain the right Cauchy-Green tensor, $\mathbf{C}$, through the following:

$$\mathbf{C} = \mathbf{F}^{\mathrm{T}} \cdot \mathbf{F} \tag{3.10}$$

The inverse of the strain tensor, $\mathbf{C}^{-1}$, is then described as:

$$\mathbf{C}^{-1} = \frac{1}{|\mathbf{C}|}\mathrm{adj}[\mathbf{C}] \tag{3.11}$$

where $|\mathbf{C}|$ and $\mathrm{adj}[\mathbf{C}]$ are the determinant and adjoint of matrix $\mathbf{C}$ respectively. The inverse of the strain tensor, $\mathbf{C}^{-1}$ is also known as the Finger tensor [Tanner *et al.* 2008; Ng and Mckinley 2008]. To show that $\mathbf{B} = \mathbf{C}^{-1}$, the following cases under uniaxial tension and simple shear are considered in the next sections.

3.2.1 Uniaxial Tension and Uniaxial Compression

The deformation gradient under uniaxial tension can be described by considering a block being stretched in direction 1 as shown in Figure 3.2.

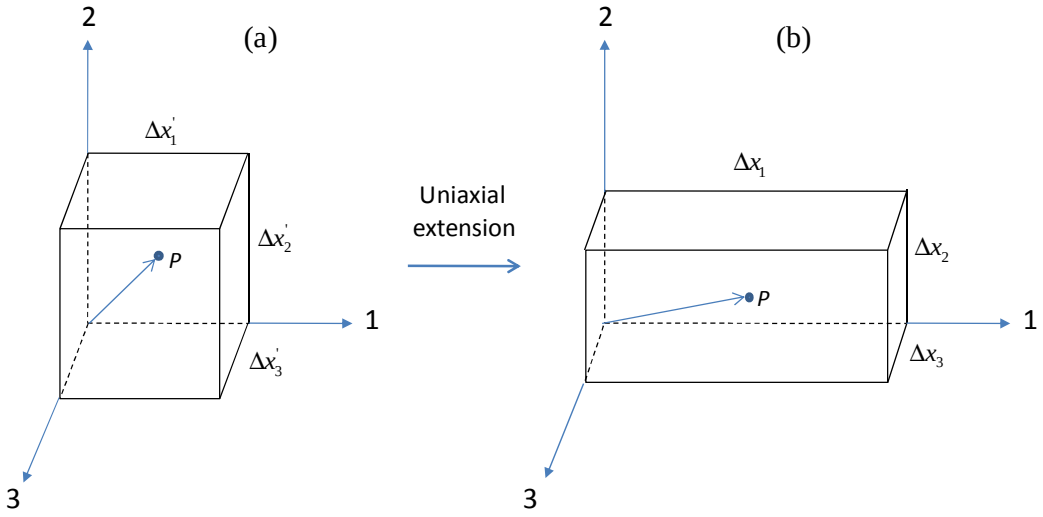

Figure 3.2. Deformation gradient under uniaxial tension for: (a) unstretched block; and (b) stretched block (reproduced from Macosko [1994]).

Consider point *P* in Figure 3.2(a) in the unstretched block with coordinates $\left(x_1', x_2', x_3'\right)$. The same point *P* in Figure 3.2(b) in the stretched block has coordinates $\left(x_1, x_2, x_3\right)$. $\Delta x_1'$, $\Delta x_2'$, and $\Delta x_3'$ represent the dimensions of the unstretched block in Figure 3.2(a), whereas Δx_1, Δx_2 and Δx_3 represent the dimensions of the stretched block in Figure 3.2(b). The coordinates of point *P* in the stretched block can be described as [Macosko 1994]:

$$x_1 = \frac{\Delta x_1}{\Delta x_1'} x_1' = \alpha_1 x_1' \tag{3.12}$$

$$x_2 = \frac{\Delta x_2}{\Delta x_2^{'}} x_2^{'} = \alpha_2 x_2^{'}$$

$$x_3 = \frac{\Delta x_3}{\Delta x_3^{'}} x_3^{'} = \alpha_3 x_3^{'}.$$

The deformation gradient, $\mathbf{F}$ can then be obtained as:

$$\mathbf{F} = \begin{bmatrix} \alpha_1 & 0 & 0 \\ 0 & \alpha_2 & 0 \\ 0 & 0 & \alpha_3 \end{bmatrix}. \tag{3.13}$$

Under uniaxial extension (Figure 3.2(b)), $\alpha_2 = \alpha_3$. For an incompressible block, $V^{'} = V$ ($V^{'}$ is the undeformed volume and V is the deformed volume), and the following relationship is obtained:

$$\Delta x_1^{'} \Delta x_2^{'} \Delta x_3^{'} = \Delta x_1 \Delta x_2 \Delta x_3 \tag{3.14}$$

or:

$$\alpha_1 \alpha_2 \alpha_3 = 1 \tag{3.15}$$

Under uniaxial tension:

$$\alpha_1 \alpha_2^2 = 1 \quad \text{and} \quad \alpha_2 = \frac{1}{\sqrt{\alpha_1}}. \tag{3.16}$$

The deformation gradient can then be described by just α_1 through:

$$\mathbf{F} = \begin{bmatrix} \alpha_1 & 0 & 0 \\ 0 & \alpha_1^{-1/2} & 0 \\ 0 & 0 & \alpha_1^{-1/2} \end{bmatrix} \tag{3.17}$$

and substituting Equation (3.17) into Equation (3.8) yields:

$$\mathbf{B} = \mathbf{F} \cdot \mathbf{F}^{\mathrm{T}} = \begin{bmatrix} \alpha_1 & 0 & 0 \\ 0 & \alpha_1^{-1/2} & 0 \\ 0 & 0 & \alpha_1^{-1/2} \end{bmatrix} \cdot \begin{bmatrix} \alpha_1 & 0 & 0 \\ 0 & \alpha_1^{-1/2} & 0 \\ 0 & 0 & \alpha_1^{-1/2} \end{bmatrix} = \begin{bmatrix} \alpha_1^2 & 0 & 0 \\ 0 & \alpha_1^{-1} & 0 \\ 0 & 0 & \alpha_1^{-1} \end{bmatrix}. \tag{3.18}$$

If Equation (3.9) is used instead to describe $\mathbf{F}$, then the following form is obtained:

$$\mathbf{F} = \begin{bmatrix} \alpha_1^{-1} & 0 & 0 \\ 0 & \alpha_2^{-1} & 0 \\ 0 & 0 & \alpha_3^{-1} \end{bmatrix}. \tag{3.19}$$

Using the same assumption of incompressible block as discussed before, the deformation can then be described by just α_1 through:

$$\mathbf{F} = \begin{bmatrix} \alpha_1^{-1} & 0 & 0 \\ 0 & \alpha_1^{1/2} & 0 \\ 0 & 0 & \alpha_1^{1/2} \end{bmatrix} \tag{3.20}$$

and substituting Equation (3.20) into Equation (3.10) yields:

$$\mathbf{C} = \mathbf{F}^{\mathrm{T}} \cdot \mathbf{F} = \begin{bmatrix} \alpha_1^{-1} & 0 & 0 \\ 0 & \alpha_1^{1/2} & 0 \\ 0 & 0 & \alpha_1^{1/2} \end{bmatrix} \cdot \begin{bmatrix} \alpha_1^{-1} & 0 & 0 \\ 0 & \alpha_1^{1/2} & 0 \\ 0 & 0 & \alpha_1^{1/2} \end{bmatrix} = \begin{bmatrix} \alpha_1^{-2} & 0 & 0 \\ 0 & \alpha_1 & 0 \\ 0 & 0 & \alpha_1 \end{bmatrix}. \tag{3.21}$$

The inverse of the strain tensor, $\mathbf{C}^{-1}$, is described using Equation (3.11), where the determinant, $|\mathbf{C}|$, and the adjoint, $\mathrm{adj}[\mathbf{C}]$, for a 3 x 3 matrix is as follows. For a

matrix, $\mathbf{A}=\begin{bmatrix} a & b & c \\ d & e & f \\ g & h & i \end{bmatrix}$, the determinant is $(aei+bfg+cdh)-(ceg+bdi+afh)$. The adjoint matrix $\mathbf{A}$ on the other hand is obtained using the following:

$$= \text{adj}[A] = \begin{bmatrix} \begin{vmatrix} e & f \\ h & i \end{vmatrix} & -\begin{vmatrix} d & f \\ g & i \end{vmatrix} & \begin{vmatrix} d & e \\ g & h \end{vmatrix} \\ -\begin{vmatrix} b & c \\ h & i \end{vmatrix} & \begin{vmatrix} a & c \\ g & i \end{vmatrix} & -\begin{vmatrix} a & b \\ g & h \end{vmatrix} \\ \begin{vmatrix} b & c \\ e & f \end{vmatrix} & -\begin{vmatrix} a & c \\ d & f \end{vmatrix} & \begin{vmatrix} a & b \\ d & e \end{vmatrix} \end{bmatrix}^{\mathrm{T}} . \tag{3.22}$$

Evaluating the inverse of the strain tensor, $\mathbf{C}^{-1}$, for Equation (3.21) yields:

$$\begin{aligned} \mathbf{C}^{-1} &= \frac{1}{\alpha_1^2\alpha_1^{-1}\alpha_1^{-1}}\begin{bmatrix} \alpha_1^2 & 0 & 0 \\ 0 & \alpha_1^{-1} & 0 \\ 0 & 0 & \alpha_1^{-1} \end{bmatrix} \\ &= \begin{bmatrix} \dfrac{\alpha_1^2}{\alpha_1^2\alpha_1^{-1}\alpha_1^{-1}} & 0 & 0 \\ 0 & \dfrac{\alpha_1^{-1}}{\alpha_1^2\alpha_1^{-1}\alpha_1^{-1}} & 0 \\ 0 & 0 & \dfrac{\alpha_1^{-1}}{\alpha_1^2\alpha_1^{-1}\alpha_1^{-1}} \end{bmatrix} = \begin{bmatrix} \alpha_1^2 & 0 & 0 \\ 0 & \alpha_1^{-1} & 0 \\ 0 & 0 & \alpha_1^{-1} \end{bmatrix}. \end{aligned} \tag{3.23}$$

It can be seen from Equations (3.23) and (3.18) that $\mathbf{B} = \mathbf{C}^{-1}$, which means that both tensors can be used to define the Lodge rubberlike model.

Equation (3.23) can be described in terms of the stretch ratio, λ, since $\lambda = \alpha_1$. Note that λ defines the ratio of the deformed and undeformed sample length. Therefore Equation (3.23) becomes:

$$\mathbf{C}^{-1} = \begin{bmatrix} \lambda^2 & 0 & 0 \\ 0 & \lambda^{-1} & 0 \\ 0 & 0 & \lambda^{-1} \end{bmatrix}. \tag{3.24}$$

Using the relationship, $\varepsilon = \ln \lambda$, where ε is the true strain, Equation (3.24) becomes:

$$\mathbf{C}^{-1} = \begin{bmatrix} (\exp \varepsilon)^2 & 0 & 0 \\ 0 & (\exp \varepsilon)^{-1} & 0 \\ 0 & 0 & (\exp \varepsilon)^{-1} \end{bmatrix} = \begin{bmatrix} \exp 2\varepsilon & 0 & 0 \\ 0 & \exp -\varepsilon & 0 \\ 0 & 0 & \exp -\varepsilon \end{bmatrix}. \tag{3.25}$$

Equation (3.25) is the strain tensor used by Tanner *et al.* [2008] and Ng and McKinley [2008] in the Lodge rubberlike model under uniaxial tension.

Since uniaxial tension of dough is performed using cylindrical samples, the Lodge rubberlike model needs to be evaluated using a cylindrical geometry sample. To obtain this, consider Figure 3.3 showing uniaxial tensile loading of a cylindrical sample.

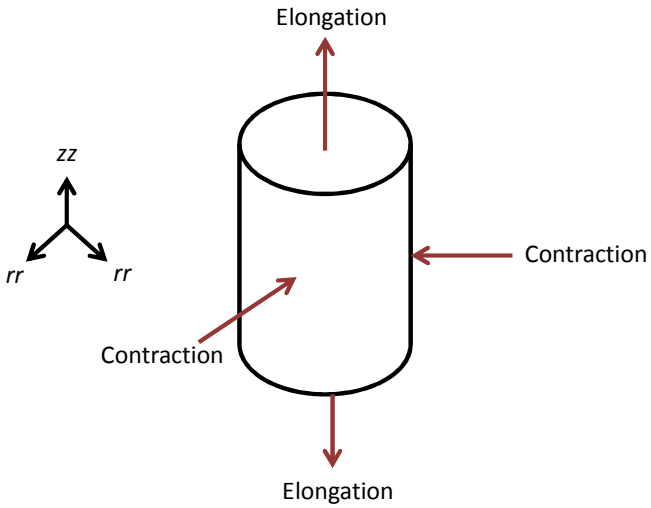

Figure 3.3. Uniaxial tension of a cylindrical sample.

The arrows in Figure 3.3 show that the sample undergoes elongation in the axial direction (zz direction) and contraction in radial direction (rr direction). The strain tensor $\mathbf{C}^{-1}\left(t,t'\right)$ is described relative to the present time t and reference time t' as [Ng and McKinley 2008]:

$$\mathbf{C}^{-1}\left(t,t'\right)=\begin{bmatrix} C_{zz}^{-1}\left(t,t'\right) & 0 & 0 \\ 0 & C_{rr}^{-1}\left(t,t'\right) & 0 \\ 0 & 0 & C_{rr}^{-1}\left(t,t'\right) \end{bmatrix} \tag{3.26}$$

which can be defined under uniaxial tension as (following Equation (3.25)):

$$\mathbf{C}^{-1}\left(t,t'\right)=\begin{bmatrix} \exp\left[2\dot{\varepsilon}\left(t-t'\right)\right] & 0 & 0 \\ 0 & \exp\left[-\dot{\varepsilon}\left(t-t'\right)\right] & 0 \\ 0 & 0 & \exp\left[-\dot{\varepsilon}\left(t-t'\right)\right] \end{bmatrix} \text{for } 0\le t'\le t \tag{3.27}$$

or:

$$\mathbf{C}^{-1}\left(t,t'\right)=\begin{bmatrix} \exp\left[2\dot{\varepsilon}\left(t\right)\right] & 0 & 0 \\ 0 & \exp\left[-\dot{\varepsilon}\left(t\right)\right] & 0 \\ 0 & 0 & \exp\left[-\dot{\varepsilon}\left(t\right)\right] \end{bmatrix} \text{for } t'<0\,. \tag{3.28}$$

In Equation (3.26), $C_{zz}^{-1}\left(t,t'\right)$ indicates stretching in the axial direction, whereas $C_{rr}^{-1}\left(t,t'\right)$ indicates contraction in the radial direction. By considering the difference of $\mathbf{C}^{-1}\left(t,t'\right)$ in the direction of stretching and the direction of contraction [Khan and Larson 1987], as shown in Figure 3.3, Tanner *et al.* [2008] used the following form of the Lodge model under uniaxial tension:

$$\sigma = \int_{-\infty}^{t} \frac{d}{dt'} G(1)\left(t-t'\right)^{-n}\left[C_{zz}^{-1}\left(t,t'\right)-C_{rr}^{-1}\left(t,t'\right)\right]dt'. \tag{3.29}$$

The stress was then evaluated using Equations (3.27) and (3.28) to become:

$$\begin{aligned}\sigma &= \int_{-\infty}^{0} nG(1)\left(t-t'\right)^{-(n+1)}\left(e^{2\varepsilon}-e^{-\varepsilon}\right)dt' \\ &+\int_{0}^{t} nG(1)\left(t-t'\right)^{-(n+1)}\left(e^{2\dot{\varepsilon}\left(t-t'\right)}-e^{-\dot{\varepsilon}\left(t-t'\right)}\right)dt'.\end{aligned} \tag{3.30}$$

By changing variables, $z = \dot{\varepsilon}\left(t-t'\right)$, Equation (3.30) becomes:

$$\sigma = n\dot{\varepsilon}^{n}G(1)\int_{0}^{\varepsilon} z^{-(n+1)}\left(e^{2z}-e^{-z}\right)dz + \dot{\varepsilon}^{n}G(1)\varepsilon^{-n}\left(e^{2\varepsilon}-e^{-\varepsilon}\right). \tag{3.31}$$

Equation (3.31) can be re-written as:

$$\frac{\sigma}{n\dot{\varepsilon}^{n}G(1)} = h = \int_{0}^{\varepsilon} z^{-(n+1)}\left(e^{2z}-e^{-z}\right)dz + \frac{1}{n}\varepsilon^{-n}\left(e^{2\varepsilon}-e^{-\varepsilon}\right) \tag{3.32}$$

where the function, h, in Equation (3.32) can be evaluated using the Gamma function or the asymptotic approximation. The function h evaluated using the Gamma function and incomplete Gamma functions, $\Gamma(a)$ and $\Gamma(a,s)$ respectively, is obtained as:

$$\begin{aligned}h \approx &\left\{\left(\frac{1}{2}\right)\left(-\frac{1}{2}\right)^{-n-1}\left[\Gamma\left(-n,-2\varepsilon\right)-\Gamma\left(-n\right)\right]-\left[\Gamma\left(-n\right)-\Gamma\left(-n,\varepsilon\right)\right]\right\} \\ &+\frac{1}{n}\varepsilon^{-n}\left(e^{2\varepsilon}-e^{-\varepsilon}\right).\end{aligned} \tag{3.33}$$

The derivation of Equation (3.33) is described in Appendix A. On the other hand, Ng and McKinley [2008] derived the following approximation form:

$$h \approx \varepsilon^{-n} \frac{1}{n}\left[\exp\left(2\varepsilon\right) + \frac{\left(1+2n\right)}{1-n}\varepsilon - 1 \right]. \tag{3.34}$$

whereas Tanner *et al.* [2008] derived the following approximation for the h function:

$$h \approx \left(1 + \frac{0.35}{1+2\varepsilon}\right)\frac{1}{n}\varepsilon^{-n}(e^{2\varepsilon} - e^{-\varepsilon}). \tag{3.35}$$

Tanner *et al.* [2011a] later used a simplified form for h:

$$h \approx \frac{1}{n}\varepsilon^{-n}(e^{2\varepsilon} - e^{-\varepsilon}). \tag{3.36}$$

Equations (3.33), (3.34), (3.35) and (3.36) are compared in Figure 3.4 by showing calculated stress using these equations. The parameters used in the comparison are: $n = 0.27$, and $G(1) = 3.02$ kPa$\cdot$s^n and the data were obtained from a uniaxial tension and uniaxial compression test from this work at a constant strain rate of 5/min. Equation (3.33) was evaluated using the online Wolfram calculator [Wolfram 2011]. It can be seen in Figure 3.4(a) that lower stresses are obtained using Equation (3.36) as compared to the other equations under uniaxial tension.

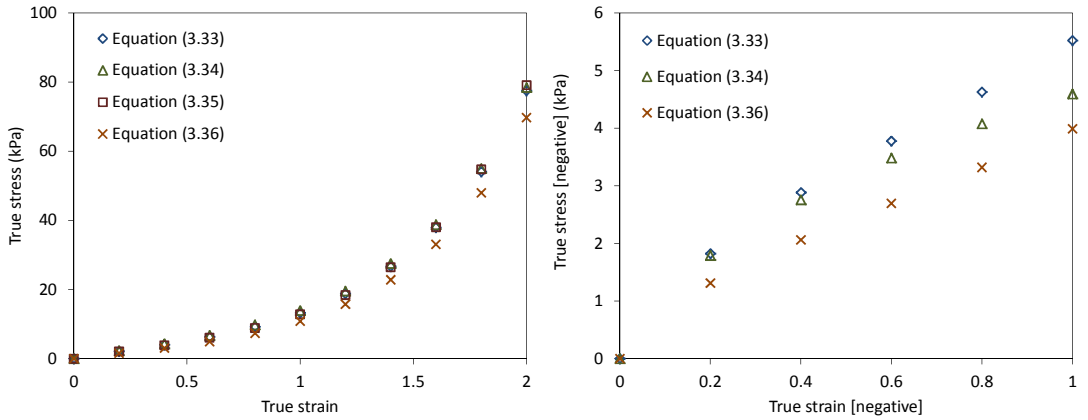

Figure 3.4. Comparison of different forms of Lodge rubberlike model equation under (a) uniaxial tension at 5/min and (b) uniaxial compression at -5/min.

Note that Equations (3.33) to (3.36) can be used to calculate stresses under uniaxial compression by using a negative strain. The term $\dot{\varepsilon}^n$ in Equation (3.32) under uniaxial compression is described as $-\left(\dot{\varepsilon}^n\right)$ rather than $\left(-\dot{\varepsilon}^n\right)$ to make $\dot{\varepsilon}$ becomes calculable. It can be seen in Figure 3.4(b) that lower stresses are obtained using Equation (3.36) as compared to the other equations. Note that the results for Equation (3.35) are not shown because the stress-strain calculated using Equation (3.35) fluctuates from negative to positive values. This is possibly due to Equation (3.35) being approximated only for uniaxial tension condition [Tanner *et al.* 2008]. Therefore Equation (3.34) is used in this thesis to evaluate the Lodge model under uniaxial tension and uniaxial compression. This is because Equation (3.34) can be evaluated easily using a spreadsheet compared to Equation (3.33) which requires each data point to be evaluated using the online Wolfram calculator [Wolfram 2011].

3.2.2 Simple Shear

The deformation gradient under simple shear can be described using the sketch and notation shown in Figure 3.5.

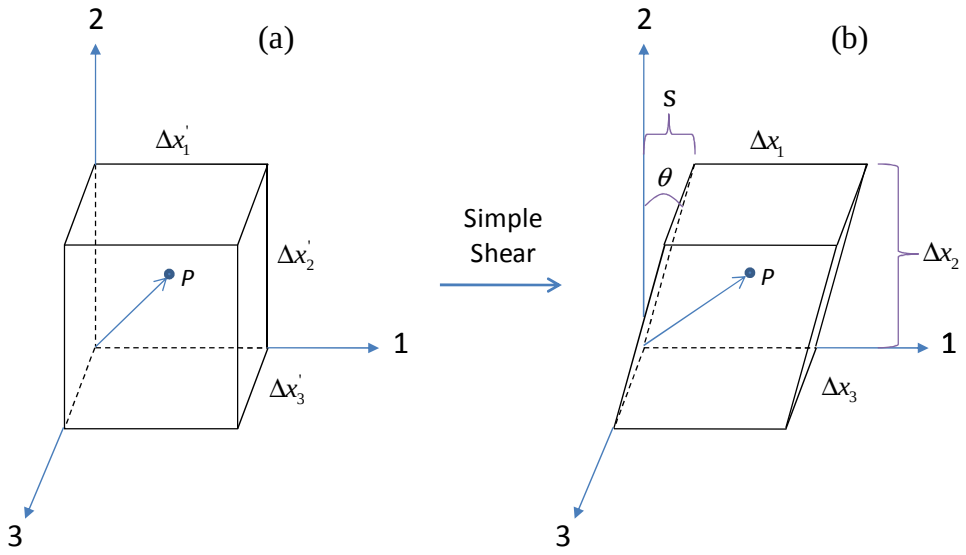

Figure 3.5. Deformation gradient under simple shear for: (a) unstretched block; and (b) sheared block (reproduced from Macosko [1994]).

Consider point P in Figure 3.5(a) in the unstretched block with coordinates $\left(x_1', x_2', x_3'\right)$. The point P is shown in Figure 3.5(b) for the stretched block with coordinates $\left(x_1, x_2, x_3\right)$. Under simple shear, $\gamma = s/\Delta x_2'$, and the coordinates of point P in the sheared block are given by [Macosko 1994]:

$$x_1 = x_1' + \frac{s}{\Delta x_2'} x_2' = x_1' + \gamma x_2' \qquad (3.37)$$

$$x_2 = x_2'$$

$x_3 = x_3^{'}$.

The deformation gradient obtained using Equation (3.7) is as follows:

$$\mathbf{F} = \begin{bmatrix} 1 & \gamma & 0 \\ 0 & 1 & 0 \\ 0 & 0 & 1 \end{bmatrix}. \tag{3.38}$$

Note that the deformation gradient in simple shear is not symmetric, which is in contrast to the deformation gradient in uniaxial tension (Equation (3.17)). The strain tensor, $\mathbf{B} = \mathbf{F} \cdot \mathbf{F}^{\mathrm{T}}$ is described as:

$$\mathbf{B} = \mathbf{F} \cdot \mathbf{F}^{\mathrm{T}} = \begin{bmatrix} 1 & \gamma & 0 \\ 0 & 1 & 0 \\ 0 & 0 & 1 \end{bmatrix} \cdot \begin{bmatrix} 1 & 0 & 0 \\ \gamma & 1 & 0 \\ 0 & 0 & 1 \end{bmatrix} = \begin{bmatrix} 1+\gamma^2 & \gamma & 0 \\ \gamma & 1 & 0 \\ 0 & 0 & 1 \end{bmatrix}. \tag{3.39}$$

On the other hand, the deformation gradient obtained using Equation (3.9) is as follows:

$$\mathbf{F} = \begin{bmatrix} 1 & -\gamma & 0 \\ 0 & 1 & 0 \\ 0 & 0 & 1 \end{bmatrix}. \tag{3.40}$$

The strain tensor $\mathbf{C} = \mathbf{F}^{\mathrm{T}} \cdot \mathbf{F}$ then becomes:

$$\mathbf{C} = \mathbf{F}^{\mathrm{T}} \cdot \mathbf{F} = \begin{bmatrix} 1 & 0 & 0 \\ -\gamma & 1 & 0 \\ 0 & 0 & 1 \end{bmatrix} \cdot \begin{bmatrix} 1 & -\gamma & 0 \\ 0 & 1 & 0 \\ 0 & 0 & 1 \end{bmatrix} = \begin{bmatrix} 1 & -\gamma & 0 \\ -\gamma & \gamma^2+1 & 0 \\ 0 & 0 & 1 \end{bmatrix}. \tag{3.41}$$

and $\mathbf{C}^{-1}$ becomes:

$$\mathbf{C}^{-1} = \frac{1}{|\mathbf{C}|}\text{adj}[\mathbf{C}] = \begin{bmatrix} \gamma^2+1 & \gamma & 0 \\ \gamma & 1 & 0 \\ 0 & 0 & 1 \end{bmatrix}. \tag{3.42}$$

It can be seen from Equations (3.39) and (3.42) that $\mathbf{B} = \mathbf{C}^{-1}$, which means that both definition for the strain tensors can be used in the Lodge rubberlike model under simple shear.

In a constant shear strain rate experiment, the strain tensor, $\mathbf{C}^{-1}$, and strain rate tensors take the following forms:

$$\mathbf{C}^{-1}(t,t') = \begin{bmatrix} C_{11}^{-1}(t,t') & C_{12}^{-1}(t,t') & 0 \\ C_{12}^{-1}(t,t') & C_{22}^{-1}(t,t') & 0 \\ 0 & 0 & C_{33}^{-1}(t,t') \end{bmatrix} \tag{3.43}$$

which can be defined under simple shear using Equation (3.42) as:

$$\mathbf{C}^{-1}(t,t') = \begin{bmatrix} \dot{\gamma}^2(t-t')^2+1 & \dot{\gamma}(t-t') & 0 \\ \dot{\gamma}(t-t') & 1 & 0 \\ 0 & 0 & 1 \end{bmatrix} \text{ for } 0 \le t' \le t \tag{3.44}$$

or:

$$\mathbf{C}^{-1}(t,t') = \begin{bmatrix} \dot{\gamma}^2t^2+1 & \dot{\gamma}t & 0 \\ \dot{\gamma}t & 1 & 0 \\ 0 & 0 & 1 \end{bmatrix} \text{ for } t' < 0. \tag{3.45}$$

Shear stress can be described using Equation (3.5) as:

$$\tau = \int_{-\infty}^{t} \frac{\partial}{\partial t'} G(1)\left(t - t'\right)^{-n} C_{12}^{-1}\left(t, t'\right) dt'. \tag{3.46}$$

Shear stress then becomes:

$$\tau = \int_{-\infty}^{0} nG(1)\left(t - t'\right)^{-n-1}\left(\dot{\gamma}\right) dt' + \int_{0}^{t} nG(1)\left(t - t'\right)^{-n-1}\left(\dot{\gamma}\right) dt'. \tag{3.47}$$

By changing variables through $z = \dot{\gamma}\left(t - t'\right)$ and evaluating the integral yields [Tanner *et al.* 2008]:

$$\tau = \frac{G(1)\dot{\gamma}^{n}}{1-n}\gamma^{1-n}. \tag{3.48}$$

Equation (3.48) is similar to those obtained by Ng and McKinley [2008].

3.2.3 Damage Function in Lodge Rubberlike Model

Tanner *et al.* [2008] used the idea of a damage function to model dough at high deformations until the post fracture region. This is because the Lodge model did not fit the dough stress-strain data at high strain, as shown by Tanner *et al.* [2008]. The stress is reduced by a damage function, f, such that:

$$\sigma_D = f\sigma \qquad \text{or} \qquad \tau_D = f\tau \tag{3.49}$$

where σ_D and τ_D are the damaged normal and shear stresses respectively, and σ and τ are the undamaged normal and shear stresses respectively for the material. The damage function, f is described as: $f \equiv (1 - D)$, where D is a function of the strain which varies from zero at small strain, up to 1 at rupture [Tanner *et al.* 2008]. The

damage function was used by Tanner *et al.* [2008] for constant strain rate elongation and shear data. The parameter f was plotted as a function of true strain, ε, for both extensional and shear data as shown in Figure 3.6.

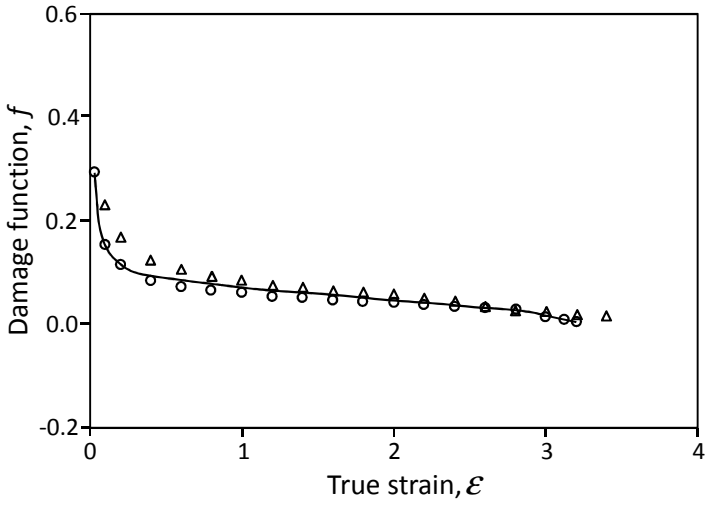

Figure 3.6. A damage function for Lodge rubberlike model [Tanner *et al.* 2008]).

The procedure for deriving the damage functions in Figure 3.6 within the Lodge rubberlike model was as follows [Tanner *et al.* 2008]. First, a strain sweep test was conducted to determine the linear viscoelastic region (LVR), followed by a frequency sweep test to determine the constants $G(1)$ and n using Equations (2.20) and (2.21) respectively (refer Section 2.3.3.3):

$$G'(t) = G'(1)\omega^n, \qquad G''(t) = G''(1)\omega^n$$

$$G(1) = G'(1)\frac{2(n!)}{n\pi}\sin\frac{n\pi}{2}.$$

These constants were then used in the Lodge rubberlike model (Equation (3.35) under uniaxial tension, and Equation (3.48) under simple shear). Tanner *et al.* [2008] showed that the Lodge model did not fit the uniaxial tension and constant shear strain

rate tests without the damage function. They derived the damage function from the extensional and shear tests. The true strain for the shear tests in Figure 3.6 is calculated using [Treloar 1975]: $\left\{\varepsilon = \ln(\lambda) = \ln\left(\frac{\gamma}{2} + \frac{\sqrt{\gamma^2+4}}{2}\right)\right\}$, (details on this equation are provided in Section 3.3.2). This was the method for calculating the damage functions shown in Figure 3.6. Finally, the modelling results were reconstructed with the inclusion of the determined damage function. An example of the reconstructed tensile test using the damage function in Figure 3.6 is shown in Figure 3.7.

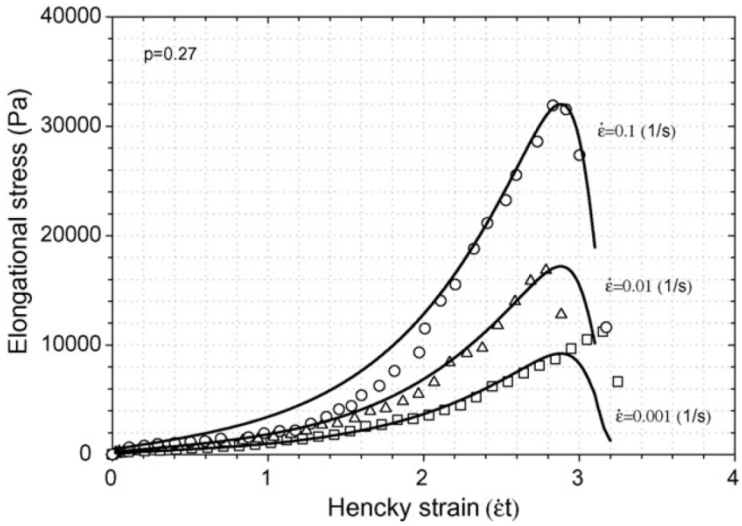

Figure 3.7. Reconstructed uniaxial tension model using damage function in Figure 3.6 [Tanner *et al.* 2008].

It is worth noting that the damage function introduced by Tanner *et al.* [2008] is an empirical function, it does not provide any physical meaning. Therefore a microstructure based model is needed to describe the damage in wheat flour dough microstructure. This can be investigated using the micromechanics model, which will be discussed later in Section 3.4.

3.3. Visco-Hyperelastic Model

3.3.1 Viscoelasticity

Viscoelastic materials can be viewed as having both viscous and elastic properties. The elastic, viscous and viscoelastic material responses under applied step strain are shown in Figure 3.8. Elastic materials stretch and return to their original state instantaneously upon application and removal of stress respectively. The ratio of stress to strain for an elastic material is defined as elastic modulus. Viscous materials on the other hand change strain in proportion to the time that the stress is applied [Janmey and Schiwa 2008]. The ratio of stress to rate of strain is defined as viscosity. Viscoleastic materials can exhibit strain and time dependent behaviour when both viscous and elastic properties are present. The theoretical and experimental behaviours of viscoelastic materials were first established in the nineteenth century by physicists Maxwell, Boltzmann and Kelvin. Considering the model of springs and dashpots, their main interest was to determine the properties of materials from creep and recovery experiments.

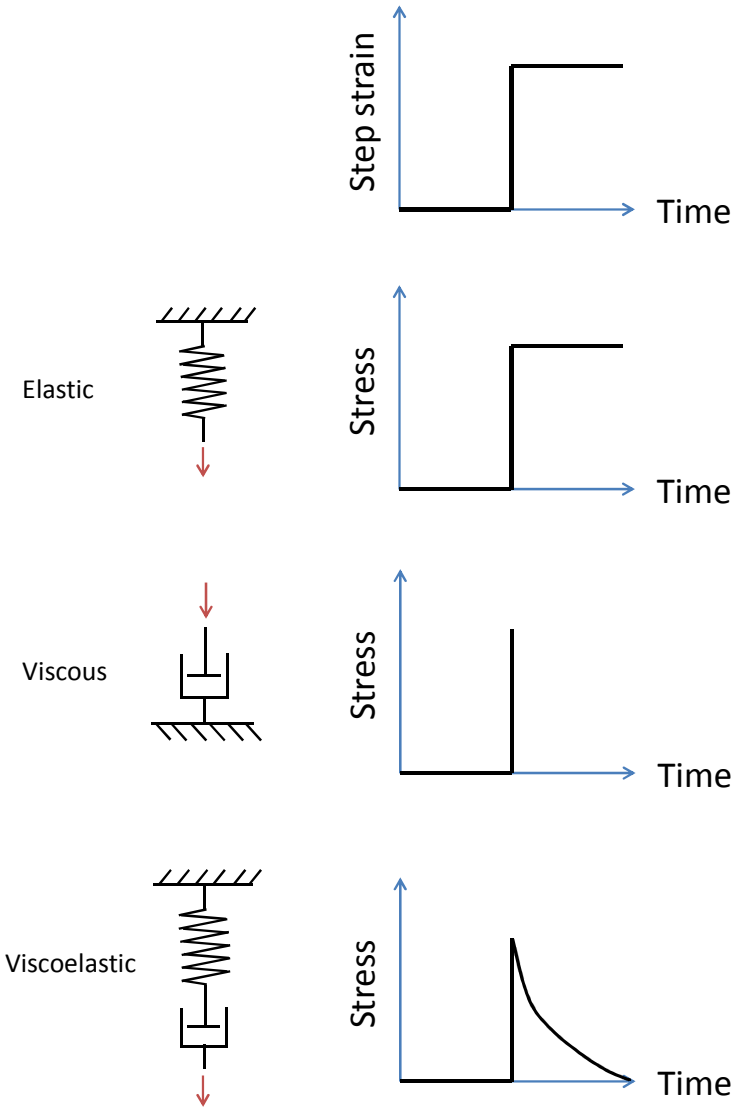

Figure 3.8. Difference between elastic, viscous and viscoelastic materials (reproduced from Vader and Wyss [2012]).

Viscoelasticity assumes a homogeneous and isotropic material, as well as separable time and strain dependent material behaviour [Williams 1980; Goh *et al.* 2004; Charalambides *et al.* 2006]. The relaxation stress under a step strain loading history can be written as a product of a function of time, $g(t)$, and a function of strain, $\sigma_0(\varepsilon)$:

$$\sigma(\varepsilon,t)=\sigma_0(\varepsilon)g(t). \tag{3.50}$$

The time function is represented by the Prony Series [Goh *et al.* 2004]:

$$g(t)=g_\infty+\sum_{i=1}^{N}g_i\exp\left(-\frac{t}{\xi_i}\right) \tag{3.51}$$

where t and ξ_i are time and relaxation time constants respectively, and g_i are dimensionless constants. The 1D equivalent of the Prony series in tension consists of a series of Maxwell elements connected in parallel with a spring as shown in Figure 3.9.

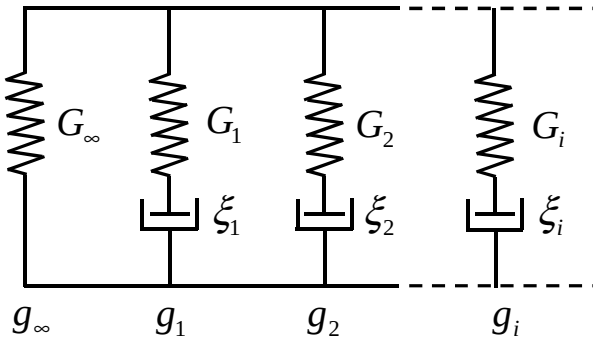

Figure 3.9. The Prony series representation.

Each g_i is defined as:

$$g_i=\frac{G_i}{G_O},\quad g_\infty=\frac{G_\infty}{G_O} \tag{3.52}$$

where G_i is the modulus of the i^{th} spring, G_∞ is the modulus of the infinite lone spring, and G_0 is the instantaneous modulus, given by $\sum_{i=1}^{N}G_i+G_\infty=G_O$. Therefore g_i

is related to g_∞ through $\sum_{i=1}^{N} g_i + g_\infty = 1$. The function $\sigma_0(\varepsilon)$ represents the instantaneous stress-strain relationship since $g(0) = 1$ and $\sigma(\varepsilon, 0) = \sigma_0(\varepsilon)$ from Equation (3.50). It can be seen that $g_\infty \sigma_0(\varepsilon)$ is the long term or equilibrium stress-strain relationship as $g(\infty) = g_\infty$ and $\sigma(\varepsilon, \infty) = g_\infty \sigma_0(\varepsilon)$ from Equation (3.50). Physically, this long term behaviour occurs as the dashpots relax the *i* springs in Figure 3.9, and only the g_∞ spring remains loaded.

Using the Leaderman form of the convolution integral [Williams 1980], the total stress is given by the algebraic sum of the entire past loading history, with each stress component being independent of the loading history. In the limit of continuous strain history, the total stress at time t is therefore given by [Williams 1980]:

$$\sigma(\varepsilon, t) = \int_0^t g(t-s) \frac{d\sigma_0(\varepsilon)}{ds} ds \tag{3.53}$$

where $\sigma_0(\varepsilon)$ is the instantaneous true stress at strain ε. The function $g(t-s)$ is described as:

$$g(t-s) = g_\infty + \sum_{i=1}^{N} g_i \exp\left(-\frac{t-s}{\xi_i}\right). \tag{3.54}$$

Therefore Equation (3.53) becomes:

$$\sigma(t) = \int_0^t \left[g_\infty + \sum_{i=1}^{N} g_i \exp\left(-\frac{t-s}{\xi_i}\right) \right] \frac{d\sigma_0(\varepsilon)}{ds} ds. \tag{3.55}$$

The stress on the left-hand side is expressed in terms of t only, provided that the strain history $\varepsilon(t)$ is known [Goh *et al.* 2004]. Equation (3.55) can be rewritten as:

$$\sigma(t) = g_\infty \sigma_0(t) + \sum_{i=1}^{N} \int_0^t g_i \exp\left(-\frac{t-s}{\xi_i}\right) \frac{d\sigma_0(s)}{ds} ds = g_\infty \sigma_0(t) + \sum_{i=1}^{N} h_i(t) \tag{3.56}$$

with $h_i(t) = \int_0^t g_i \exp\left(-\frac{t-s}{\xi_i}\right) \frac{d\sigma_0(s)}{ds} ds$.

The convolution integral in Equation (3.56) is computed using a numerical algorithm based on finite time increments [Kaliske and Rothert 1997]. For a time interval (t_n, t_{n+1}) and time step $\Delta t = t_{n+1} - t_n$, the exponential term in the integrand is written as:

$$\exp\left(-\frac{t_{n+1}}{\xi_i}\right) = \exp\left(-\frac{t_n}{\xi_i}\right) \exp\left(-\frac{\Delta t}{\xi_i}\right). \tag{3.57}$$

The term h_i at t_{n+1} can be separated into two components: the first component corresponds to deformation history during period $0 \le s \le t_n$ while the second component corresponds to the period, $t_n \le s \le t_{n+1}$. Therefore:

$$h_i(t_{n+1}) = g_i \int_0^{t_{n+1}} \exp\left(-\frac{t_{n+1}-s}{\xi_i}\right) \frac{d\sigma_0(s)}{ds} ds \tag{3.58}$$

which becomes:

$$h_i(t_{n+1}) = g_i \int_0^{t_n} \exp\left(-\frac{t_{n+1}-s}{\xi_i}\right) \frac{d\sigma_0(s)}{ds} ds + g_i \int_{t_n}^{t_{n+1}} \exp\left(-\frac{t_{n+1}-s}{\xi_i}\right) \frac{d\sigma_0(s)}{ds} ds. \tag{3.59}$$

The first integral above is integrated from 0 to t_n, which yields:

$$\exp\left(-\frac{\Delta t}{\xi_i}\right) g_i \int_0^{t_n} \exp\left(-\frac{(t_n - s)}{\xi_i}\right) \frac{d\sigma_0(s)}{ds} ds \tag{3.60}$$

The result is included in Equation (3.56):

$$\begin{aligned} &\sigma(t_{n+1}) = g_\infty \sigma_0(t_{n+1}) \\ &+\sum_{i=1}^{N} \left(\exp\left(-\frac{\Delta t}{\xi_i}\right) h_i(t_n) + g_i \int_{t_n}^{t_{n+1}} \exp\left(-\frac{t_{n+1} - s}{\xi_i}\right) \frac{d\sigma_0(s)}{ds} ds \right). \end{aligned} \tag{3.61}$$

$\frac{d\sigma_0(s)}{ds}$ in Equation (3.61) can be expressed in terms of discrete time steps:

$$\frac{d\sigma_0(s)}{ds} = \lim_{\Delta s \to 0} \frac{\Delta \sigma_0(s)}{\Delta s} = \lim_{\Delta t \to 0} \frac{\sigma_0^{n+1} - \sigma_0^n}{\Delta t}. \tag{3.62}$$

Substituting Equation (3.62) into Equation (3.61) and performing the last integral in Equation (3.61) leads to a function for updating the stress $\sigma(t_{n+1})$ [Goh *et al.* 2004]:

$$\begin{aligned} &\sigma(t_{n+1}) = g_\infty \sigma_0(t_{n+1}) \\ &+\sum_{i=1}^{N} \left(\exp\left(-\frac{\Delta t}{\xi_i}\right) h_i(t_n) + g_i \frac{1 - \exp\left(-\frac{\Delta t}{\xi_i}\right)}{\frac{\Delta t}{\xi_i}} \left[\sigma_0(t_{n+1}) - \sigma_0(t_n)\right] \right). \end{aligned} \tag{3.63}$$

Equation (3.63) can be evaluated with various hyperelastic potentials and strain histories. The true stress, $\sigma_0(t_n)$ used will be discussed in Section 3.3.2. The advantage of this analytical equation is that it can be readily fitted to experimental stress–strain data which are measured at known time intervals. The equation offers a

very practical method for determining material constants at any deformation history. A spreadsheet can be set up so that the calculations using the analytical equation are matched with the experimental data via a least squares error method.

3.3.1.1 Viscoelastic Model in Abaqus Version 6.9

In the newer version of the commercial finite element software, Abaqus version 6.9 [Abaqus 2010], an updated version of finite viscoelastic model has been introduced to replace the former Abaqus version 6.8 [Abaqus 2009]. A modification is performed to Equation (3.55) as follows:

$$\sigma(t)=\lambda(t)\int_0^t\left[g_\infty+\sum_{i=1}^{N}g_i\exp\left(-\frac{t-s}{\xi_i}\right)\right]\frac{dP_0(\varepsilon)}{ds}ds. \tag{3.64}$$

Notice the difference where σ_0 in Equation (3.55) represents the true stress term, whereas P_0 in Equation (3.64) represents the nominal stress term. The stretch ratio, $\lambda(t)$ is introduced in Equation (3.64) to convert the nominal stress term in the integral into true stress term after integration. True stress and nominal stress are related through:

$$\sigma_0(t_n)=P_0(t_n)\cdot\lambda(t_n). \tag{3.65}$$

Evaluating Equation (3.64) using the same approach as before yields:

$$\sigma(t)=\lambda(t)\,g_\infty P_0(t)+\lambda(t)\sum_{i=1}^{N}\int_0^t g_i\exp\left(-\frac{t-s}{\xi_i}\right)\frac{dP_0(s)}{ds}ds \tag{3.66}$$

which then becomes:

$$\sigma(t) = g_\infty \sigma_0(t) + \lambda(t) \sum_{i=1}^{N} \int_0^t g_i \exp\left(-\frac{t-s}{\xi_i}\right) \frac{dP_0(s)}{ds} ds. \tag{3.67}$$

Equation (3.67) is then evaluated using the same finite time increment algorithm as in before, which finally yields:

$$\begin{aligned} &\sigma(t_{n+1}) = g_\infty \sigma_0(t_{n+1}) \\ &+\lambda(t_{n+1}) \sum_{i=1}^{N} \left(\exp\left(-\frac{\Delta t}{\xi_i}\right) h_i(t_n) + g_i \frac{1-\exp\left(-\frac{\Delta t}{\xi_i}\right)}{\frac{\Delta t}{\xi_i}} \left[P_0(t_{n+1}) - P_0(t_n) \right] \right). \end{aligned} \tag{3.68}$$

The difference between Equations (3.68) and Equation (3.63) will be investigated in Section 3.3.3 where the stress calculated via these two equations will be plotted versus strain.

3.3.2 Hyperelasticity

A hyperelastic material is defined as an ideally elastic material, but may be subjected to large deformations and still show complete recovery [Ward 1971]. Hyperelasticity is closely related to rubber elasticity, which can be described from the concept of a strain energy function derived from thermodynamic considerations. Different types of strain energy function can be defined, depending on the experimental conditions. Strain energy functions can be described from either a phenomenological or a statistical treatment. For polymers, the strain energy function is represented as the Helmholtz free energy of a molecular network with a Gaussian chain distribution [Treloar 1975], and the mathematical representation of this model is an idealized

form of the concept of an ideal gas. The theory can be described from the First Law of Thermodynamics:

$$dW = dU - dQ \tag{3.69}$$

where dW is work performed on the system by the surroundings, dU and dQ are differential change in internal energy and heat respectively. Under adiabatic conditions, $dQ = 0$ and $dW = dU$. The strain energy function W for an isotropic incompressible solid undergoing a pure homogeneous deformation is given by [Ward 1971]:

$$W = f\left(I_1, I_2, I_3\right) \tag{3.70}$$

where f is a function of I_1, I_2 and I_3, which are the first, second and third strain invariants respectively expressed as: $I_1 = \lambda_1^2 + \lambda_2^2 + \lambda_3^2$, $I_2 = \lambda_1^2\lambda_2^2 + \lambda_2^2\lambda_3^2 + \lambda_3^2\lambda_1^2$ and $I_3 = \lambda_1\lambda_2\lambda_3$. The third strain invariant, I_3, is assumed to be unity due to the assumption of incompressibility of dough, as investigated experimentally by Charalambides *et al.* [2002a] and Wang *et al.* [2006]. λ_1, λ_2 and λ_3 are the stretch ratios in the three principal axis, which are defined for uniaxial deformation and pure shear as:

$$\begin{aligned} &\lambda_1 = \lambda, \quad \lambda_2 = \lambda_3 = \frac{1}{\sqrt{\lambda}} && \text{(uniaxial deformation)} \\ &\lambda_1 = \lambda, \quad \lambda_2 = 1, \quad \lambda_3 = \frac{1}{\lambda} && \text{(pure shear)} \end{aligned} \tag{3.71}$$

where λ is the stretch ratio in the direction of the applied load. I_1, I_2 and I_3 in the case of uniaxial deformation and pure shear can be described as:

$$\begin{aligned} &I_1 = \lambda^2 + 2\lambda^{-1} \ , \quad I_2 = 2\lambda + \lambda^{-2} \ , \quad I_3 = 1 && \text{(uniaxial deformation)} \\ &I_1 = I_2 = 1 + \lambda^2 + \lambda^{-2} \ , \quad I_3 = 1. && \text{(pure shear)} \end{aligned} \tag{3.72}$$

For uniaxial tension and uniaxial compression, the true stress used in Equations (3.63) or (3.68) is given as a function of λ:

$$\sigma_0(\lambda) = \frac{\partial W}{\partial \lambda}\lambda \tag{3.73}$$

whereas for simple shear, the shear stress is expressed using the chain rule as [Gamonpilas *et al.* 2010]:

$$\sigma_0(\lambda) = \tau_0(\lambda) = \frac{dW}{d\gamma} = \frac{dW}{d\lambda}\frac{d\lambda}{d\gamma} \tag{3.74}$$

where λ is related to the shear strain, γ through [Treloar 1975]:

$$\lambda = \frac{\gamma}{2} + \frac{\sqrt{\gamma^2 + 4}}{2} \tag{3.75}$$

and therefore the true strain, ε is related to γ through:

$$\varepsilon = \ln(\lambda) = \ln\left(\frac{\gamma}{2} + \frac{\sqrt{\gamma^2 + 4}}{2}\right). \tag{3.76}$$

For small strain however, Equation (3.76) can be evaluated using the Taylor series and is approximated as:

$$\varepsilon = \frac{\gamma}{2}. \tag{3.77}$$

The difference between Equations (3.76) and (3.77) is shown in Figure 3.10. It can be seen that for shear strain up to 1.5, a similar true strain is obtained using both equations.

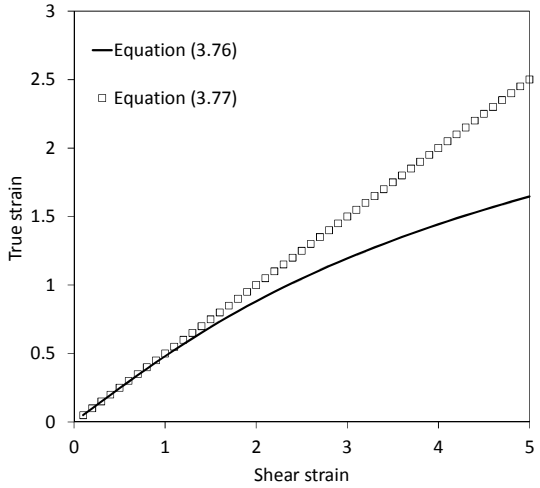

Figure 3.10. True strain obtained using Equations (3.76) and (3.77).

The hyperelastic model used in this thesis is the van der Waals model, which, as the name implies, represents the analogy in the thermodynamic interpretation of the equation of state for rubber and gas. The model analogy can be described by comparing the equation of state of ideal gas and a rubber network model, as discussed by Eisele *et al.* [1981] and Vilgis [1992].

The van der Waals strain energy function is given by [Kilian 1982; Abaqus 2009]:

$$W = -\mu\left\{\left(\lambda_m^2 - 3\right)\left[\ln\left(1 - \sqrt{\frac{\mathrm{I}_1 - 3}{\lambda_m^2 - 3}}\right) + \sqrt{\frac{\mathrm{I}_1 - 3}{\lambda_m^2 - 3}}\right] + \frac{2}{3}a\left(\frac{\mathrm{I}_1 - 3}{2}\right)^{\frac{3}{2}}\right\} \tag{3.78}$$

where μ is the instantaneous initial shear modulus, λ_m is the locking stretch constant and a is a global interaction parameter. The constants, λ_m and a are dimensionless. The locking stretch constant, λ_m describes the stretch when chains unfold and lock, whereas the global interaction parameter, a is the interaction between rubber chains [Enderle and Kilian 1987; Vilgis 1992].

The true stress form for tension and compression, using Equation (3.73) can be described from the model as:

$$\sigma_0(\lambda) = \mu\lambda\left(\lambda - \frac{1}{\lambda^2}\right)\left[\frac{\sqrt{\lambda_m^2 - 3}}{\sqrt{\lambda_m^2 - 3} - \sqrt{\lambda^2 + 2\lambda^{-1} - 3}} - a\sqrt{\frac{\lambda^2 + 2\lambda^{-1} - 3}{2}}\right] \tag{3.79}$$

where $\lambda > 1$ for tension and $\lambda < 1$ for compression. For simple shear, the shear stress, $\tau_0(\lambda)$ can be obtained using Equation (3.74):

$$\sigma_0(\lambda) = \tau_0(\lambda) = \mu\left(\frac{\lambda^3 - \lambda^{-1}}{\lambda^2 + 1}\right)\left[\frac{\sqrt{\lambda_m^2 - 3}}{\sqrt{\lambda_m^2 - 3} - \sqrt{\lambda^2 + \lambda^{-2} - 2}} - a\sqrt{\frac{\lambda^2 + \lambda^{-2} - 2}{2}}\right]. \tag{3.80}$$

Equations (3.79) and (3.80) are used with Equations (3.63) or (3.68) to describe the visco-hyperelastic model. The van der Waals model was selected for the implementation in finite element analysis because it is the most suitable model available in Abaqus for fitting data collected from more than one mode of deformation [Charalambides 2006; Wanigasooriya 2006].

A parametric study was performed to check the effect of the van der Waals model parameters to the stress-strain curve. The van der Waals model parameters were first

set to: μ = 5 kPa, λ_m = 5 and a = 0.5. Two of these were then kept constant while varying the third in a parametric study. Figure 3.11 shows the parametric study corresponding to a strain rate of 5/min. It can be seen that the stress-strain curve of the model increased by increasing μ (Figure 3.11(a)), whereas the curve was 'lowered' by increasing λ_m and a, as shown in Figures 3.11(b) and 3.11(c) respectively.

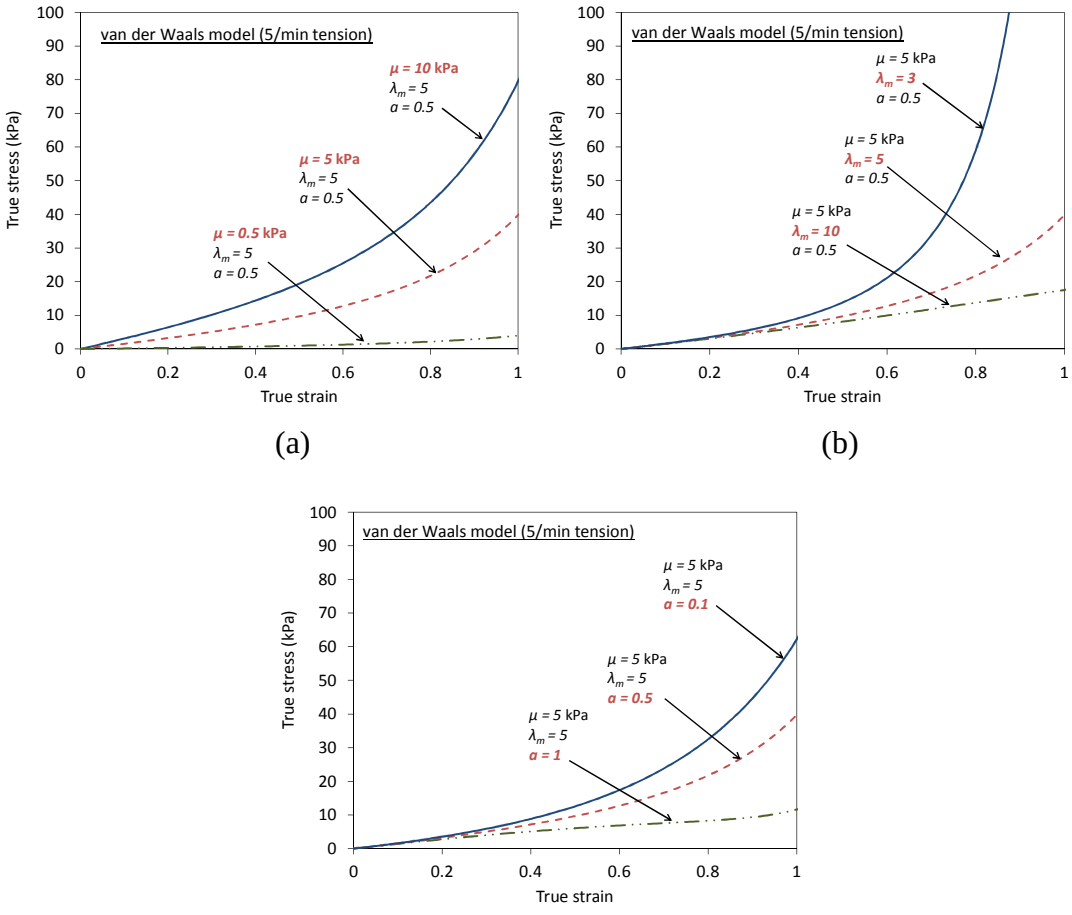

Figure 3.11. Parametric study of the van der Waals model by varying parameters: (a) the instantaneous initial shear modulus, μ; (b) the locking stretch constant λ_m; and (c) the global interaction parameter, a.

3.3.3 Implementation of the Visco-Hyperelastic Model in Finite Element Analysis

It is important that the analytical visco-hyperelastic model discussed in the previous section is checked for accuracy within the finite element (FE) simulation in Abaqus so that the model can be confidently used for numerical simulations. Therefore, the analytical model, Equations (3.63) and (3.68) were compared to the finite element simulations performed using Abaqus version 6.8 [Abaqus 2009] and Abaqus version 6.9 [Abaqus 2010] respectively. A personal computer with Intel Core 2 processor and 4 MB SDRAM was used to perform the numerical simulation. It took less than two minutes to perform each simulation. The simulation was performed under uniaxial compression, uniaxial tension and simple shear modes at a true strain rate of 5/min. A single axisymmetric element was selected for uniaxial tension and uniaxial compression and a plane stress element was selected for simple shear. Discussion on the different elements available for 2D FE model in Abaqus is provided in Appendix B. The boundary conditions used in the FE simulation are shown in Figure 3.12, where the roller allows the node to move in a defined direction and the arrow indicates an applied deformation.

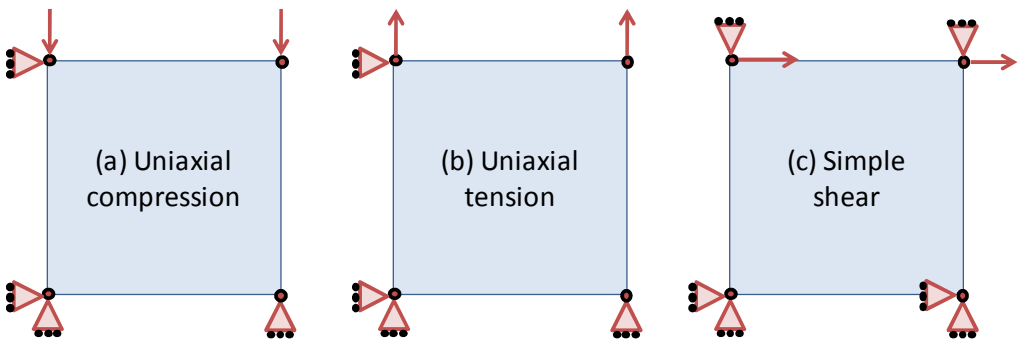

Figure 3.12. Boundary conditions used in the finite element simulation for: (a) uniaxial compression; (b) uniaxial tension; and (c) simple shear.

The material model parameters shown in Table 3.1 were used, where the strain-dependent constants represent the van der Waals model parameters, and the time-dependent constants represent the Prony series.

Table 3.1. Parameters used for the validation of the numerical implementation of the van der Waals model in Abaqus.

Strain dependent constants			**Time dependent constants**					
			i	1	2	3	4	∞
μ (kPa)	λ_m	a	ξ_i (s)	0.1	10	100	1000	
3.29	4.64	0.25	g_i	0.867	0.092	0.004	0.028	0.007

The results are shown in Figure 3.13. It can be seen that the analytical models, Equations (3.63) and (3.68), agree with the FE results using Abaqus version 6.8 and Abaqus version 6.9 respectively under uniaxial tension and uniaxial compression (Figures 3.13(a) and 3.13(b)). However, it is shown in Figure 3.13(c) that the FE results under simple shear do not agree with the analytical model above a shear strain value of approximately 0.6. This can be due to the boundary conditions shown in Figure 3.12(c), which are defined in the FE simulation to represent the boundary conditions under shear rheometry tests. The difference between the analytical and finite element models was then shown in Figure 3.13(d), where the error is calculated as: $\left|\left(\text{finite\_element - analytical}\right)/\left(\text{analytical}\right)\right|\times 100$. It is worth noting that simulation for simple shear in this thesis will be performed for shear strain up to 1.

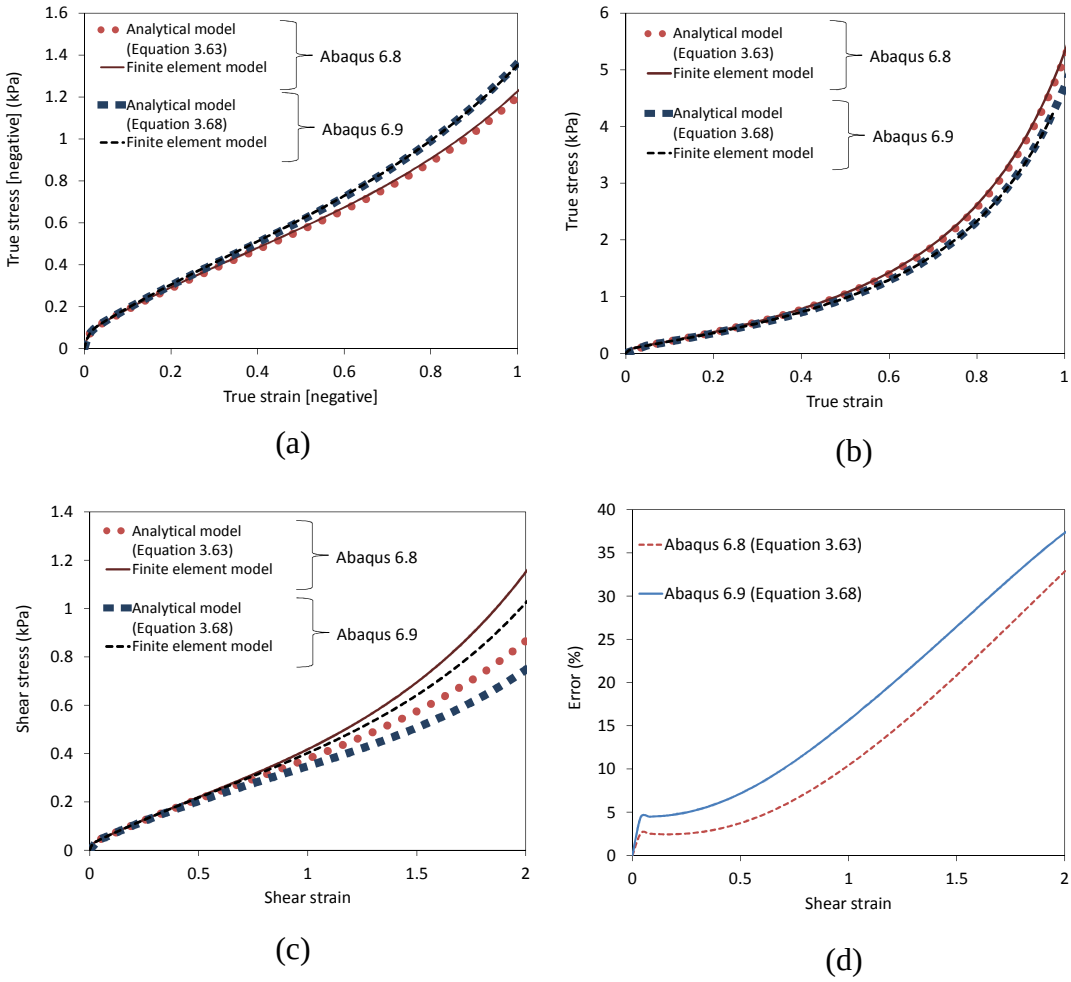

Figure 3.13. Comparison between finite element and analytical models of the visco-hyperelastic model under: (a) uniaxial compression at true strain rate of -5/min; (b) uniaxial tension at true strain rate of 5/min; (c) simple shear at shear strain rate of 5/min; and (d) error versus shear strain representing the difference between analytical and finite element model in (c).

To investigate the simple shear under large deformation, a simulation was performed using an example model available in Abaqus User Manual [Abaqus 2009] (Section 1.3.29: simple shear, Abaqus Verification Manual). This is based on the study by Dienes [1979]. The material properties used in the model were: Young's modulus = 1.0 (unit), Poisson's ratio = 0.0, and density = 1.346×10^{-4} (unit). A plane stress

element was used in the model. The results are shown in Figure 3.14. σ_{xy} , σ_{xx} and σ_{yy} indicate shear stress and normal stresses in *x* and *y* directions respectively in Figure 3.14. Notice that at small shear strain $(\gamma = 0.3)$, the normal stresses, σ_{xx} and σ_{yy} are zero (Figure 3.14(b)). However, as the strain increases, the normal stresses increase before they start to oscillate at a shear strain of 3. This is due to a significant rigid body rotation as the shear strain increases, as discussed by Dienes [1979]. The results indicate a complex behaviour in simple shear under large deformation and this will not be investigated further in this thesis. The reader can also refer to an analytical study by Horgan and Murphy [2010] on large deformation simple shear loading.

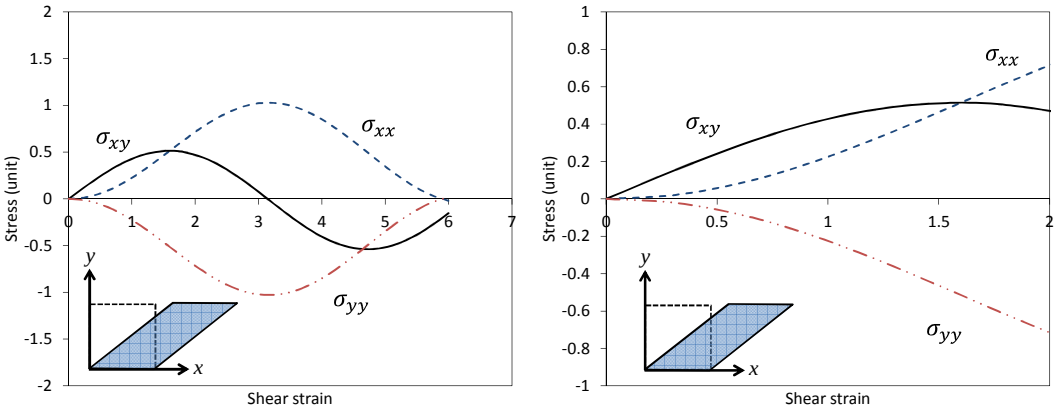

Figure 3.14. (a) and (b) Investigation of simple shear under large deformation using the example model in Abaqus User Manual [Abaqus 2009] (Section 1.3.29: simple shear, Abaqus Verification Manual).

The difference between the finite viscoelastic model in Abaqus versions 6.8 and 6.9 are highlighted in their respective Abaqus theory user manuals [Abaqus 2009; 2010]. This has also been discussed theoretically by Ciambella [2009] and Ciambella *et al.* [2009] whose suggested that the the finite viscoelastic model in Abaqus version 6.8

(Equation (3.59)) cannot describe accurrately the 3D FE viscoelastic model at large strain. The reason for this is that the model using Equation (3.59) does not provide a symmetric integral function when evaluated in 3D.

3.4 Viscoplastic Model

The viscoplastic material model available in Abaqus [2010] is described through a strain rate dependent yield behaviour. This is performed using a direct entry of stress and plastic strain test data at different strain rates into Abaqus CAE. The model is illustrated schematically in Figure 3.15.

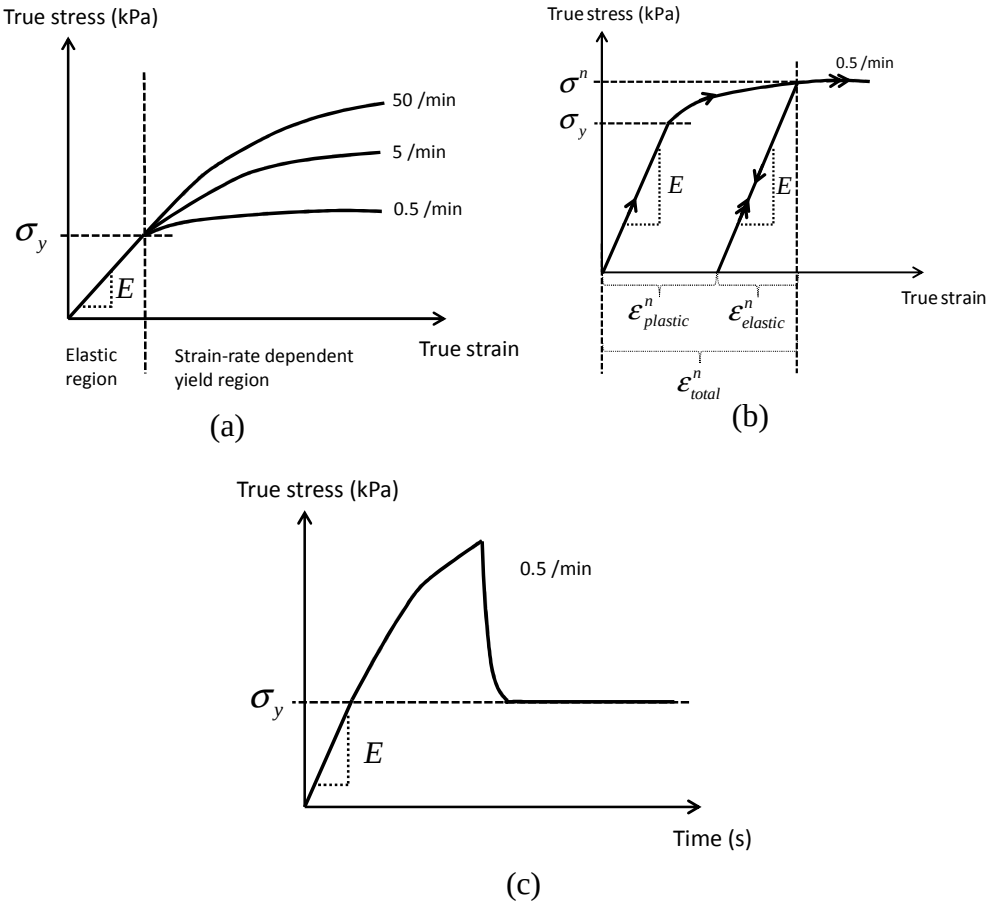

Figure 3.15. Description of viscoplastic material model under: (a) uniaxial extension test at different rates; (b) elastic and plastic strain in a cyclic test; and (c) stress relaxation test.

The viscoplastic model is divided into two regions, elastic region and strain-rate dependent yield region, as shown in Figure 3.15(a). In the former region, a value of modulus, E, and yield stress, σ_y, are defined. In the latter region, the rate-dependent behaviour is described using elastic and plastic strains in Figure 3.15(b). The plastic strain is calculated using the following:

$$\varepsilon_{plastic}^{n} = \varepsilon_{total}^{n} - \varepsilon_{elastic}^{n} = \varepsilon_{total}^{n} - \frac{\sigma^{n}}{E} \tag{3.81}$$

where $\varepsilon_{plastic}^{n}$, ε_{total}^{n} $\varepsilon_{elastic}^{n}$ and σ^{n} are the plastic true strain, total true strain, elastic true strain and true stress respectively at the n^{th} experimental data point in the 'yield regions' of Figure 3.15(a). Note that the yield stress value is selected to fit the relaxation stress in Figure 3.15(c). The elastic modulus, on the other hand is obtained to fit the unloading-reloading slope in Figure 3.15(b). To conclude, the following parameters are needed for input in Abaqus: elastic modulus and Poisson's ratio, and corresponding yield stress, plastic strain and plastic strain rate data.

3.5 Micromechanics Models

Micromechanics models are often used to investigate the effect of complex structures or multi-phase materials on the global mechanical behaviour. They have been developed and applied for composite materials through either analytical or finite element models. Analytical models are based on the ones such as the Mori-Tanaka or Eshelby models [Stapountzi *et al.* 2010], whereas the finite element models considers the microstructure of a material, either by using the embedded cell or unit cell geometries. The embedded cell geometry uses a representation of a cut-out image of

the real microstructure of a composite material, as shown in Figure 3.16(b). The composite material in Figure 3.16(a) can be defined as circular fillers surrounded by matrix material, where both fillers and matrix constituents are separated by interfaces [Mishnaevsky Jr. 2007] and have different material properties. However, to model the real microstructure of a material in such a way would require a large number of elements in a finite element software such as Abaqus (e.g. 475×10^3 elements needed in a simulation of particulate composites by Tarleton *et al.* 2012), which can take a lot of computational memory and time to simulate.

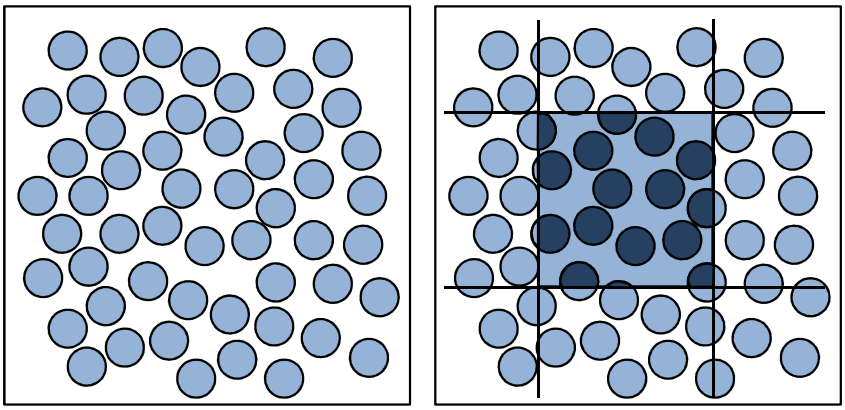

(a) (b)

Figure 3.16. (a) Real microstructure of a material; and (b) a cut-out image to represent the embedded cell geometry (reproduced from Bohm [2011]).

The unit cell geometry on the other hand assumes a periodic phase arrangement, i.e. a repeating unit cell of the microstructure, as shown in Figure 3.17 [Mishnaevsky Jr. 2007]. The boundary areas for possible models are shown in Figure 3.17, where different arrangements can be used to represent the unit cell geometry. This provides an advantage of being less expensive to model as compared to the embedded cell geometry in Figure 3.16(b).

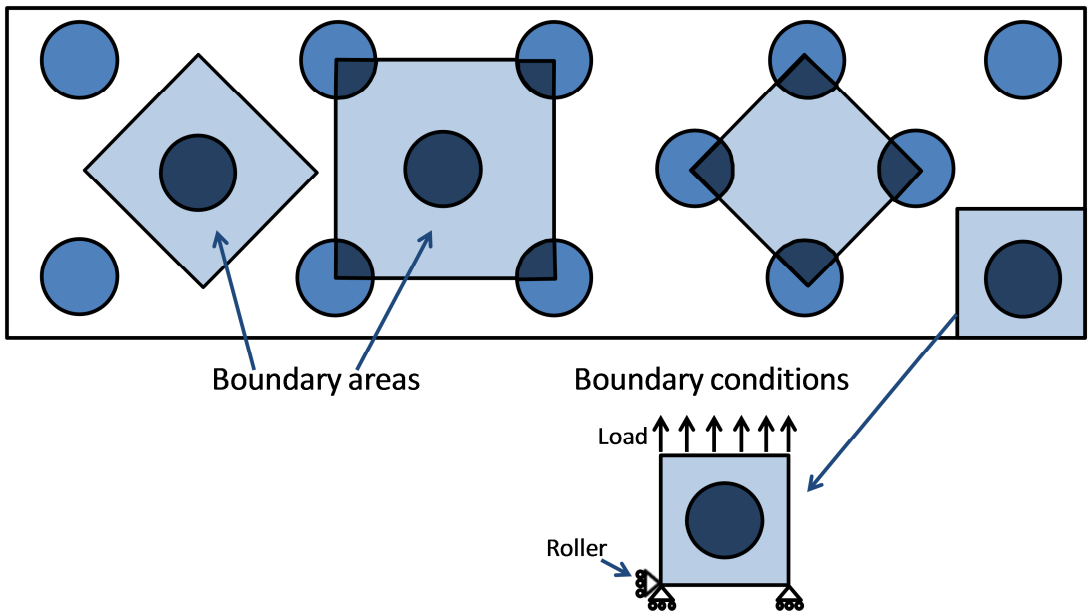

Figure 3.17. Different arrangement of unit cell model (reproduced from Mishnaevsky Jr. [2007]). The boundary areas for a unit cell model and the boundary conditions under uniaxial tension are shown.

Both embedded cell and unit cell geometries allow interactions between the filler and the matrix interface to be specified, as shown in Figure 3.18 for the unit cell geometry. This includes the debonding between filler and matrix (Figure 3.18(a)), a crack in the particle (Figure 3.18(b)) or a void in the matrix (Figure 3.18(c)).

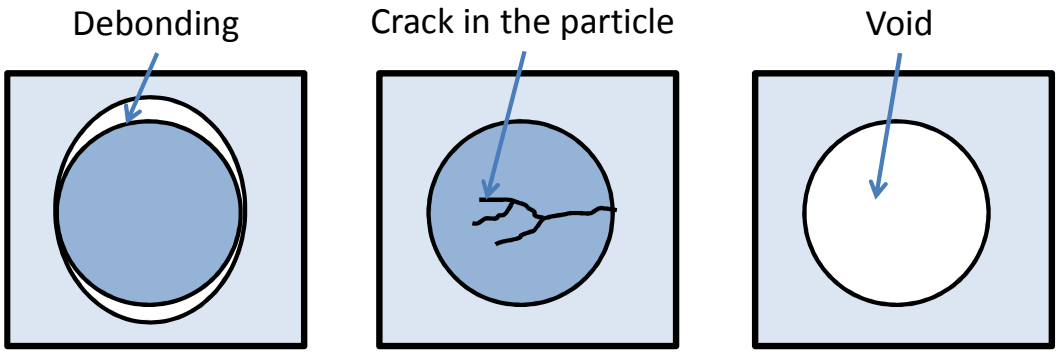

Figure 3.18. Failure or damage between the filler and matrix in the unit cell model using (a) debonding; (b) crack in the particle; and (c) void in the matrix (reproduced from Mishnaevsky Jr. [2007]).

3.5.1 Cohesive Interaction in Micromechanics Models

A cohesive interaction is considered to model the debonding between filler and matrix shown in Figure 3.18(a). The filler is initially bonded to the matrix. To describe the cohesive interaction, consider Figure 3.19 for two plates in cohesion subjected to load in different directions. The applied load causes the cohesion between the two plates to fail. The three modes of failure are usually referred to as opening Mode I (normal tension mode), Mode II (shear mode) or Mode III (out of plane shear mode).

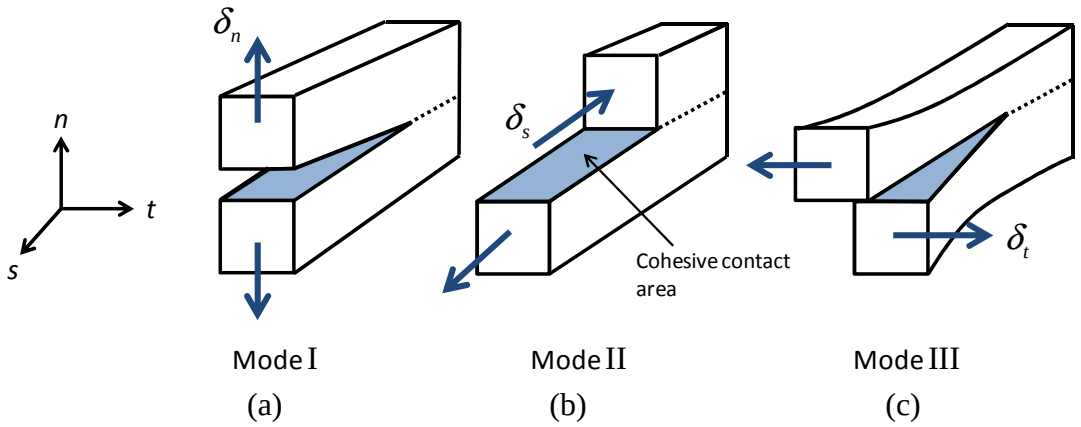

Figure 3.19. Different damage opening modes: (a) mode I (normal mode); (b) mode II (shear mode); and (c) mode III (out of plane shear mode) (reproduced from Krueger [2006]).

The traction versus separation law is used to model the cohesive element interaction, where the nominal traction stress vector, $\mathbf{t}$, is described as:

$$\mathbf{t} = \mathbf{K}\boldsymbol{\delta} = \begin{Bmatrix} t_n \\ t_s \\ t_t \end{Bmatrix} = \begin{bmatrix} K_{nn} & K_{ns} & K_{nt} \\ K_{ns} & K_{ss} & K_{st} \\ K_{nt} & K_{st} & K_{tt} \end{bmatrix} \begin{Bmatrix} \delta_n \\ \delta_s \\ \delta_t \end{Bmatrix} \tag{3.82}$$

where $\mathbf{K}$ is the coefficient tensor and $\boldsymbol{\delta}$ is the separation vector. The subscript in Equation (3.82) refers to the directions shown in Figure 3.19. For example, K_{nn}, K_{ss} and K_{tt} represent the normal, shear and tangential coefficients respectively. Equation (3.82) is described as a coupled traction-separation behaviour. For uncoupled traction-separation behaviour, Equation (3.82) is reduced to:

$$\mathbf{t} = \mathbf{K}\boldsymbol{\delta} = \begin{Bmatrix} t_n \\ t_s \\ t_t \end{Bmatrix} = \begin{bmatrix} K_{nn} & 0 & 0 \\ 0 & K_{ss} & 0 \\ 0 & 0 & K_{tt} \end{bmatrix} \begin{Bmatrix} \delta_n \\ \delta_s \\ \delta_t \end{Bmatrix}. \tag{3.83}$$

For a 2D traction separation behaviour, which considers only Mode I and Mode II damage only, Equation (3.83) reduces to:

$$\mathbf{t} = \mathbf{K}\boldsymbol{\delta} = \begin{Bmatrix} t_n \\ t_s \end{Bmatrix} = \begin{bmatrix} K_{nn} & 0 \\ 0 & K_{ss} \end{bmatrix} \begin{Bmatrix} \delta_n \\ \delta_s \end{Bmatrix}. \tag{3.84}$$

The traction versus separation law for each mode of failure can be separated into two regions [Camanho and Davila 2002; Abaqus 2009; Abaqus 2010], as shown in Figure 3.20.

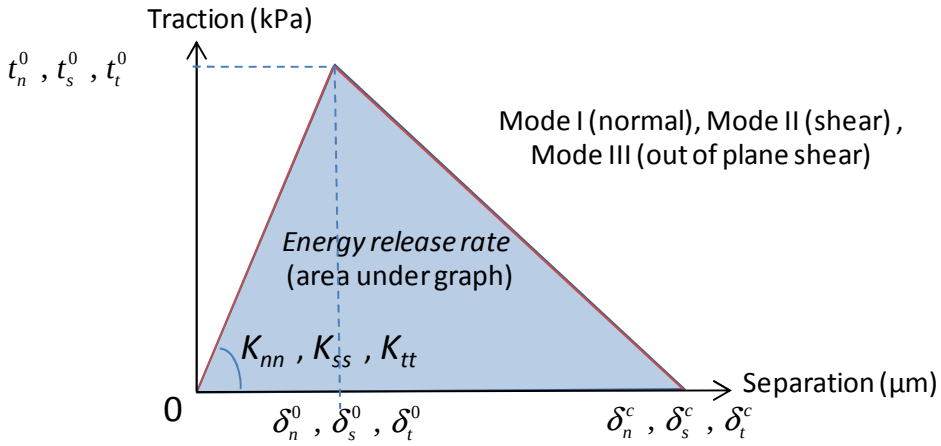

Figure 3.20. Traction versus separation curve.

In the first region, the traction-separation is linear elastic and is described using Equation (3.83). In the second region, which occurs at a critical normal stress, t_n^o, damage initiates. Damage is activated, in terms of a maximum stress criterion expressed as:

$$\max\left\{\frac{\langle t_n \rangle}{t_n^0}, \frac{t_s}{t_s^0}, \frac{t_t}{t_t^0}\right\} = 1 \tag{3.85}$$

where the symbol $\langle t_n \rangle$ represents the Macaulay bracket, defined as $\langle t_n \rangle = \frac{1}{2}\left(|t_n| + t_n\right)$, implying that damage is not initiated in compression. Progressive damage in the interface occurs until complete failure. The damage evolution law describes the rate at which the cohesive stiffness is degraded after the damage initiation criterion is reached. For a 2D traction separation behaviour (Equation (3.84)), the energy that is dissipated as a result of the damage process, i.e. the energy release rate, G_c, is equal to the area under the traction-separation curve in Figure 3.20, i.e. $G_{nc} = \frac{t_n^0 \delta_n^c}{2}$ and $G_{sc} = \frac{t_s^0 \delta_s^c}{2}$ for pure normal and shear loading conditions respectively. For mixed mode loading conditions which do arise at the interface of the circular particles, the FE software, Abaqus uses a linear mixed mode failure locus with the total energy release rate, *G*, being equal to:

$$G = G_n + G_s \qquad \text{and} \qquad \frac{G_n}{G_{nc}} + \frac{G_s}{G_{sc}} = 1 \tag{3.86}$$

where G_n and G_s are the energy release rate for pure normal and shear loading conditions respectively. The application of the cohesive law for the micromechanics model will be provided in detail in the Chapter 5 (Section 5.3.3).

3.6 Other Material Models for Wheat Flour Dough

3.6.1 Phan-Thien-Tanner (PTT) Model

The Phan-Thien-Tanner (PTT) model has been suggested for wheat flour dough by Phan-Thien *et al.* [1997]. In the PTT model, the stress tensor, $\boldsymbol{\sigma}$, is described as a combination of a hyperelastic stress tensor, $\boldsymbol{\sigma}_E$, and a viscoelastic stress tensor, $\boldsymbol{\sigma}_v$:

$$\boldsymbol{\sigma} = \boldsymbol{\sigma}_E + \boldsymbol{\sigma}_V . \tag{3.87}$$

The hyperelastic stress tensor, $\boldsymbol{\sigma}_E$ is described as:

$$\boldsymbol{\sigma}_E = \frac{G_E}{1+a} f(\gamma)\left(\mathbf{B} - a\mathbf{B}^{-1}\right) \tag{3.88}$$

where G_E is the elastic modulus, a is a constant related to the second normal stress difference, $f(\gamma)$ is a strain-softening function, and $\mathbf{B}$ is the left Cauchy-Green tensor. The viscoelastic stress tensor, $\boldsymbol{\sigma}_V$ on the other hand is described as:

$$\boldsymbol{\sigma}_V = f(\gamma)\sum_{j=1}^{N}\boldsymbol{\sigma}^{(j)} \tag{3.89}$$

where $\boldsymbol{\sigma}^{(j)}$ is [Phan-Thien *et al.* 2000]:

$$\boldsymbol{\sigma}^{(j)} + \lambda_j\left\{\frac{d\boldsymbol{\sigma}^{(j)}}{dt} - \mathbf{L}\boldsymbol{\sigma}^{(j)} - \boldsymbol{\sigma}^{(j)}\mathbf{L}^{\mathrm{T}}\right\} = 2\eta_j\mathbf{D}. \tag{3.90}$$

where the subscript and superscript (j) refers to discrete relaxation spectrum for $j = 1,...,N$ in Equation (3.89). The constants, λ_j and η_j are the relaxation time constant and viscosity respectively. $\frac{d}{dt}$ is the time derivative, $\mathbf{L}$ is the velocity gradient tensor, and $\mathbf{D}$ is the strain rate tensor. The constants, G_E, λ_j and η_j are determined from rheometric oscillatory tests through the following equations:

$$G^*(\omega) = G_E + \sum_j \frac{i\omega\eta_j}{1+i\lambda_j\omega} \tag{3.91}$$

$$\eta^*(\omega) = \frac{G_E}{i\omega} + \sum_j \frac{\eta_j}{1 + i\lambda_j \omega}$$

where $G^*(\omega)$ and $\eta^*(\omega)$ are the complex modulus and shear viscosity respectively, and ω is the rheometer test frequency in rad/s. The parameters, a and $f(\gamma)$ are determined from constant shear strain rate experiments. Phan-Thien *et al.* [1997] used the following equation for $f(\gamma)$:

$$f(\gamma) = \frac{1}{\left(1 + \gamma/\gamma_s\right)^{(1-m)/2}} \exp\left\{-\left(\frac{\gamma}{\gamma_p}\right)^4\right\} \tag{3.92}$$

where γ is the shear strain, γ_s represents the strain at which shear thinning occurs with exponent m, and γ_p is the strain at which "rupture" occurs under shear.

The PTT model has been investigated by Phan-Thien *et al.* [1997; 2000] for wheat flour dough under shear and oscillatory rheometry tests. The PTT model has been shown to fit reasonably well the Large Amplitude Oscillatory Shear (LAOS) tests Phan-Thien *et al.* [2000]. However, no numerical investigation is performed using the PTT model in a finite element method.

3.6.2 Pom-Pom Model

The Pom-Pom model describes the effect of branching on large deformation rheology [McLeish and Larson 1998], as illustrated in Figure 3.21.

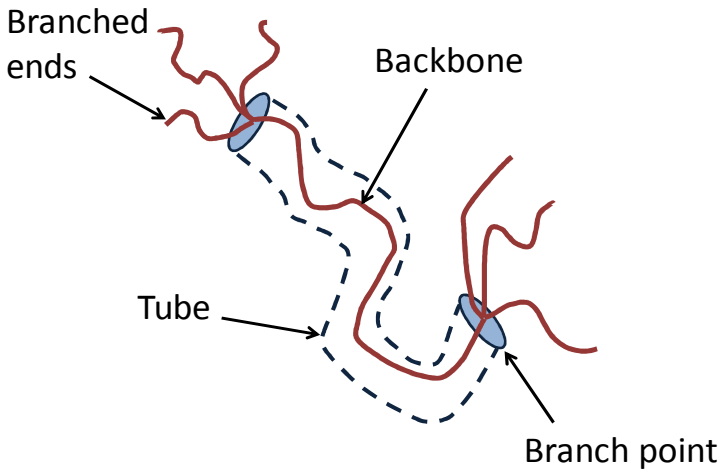

Figure 3.21. The Pom-Pom model (reproduced from Ng [2007]).

The branch point in Figure 3.21 acts as a constraint at the end of the polymer backbone to deform and flow. However, the constraint is not permanent and will release, allowing the branched point to retract into the tube if the backbone is stretched to a certain limit. The Pom-Pom model is described using the following equation:

$$\boldsymbol{\sigma} = G\phi^2\mathbf{S} \tag{3.93}$$

where G is a modulus related to relaxation modulus, $G(t)$; the latter can be obtained from the linear viscoelastic region [Clemeur *et al.* 2003]. The parameter, $\mathbf{S}$ is the orientation tensor and ϕ is a measure of the backbone stretching. The orientation tensor, $\mathbf{S}$, is described using:

$$\mathbf{S} = \frac{\mathbf{A}}{\mathrm{Tr}(\mathbf{A})}. \tag{3.94}$$

$\mathbf{A}$ is a tensor described by [Rubio and Wagner 2000]:

$$\mathbf{A} = \frac{1}{3\lambda_b} \int_{-\infty}^{t} \exp\left(\frac{t - t'}{\lambda_b} \right) \mathbf{C}^{-1}\left(t'\right) dt' \tag{3.95}$$

for reference time t' and time t. The parameter, $\mathbf{C}^{-1}\left(t'\right)$ is the Finger tensor and λ_b is a time-scale parameter.

The backbone stretching parameter, ϕ, in Equation (3.93) is defined as:

$$\frac{D\phi}{Dt} = \phi\left(\nabla v : \mathbf{S}\right) - \frac{1}{\lambda_s}\left(\phi - 1\right) \text{ ; for } \quad \phi < q. \tag{3.96}$$

where ∇v is the tube deformation rate vector. The symbol ":" represents the diagonal product of two tensors. The term $\frac{D\phi}{Dt}$ is described as the backbone relaxation, which occurs at a fixed characteristic stretch relaxation time scale, λ_s, while the orientation can also relax separately at a time scale of λ_b, as shown in Equation (3.95). Equation (3.96) is valid for a backbone that is stretched to a stretch limit, q. A visual representation of the stretch limit is shown in Figure 3.22. When the backbone stretching parameter, ϕ, is equal/larger than 1 but less than q, the branches are located outside the backbone tube. However, when the tube is stretched to the value of q, the branches are withdrawn into the backbone tube. This is defined as the limit of the backbone stretching parameter.

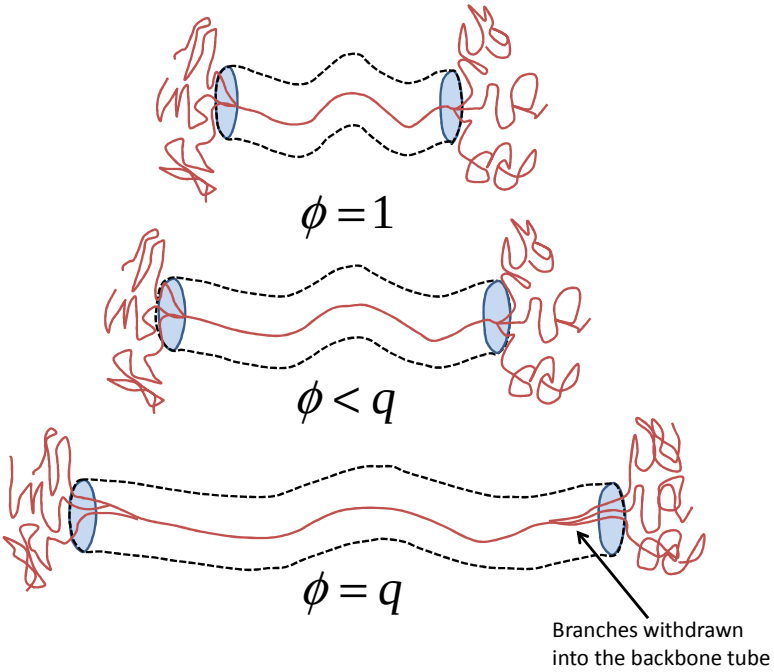

Figure 3.22. The structure of a pom-pom polymer with a backbone that is stretched to a stretch limit q (reproduced from McLeish and Larson [1998]).

The Pom-Pom model has been suggested as a suitable constitutive law for dough in previous literature [Dobraszczyk 2004; Ng 2007; Tanner *et al.* 2007], but to the author's knowledge, there is no published work on the use and validity of the Pom-Pom model for dough. This is possibly due to difficulties in determining the backbone stretching parameter for different modes of deformation, as discussed by Ng [2007].

3.7 Conclusion

This chapter discusses various material models that have been applied to dough. The Lodge rubberlike model was first described based on previous work on wheat flour dough [Ng and McKinley 2008; Tanner *et al.* 2008; 2011a]. Tanner *et al.* [2008] used the idea of a damage function in the Lodge rubberlike model to model dough under

high deformations. The visco-hyperelastic model was described next based from previous work on wheat flour dough [Charalambides *et al.* 2006], as well as the viscoplastic model available in Abaqus [2009; 2010]. This is followed by micromechanics models, which are used to investigate complex microstructures in composite materials. The models can be simulated in finite element software using the embedded cell or unit cell geometries. The geometries allow damage between the filler and matrix interface to be specified using the cohesive interaction law available in Abaqus [2009; 2010]. The interaction is defined using the traction versus separation behaviour [Camanho and Davila 2002]. Finally, other rheological models that have been suggested for dough are described, namely the Phan-Thien-Tanner (PTT) and Pom-Pom models.

Chapter 4. Experimental Work

4.1 Introduction

Wheat flour dough can be viewed as a composite material consisting of two main constituents, namely starch and gluten [Amemiya and Menjivar 1992]. The microstructure of dough, starch and gluten has been discussed in detail in Chapter 2. However, experimental investigation is normally performed only on dough [Ng 2007; Charalambides *et al.* 2006; Tanner *et al.* 2008; Lefebvre 2009] by assuming it as a homogenous material. Therefore in this chapter, investigation on the mechanical behaviour of dough will include starch, gluten and dough in an attempt to treat dough as a composite material. This includes mechanical loading tests under different modes, namely uniaxial tension, uniaxial compression and shear rheometry. Microstructure investigation is also performed on wheat flour dough using Cryogenic Scanning Electron Microscopy (Cryo-SEM).

This chapter is divided into four sections. In Section 4.2, sample preparation involved for the mechanical tests and microstructure studies on dough, starch and gluten are described. The dough mixing procedure is described first, followed by the dough washing procedure to separate the starch and gluten constituents. In Section 4.3, experimental details of the uniaxial tension, uniaxial compression, shear rheometry and Cryo-SEM tests are summarised. In Section 4.4, mechanical test results from gluten, starch and dough samples are shown, as well as the microstructure results obtained using the Cryo-SEM. Finally, in Section 4.5, the mechanical and microstructure test results are discussed followed by a proposal for a new microstructure theory for dough.

4.2 Sample Preparation

4.2.1 Dough Mixing

Wheat flour dough produced in industry normally consists of wheat flour, water, salt, yeast, emulsifiers and sweetener. A simple mixture of wheat flour, salt (sodium chloride) and water are considered here to provide a simpler mechanical/rheological study. The mixer used in this work is manufactured by National Manufacturing Co. with the capability of recording torque and speed during mixing to a computer, as shown in Figure 4.1. The mixer movement consists of four planetary pins on the head revolving around two stationary pins at the bottom of the mixing bowl. It is worth noting that this is the same mixer used by Xiao [2005] and Wanigasooriya [2006] in their wheat flour dough studies. Details and discussion on the mixer movement are provided in Appendix C.

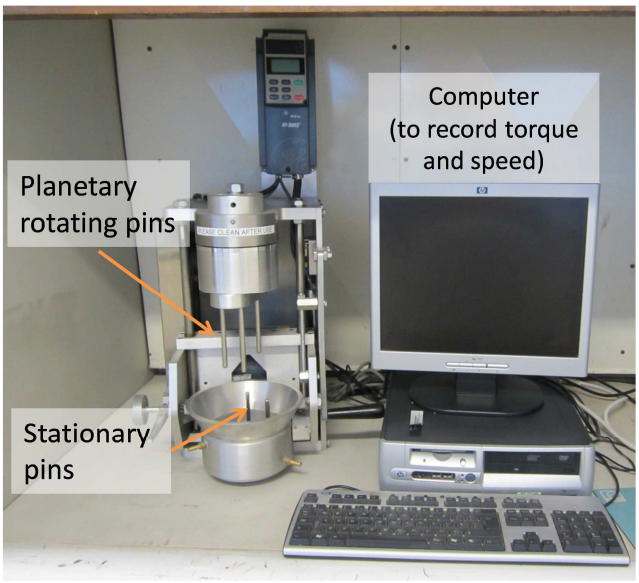

Figure 4.1. Dough mixer used in this work.

The flour used is a strong white bread flour purchased from the Wessex Mill in Oxford, United Kingdom. A mixture of 198.5 g of wheat flour, 120 g of distilled water and 1.5 g of sodium chloride is used to make the dough (62 %, 37.5 % and 0.5 % weight percentage of wheat flour, water and salt respectively). The recipee is the same as those performed in previous work on dough at Imperial College [Xiao 2005; Wanigasooriya 2006]. At the speed of 118 rpm, the optimum mixing time is 100-130 seconds, where this corresponds to the peak in mixing torque, as illustrated in Figure 4.2 where torque versus mixing time is plotted. It was found that increasing the mixing time, i.e. >130 seconds reduces the torque value, as indicated in the overmixed region in Figure 4.2. The environment was controlled at 50 % relative humidity and a temperature of 22 ^{0}C .

The mixed dough was separated into two portions and wrapped using cling film. One portion was used for the mechanical and microstructure tests on dough, whereas the other portion was used for the dough washing procedure which is described in the next section. Paraffin oil was applied on the former dough portion to maintain the moisture of the sample constant.

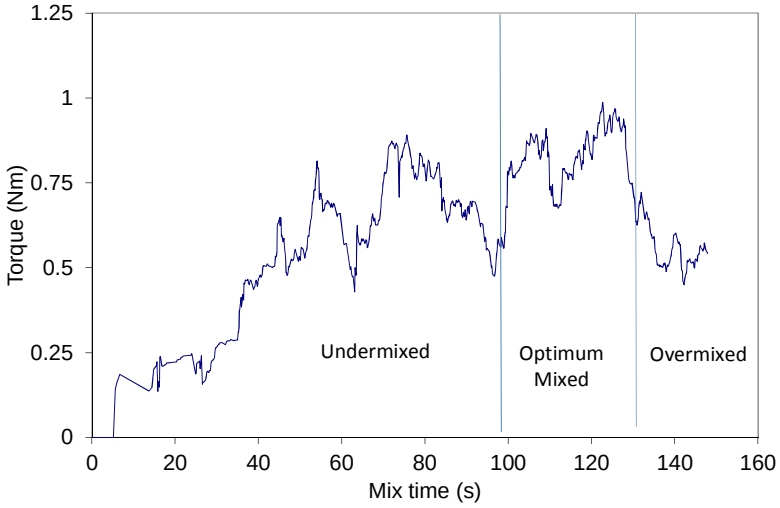

Figure 4.2. Torque versus mixing time of a dough sample.

4.2.2 Dough Washing

As stated in the previous section, a portion of the mixed dough was used for the dough washing procedure. The latter followed guidelines by Abang-Zaidel *et al.* [2008], such that the starch in the dough was removed by washing the dough under running tap water. During washing, the sample was gently rubbed using fingers to ensure that as much as possible starch was removed from the gluten matrix. The starch was assumed to be absent when no cloudiness appeared after the gluten was squeezed into a container of clean water. The remaining free water in the gluten is allowed to drip out by resting the gluten sample for approximately 120 minutes on a water absorbent paper. The gluten matrix was then collected, weighed and wrapped in a cling film. To obtain dry gluten, the wet gluten was cut into small pieces and was allowed to dry at a temperature of 22 ^{0}C and 50 % relative humidity overnight. The dry gluten was then weighed.

A similar procedure to the one described above was performed to collect the starch granules in this work. Rather than draining the water containing starch during the washing, it was collected in a container. The container with water and starch was then allowed to rest for two hours so that the starch sediments filled the bottom of the container. The clear water on top of the container was then drained. The starch sediment was poured into a large steel tray, and was allowed to dry at a temperature of 22 ^{0}C and 50 % relative humidity overnight. The dry starch was then collected and its mass was measured.

4.2.2.1 Gluten Samples

The wet gluten as obtained from the dough washing procedure described in the previous section was used for all the mechanical tests and microstructure analysis on gluten.

4.2.2.2 Starch Samples

The reconstituted wet starch was obtained by adding the dry starch prepared as described in Section 4.2.2 with a prescribed amount of water. The amount of water added to the dry starch needs to represent the water content of starch in mixed dough. Thus the water distribution between flour components, i.e. starch and gluten, needs to be known. A few methods are available to measure this, namely the simple liquid summation method and the water vapour absorption method [Roman-Gutierrez *et al.* 2002a; 2002b]. These are discussed in Section 2.2.5.

The simple liquid addition method was initially performed in this work by measuring the weight of starch and gluten obtained from the dough washing procedures. First,

the wet and dry gluten weights were measured experimentally, which are referred to as [2b] and [1b] in Table 4.1 ([2b] implies row [2], column [b]). The water content of gluten was calculated as: [3b]=[2b]-[1b]. This was then used to obtain the wet and dry starch weight, [2a] and [1a] respectively, from the known weight of dough [2c] and dry flour [1c]: i.e. [2a]=[2c]-[2b]. It should be noted that the value calculated in [1a] (dry starch) is somewhat larger than the experimentally measured value (~ 165 g). This may be due to some starch being lost during the starch preparation procedure. The water content of starch [3a] is then calculated as the difference between water of dough [3c] and water of gluten [3b]. The distribution of water, [4], was obtained by: i.e. [4a]=[3a]/[3c]. Finally the (water-content)/(dry-weight), [5], was obtained by dividing row [3] by row [1], e.g. [5a]=[3a]/[1a].

Table 4.1. Starch and gluten composition in dough using simple liquid summation method.

	[a] Starch	+	[b] Gluten	=	[c] Flour/Dough
[1] Dry weight(g)	171		27.5		198.5
[2] Wet weight (g)	231.8		86.7		318.5
[3] Water content (g)	60.8		59.2		120
[4] Distribution of water (%)	52		48		100
[5] Water-content/Dry-weight (w/w)	0.35		2.15		0.60

The starch sample obtained using the formulation summarised in Table 4.1, [5a], is referred to as starch 1. It was found that starch 1 was very dry and powdery when moulded into a cylindrical shape for the compression tests. Under uniaxial compression, the starch crumbled rather than uniformly deformed, as shown in Figure 4.3.

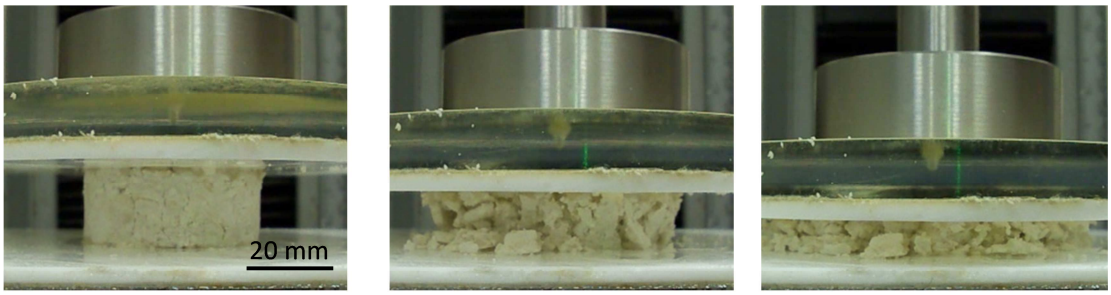

Figure 4.3. Uniaxial compression results of starch 1 at -5/min. True strain is evaluated through Equation (2.5). The uniaxial compression test method is discussed in Section 4.3.2.

The alternative was to use the water content data for dough and gluten reported by Roman-Gutierrez *et al.* [2002b]. They used the water vapour absorption method and measured the ability of the individual flour components to trap water molecules by measuring the mass of an initially dry sample, placed on an atmospheric microbalance in a continuous flow of air, at controlled relative humidity. The mass of water absorbed at different humidities was then used to determine the theoretical distribution of water in dough, through the Guggenheim-Anderson-de-Boer (GAB) model, which is discussed in Section 2.2.5. The theoretical water distribution among flour components for a strong wheat flour was approximately 88 % for starch and 12 % for gluten/others at 60 % relative humidity and 25 ^{0}C . It is worth noting that the flour used in this work is also a strong wheat flour, similar to the one used by Roman-Gutierrez *et al.* [2002b]. Therefore, their suggested water distribution values were used to estimate the water content of starch, as shown in [4] in Table 4.2. The entries in Table 4.2 were calculated in the same way as those in Table 4.1.

Table 4.2. Starch and gluten composition in dough using water vapour absorption method.

	[a] Starch	+	[b] Gluten	=	[c] Flour/Dough
[1] Dry weight (g)	171		27.5		198.5
[2] Wet weight (g)	276.6		41.9		318.5
[3] Water content (g)	105.6		14.4		120
[4] Distribution of water (%)	88		12		100
[5] Water-content/Dry-weight (w/w)	0.62		0.52		0.60

The starch sample obtained using the formulation in Table 4.2 is referred to as starch 2. Note that, compared to starch 1, a larger amount of water was added for starch 2. As a result, it was found that starch 2 formed a paste-like substance which could easily be formed into compression test samples, and the starch was uniformly deformed during uniaxial compression tests, as shown in Figure 4.4. It was decided that the formulation in Table 4.2 would be used for the mechanical tests on starch in this work. It would be interesting to investigate the difference in microstructure of starch 1 and 2 using Cryo-SEM in the future.

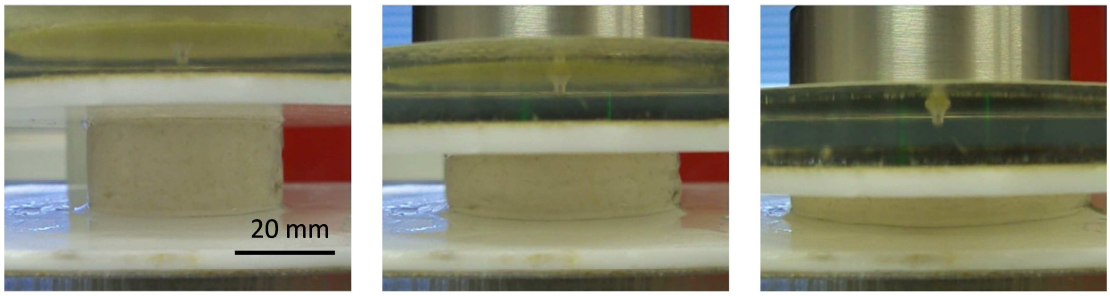

Figure 4.4. Uniaxial compression results of starch 2 at -5/min.

4.3 Experimental Methods

4.3.1 Uniaxial Tension

The geometry for uniaxial tension tests were discussed in Section 2.3.1. A cylindrical "I" shaped mould made from Perspex is used to prepare specimens for the uniaxial tension tests, as shown in Figure 4.5. The "I" shaped geometry is chosen as sample preparation is relatively easy compared to dumbbell shaped and cylindrical flared end (CFE) moulds. No heating is needed at the sample ends if the "I" shaped geometry is used. The sample ends were air dried quickly so that the end sections could be glued to the test platens and therefore will not flow during the test. This has been described already in detail in Section 2.3.1.

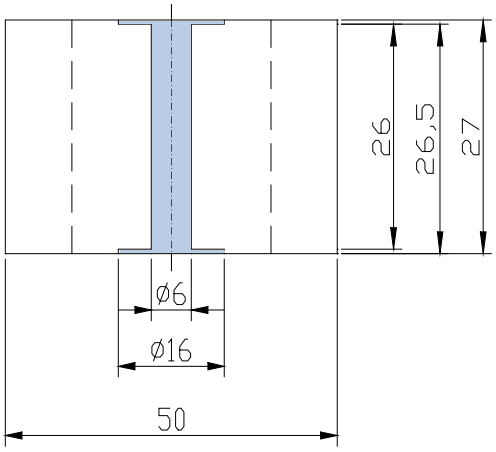

Figure 4.5. Geometry of "I" shaped mould used [Wanigasooriya 2006]. All units shown are in milimeter (mm).

The mould was cut into two halves along its length. A rod of dough approximately 6 mm in diameter is placed into one half of the mould and the other half is then used to "close" the mould. To eliminate sticking of the sample onto the surface of the mould, paraffin oil was used as a lubricating agent. The two halves of the mould were

pressed together, and the excess dough was cut off from the two ends using a pair of scissors. The ends of the specimen surfaces were flattened by placing the mould between two PTFE platens. A small weight was placed on top of one of the plates for 10-15 minutes. The two plates were removed by a sliding motion and any excess material was scraped off using the edge of a Perspex plate.

The sample was then left to relax for 45 minutes before testing, as shown in Figure 4.6(a). The exposed end sections of the sample were left to air dry during this time period. After that, one half of the mould was then taken out (Figure 4.6(b)), before lines was marked on the sample surface, as shown in Figure 4.6(c). The marking was performed using food colour (Supercook black), which was spray painted through a stencil with horizontal lines opening. The sample was then glued on the loading platens using Cyanoacrylate adhesive. The adhesive was left to cure for approximately three minutes. The mould was then carefully removed from the sample, and the paraffin oil applied earlier assisted the removal process. Figure 4.6(d) shows the sample just before the test starts.

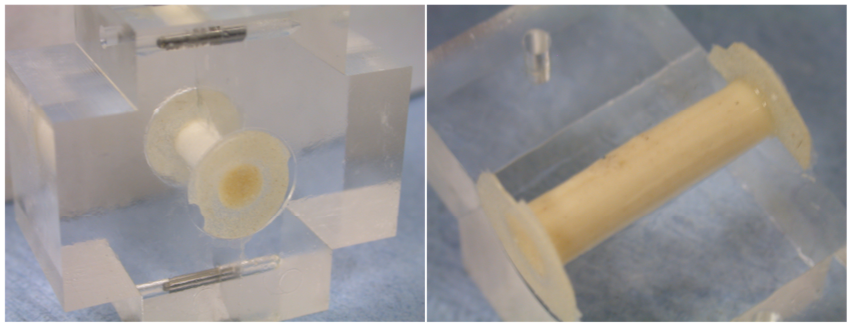

(a) (b)

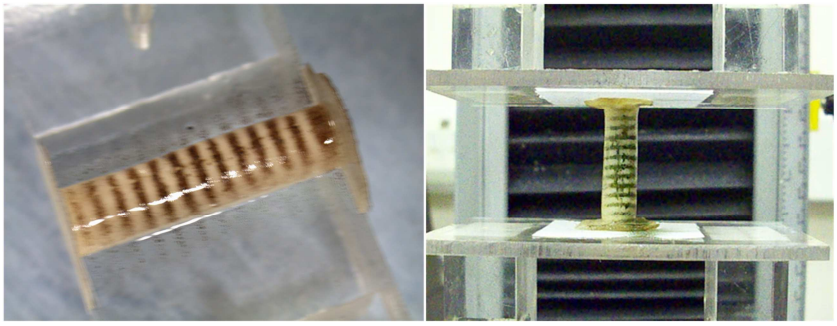

(c) (d)

Figure 4.6. (a) The dough sample in the mould, where the end sections were exposed to air; (b) sample after a half of the mould was taken out; (c) sample after being marked; and (d) sample after glued to the loading platens and the mould was removed.

All tests were performed in a controlled environment laboratory of 22 ^{0}C and 50 % relative humidity. An Instron 5543 testing machine with a 100 N load cell, capable of performing true strain rate tests, was used for the extension measurements. The tests were performed at constant true strain rates (CTSR) as opposed to constant crosshead speeds (CCS). To keep the strain rate constant, the crosshead speed was set to decrease exponentially with time. Kouassi-Koffi *et al.* [2010] investigated the difference between CTSR and CCS tests on dough, and they found that CTSR and CCS tests produce quit similar results for true strain up to ~ 0.25. However at large strain, CCS tests give higher consistency index and power law constant, k and n respectively than CTSR tests when plotted using power law equation, i.e. Equation

(3.1). This is because the true strain rate for CCS tests is not constant compared to CTSR tests.

4.3.2 Uniaxial Compression

Compression tests were performed following the procedures outlined by Charalambides *et al.* [2005; 2006]. The materials and apparatus needed are shown in Figure 4.7.

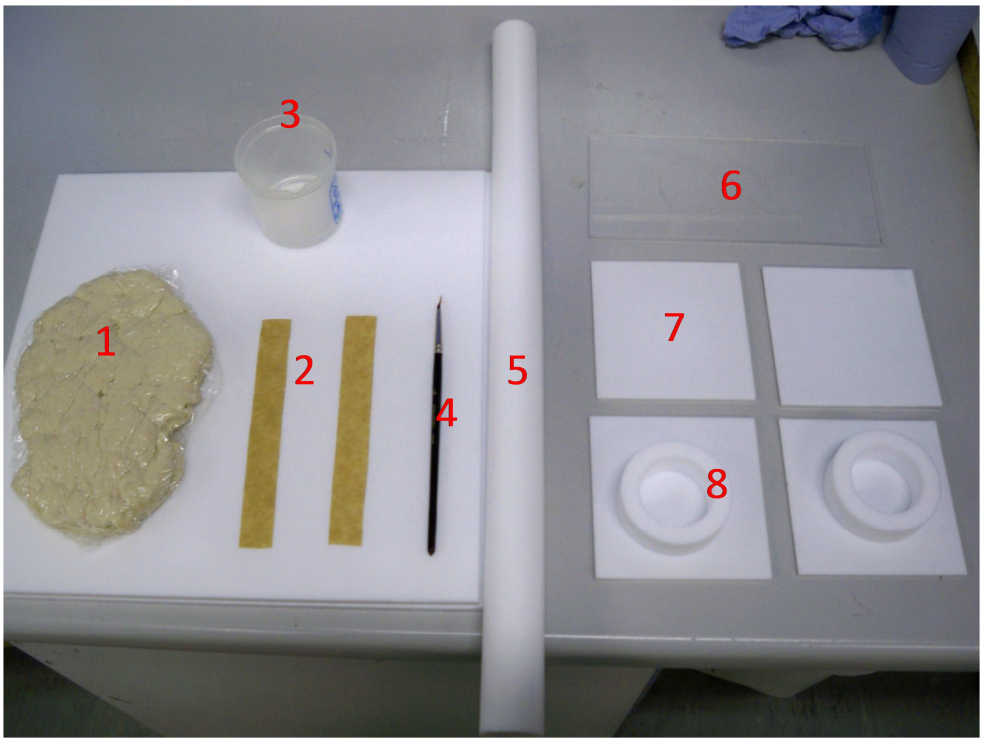

Figure 4.7. Materials and apparatus for uniaxial compression tests: 1) dough, 2) grease-proof paper, 3) paraffin oil, 4) paint brush, 5) PTFE roller, 6) Perspex plate, 7) PTFE plate, and 8) ring mould.

Ring moulds of 40 mm diameter and height of 20 mm were used. A ring mould and a square PTFE plate were coated with paraffin oil. Greaseproof paper was used around the internal surface of the mould to assist removal of the sample from the mould. A

portion of dough was pressed into the ring mould (see Figure 4.8(a)), and any excess dough was removed using a Perspex plate, as shown in Figure 4.8(b). No excess of dough can be seen in Figure 4.8(c) by placing the Perspex plate on top of the sample. A PTFE plate was then placed on top of the mould filled with dough.

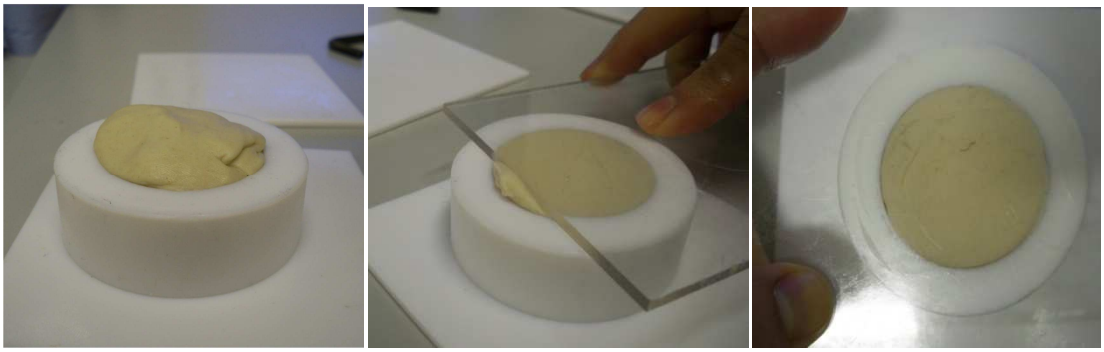

(a) (b) (c)

Figure 4.8. (a) Sample in the mould; (b) excess dough being removed; and (c) no excess dough on top as observed using Perspex plate.

After approximately 10 minutes, the top PTFE plate and mould were removed through a sliding motion, as shown in Figure 4.9(a). The sample was then allowed to relax for at least 45 minutes, as shown in Figure 4.9(b). During the relaxation period, paraffin oil was applied on the top surface of the exposed sample. The greaseproof paper used earlier helps to support the sample edge during the relaxation period (Figure 4.9(b)). The sample was transferred from the PTFE sheet to the bottom of the loading platen through a sliding motion. The greaseproof paper was then peeled off from the sample, as shown in Figure 4.9(c), just before the tests.

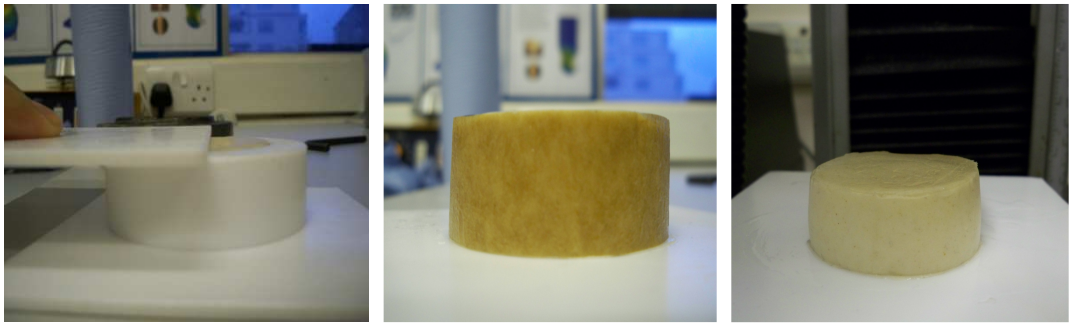

(a) (b) (c)

Figure 4.9. (a) PTFE plate removed by sliding motion; (b) sample was allowed to relax for 45 minutes with greaseproof paper; and (c) sample after being transferred to the loading platen.

The tests were conducted under lubricated conditions using a 500 centistokes silicone lubricant **(**Polysiloxanes) applied at the sample and platen interface [Charalambides *et al.* 2005]. Any residual paraffin oil was removed using absorbent paper at this stage before applying the silicone lubricant. An Instron 5543 testing machine with a 1 kN load cell, capable of performing true strain rate tests, is used for the measurements. The tests were performed at constant strain rates until true strain values reached -1. A strain value larger than -1 is not proposed in this study due to the lubricant's inability to provide frictionless conditions at such high strains [Charalambides *et al.* 2005; 2006].

Cyclic-compression tests were also performed. The sample is compressed and subsequently unloaded to zero stress at the same strain rate; subsequent reloading-unloading cycles followed at the same strain rate. An additional PTFE film of 25 μm thickness was positioned between the top, reversing platen and the sample as an extra precaution to ensure that zero tension is applied on the sample during the unloading phase of the test. An example of the applied true strain versus time plot for cyclic tests on gluten is shown in Figure 4.10.

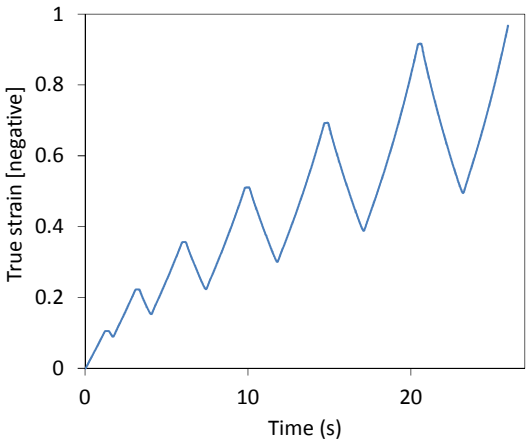

Figure 4.10. True strain versus time for cyclic-compression of gluten at -5/min.

4.3.3 Shear Rheometry

The sample was mounted on a AR2000ex (TA Instruments) rheometer. All the tests were performed using the parallel plate configuration (Figure 4.11a). Sand paper of 100 grit size grade was attached on the plate surface to prevent the slippage of the sample during the tests [Tanner *et al.* 2008], as shown in Figures 4.11(a) to 4.11(c). Waterproof sand paper (Mirka Wet and Dry) was used to prevent swelling of the sandpaper when in contact with wet samples [Harito 2010]. The tests are best performed using cone and plate geometry, as shear strain in the geometry is uniform throughout the gap. However, if sandpaper is used to prevent slippage, then the parallel plate geometry is more practical. It is easier to apply adhesive backed sand-paper onto the parallel plate than on the cone and plate geometry. Most of the reported shear tests on dough are previously performed using the parallel plate geometry [Phan-Thien *et al.* 1997; Ng and McKinley 2008; Lefebvre 2009]. This has been described already in detail in Section 2.3.3. A 40 mm diameter parallel plate is used for the tests.

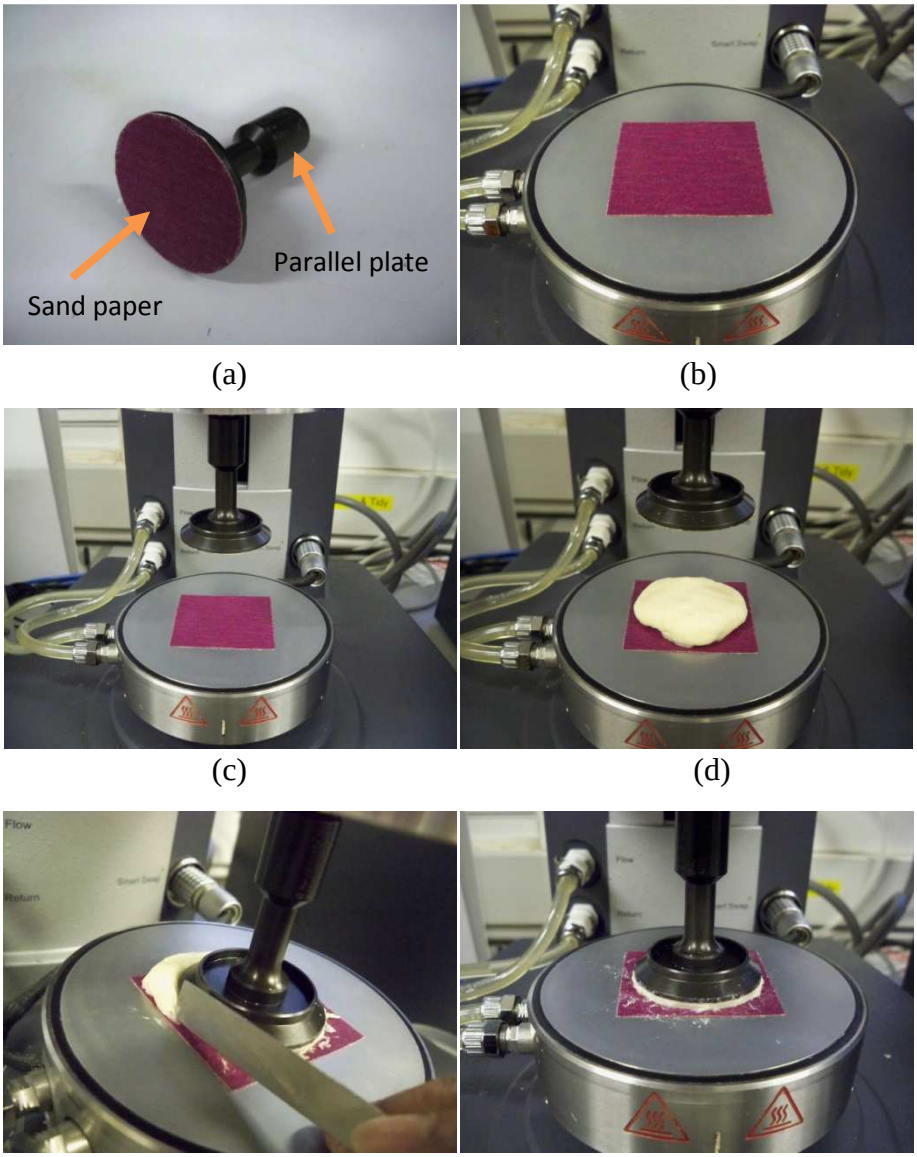

Figure 4.11. Sample preparation for shear rheometry test: (a) sand paper attached to the surface of a parallel plate; (b) sand paper attached on the base plate; (c) the parallel plate attached to the rheometer; (d) a dough sample is placed on the base plate; (e) the excess dough at the side of the plates was removed; and (f) the sample was allowed to rest for 45 minutes.

The sample was placed on the peltier plate (base plate) of the rheometer (Figure 4.11(d)), and the top plate was lowered to make contact with the sample. A 3 mm gap was set between the plate and the base. The excess dough at the side of the plates was

removed using a sharp blade, as shown in Figure 4.11(e). The sample was allowed to rest in this configuration for 45 minutes until the normal stress reduced significantly (Figure 4.11(f)). This step of reducing the normal stress is crucial in the sample preparation since the residual stress from the mixing and specimen mounting influences the measurement of shear stress of the dough [Phan-Thien *et al.* 1997]. A thin layer of silicon oil was applied at the sides during the rest time to prevent drying at the edges of the sample. The temperature of 22 ^{0}C at the rheometer base (peltier plate) is controlled by a water circulating temperature control unit (Julabo AWC 100).

4.3.4 Cryo-SEM

The Cryo-SEM test equipment (model ALTO 2100) manufactured by Gatan was used to observe the microstructure of dough. A schematic of the equipment consisting of a Cryostage, Prep-chamber, and Slush station is shown in Figure 4.12.

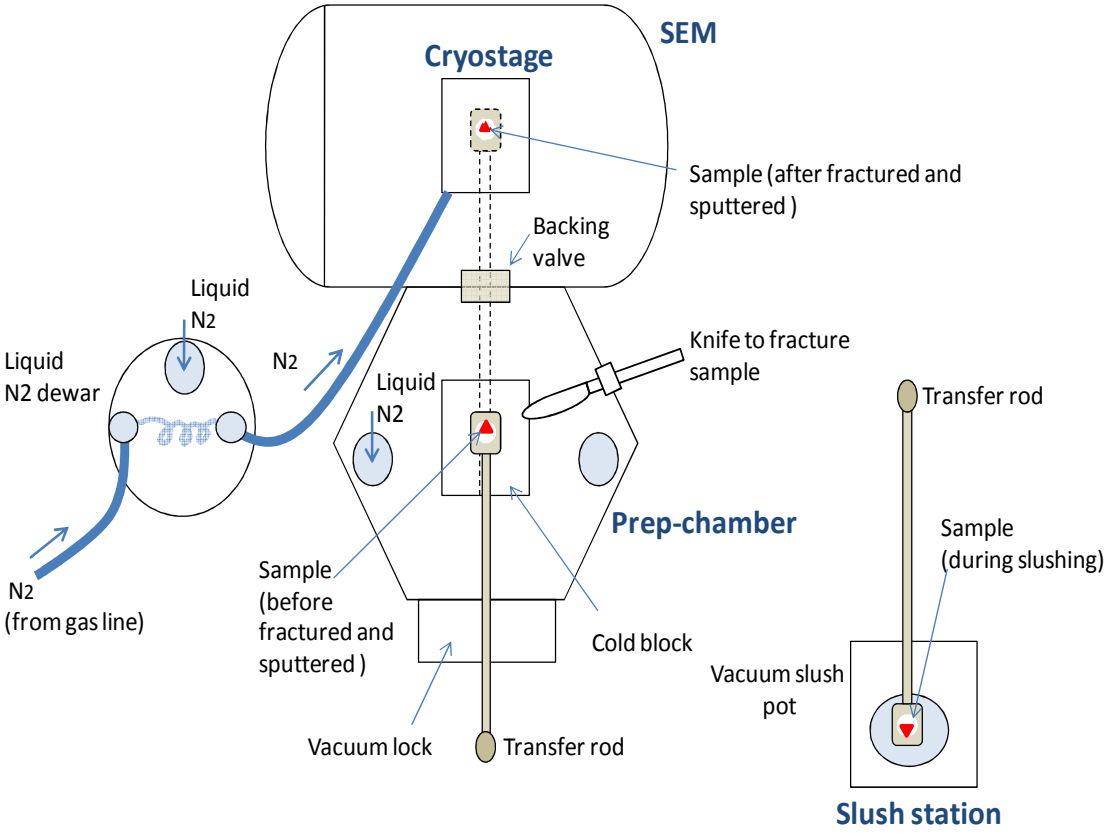

Figure 4.12. Cryo-SEM test configuration for a dough sample.

The Cryostage is placed inside the SEM chamber (Figure 4.13(a)), which is connected to the prep-chamber through an opening (backing valve) at the side of the SEM unit (Figure 4.13(b)). The Cryostage and the Prep-chamber are connected to a controller and liquid nitrogen circulation system to control the temperature (Figure 4.12).

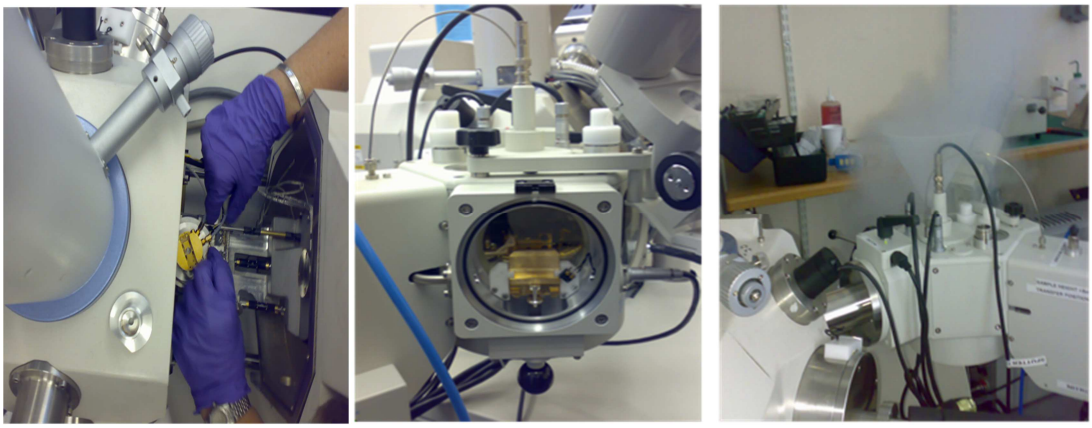

(a) (b) (c)

Figure 4.13. (a) The Cryo-stage is installed in the SEM chamber; (b) prep-chamber; and (c) evaporated liquid nitrogen during the cooling down process.

At the beginning of the Cryo-SEM test preparation, the Prep-chamber and Cryostage inside the SEM need to be cooled down with liquid nitrogen at a temperature of approximately -185 ^{0}C (Figure 4.13(c)). Once the light indicator next to the backing valve (the valve between SEM and Prep-chamber in Figure 4.12) turned green, the Cryo-SEM test equipment is ready for the experiment. A small piece of dough (approximately 5 mm size) was glued on a sample holder, which is connected to a transfer rod. The sample was then placed in a vacuum slush pot containing liquid nitrogen at the Slush station, as shown in Figure 4.14. Once exposed to liquid nitrogen (Figure 4.14(b)), the sample was covered using a PTFE cover at the Slush station (Figure 4.14(c)) and moved to the Prep-chamber under vacuum (Figure 4.14(d)). The sample needs to be under vacuum at the Slush station to maintain the same vacuum condition when transferred to the Prep-chamber. In addition, the PTFE cover prevents water from the ambient surrounding atmosphere to accumulate on the sample's surface once exposed to liquid nitrogen.

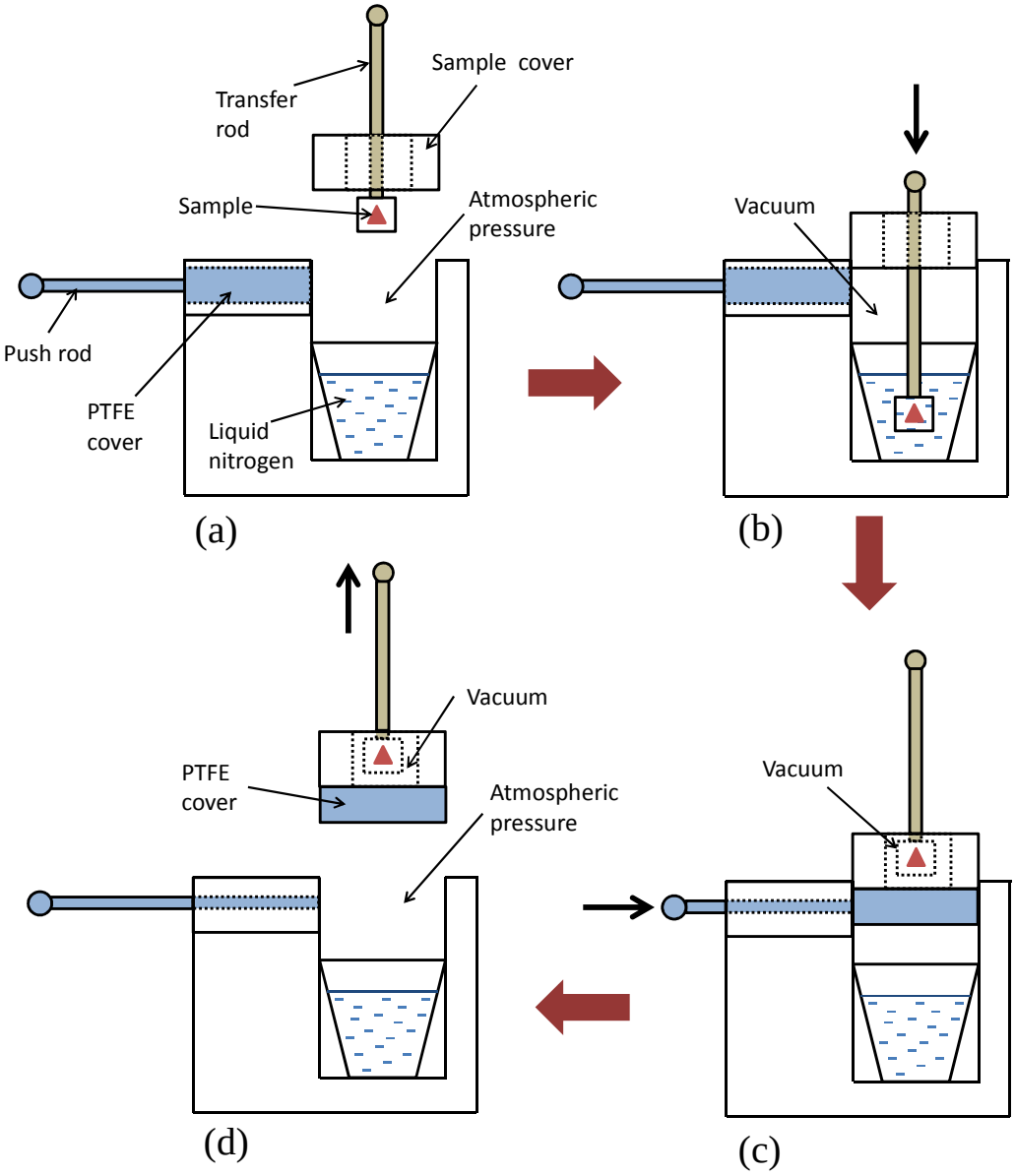

Figure 4.14. Exposure of dough sample into liquid nitrogen at the Slush station.

Inside the Prep-chamber, the sample was transferred to the Cold block where it was fractured using a sharp blade to reveal its internal surface (see Figure 4.12). To eliminate ice that has formed on the surface of the sample, a process called sublimation was performed. Sublimation was conducted by transferring the sample from the colder temperature stage inside the Prep-chamber to a higher reference temperature inside the SEM. The sample was left there for a period of time to remove

ice on the sample's surface. During this process, it is important to record the temperature and time setting for reasons which will be discussed in Section 4.4.4. The sample was then transferred back to the Cold block in the Prep-chamber and gold sputtered for 90 seconds. The imaging was finally performed at the Cryostage after the gold sputter process (Figure 4.12).

4.4 Experimental Results

4.4.1 Uniaxial Tension

The tensile behaviour of gluten at two different strain rates (5/min and 0.5/min) is shown in Figures 4.15(a). Gluten shows strain hardening at large strain as well as strain rate dependent behaviour. The sample is deformed uniformly, as shown in Figure 4.15(b). The results for different samples at the same rate, i.e. 5/min are shown as filled and unfilled points in Figure 4.15(a) to indicate repeatability. Note that the experimental results in this section are obtained from at least four replicate samples using the same batch of flour.

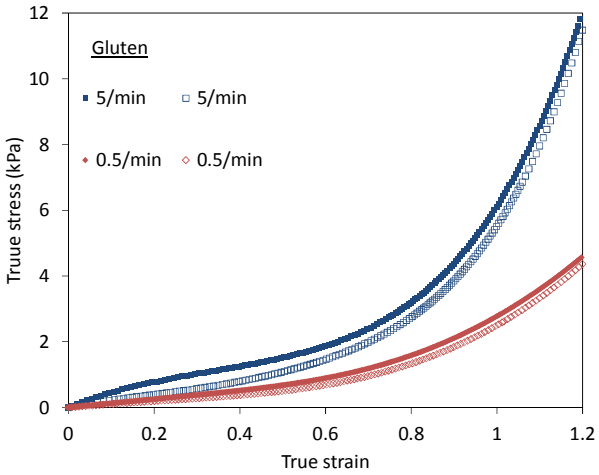

(a)

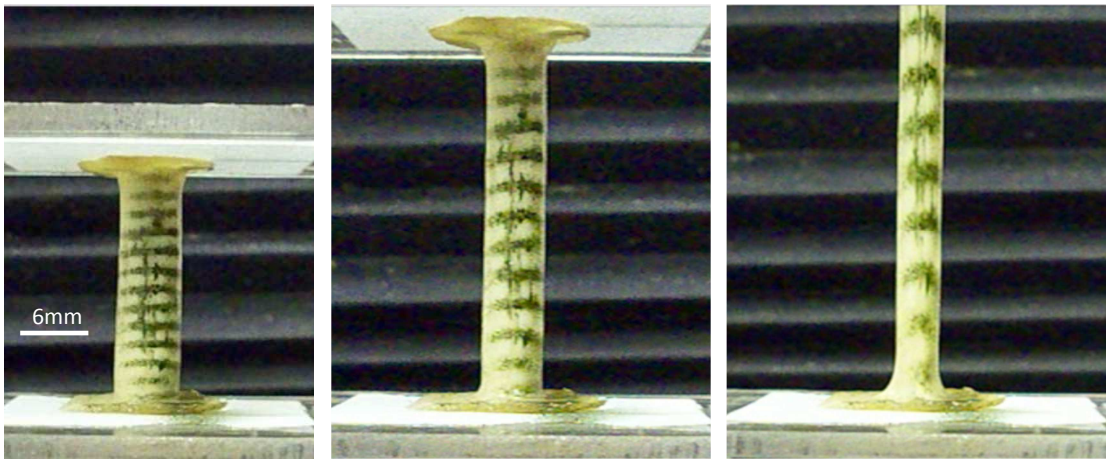

True strain 0.1 True strain 0.5 True strain 1.0

(b)

Figure 4.15. (a) Uniaxial tension test results on gluten; and (b) sample deformation at different true strain values during tensile tests at 5/min.

The results from tensile tests of dough at different strain rates are shown in Figure 4.16(a). A strain rate dependent behaviour is observed at the strain rate tests of 5/min and 0.5/min, which is similar to the gluten test results in Figure 4.15. Images of a dough sample under tensile test at different strain values are shown in Figure 4.16(b). Notice that the deformation of dough in Figure 4.16(b) is less uniform compared to the images of gluten in Figure 4.15(b). This is possibly due to dough being softer than

gluten, as shown by the difference between the stress-strain results in in Figure 4.16(a) and 4.15(a) respectively.

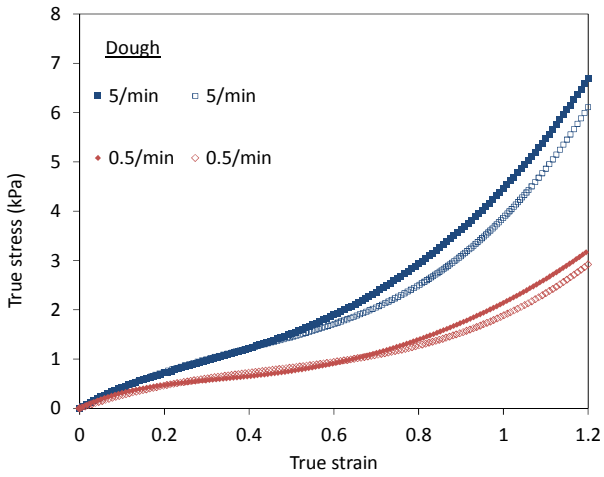

(a)

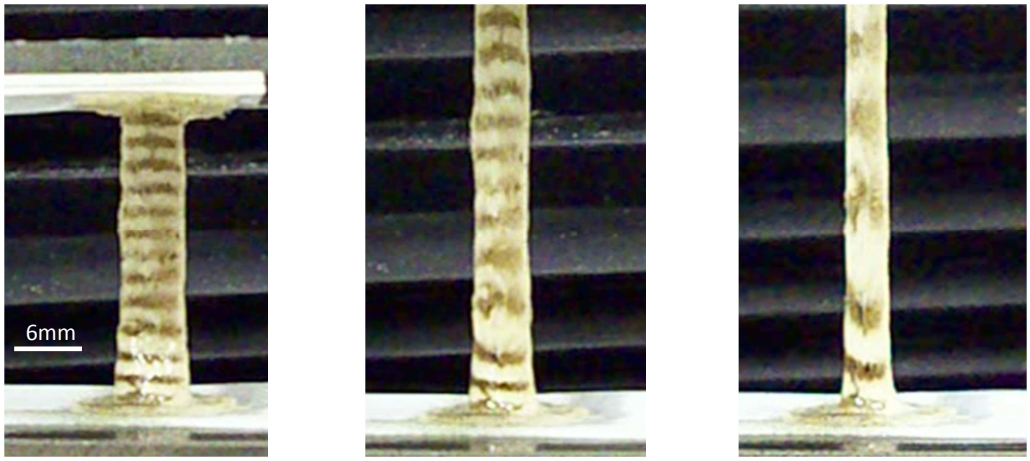

True strain 0.1 True strain 0.5 True strain 1.0

(b)

Figure 4.16. (a) Uniaxial tension test results on dough; and (b) sample deformation at different true strain values during tensile tests at 5/min.

It should be noted that uniaxial tension tests on starch were not performed because it was found that starch could not be formed into the “I” shaped specimens, or any other tensile specimen geometry. This is because the starch samples did not form a cohesive enough paste.

4.4.2 Uniaxial Compression

The compression test results from gluten samples are shown in Figure 4.17(a). Gluten shows strain rate dependent behaviour. Lower stresses are observed for gluten under compression mode as compared to tensile mode in Figure 4.15(a) at the same strain, which indicates that the stress-strain result of gluten in tension is not just a 'reverse' to compression. The sample condition is shown in Figure 4.17(b) at different strain values.

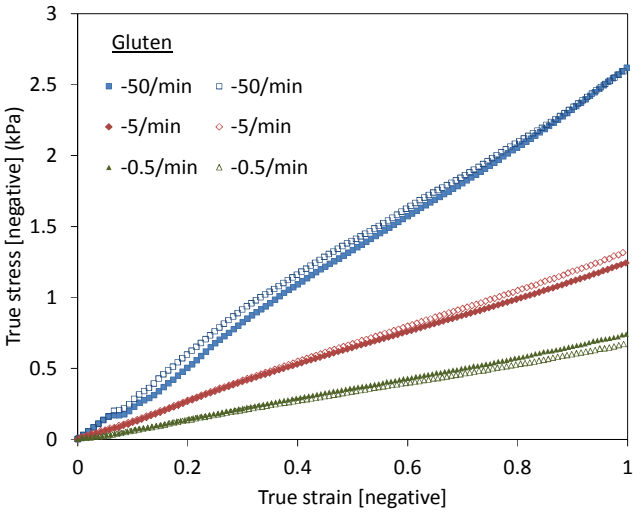

(a)

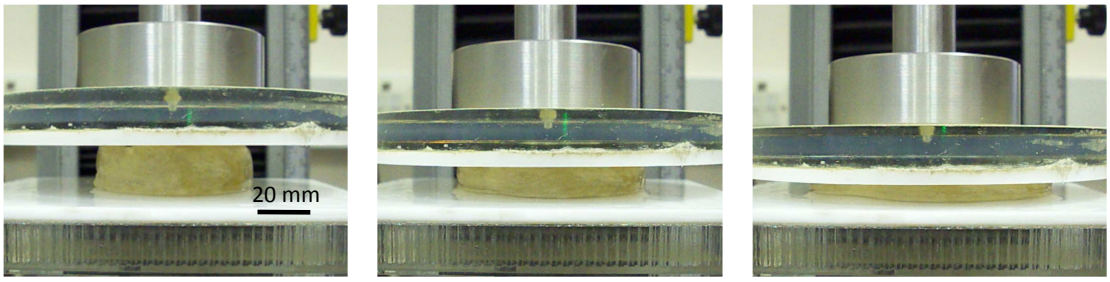

True strain -0.1 True strain -0.5 True strain -1.0

(b)

Figure 4.17. (a) Uniaxial compression test results on gluten; and (b) sample deformation at different true strain values during compression tests at -5/min.

The results from the compression tests of starch are shown in Figure 4.18(a). The starch is prepared using the methods described in Section 4.2.2.2. The starch also shows strain rate dependent behaviour. The sample deformation is shown in Figure 4.18(b) at different strain values.

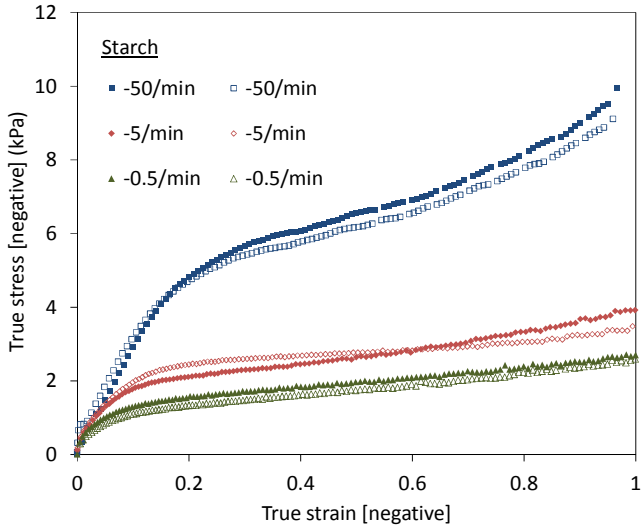

(a)

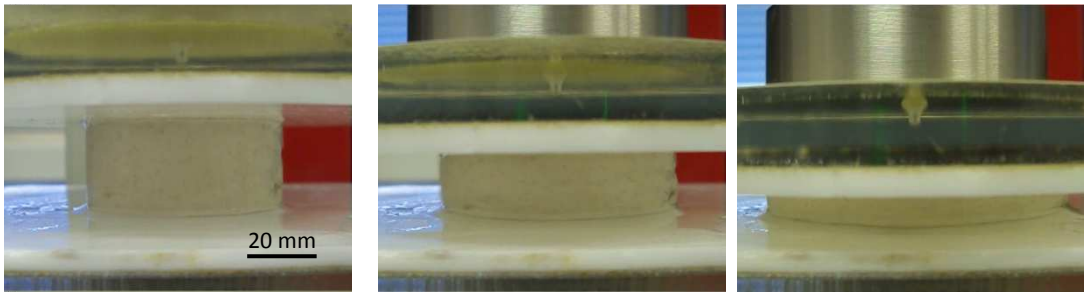

True strain -0.1 True strain -0.5 True strain -1.0

(b)

Figure 4.18. (a) Uniaxial compression test results on starch; and (b) sample deformation at different true strain values during compression tests at -5/min.

The results from compression tests on dough are shown in Figure 4.19(a). The dough shows strain rate dependent behaviour, which is similar to the gluten and starch results shown in Figures 4.17 and 4.18 respectively. Images of the dough sample at different strain values are shown in Figure 4.19(b). The stress-strain results obtained

for dough shows similar rate-dependent behaviour to the findings by Charalambides *et al.* [2006]. A rate dependent behaviour for dough under uniaxial compression is also reported by Swilinski *et al.* [2004] and Launay and Michon [2008].

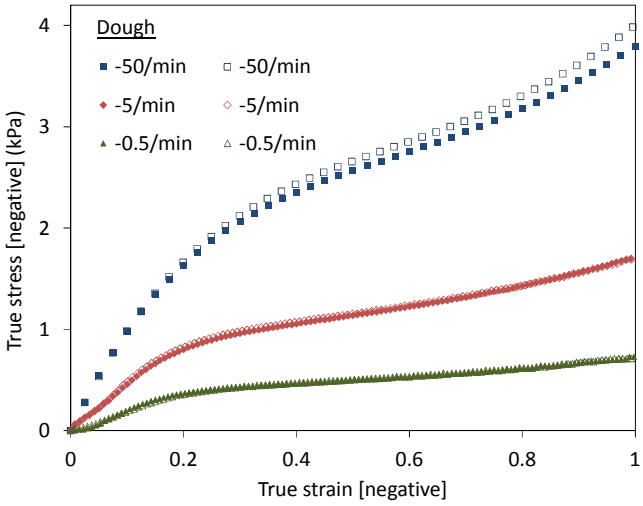

(a)

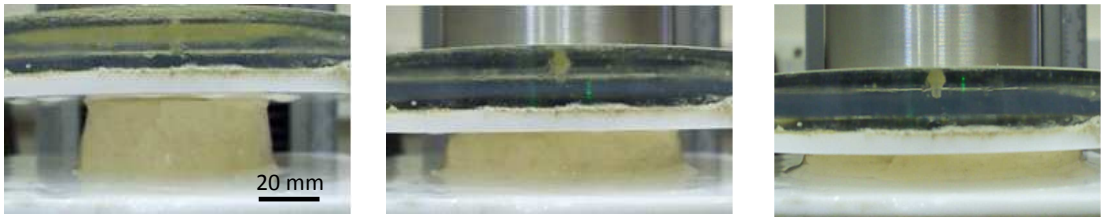

True strain -0.1 True strain -0.5 True strain -1.0

(b)

Figure 4.19. (a) Uniaxial compression test results on dough; and (b) sample deformation at different true strain values during compression tests at -5/min.

4.4.2.1 Compression Relaxation

Compression relaxation tests of gluten, starch and dough are shown in Figure 4.20. The samples were compressed to the required strain values at a constant strain rate of 5/min and held fixed for a period of time (i.e. 1000 seconds) while the stress decay is recorded. At lower strain (true strains -0.2 and -0.05), the stress in gluten relaxes to zero values after 1000 seconds. The stress in starch on the other hand shows an

almost instantaneous reduction as soon as the relaxation experiments begin. However, the stress in starch is still significant after 1000 seconds for all the applied strains. It is worth noting that the stress for dough reduced more than starch and gluten after 1000 seconds. Finally, it is suggested that the instantaneous reduction of stress in dough (Figure 4.20(c)) is caused by starch, whereas the long time stress relaxation is caused by gluten.

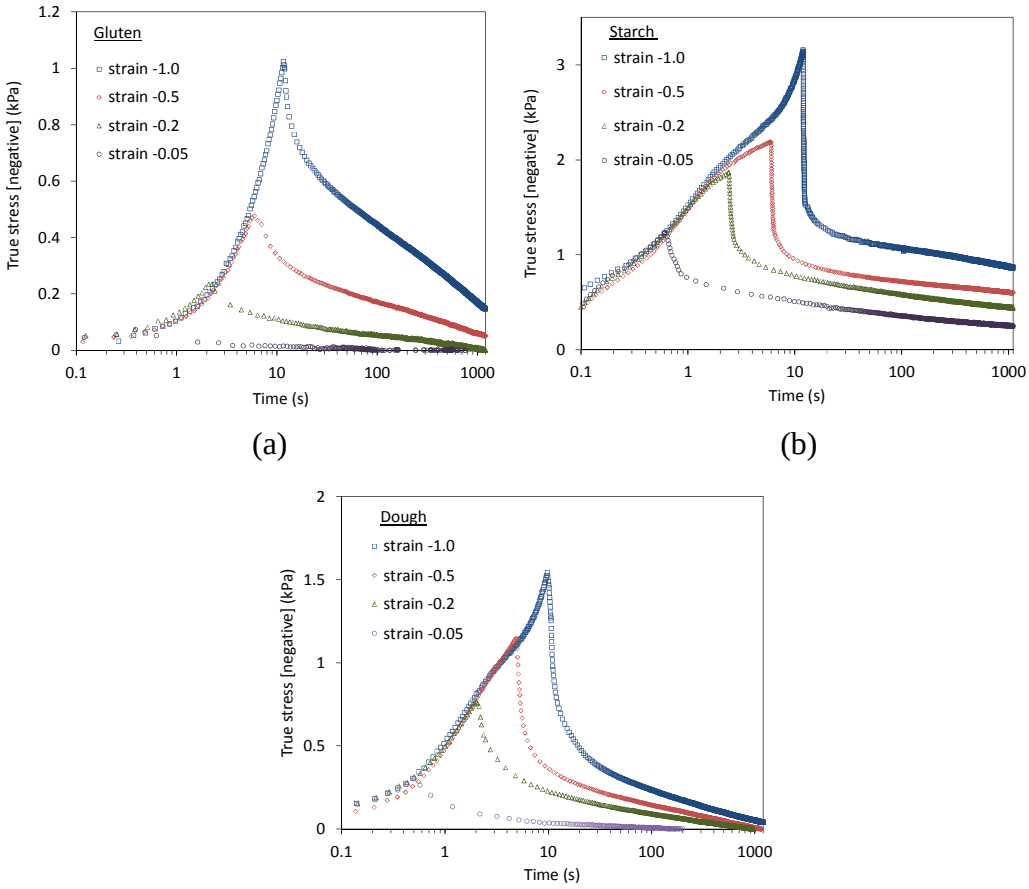

Figure 4.20. Compression relaxation test results on: (a) gluten; (b) starch; and (c) dough. All the tests are performed at -5/min.

4.4.2.2 Compression Loading-Unloading

The results from the compression loading-unloading tests of gluten, starch and dough are shown in Figure 4.21. The samples were compressed to the required strain values at a constant strain rate of -5/min before being unloaded at the same rate until the load is removed. Different samples are used for each strain shown in Figure 4.21. During the unloading period, it can be seen that the strain does not recover completely to its initial state for all the samples tested (Figure 4.21). In particular, gluten shows non-linear unloading curves even though the loading curves are approximately linear (Figure 4.21(a)). This is in contrast to the starch and dough, which show non-linear loading and unloading curves (Figure 4.21(b) and 4.21(c)). It can also be seen that the unloading-reloading curves of starch is almost vertical compared to gluten and dough. Repeatability is observed from the initial loading parts of the stress-strain curve corresponding to different strains which approximately overlap each other.

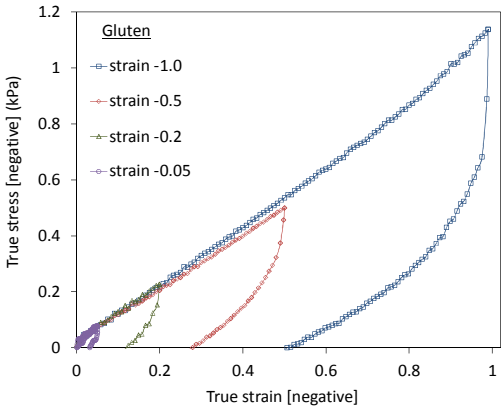

(a)

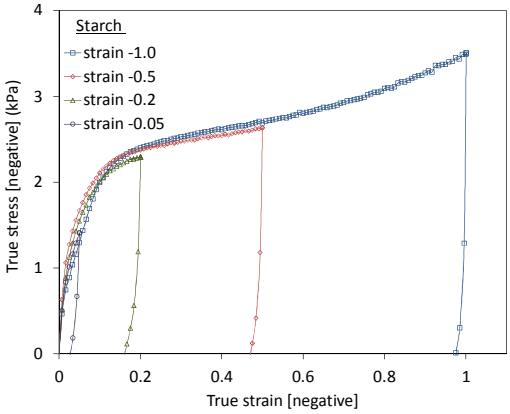

(b)

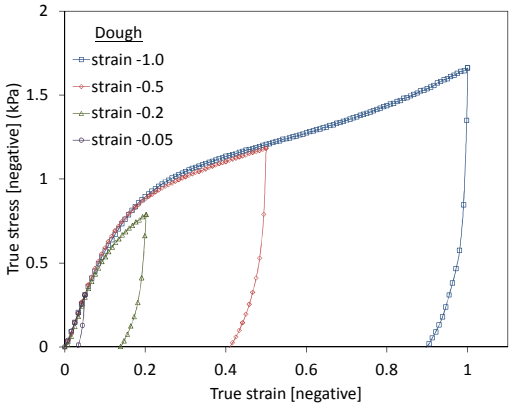

(c)

Figure 4.21. Compression loading-unloading test results on: (a) gluten; (b) starch; and (c) dough. All the tests are performed at -5/min.

4.4.2.3 Cyclic Compression

Cyclic compression test results for starch, gluten and dough are shown in Figure 4.22. During unloading, a larger strain recovery is observed for gluten (Figure 4.22(a)) as compared to starch (Figure 4.22(b)) and dough (Figure 4.22(c)). This is similar to the findings in the previous section for the loading-unloading tests. These findings suggest that gluten and starch behave like rubberlike and viscoplastic materials respectively. This will be investigated further in Chapter 5.

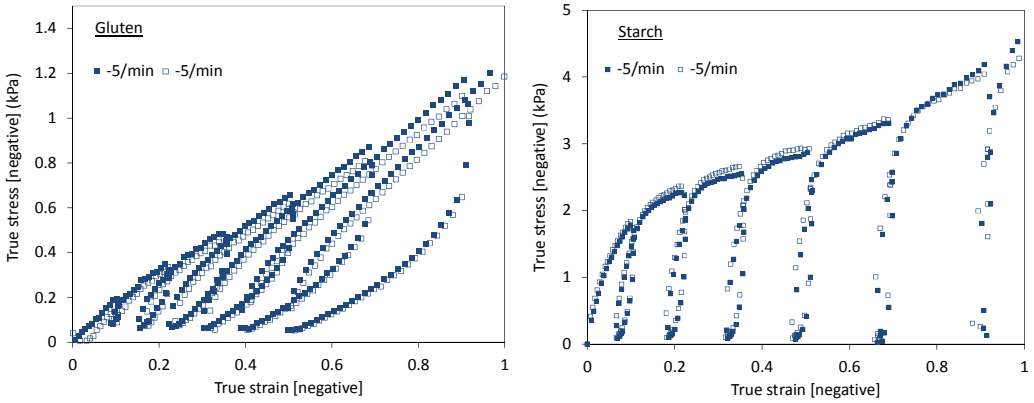

(a) (b)

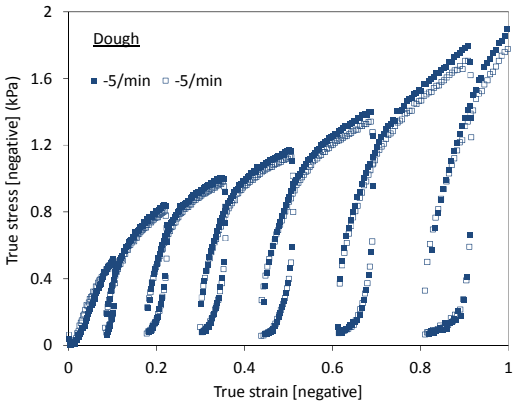

(c)

Figure 4.22. Cyclic compression test results on: (a) gluten; (b) starch; and (c) dough. All the tests are performed at -5/min.

4.4.3 Shear Rheometry Tests

4.4.3.1 Shear Strain Sweep and Shear Frequency Sweep

The results from Small Amplitude Oscillatory Shear (SAOS) tests on dough and gluten, namely the shear strain sweep and frequency sweep tests, are shown in Figures 4.23(a) and 4.23(b) respectively. The shear strain sweep tests on dough and gluten were performed at 1 Hz for shear strains up to 100 %, following the procedure by Tanner *et al.* [2008]. Dough is shown to have higher G' and G'' values than gluten in the linear viscoelastic region (LVR) in Figure 4.23(a). However, the LVR limit for

gluten is higher than dough, which is consistent to the findings by Uthayakumaran *et al.* [2002]. Frequency sweep tests were subsequently performed on dough and gluten in the LVR strain range (0.1 % strain) at a frequency range of 0.1-30 Hz. The results show higher $G^{'}$ and $G^{''}$ values for dough than gluten (Figure 4.23(b)), which is consistent to the shear strain sweep results in the LVR limit (Figure 4.23(a)). Note that almost linear curves of the $G^{'}$ and $G^{''}$ in Figure 4.32(b) can be represented using a simple power law equation (Equation 2.20 in Chapter 2): i.e. $G^{'}(t) = G^{'}(1)\omega^{n}$. This will be discussed later in Section 5.2 in Chapter 5.

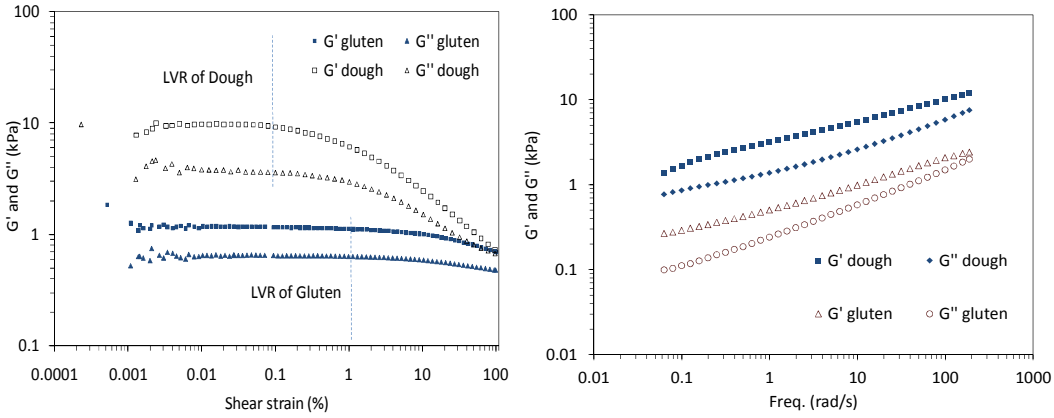

(a) (b)

Figure 4.23. Small Amplitude Oscillatory Shear (SAOS) test results on dough and gluten: (a) shear strain sweep; and (b) shear frequency sweep at 0.1 % strain.

4.4.3.2 Constant Shear Strain Rate

Figures 4.24(a) and 4.24(b) show the results from the constant shear strain rate (CSSR) tests performed on gluten. The gluten shows strain rate dependent behaviour. The deformation of the samples at different shear strains is shown in Figure 4.24(b). At the shear strain range of 10 to 20, it was visually noticed that the sample slipped at the edge of the plate (Figure 4.24(b)). The rotational motion of the rheometer plate at

large strain caused the sample to roll up and get ejected from the geometry gap, as shown in Figure 4.23(b) for shear strain 20. This has caused the drop of the shear stress shown in Figure 4.23(a). A similar slippage was also observed for shear strain rates of 50/min and 0.5/min. This indicates that the maximum shear strain seems to be independent of the strain rate. Note that a similar gluten sample slippage was also reported by Ng and McKinley [2008].

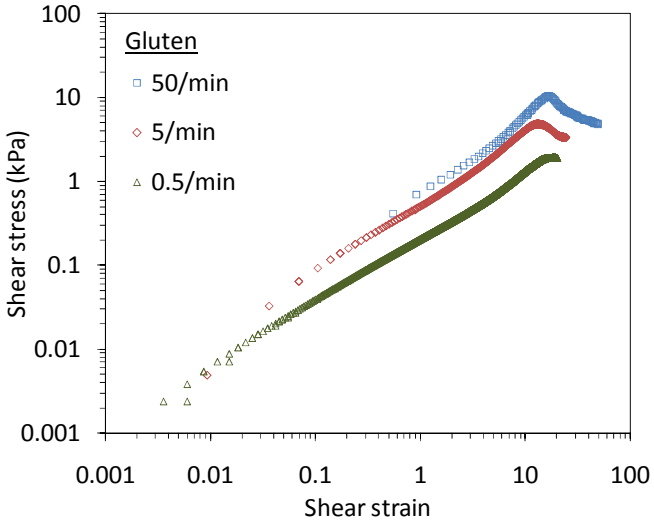

(a)

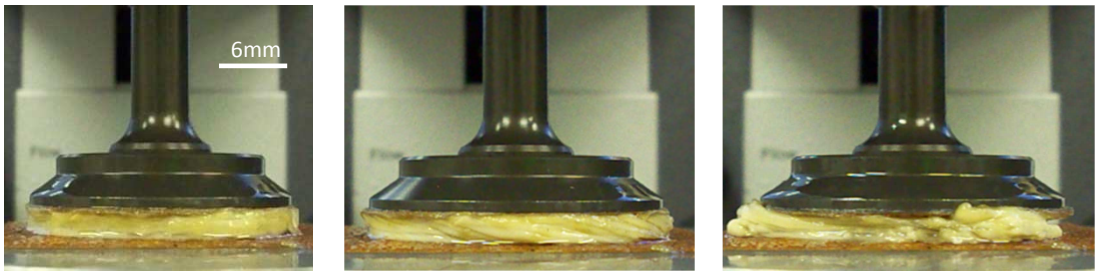

Shear strain 0.1 Shear strain 3 Shear strain 20

(b)

Figure 4.24. (a) Constant shear strain rate test results on gluten; and (b) sample deformation during shear tests at 5/min.

Figure 4.25(a) shows stress-strain curves from CSSR tests on dough samples. A rate dependent behaviour is again observed which is more pronounced than in gluten. Images of the sample deformation during the shear tests are shown in Figure 4.25(b). Similar to gluten, the sample slipped at the edge of the plate at a shear strain of approximately 20. This is in agreement with published data by Phan-Thien *et al.* [1997] and Tanner *et al.* [2008].

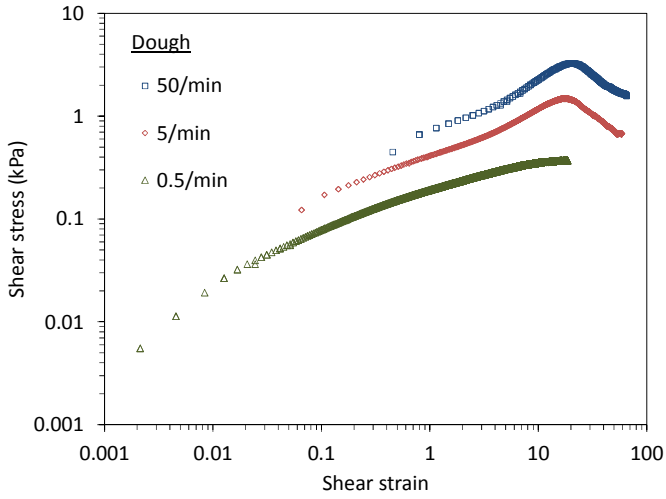

(a)

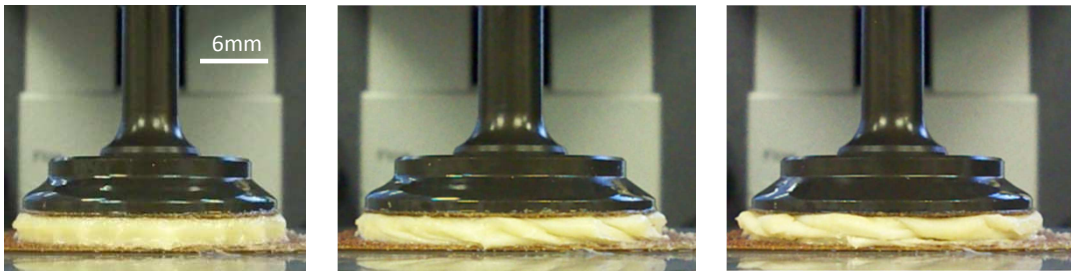

Shear strain 0.1 Shear strain 3 Shear strain 20

(b)

Figure 4.25. (a) Constant shear strain rate test results on dough; and (b) sample deformation shear tests at 5/min.

To demonstrate the effect of the correction factor discussed in Chapter 2, Equation (2.12) is used to correct the shear stress of dough and gluten through:

$$\tau_E = \tau_R \left[\frac{3}{4} + \frac{1}{4} \frac{\gamma_E}{\tau_R} \frac{\partial \tau_R}{\partial \gamma_E} \right].$$

The results are shown in Figure 4.26 as a comparison between the rheometer output and results calculated using Equation (2.12). It can be seen that the difference is larger for dough than gluten. A small correction factor for gluten was also reported by Ng *et al.* [2011].

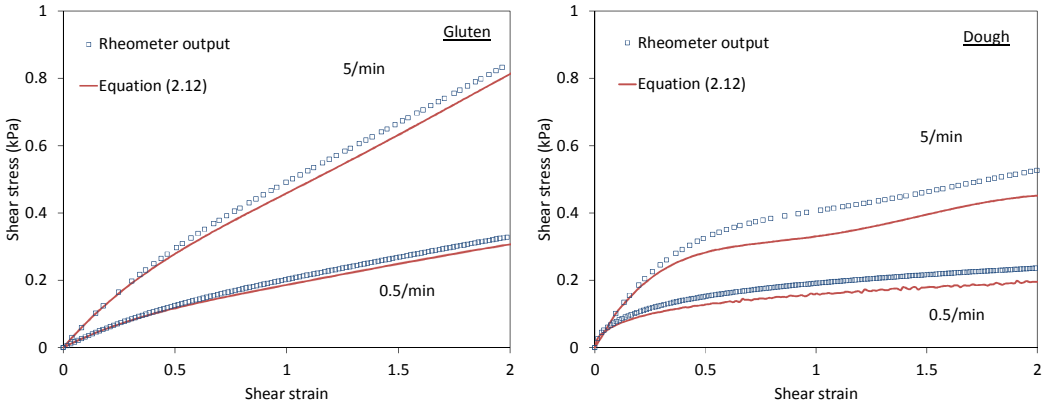

(a) (b)

Figure 4.26. Rheometer output versus corrected shear stress using Equation (2.12).

It is worth noting that shear rheometry test results on starch are not shown because they showed non-repeatability, which is believed to be due to the sample slipping out of the rheometer. This is again because the starch did not form a cohesive enough paste material.

4.4.4 Cryo-SEM

4.4.4.1 Effect of Sublimation

An investigation was performed to study the effect of sublimation on the observed dough microstructure. The Cryo-SEM test procedure is as described in Section 4.3.4. A sublimation setting of -90 ^{0}C and 2 minutes was used on a dough sample and was compared with a non-sublimated sample. The results are shown in Figure 4.27 at two different magnifications, i.e. Figures 4.27(a) and 4.27(c) at 1000 and 3000 times magnifications respectively.

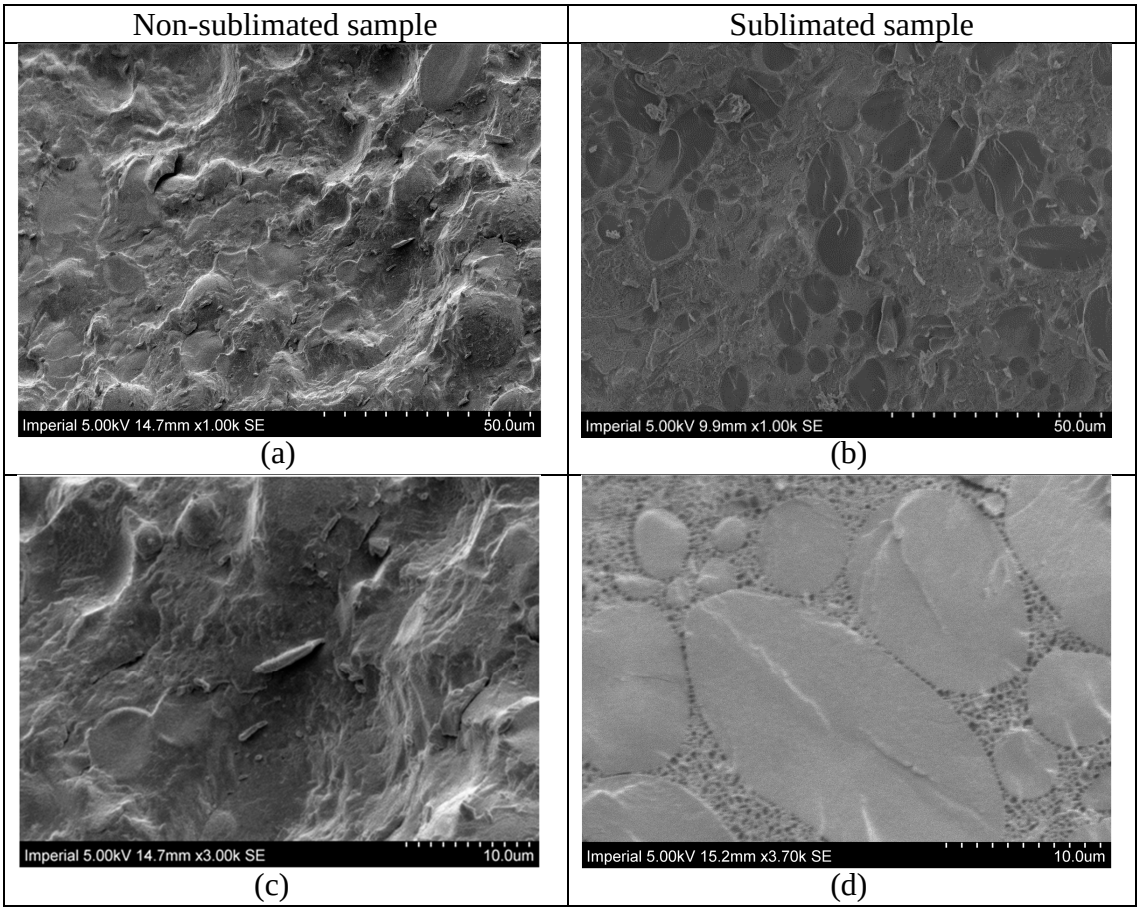

Figure 4.27. Cryo-SEM images of dough for: non-sublimated sample ((a) and (c)); and sublimated sample ((b) and (d)) at a sublimation setting of -90 ^{0}C for 2 minutes.

A significant difference is observed between the non-sublimated sample (Figures 4.27(a) and 4.27(c)) and the sublimated sample (Figures 4.27(b) and 4.27(d)), where the starch granules and gluten structure are clearly visible in the latter.

To investigate the effect of sublimation settings, a different sublimation setting, i.e. $-70\ ^{0}C$ and 10 minutes was used, and the resulting image was compared to the image corresponding to the sublimation setting of $-90\ ^{0}C$ and 2 minutes as shown in Figures 4.27(b) and 4.27(d). The former sublimation settings were obtained from Jinhee *et al.* [2009] for dough. The comparison results are shown in Figure 4.28.

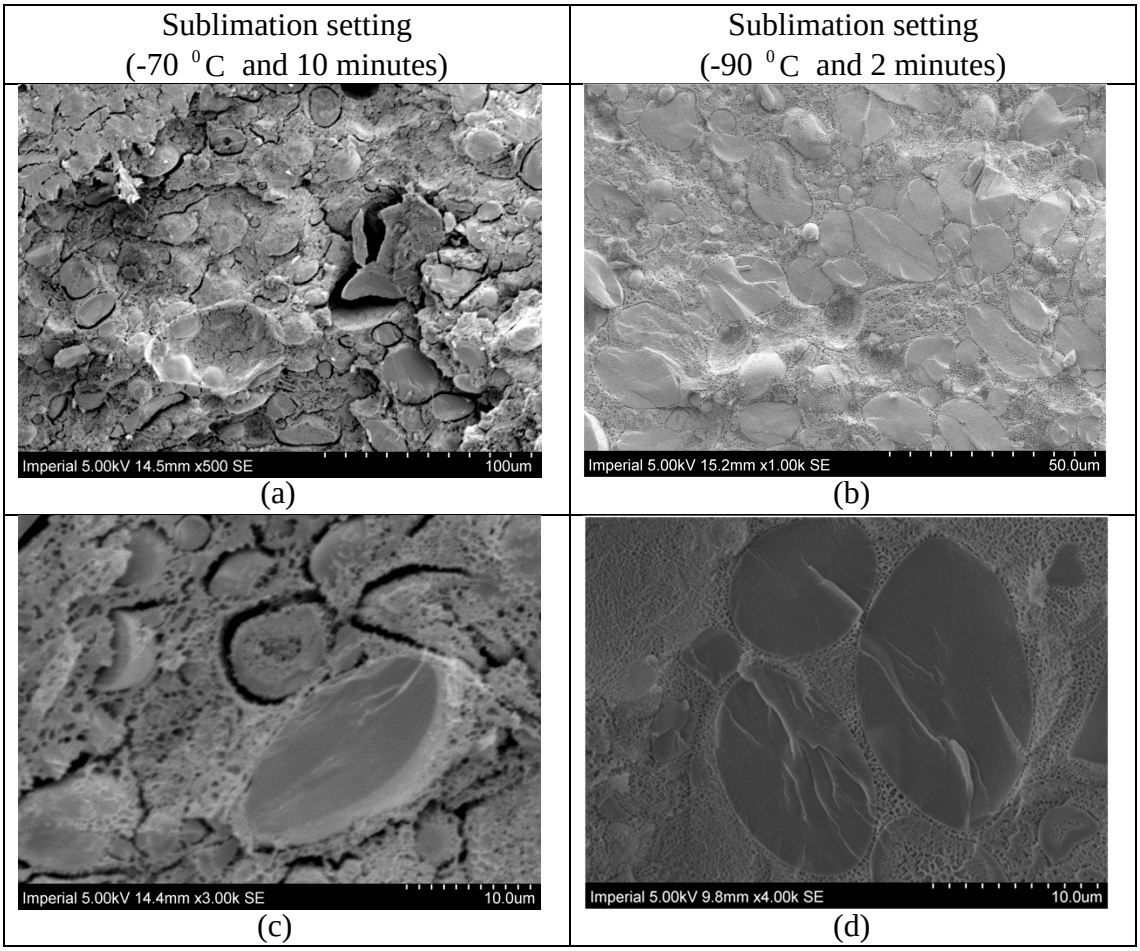

Figure 4.28. (a) and (c) Sublimation setting comparison of -70 ^{0}C and 10 minutes; (b) and (d) Sublimation setting of -90 ^{0}C and 2 minutes.

It is apparent that the starch and gluten microstructure are clearly visible with no cracks observed on the surface, when the sublimation setting of -90 ^{0}C and 2 minutes was used (see Figures 4.28(b) and 4.28(d)). In contrast, cracks are observed in the image taken at the sublimation setting of -70 ^{0}C and 10 minutes (Figures 4.28(a) and 4.28(c)). Therefore the sublimation setting of -90 ^{0}C and 2 minutes was used for the remaining Cryo-SEM tests performed in this thesis.

4.4.4.2 Microstructure of Gluten, Starch and Dough

Figure 4.29(a) shows the microstructure of the gluten samples prepared using the Cryo-SEM method. No starch granule is physically observed on the gluten surface. The small holes in the gluten microstructure in Figure 4.29(a) are artefacts due to evaporation of ice during the sublimation process. A similar microstructural image of gluten is also observed by Kontogiorgos and Goff [2006], as shown in Figure 4.29(b).

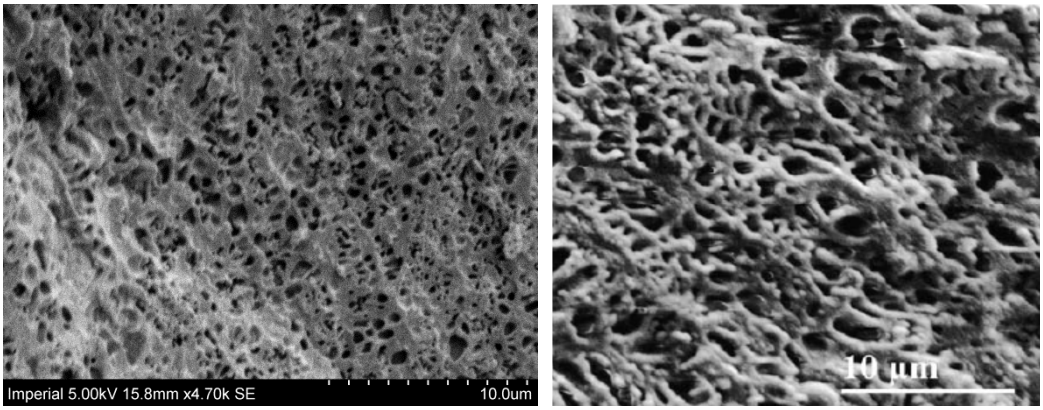

(a) (b)

Figure 4.29. (a) Microstructure of native gluten obtained from dough washing procedure; and (b) microstructure of gluten obtained by Kontogiorgos and Goff [2006].

Figure 4.30 shows SEM images of dry starch obtained after dough washing procedures described in Section 4.2.2. The starch consists of larger ellipsoidal type A and smaller circular type B varieties [Tanner *et al.* 2011b], as shown in Figure 4.30(a) and 4.30(b). No damaged starch is observed which is encouraging as it is proof that the washing and drying procedure followed in this work did not alter the starch granules. This is consistent with the discussion on starch in Section 2.2.4, where the hydration process of starch is reversible at room temperature, i.e. 22 ^{0}C .

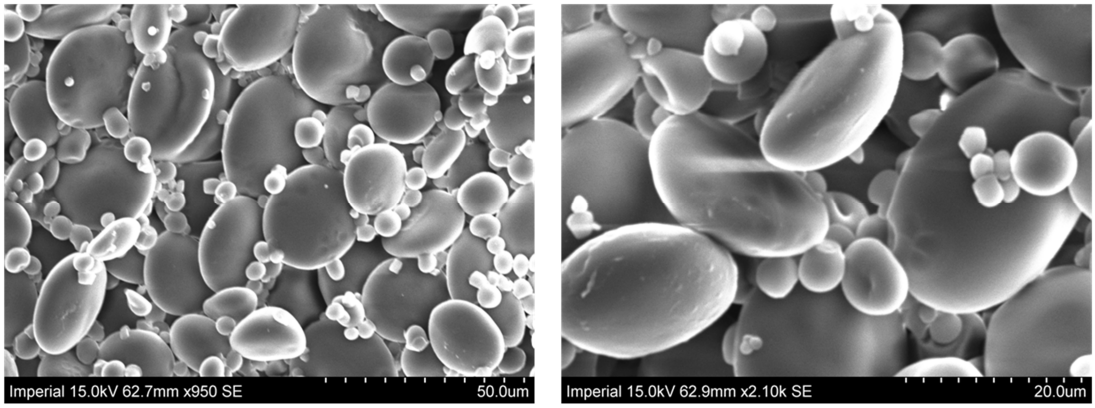

(a) (b)

Figure 4.30. SEM images of dry starch, which consists of larger ellipsoidal type A and smaller circular type B varieties.

Figure 4.31 shows the microstructure of an undeformed dough obtained using the Cryo-SEM tests. The larger ellipsoidal type A and smaller circular type B starch are surrounded by gluten, as shown in Figures 4.31(a) and 4.31(b). The starch granules are bonded to the gluten, and the boundary between the starch and gluten is clearly visible, as shown in Figure 4.31(b) at larger magnification.

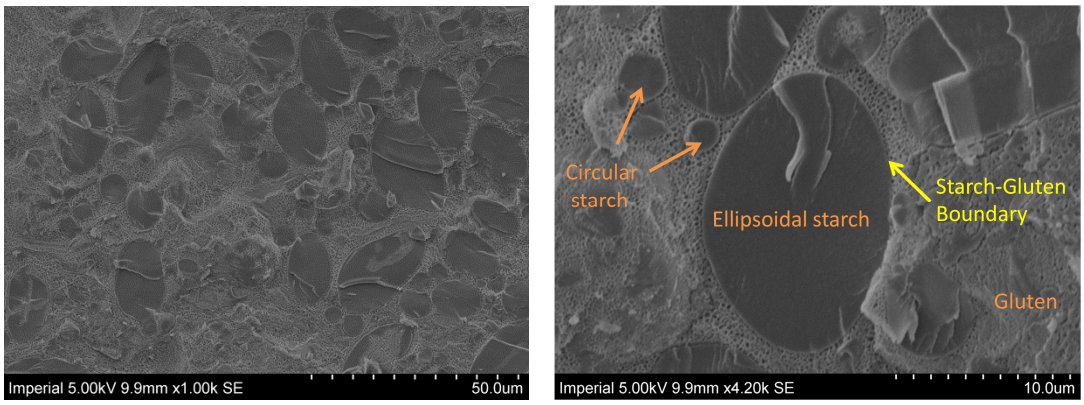

(a) (b)

Figure 4.31. Cryo-SEM images of undeformed dough.

In order to investigate the degree of swelling in starch, the dimension of the starch particles in Figures 4.30 and 4.31 were compared. Measurements of the starch particles were performed along two orthogonal axes of symmetry (α and β) to reveal the aspect ratio, as shown in Figure 4.32. The results are shown in Figure 4.32 for the larger ellipsoidal type A starch (Figure 4.32(a)) and the smaller circular type B starch (Figure 4.32(b)). It appears that swelling is not apparent for starch in dough when compared to the dry starch for type A and B starches. This agrees to the results obtained by Tester and Morrison [1990] (Figure 2.5), which shows that starch swelling is not apparent at room temperature.

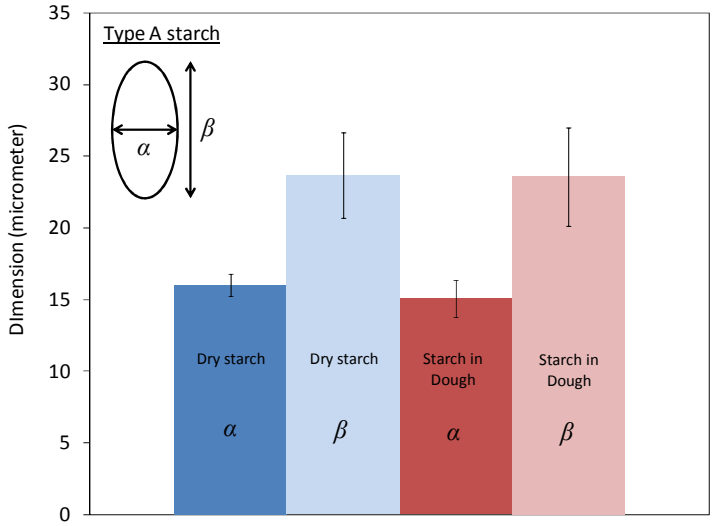

(a)

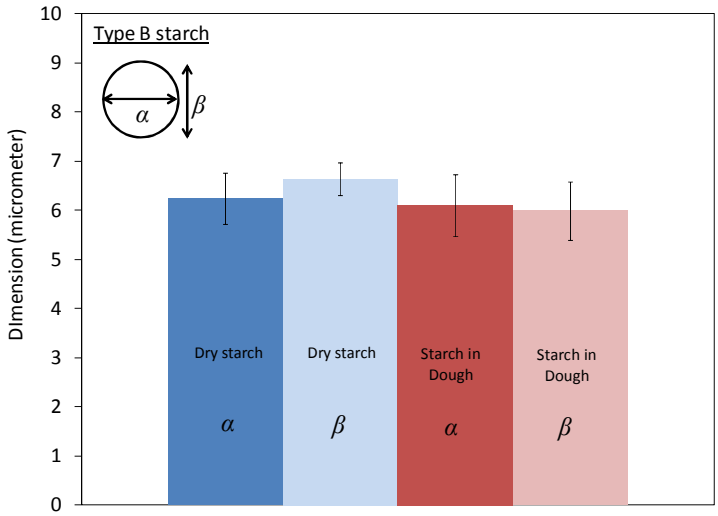

(b)

Figure 4.32. Starch granule dimensions difference between starch in dough and dry starch for (a): type A starch; and (b) type B starch.

4.4.4.3 Effect of Deformation on Microstructure of Dough

The microstructure of dough after being deformed is investigated using Cryo-SEM. Dough samples were stretched or compressed manually, and were compared to an undeformed sample. Both samples were exposed to liquid nitrogen under vacuum conditions before being transferred to the Cryo-SEM chamber. The same sublimation setting of -90 ^{0}C for 2 minutes was used for both samples.

The images are shown in Figure 4.33. The images of undeformed dough and gluten are shown in Figures 4.33(a) and 4.33(b) as reference. Evidence of debonding at the starch-gluten interface is observed for the stretched sample (Figure 4.33(d)), such debonding was not present in the undeformed sample (Figure 4.33(a)). This suggests that the dough may be undergoing damage [Tanner *et al.* 2008] due to the starch-gluten interaction weakening at large deformations. In contrast, debonding is not as apparent when the dough was subjected to a compressive load (Figure 4.33(c)). Finally, it is worth noting that the procedure to deform dough before exposure to liquid nitrogen was performed as quickly as possible to prevent the effect of stress relaxation and recovery on dough. However, it is impossible to avoid relaxation at very short time, i.e. the stress relaxation of dough for time less than 10 seconds shown in Figure 4.20(c).

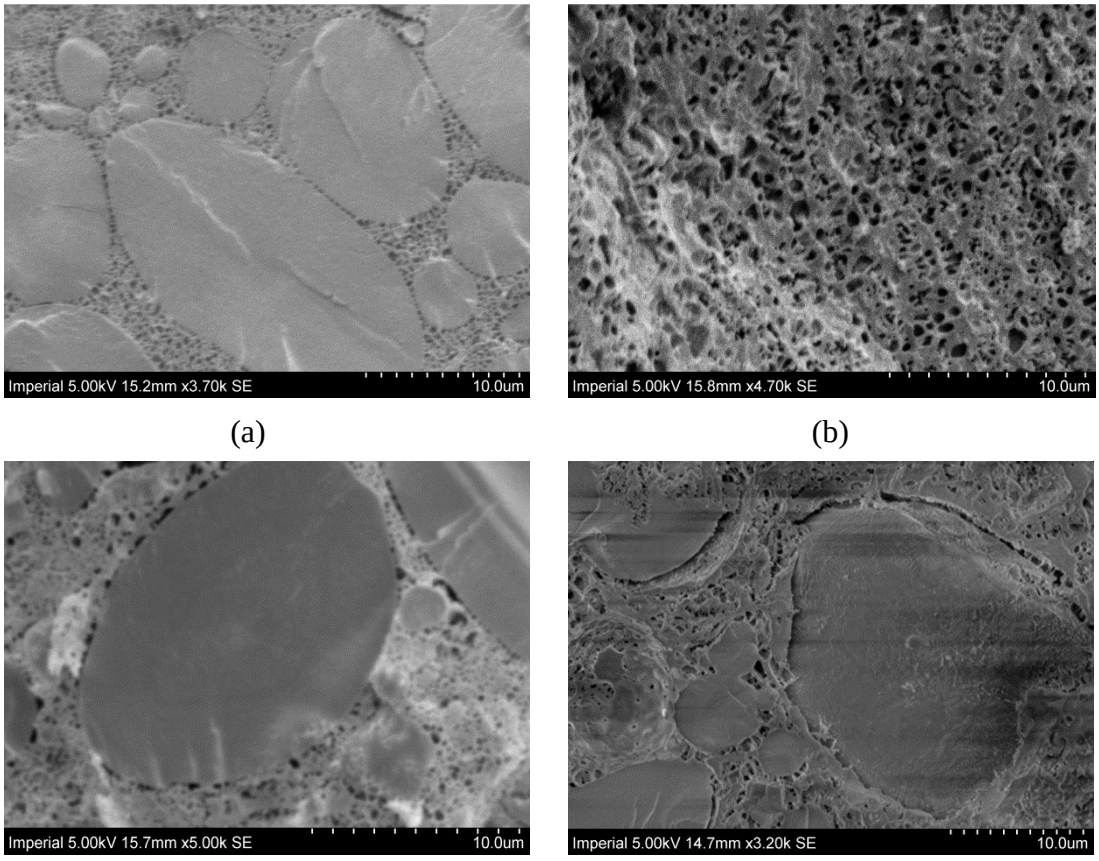

Figure 4.33. Microstructure of: (a) undeformed dough; (b) undeformed gluten washed under running tap water; (c) compressed dough; and (d) stretched dough.

4.5 Discussion

The experimental results of this chapter are reviewed and summarised in this section. The results from Small Amplitude Oscillatory Shear (SAOS) tests show that the gluten has lower storage and loss moduli values than dough. The results from uniaxial compression, uniaxial tension and shear performed at 5/min for dough, starch and gluten are compared in Figure 4.34. Under uniaxial compression, the starch has the highest stress-strain curve followed by dough and gluten, as shown in Figure 4.34(a). However, a different stress-strain pattern is observed under uniaxial tension and simple shear, as shown in Figures 4.34(b) and 4.34(c) respectively. The dough stress-

strain curves under tension and shear are seen to cross over the curves for gluten and therefore leading to lower stress values than in gluten.

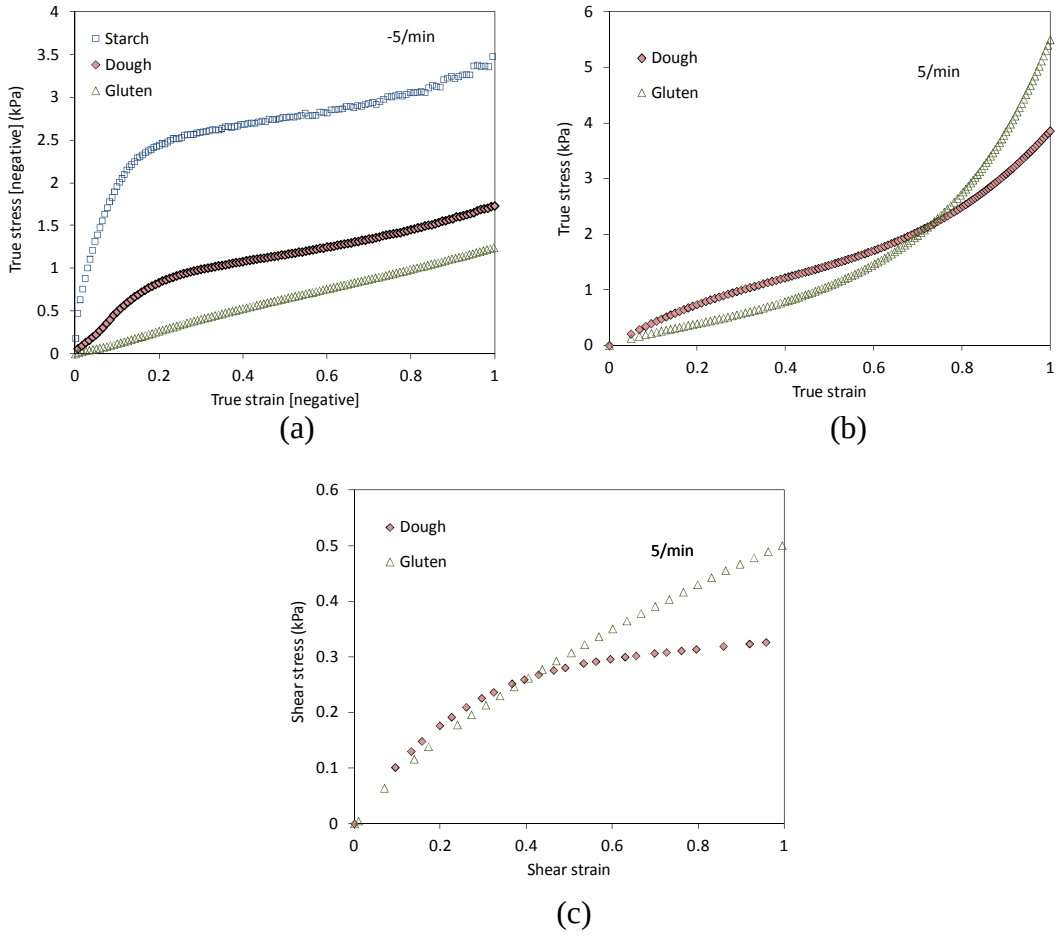

Figure 4.34. Comparison of dough, gluten and starch from large deformation tests: (a) uniaxial compression; (b) uniaxial tension; and (c) constant shear strain rate. All the tests are performed at 5/min.

The microstructure test results show evidence of debonding at the starch-gluten interface for the stretched sample (Figure 4.33(d)), while debonding is not apparent when the dough was subjected to a compressive load (Figure 4.33(c)).

It is therefore suggested that the mechanical behaviour of dough can be described using starch as a filler contained in a gluten matrix. The filler-matrix interaction can

be represented by the starch-gluten interaction in dough. The interaction can be classified as being in the: well bounded composite region, partially debonded region and fully debonded region, as shown in Figures 4.35(a), 4.35(b) and 4.35(c) respectively [Meddad and Fisa 1997]. At a small strain, the filler-matrix interface is well bonded, indicating no filler-matrix interface damage, as shown in Figure 4.35(a). Partial debonding occurs as the strain increases, as indicated in Figure 4.35(b), before finally the filler-matrix interface is fully debonded in Figure 4.35(c). This hypothesis will be investigated further in the next chapter.

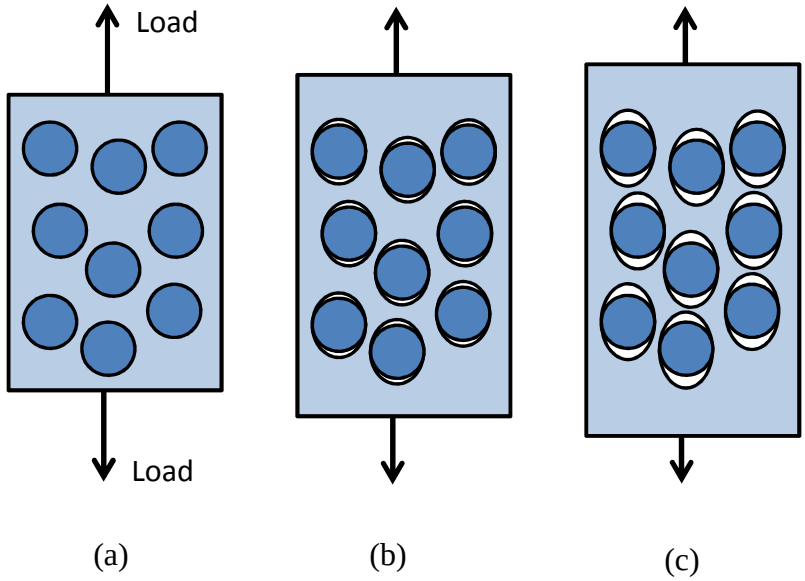

Figure 4.35. Filler-matrix debonding concept for polymeric materials by Meddad and Fisa [1997] for: (a) well bonded composite region; (b) partially debonded region; and (c) fully debonded region.

4.6 Conclusion

An experimental investigation on the mechanical behaviour of dough, starch and gluten is performed in this chapter. The flour used is strong white bread flour,

purchased from the Wessex Mill in Oxford, United Kingdom. The sample preparation involved mixing flour, water and salt to produce dough. The mixed dough was then washed using water to separate the starch and gluten constituents. Dough, wet gluten and reconstituted wet starch were used for uniaxial tension, uniaxial compression, shear rheometry and Cryo-SEM tests. Experimental results for gluten, starch and dough were then shown and discussed. Rate-dependent behaviour is observed from all the samples tested in uniaxial compression, uniaxial tension and shear tests. Cryo-SEM images show starch embedded in gluten matrix, where starch consists of large ellipsoidal-shaped and small circular-shaped fillers. No trace of starch was observed on the gluten matrix based on the Cryo-SEM images of washed gluten. A comparison performed between the mechanical test results showed that dough is stiffer than gluten at Small Amplitude Oscillatory Shear (SAOS) tests, namely shear strain sweep and shear frequency sweep tests. However, in large deformation tests, namely uniaxial tension and simple shear, the dough stress-strain curves cross over the gluten curve at larger deformations. On the other hand, uniaxial compression test results showed that the stress-strain curve of dough is always higher than gluten, indicating that possibly no considerable damage occurs under compression. This is supported by the Cryo-SEM observation of dough when compressed manually, where damage in terms of debonding is less apparent. Finally, a filler-matrix debonding concept by Meddad and Fisa [1997] for polymeric materials was proposed to represent the mechanical behaviour of wheat flour dough.

Chapter 5. Rheological and Micromechanical Modelling of Wheat Flour Dough

5.1 Introduction

Baking performance and quality of bread are strongly dependent on the mechanical behaviour of dough. Even though wheat flour dough is a simple mixture of wheat flour, salt and water, its mechanical behaviour is complex, as shown in Chapter 4. Two major components of wheat flour dough that are believed to influence the viscoelastic properties of dough are starch and gluten [Amemiya and Menjivar 1992].

The interaction between starch and gluten can be modelled as a composite material, where starch is modelled as a harder filler and gluten as a softer matrix. However the experimental study on the stress-strain behaviour of dough and gluten showed that gluten is stronger than dough at large strain, as discussed in Chapter 4. This is in contrast with the composite material theory, where in the case of a stiffer filler, the composite material is expected to be stiffer than its matrix. It is believed that the reason for this is due to damage or debonding of the starch-gluten interface [Meddad and Fisa 1997].

This chapter investigates the mechanical behaviour of dough, gluten and starch. The possibility of damage at the interface between the starch and gluten is investigated. This is performed by using a two phase (starch and gluten) composite material model and comparing the model predictions to experimental stress-strain data for dough tested under various loading conditions.

5.2 Lodge Rubberlike Model

Dough has been shown to behave like a critical gel by various researchers [Gabriele *et al.* 2001; Ng *et al.* 2006; Lefebvre 2006; Migliori and Gabriele 2010; Tanner *et al.* 2008; 2011a]. A critical gel material can be modelled using the Lodge rubberlike model [Lodge 1964], based on the study by Winter and Chambon [1986] and Winter and Mours [1997]. Discussion on the critical gel materials is provided in Section 2.3.3.3 in Chapter 2. Under uniaxial tension, the Lodge rubberlike model is approximated as (Equations (3.32) and (3.34) in Chapter 3) [Ng and McKinley (2008)]:

$$\sigma_{zz}-\sigma_{rr}\approx\sigma\approx G(1)\dot{\varepsilon}^{n}\varepsilon^{-n}\left(\exp\left(2\varepsilon\right)+\frac{\left(1+2n\right)}{1-n}\varepsilon-1\right)$$

where $\dot{\varepsilon}$ is strain rate and ε is log or Hencky strain. σ_{zz} and σ_{rr} are referred to as the axial and radial stresses in a cylindrical specimen respectively. The above equation is also used for uniaxial compression loading too, where a negative strain is used to indicate compressive strain.

The shear stress, τ, under simple shear loading is (Equation (3.48) in Chapter 3) [Tanner *et al.* 2008; Ng and McKinley 2008]:

$$\tau=\frac{G(1)\dot{\gamma}^{n}}{1-n}\gamma^{1-n}.$$

The stress relaxation constant, $G(1)$ and power law constant, n, are determined from small amplitude oscillatory shear (SAOS) tests (i.e. strain sweep and frequency sweep tests), following the procedures in Tanner *et al.* [2008] and Ng and McKinley [2008].

The strain sweep tests were performed at 1 Hz and the results are shown in Figure 5.1(a). This is similar to the results shown in Figure 4.23(a). It is observed that a strain amplitude of 0.1 % is within the linear viscoelastic region of dough. The frequency sweep tests were therefore performed at 0.1-30 Hz and 0.1 % strain. The data are shown in Figure 5.1(b), which is similar to the results shown in Figure 4.23(b). The storage and loss moduli plots are each approximated with a power law such that (Equation (2.20) in Chapter 2):

$$G'(t) = G'(1)\omega^n, \qquad G''(t) = G''(1)\omega^n$$

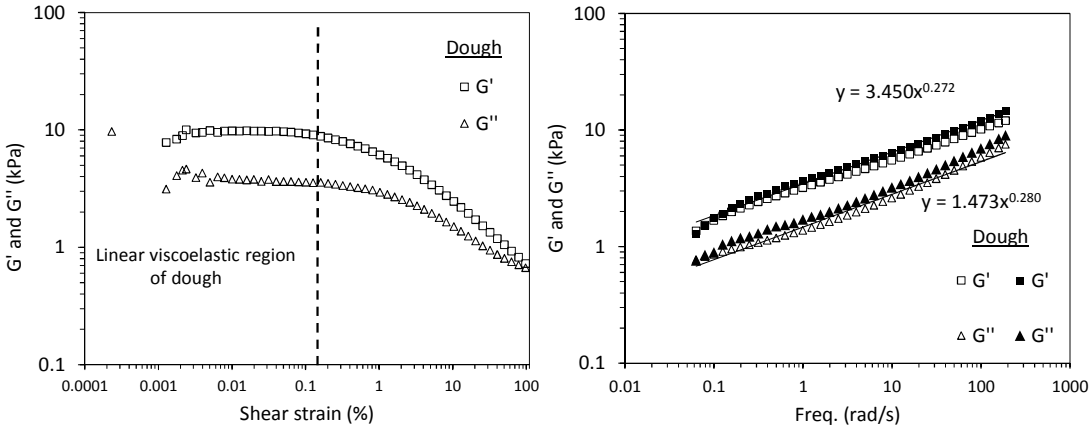

(a) (b)

Figure 5.1. SAOS test results of dough: (a) strain sweep tests in the shear strain range of up to 100 % at 1 Hz; and (b) frequency sweep at 0.1 % shear strain at 0.1-30 Hz.

Therefore the power law constant, n, was obtained from the average of the two exponents shown in Figure 5.1(b), where $n \approx 0.27$. This value was used to calculate $G(1)$ using the following relationship (Equation 2.21 in Chapter 2) [Tanner *et al.* 2008]:

$$G(1) = G^{'}(1)\frac{2(n!)}{n\pi}\sin\frac{n\pi}{2}$$

where $n!$ is the factorial function of the power law constant, which is equal to 0.902 for $n = 0.27$, and $G^{'}(1)$ is equal to 3.45 kPa/(rad/s)$^{0.27}$, as shown in Figure 5.1(b). Thus $G(1)$ is calculated as 3.02 kPa s$^{0.27}$.

Figure 5.2 shows the fit of the Lodge model to the dough test data under large deformation. The model leads to considerably higher stress values than the tension and shear test data, therefore suggesting the use of a damping function [Ng *et al.* 2006] or a damage function [Tanner *et al.* 2008; 2011a]. In contrast, the model is closer to the compression test data, indicating that possibly less damage occurs under compression. In order to quantify the 'damage factor', the ratio of the experimental stress value to the Lodge model calculation is plotted against log strain, as shown in Figure 5.2(d). Absolute/positive true stress and log strain are used for uniaxial compression, whereas the true strain for the shear tests is calculated using (Equation (3.76) in Chapter 3) [Treloar 1975]:

$$\varepsilon = \ln(\lambda) = \ln\left(\frac{\gamma}{2} + \frac{\sqrt{\gamma^2 + 4}}{2}\right)$$

A lower value of the experimental over Lodge model ratio indicates that a larger damage factor is needed in order to replicate the test results. It can be seen that the ratio for shear is the lowest followed by tension and compression. This suggests that debonding at the starch-gluten interface is possibly an important damage mechanism in dough. This can readily occur under shear and tension. During compression, debonding only arises from shear generated off-axis at 45° from the direction of the

applied load, therefore the damage factor has lower values than in tension or shear loading.

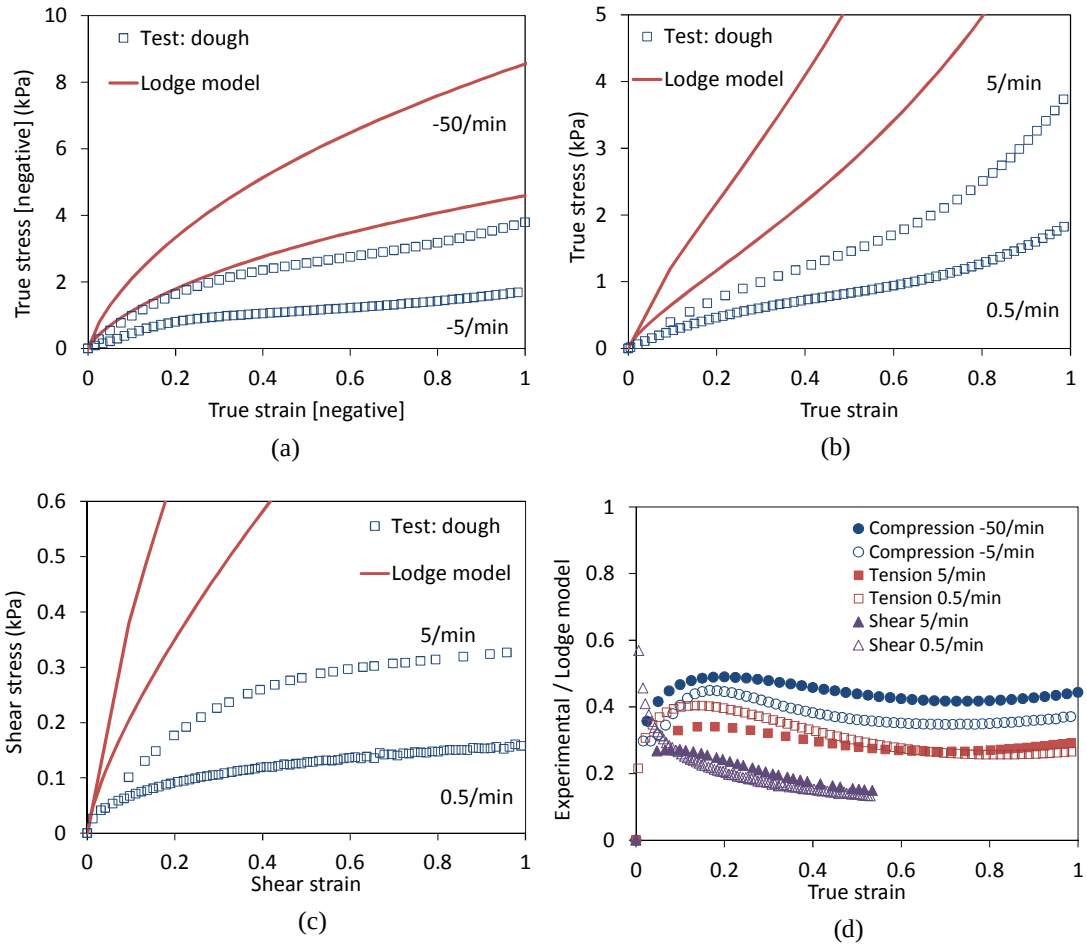

Figure 5.2. Dough test data at 5/min and Lodge rubberlike model fit results under: (a) compression; (b) tension; (c) shear; and (d) Experimental over Lodge model ratio under different modes of deformation.

5.3 Micromechanics Model

5.3.1 Material Model for Gluten

The results from the mechanical tests on gluten are shown in Figure 5.3.

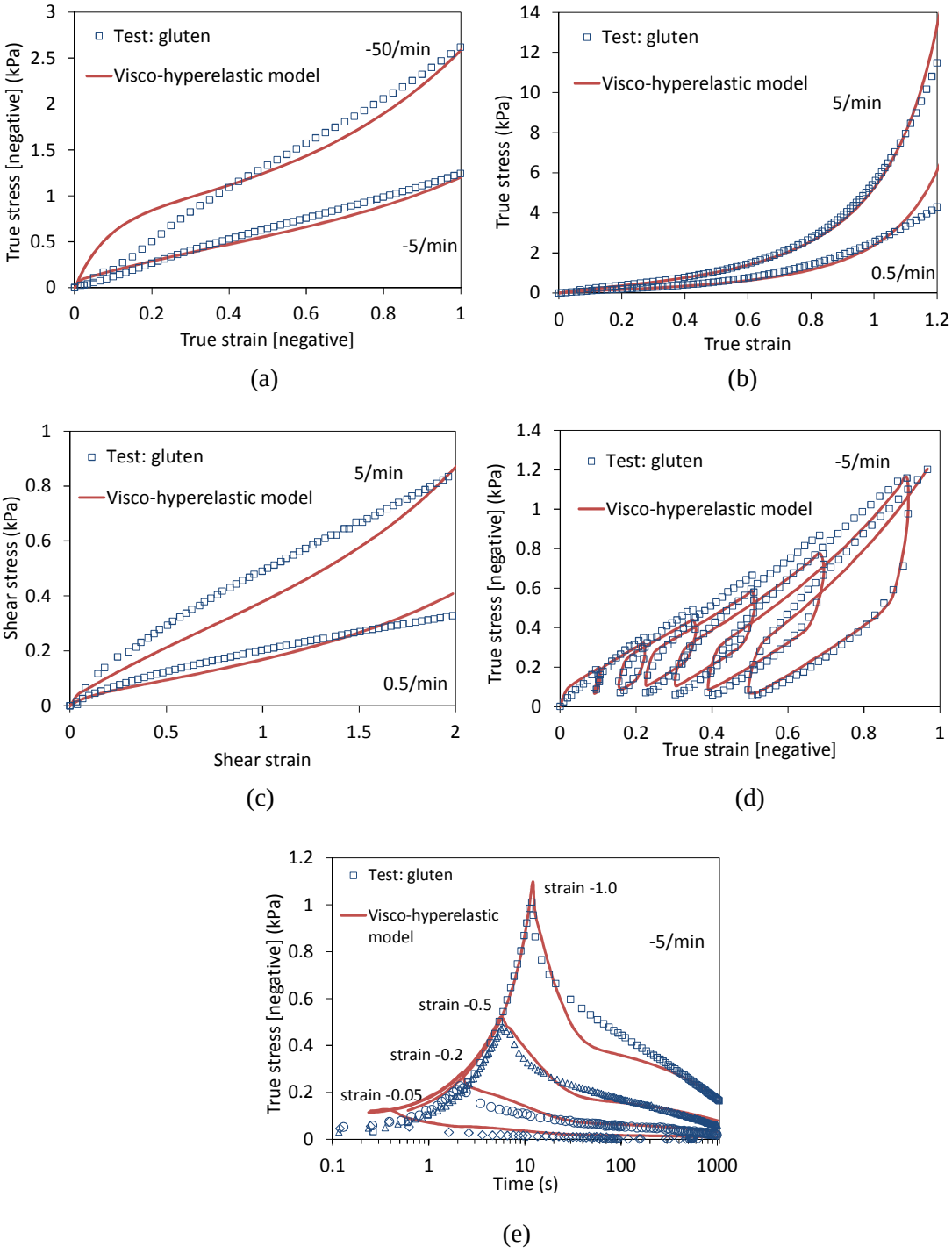

Figure 5.3. Gluten test results and calibration of visco-hyperelastic (van der Waals) material model under: (a) compression; (b) tension; (c) shear; (d) cyclic-compression; and (e) compression-relaxation. The model is described by the visco-hyperelastic model in Section 3.3 in Chapter 3.

Gluten shows rate dependent behaviour under compression, tension and shear modes, and energy dissipation under a cyclic-compression mode. Details of the experimental results of gluten are provided in Chapter 4.

Material parameters of gluten under large deformation were determined using a visco-hyperelastic material model, where the van der Waals strain energy function and the Prony series time-dependent function were used. For the the van der Waals strain energy function, the true stress form for uniaxial tension and uniaxial compression can be described using $\sigma_0(\lambda) = \frac{\partial W}{\partial \lambda}\lambda$, where W is the hyperelastic potential and λ is the stretch ratio. The stress for uniaxial tension and uniaxial compression, $\sigma_0(\varepsilon)$, can then be derived as (Equation (3.79) in Chapter 3):

$$\sigma_0(\lambda) = \mu\lambda\left(\lambda - \frac{1}{\lambda^2}\right)\left[\frac{\sqrt{\lambda_m^2 - 3}}{\sqrt{\lambda_m^2 - 3} - \sqrt{\lambda^2 + 2\lambda^{-1} - 3}} - a\sqrt{\frac{\lambda^2 + 2\lambda^{-1} - 3}{2}}\right]$$

where μ is the instantaneous initial shear modulus, λ_m is the locking stretch constant and a is the global interaction parameter [Abaqus 2009; 2010].

For simple shear loading, shear stress, $\tau(\lambda)$, is (Equation (3.80) in Chapter 3):

$$\sigma_0 = \tau(\lambda) = \mu\left(\frac{\lambda^3 - \lambda^{-1}}{\lambda^2 + 1}\right)\left[\frac{\sqrt{\lambda_m^2 - 3}}{\sqrt{\lambda_m^2 - 3} - \sqrt{\lambda^2 + \lambda^{-2} - 2}} - a\sqrt{\frac{\lambda^2 + \lambda^{-2} - 2}{2}}\right].$$

For the Prony series time-dependent function, the following form is used (Equation (3.63) in Chapter 3):

$$\sigma(t_{n+1}) = g_\infty \sigma_0(t_{n+1}) + \sum_{i=1}^{N}\left(\exp\left(-\frac{\Delta t}{\xi_i}\right) h_i(t_n) + g_i \frac{1-\exp\left(-\frac{\Delta t}{\xi_i}\right)}{\frac{\Delta t}{\xi_i}} \left[\sigma_0(t_{n+1}) - \sigma_0(t_n)\right] \right).$$

A detailed derivation is given in Chapter 3 (Section 3.3). The function can be evaluated for various strain histories.

The visco-hyperelastic model described above was calibrated using the gluten test data in Figure 5.3. The calibration was performed simultaneously using a least squares method [Goh *et al.* 2004; Charalambides *et al.* 2006]. A constraint was defined during the calibration procedure where the time dependent constants, g_i, are set to be non-negative values. The parameters for the model are shown in Table 5.1.

Table 5.1. Visco-hyperelastic model parameters for gluten.

Material	**Strain dependent constants**			**Time dependent constants**					
				i	1	2	4	5	∞
	μ (kPa)	λ_m	a	ξ_i (s)	0.1	10	100	1000	
Gluten	3.29	4.64	0.25	g_i	0.867	0.092	0.004	0.028	0.007

The model agrees reasonably well with the gluten test data (Root Mean Square Percentage Error (RMSPE) = 24 %), as shown in Figure 5.3, justifying the assumption of the rubberlike, rate dependent behaviour of gluten. The RMSPE is calculated using the following equation [Hagan 2009]:

$$\text{RMSPE} = \sqrt{\frac{1}{n}\sum_{i=1}^{n}\left(\frac{x_d - x_m}{x_d}\right)^2}.$$

It is worth noting here that methods have been suggested by Ng and McKinley [2008] and Tanner *et al.* [2011a] to derive the discrete Prony series terms from the power law fit to relaxation or storage modulus data. For this, storage oscillatory tests in the linear viscoelastic region for gluten were shown in Figure 5.4. This is similar to the results in Figure 4.23(b).

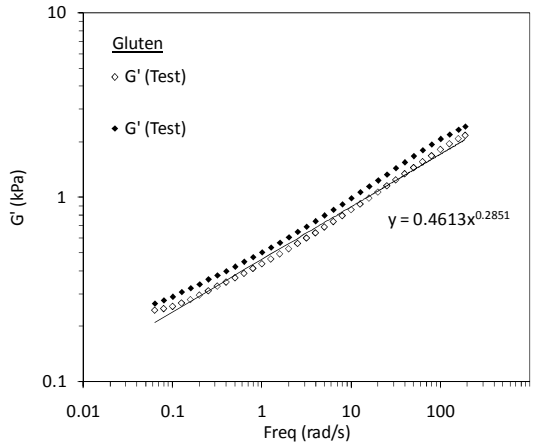

Figure 5.4. Storage modulus of gluten obtained using at 0.1 % shear strain at 0.1-30 Hz.

The Prony series constants were then obtained using the following equation [Macosko 1994; Tanner 2000]:

$$g_i = H(\xi_i)\frac{r^{n/2} - r^{-n/2}}{n} \tag{5.1}$$

where n is the power law constant and r is the ratio of two successive relaxation time constants (for this work, $r = 10$ for $\xi_i = 0.1,\ 1,\ 10,\ 100,$ and 1000). The constant, $H(\xi_i)$ in Equation (5.1) is given by:

$$H(\xi_i) = \frac{G(1)\xi_i^{-n}}{(n-1)!} \tag{5.2}$$

The Prony series terms obtained using Equation (5.2) are shown in Table 5.2.

Table 5.2. Visco-hyperelastic model parameters for gluten, where the time dependent constants were obtained using Equation (5.2).

Material	**Strain dependent constants**			**Time dependent constants**						
				i	1	2	3	4	5	∞
	μ (kPa)	λ_m	a	ξ_i (s)	0.1	1	10	100	1000	
Gluten	1.14	4.64	0.25	g_i	0.499	0.258	0.133	0.068	0.035	0.007

The visco-hyperelastic model calibration using the parameters in Table 5.2 is shown in Figure 5.5. It is apparent that the values in Table 5.1 lead to a better agreement with the experimental results of gluten (Figure 5.3). It was found that the resulting Prony Series terms did not lead to a good fit to the experimental data of Figure 5.5 and therefore this method was not investigated further.

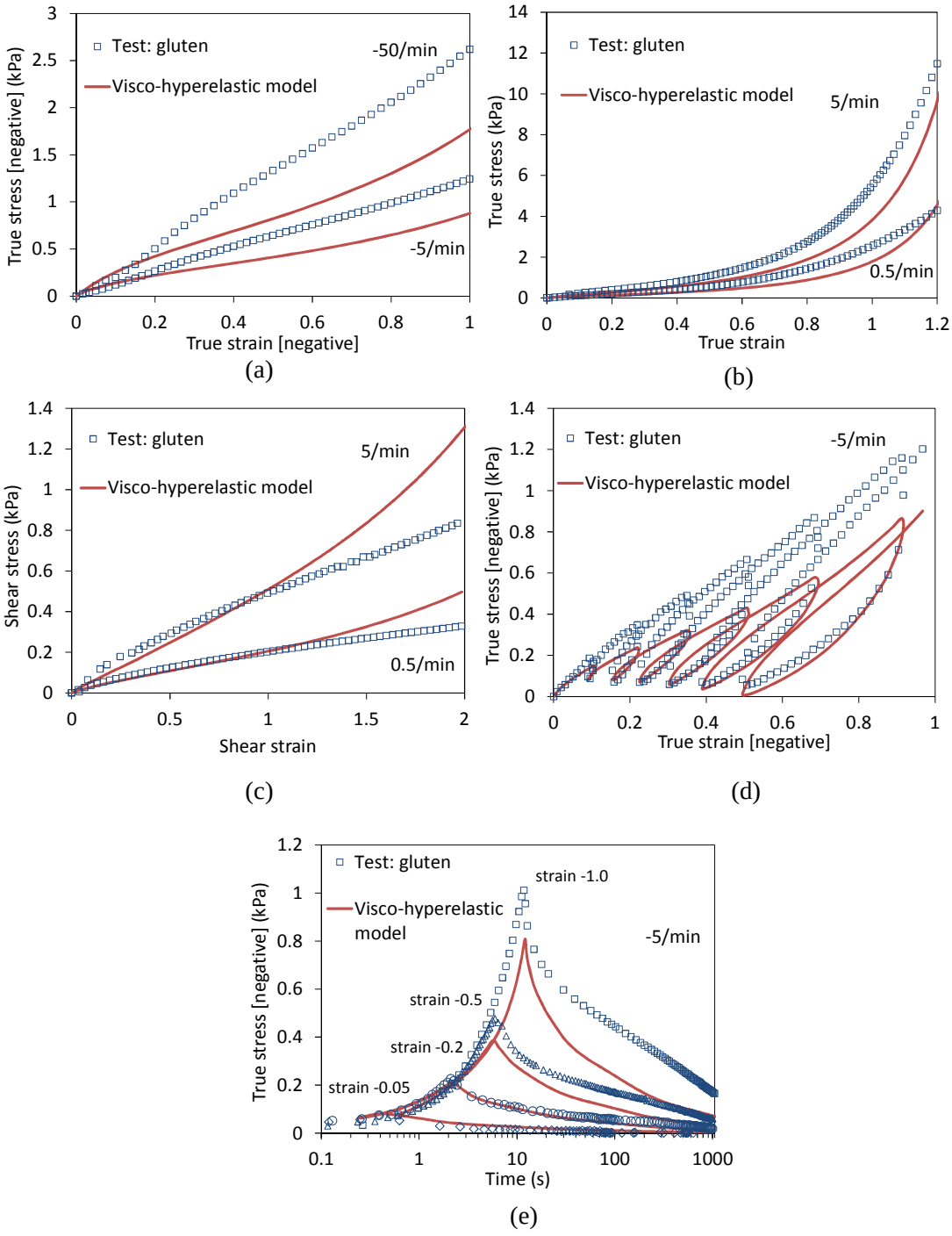

Figure 5.5. Gluten test results and calibration of visco-hyperelastic (van der Waals) material model under: (a) compression; (b) tension; (c) shear; (d) cyclic compression; and (e) compression relaxation. The material parameters are shown in Table 5.2.

5.3.2 Material Model for Starch

Figure 5.6 shows the results from the compression and compression-relaxation experiments on starch. Only compression test results are shown for starch. This is due to difficulties in preparing samples for tensile tests as discussed in Section 4.4.1 in Chapter 4. In addition it was found that the starch samples showed edge fractures during shear at small strains which led to irreproducible results (Section 4.4.3.2).

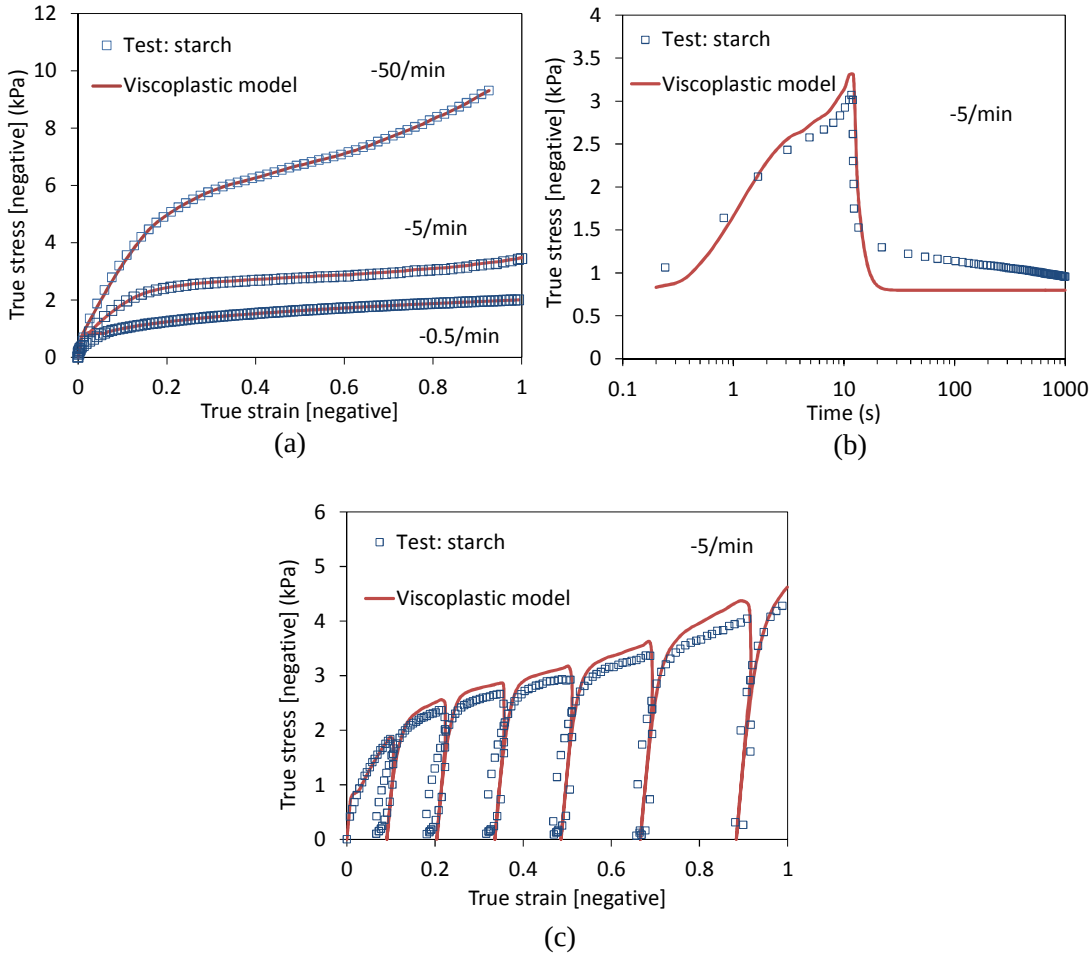

Figure 5.6. Starch tests results and calibration of visco-hyperelastic material model with starch tests data under: (a) compression; (b) compression-relaxation at strain of -1; and (c) cyclic-compression.

The starch test results in Figure 5.6(a) show a rate dependent behaviour, which is similar to the results from gluten shown in Figure 5.3. However, the almost vertical unloading-reloading parts of the cyclic results for starch (Figure 5.6(c)) as well as the less dramatic relaxation (Figure 5.6(b)), when compared to gluten results in Figure 5.3, indicate a viscoplastic behaviour. Therefore, a viscoplastic material model was considered to represent the mechanical behaviour of starch. In the Finite Element Analysis software Abaqus [2009], which will be used for the micromechanics model in the following section, viscoplasticity can be implemented through a strain rate dependent yield behaviour which follows an initial elastic region. The software allows a direct tabular entry of corresponding equivalent stress and equivalent plastic strain test data at different plastic strain rates. The plastic strain is calculated through (Equation (3.81) in Chapter 3):

$$\varepsilon_{plastic}^{n} = \varepsilon_{total}^{n} - \varepsilon_{elastic}^{n} = \varepsilon_{total}^{n} - \frac{\sigma^{n}}{E}$$

where $\varepsilon_{plastic}^{n}$, ε_{total}^{n} $\varepsilon_{elastic}^{n}$ and σ^{n} are the plastic true strain, total true strain, elastic true strain and true stress respectively at the n^{th} experimental data point in the 'yield regions' of Figure 5.6(a). Plastic strain rates are calculated in a similar fashion. The initial yield stress, $\sigma_y = 0.8$ kPa is selected to fit the stress relaxation data after 100 seconds (Figure 5.6(b)). The elastic modulus, $E = 90$ kPa , on the other hand is estimated through the slope of the unloading-reloading data in Figure 5.6(c). Lastly, the Poisson's ratio, v , is taken to be 0.49 assuming an incompressible material [Charalambides *et al.* 2002; Wang *et al.* 2006]. The viscoplastic model is in reasonable agreement with the starch test data shown in Figure 5.6.

5.3.3 Micromechanics Model for Dough

A simple composite model was developed using Abaqus [Abaqus 2009], using a single-particle model, which consisted of a single 2D circular filler representing starch surrounded by matrix representing the gluten phase, as shown in Figure 5.7(c). Gluten and starch were modelled through the visco-hyperelastic and the viscoplastic models shown in Figures 5.3 and 5.6 respectively. The diameter of the filler is set to 20 μm, which is of the same order as the size of type A starch in dough as seen in Figure 4.33. An average starch volume fraction value of 45 % was calculated from Cryo-SEM images of dough. This is performed by converting the Cryo-SEM image of dough to binary form using the image analysis toolbox in MATLAB [MATLAB 2009], with an example shown in Figures 5.7(a) and 5.7(b).

The black pixels in Figures 5.7(b) represent the gluten matrix and the white pixels represent the starch granules. The starch volume fraction was determined from the ratio of the black and white pixels, i.e. the assumption that the 2D areal and 3D volume fractions are equal was made [Underwood 1970]. The starch volume fraction obtained from images taken from the Cryo-SEM experiments is $45\,\% \pm 3\,\%$. The value is close to the 46 % starch volume fraction obtained in Tanner *et al.* [2011b]. An example particle size distribution from Figure 5.7(b) is shown in Figure 5.7(d), where the Feret diameter shown is the mean length of the distance between two tangents on opposite sides of the particle outline parallel to randomly fixed position [Stapountzi 2008]. It is worth noting that the starch particle distribution for type A and type B in Figure 5.7(b) is 35.4 % and 19.5 % respectively, which gives a total of 44.9 % volume fraction.

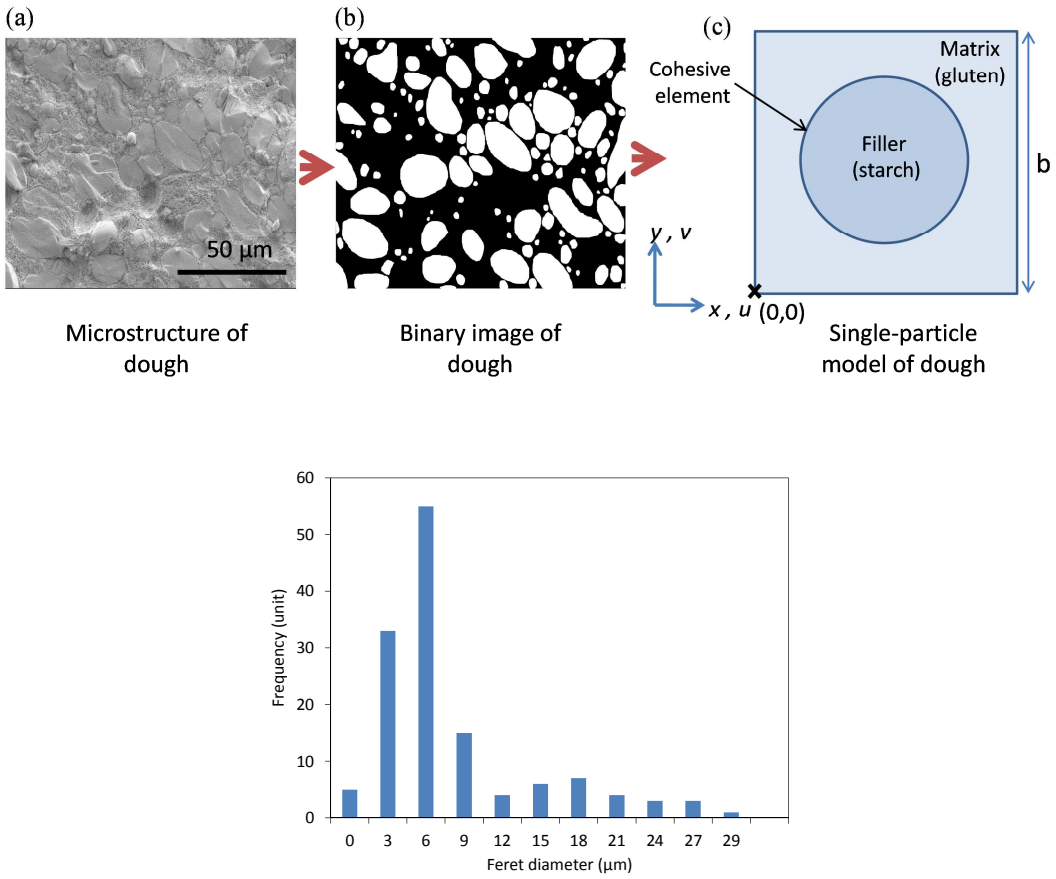

(d)

Figure 5.7. Volume fraction measurement of dough: (a) Cryo-SEM image of dough; (b) binary image of dough; (c) a single-particle model of dough; and (d) particle size distribution obtained from Figure 5.7(b).

The single-particle model was loaded uniaxially as well as in simple shear mode. The analysis was performed using Abaqus/Explicit [Abaqus 2009] with first order, plane stress elements. In an attempt to simulate as close to 3D as possible, generalised plane strain elements were also considered. These however led to results very close to plane stress (see Figure 5.8(a) under uniaxial tension) so plane stress elements were used throughout. The mesh density was chosen following a mesh sensitivity study where the mesh was refined sequentially until the numerical results converged to within ±1 % (see Figure 5.8(b)).

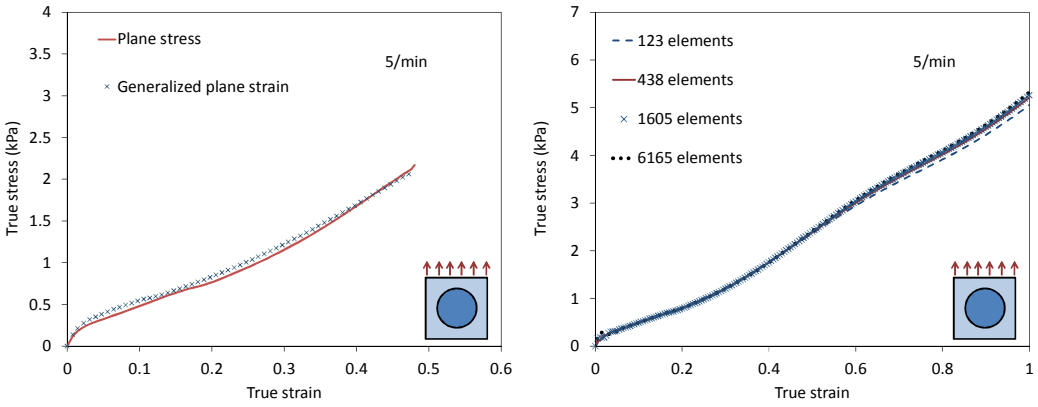

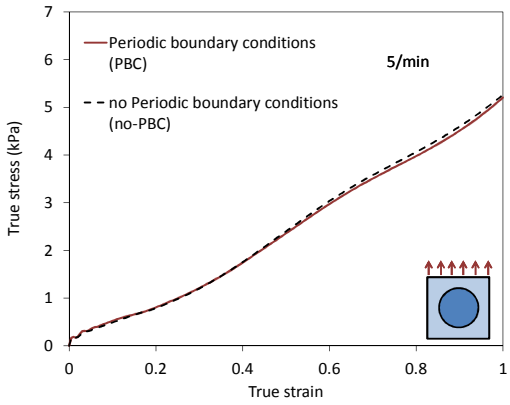

(c)

Figure 5.8. Single-particle model (without damage/debonding) under uniaxial tension mode at 5/min for: (a) plane stress versus generalized plane strain element; (b) mesh sensitivity study; and (c) periodic boundary conditions effect. Note that the simulation results in (a) was performed using Abaqus/Standard since generalized plane strain element is not available in Abaqus/Explicit.

Under tension and compression modes, the following boundary conditions are used:

$$u(0,0) = v(x,0) = 0$$
$$v(x,b) = \delta \tag{5.3}$$

where δ the applied displacement is $\delta > 0$ in tension and $\delta < 0$ in compression, u and v are displacements in the x and y direction respectively, b is the height of the single-particle model, and $(0,0)$ is the origin coordinate at the lower left corner of the single particle model, as shown in Figure 5.7(c). Under simple shear, the following boundary conditions are used:

$$u(x,0) = v(x,0) = 0$$
$$u(x,b) = \delta ; v(x,b) = 0. \tag{5.4}$$

Periodic boundary conditions were added for the model to undergo similar displacements on the vertical sides of the geometry in Figure 5.7(c). The following equations are used to define the periodic boundary conditions:

$$\begin{bmatrix} u^{i+1} \\ v^{i+1} \end{bmatrix} = \begin{bmatrix} u^{0} \\ v^{0} \end{bmatrix} + \begin{bmatrix} u^{i} \\ v^{i} \end{bmatrix} \tag{5.5}$$

where u^{i+1}, v^{i+1}, u^{0} , v^{0}, u^{i} and v^{i} are the displacements shown in Figure 5.9.

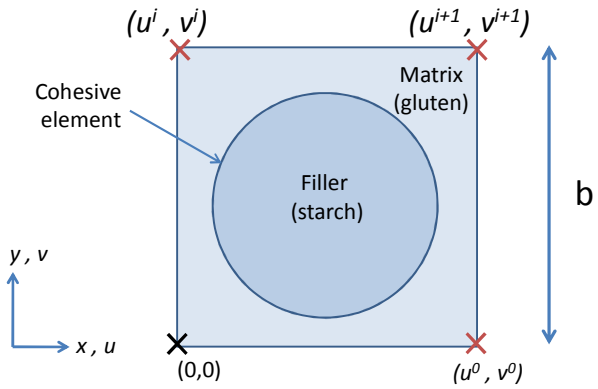

Figure 5.9. Periodic boundary conditions used for the single-particle model of dough.

However it was found that a very similar stress-strain curve was obtained when a comparison was performed between the results obtained with and without periodic boundary conditions (typical difference between results ~ 0.5 %, results in Figure 5.8(c)). This indicates that the boundary conditions in Equations (5.3) and (5.4) are sufficient for the single particle model. Finally, the output strain and strain rate ranges in all the simulations were checked to ensure that they lied within the strain and strain rate calibration ranges shown in Figures 5.3 and 5.6.

The numerical results when no debonding/damage is allowed at the starch/gluten interface are first shown in Figure 5.10 for the rate of 5/min. It is observed that the numerical predictions are close to the experimental stress-strain curves of dough for strains up to approximately 0.2 in compression and tension and 0.4 in shear loading. This gives further confidence that the constituents of dough, i.e. starch and gluten have been modelled correctly. For higher strains, the experimental data are lower for all loading conditions. Even though shear and normal displacements coexist during shear and tensile loading of the micromechanics model, the comparison is still useful as it helps to form an approximate estimate of the critical stresses for the initiation of debonding damage; approximately 0.3 kPa in shear and 1.0 kPa in tension, as shown in Figure 5.10.

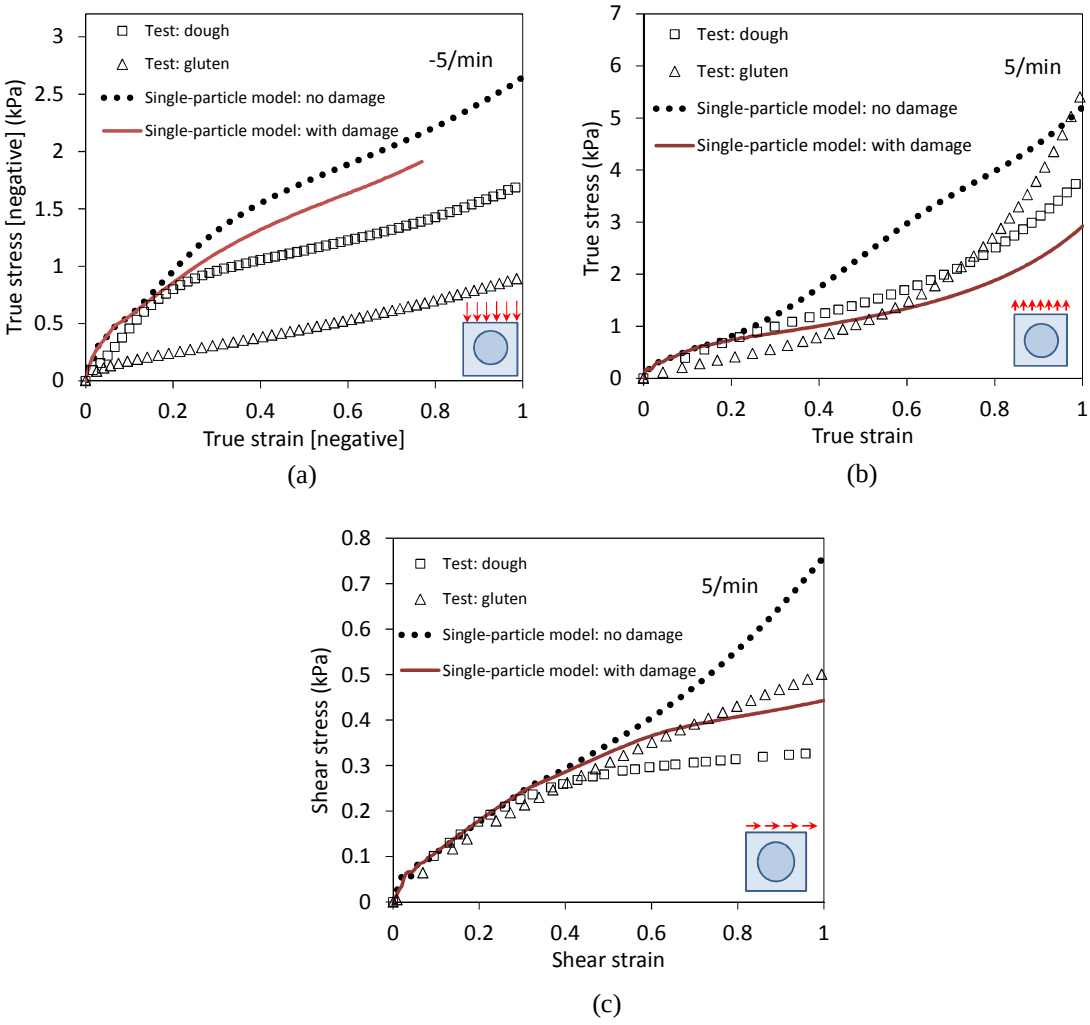

Figure 5.10. Dough tests data at 5/min and calibration of the single-particle model under: (a) compression; (b) tension; and (c) shear.

Next, the interface between starch and gluten in Figure 5.7(c) was modelled using the cohesive element interaction available in Abaqus [Camanho and Davila 2002]. The interaction is defined by the traction versus separation behaviour, as shown in Figure 5.11.

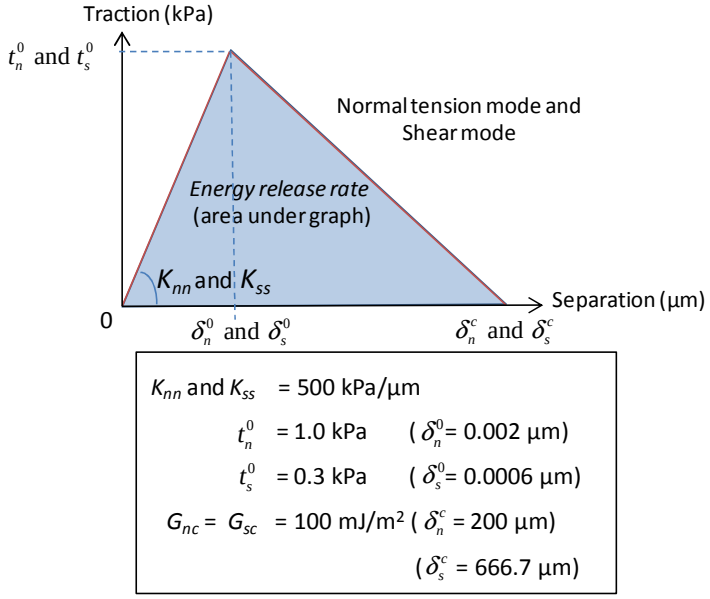

Figure 5.11. Cohesive element parameters used in the micromechanics model under normal and shear loading.

Details on the cohesive element interaction are provided in Section 3.5.1 in Chapter 3. K_{nn} and K_{ss} in Figure 5.11 are the normal and shear coefficients respectively. Damage is activated in the normal and shear loading modes, at the critical normal stress, t_n^0 or critical shear stress, t_s^0. The energy that is dissipated as a result of the damage process, i.e. the energy release rate, G_c, is equal to the area under the traction-separation curve in Figure 5.11, i.e. $G_{nc} = \frac{t_n^0 \delta_n^c}{2}$ and $G_{sc} = \frac{t_s^0 \delta_s^c}{2}$ for pure normal and shear loading conditions respectively.

Having already made estimates for t_n^0 and t_s^0 as 1.0 kPa and 0.3 kPa respectively, the values of G_{nc}, G_{sc}, K_{nn} and K_{ss} need to be next determined. In the absence of direct experimental data, the simplifying assumption that $G_{nc} = G_{sc}$ and $K_{nn} = K_{ss}$ is first made. The value of $K_{nn} = K_{ss} = 500$ kPa/μm is then selected to reduce severe mesh

distortion of the cohesive elements during the large strain simulations. This is because the values of K_{nn} and K_{ss} must be high enough to prevent interpenetration of the element faces and to prevent artificial compliance from being introduced into the model by the cohesive elements [Song *et al.* 2008]. The damage energy, $G_{nc} = G_{sc} =$ 100 mJ/m^2 is next obtained from peel tests of dough from a steel substrate performed by Dobraszczyk [1997]. These cohesive zone parameters were used to predict the dough response under all loading conditions and the results are compared to experimental data in Figure 5.10.

For tension and shear loading, when the interaction of starch and gluten is strong, as indicated for the dough with no damage, the stress-strain curve is above the gluten stress-strain curve under tension and shear. When damage is activated, the interface softens and debonds, causing the dough stress-strain curves under tension and shear to cross over the curves for gluten, leading to lower stress values than in gluten. This observation explains the trends in data published by other researchers [Uthayakumaran *et al.* 2002; Ng 2007]. In contrast, damage is less apparent under compression and the stress-strain curve for dough is always higher than gluten.

The model predictions for the full range of loading conditions are shown in Figure 5.12. The correct trends are predicted. For compression at -5/min and -50/min the errors are RMSPE = 25.5 % and RMSPE = 17.7 % respectively. Note that the simulations for compression aborted before the strain of one was reached due to large mesh distortion. The cyclic compressive loading shows good agreement to the test data. For tension at 5/min and 0.5/min, the errors are RMSPE = 18.8 % and RMSPE = 8.8 % respectively. The error for 5/min shear loading is RMSPE = 20.3 %. The

errors are very large for shear at 0.5/min (RMSPE = 71.2 %). A probable reason is that the cohesive zone parameters could be rate dependent [Geiβler and Kaliske 2010].

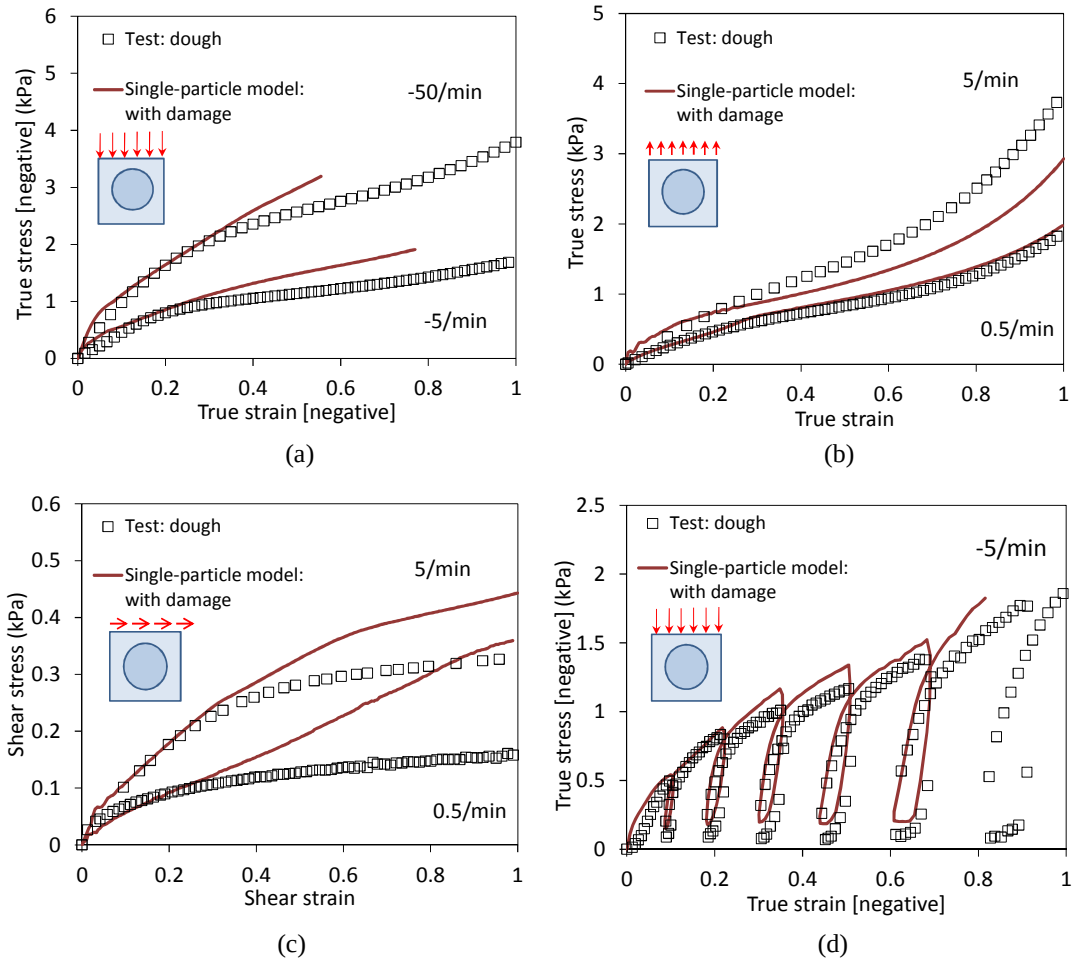

Figure 5.12. Dough tests data and calibration of the single-particle model under: (a) compression; (b) tension; (c) shear; and (d) cyclic-compression.

In order to check the rate dependence possibility, Figure 5.13 shows the numerical curve for shear loading at 0.5/min with no debonding allowed. By comparing this curve with the experimental data, it is apparent that debonding occurs at a stress of approximately 0.1 kPa which is a great deal lower than the assumed value of 0.3 kPa in Figure 5.10. Indeed, when the critical shear stress is reduced to 0.1 kPa, the

numerical curve is very close to the experimental data as shown in Figure 5.13. However, implementing cohesive zone parameters as a function of rate requires thorough, direct, experimental measurement and justification. Suitable experiments could involve a single starch granule being pressed on a gluten surface and subsequently retracted, possibly through an Atomic Force Microscope as is performed in synthetic polymer characterisation [Haupt *et al.* 1999]. Such a task for the case of starch/gluten interface would be quite complex though, taking into account the nature of these soft, difficult to handle materials.

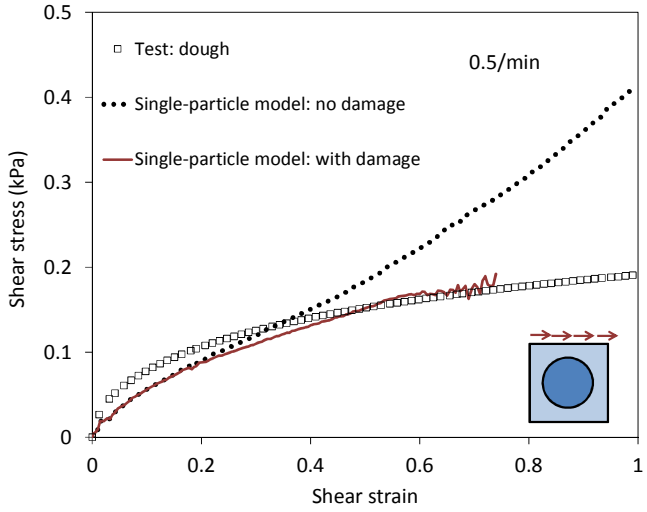

Figure 5.13. Dough shear tests data at 0.5/min and calibration of the single-particle model using lower shear stress initiation value of 0.1 kPa. The other parameters for the single-particle model with damage are the same as in Figure 5.10.

As already mentioned, the value of $G_{nc} = G_{sc}$ = 100 mJ/m^2 used in Figure 5.11, was obtained from peel tests of dough performed by Dobraszczyk [1997]. Those peel tests were performed to measure the 'stickiness' of dough on a steel plate, whereas in dough, the surface energy should be that of the starch and the gluten interface.

Blancher *et al.* [2005] on the other hand obtained the free surface energy of dry flour using the contact angle measurement as $50\,\mathrm{mJ/m^2}$.

Following the above remarks, as well as for investigating the 'uniqueness' of the set of cohesive parameters that were selected above (see Figure 5.11), it was decided to perform another simulation with a set of parameters such that $G_{nc} = G_{sc}$ were set to 50 $\mathrm{mJ/m^2}$. The values of the other two parameters which led to a good agreement with the tensile data at 5/min were t_n^0 = 2 kPa and t_s^0 = 0.2 kPa. The results from this set of parameters are shown in Figure 5.14 together with the experimental data as well as the numerical result corresponding to the earlier set of cohesive parameters (Figure 5.11). Even though the parameters are different, the global results are very close. Therefore, the usual problem in inverse parameter identification is demonstrated, that of non-uniqueness. In order to solve this problem, direct experimental identification of the cohesive parameters is required as already suggested above.

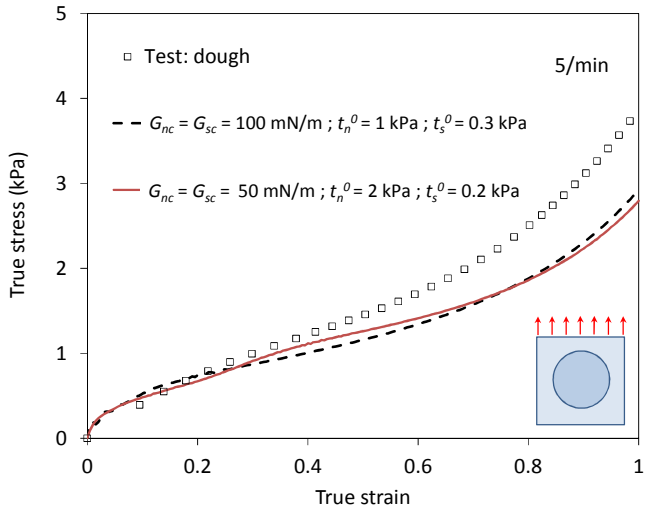

Figure 5.14. The effect of two different sets of values for the cohesive parameters on global results under uniaxial tension.

In all simulations above, it was indicated that the critical shear stress for damage initiation is significantly lower than the critical normal stress. This implies that the condition for damage initiation will be largely determined by the shear critical stress for mixed mode loading. Therefore, it seems that the shear critical stress is a very important parameter for dough and its mechanical behaviour.

In order to investigate whether the single-particle model in Figure 5.7(c) actually represents the microstructure of dough in Figure 5.7(b), a comparison between the single-particle model and a multi-particle model was performed. The multi-particle model was developed by converting the binary image in Figure 5.7(b) into a set of convex polygons representing the particles. This was achieved by using the convex hull algorithm in the MATLAB image analysis toolbox [MATLAB 2009]. The coordinates of the polygon vertices were then exported into Abaqus using a Python script to generate a mesh, as shown in Figure 5.15(a). Details on the microstructure model procedure are provided in Tarleton *et al.* [2012]. Cohesive elements were assigned along the interface of every particle and the same cohesive law and material models as used in the single particle model were applied. Simulation of the multi-particle model was conducted in Abaqus/Explicit using plane stress elements, which is similar to the elements used for the single particle model. The results under uniaxial compression, tension and shear obtained using the single particle model and the multi-particle model consisting of 141 particles are compared in Figure 5.15. Note that the results in Figure 5.15 were obtained without periodic boundary conditions since it is difficult to define periodic boundary conditions for the multi-particle model.

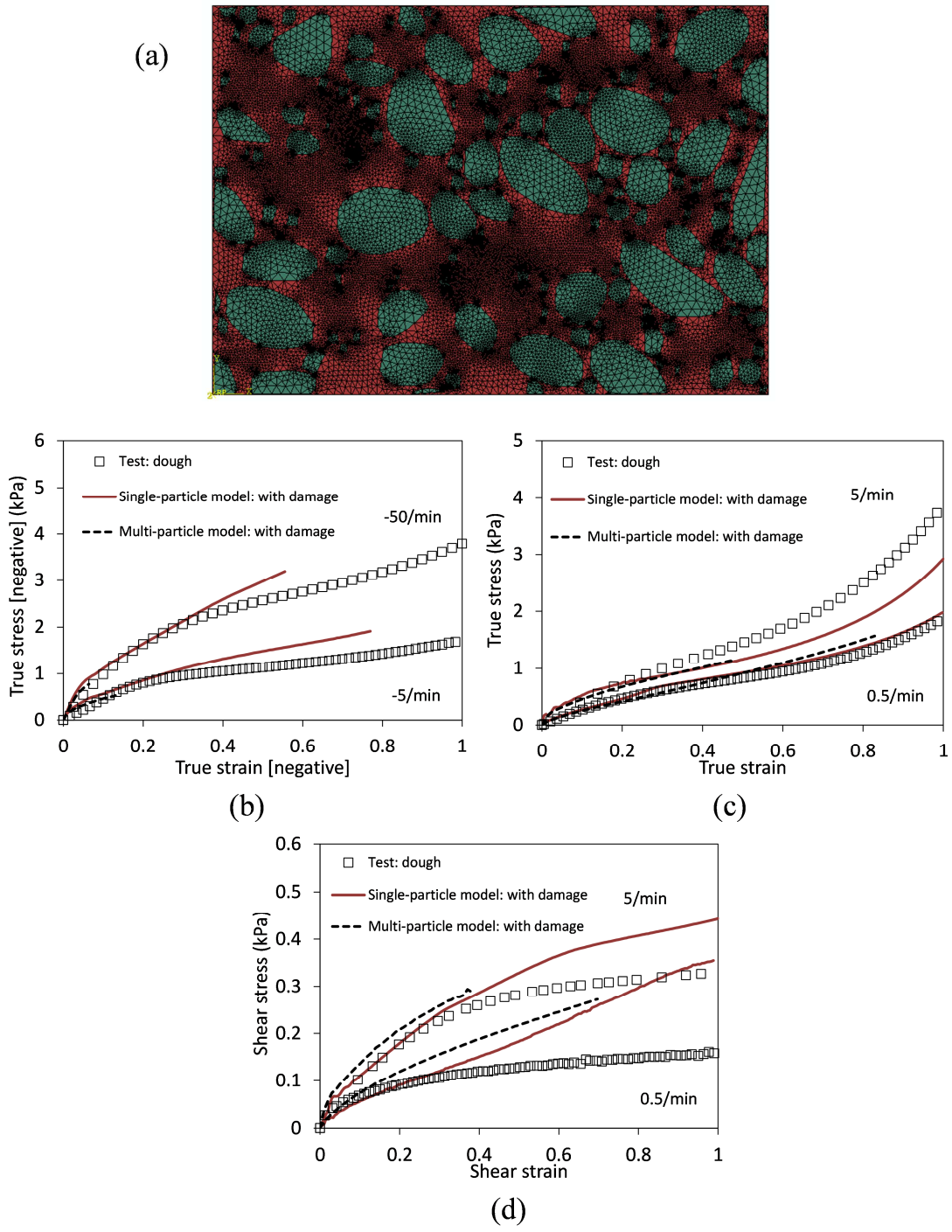

Figure 5.15. (a) Multi-particle model produced using the image in Figure 5.7(b); and comparison results between the single-particle model and the multi-particle model under: (b) uniaxial compression; (c) uniaxial tension; and (d) simple shear. The cohesive parameters used are as shown in Figure 5.11.

Good agreement is seen between the models, especially for uniaxial tension results, indicating that the single-particle model can be used to represent the microstructure of dough. Note that simulation under uniaxial compression for the multi-particle model can be performed only up to true strain 0.1 due to interface failure/softening causing element distortion in the matrix.

A comparison was also performed between the 2D single-particle model and 3D single-particle models using spherical and cylindrical geometries. The same volume fraction, material models and cohesive law as used in the 2D single particle model were applied. The simulation results at 5/min under uniaxial tension are shown in Figure 5.16. Reasonable agreement is observed between all the models, a further proof that the simple, 2D, single-particle model is sufficiently accurate for use in predictive models for the mechanical behaviour of dough.

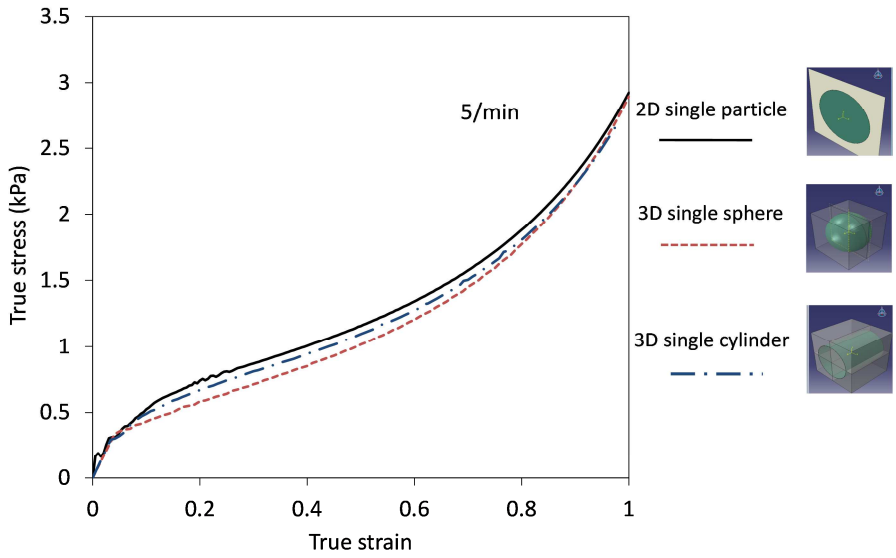

Figure 5.16. Comparison results between the 2D single-particle and 3D single-particle models under uniaxial tension mode.

5.4 Conclusion

Mechanical loading tests were performed on starch, gluten and dough, which revealed a rate dependent behaviour for both the starch and gluten constituents of dough. A starch volume fraction of 45 % was measured experimentally from Cryo-SEM images. Starch and gluten were modelled as visco-hyperelastic and viscoplastic materials respectively. A single-particle model was developed, which consists of a single 2D round filler representing starch surrounded by gluten matrix. The interaction between the starch and gluten was defined using cohesive elements. The simple composite model leads to similar trends as those shown by the experimental data, indicating possible debonding of starch and gluten in dough under tension and shear. This argument was supported further by Cryo-SEM images of stretched dough as well as the apparent need for damage functions when the Lodge constitutive model was used to represent the mechanical test data of dough. Good agreement is seen between single-particle and multi-particle models, as well as with 3D single-particle models with spherical and cylindrical geometries, indicating that the 2D single-particle model can be used to accurately represent the microstructure of dough. Finally, a direct experimental identification of the cohesive zone parameters is needed in order to identify the values for the critical damage initiation stress as well for the critical energy release rate in both normal and sliding deformations as a function of test rate. Only then can numerical models such as the ones presented here can be fully validated against experimental data. However, the small size of starch particles and soft nature of the interface renders such tests quite a considerable challenge.

Chapter 6. Numerical Study of Ram Extrusion of Wheat Flour Dough

6.1 Introduction

Extrusion is one of the common manufacturing processes in wheat flour dough production lines, as shown in Figure 1.2 in Chapter 1. The process involves shaping dough to a smaller size after mixing, which then goes through to the next processes, namely sheeting and cutting. The shape of the dough after extrusion, also known as extrudate, depends on the shape of the extruder's die mouth, as well as the mechanical properties of dough. Studies on ram extrusion have been performed by various researchers and in particular for paste-like materials, such as cellulose paste [Rough *et al.* 2000; Mascia *et al.* 2006], talc-based paste [Martin *et al.* 2004], and Plasticine clay [Aydin *et al.* 2000].

In order to investigate the behaviour of dough during extrusion, a laboratory ram extrusion rig was designed and manufactured by previous researchers at Imperial College [Wanigasooriya 2006; Lim 2007]. The ram extruder uses the same design as a piston driven capillary rheometer, where a material is forced through a shaped die with the aid of a piston that travels along a barrel. Experimental extrusion pressures were then compared to numerical model predictions performed using Abaqus [Wanigasooriya 2006; Lim 2007; Tow 2009]. It has been shown in Chapter 5 that dough can be modelled using a micromechanics model consisting of starch and gluten. However, to model dough using the micromechanics model would be difficult because of the complexity of the model, as already discussed in Chapter 5. An

alternative to this is a continuum material model which is readily available in commercial finite element software, i.e. Abaqus [2010].

Therefore this chapter will investigate the numerical model of dough extrusion using a continuum material model, which will be compared to the experimental results of dough extrusion performed by Wanigasooriya [2006] and Lim [2007]. In particular, this work aim is to improve numerical modelling issues highlighted by the researchers mentioned before, namely the severe mesh distortion in the extrusion model and the contact behaviour between dough surface and extrusion die wall.

6.2 Experimental Work

The extrusion rig used is shown in Figure 6.1. The rig consists of a 25 mm diameter Poly (Methyl Methacrylate) (PMMA) barrel in which the internal bore was polished. The barrel was split in two halves to facilitate filling and to avoid air bubbles. Each half was filled with dough and then the two halves were clamped together. A steel piston with a PTFE plug was used with an Instron 5543 testing machine to give extrusion speeds of 50 mm/min and 500 mm/min. The loads were measured using 5 kN and 100 N load cells. The dies were mounted on the base of the barrel and then placed on a frame to allow the extrudate to flow out freely.

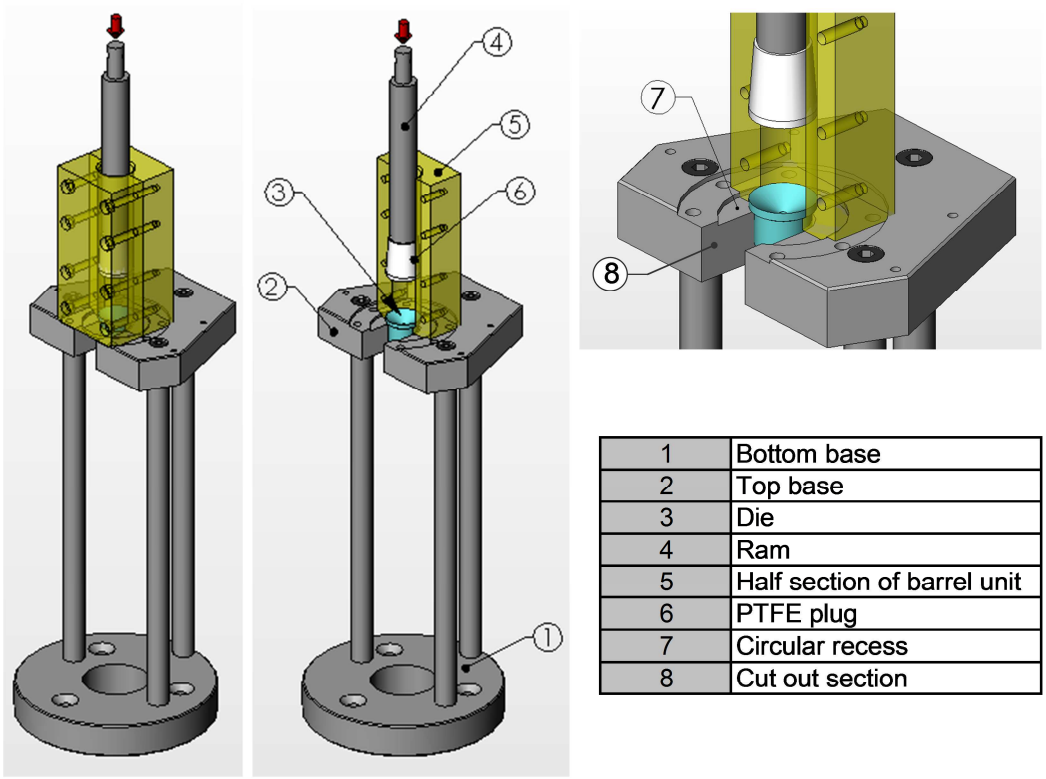

1	Bottom base
2	Top base
3	Die
4	Ram
5	Half section of barrel unit
6	PTFE plug
7	Circular recess
8	Cut out section

Figure 6.1. Extrusion rig set up [Wanigasooriya 2006].

Dies with different angles were used for the experiments, as shown in Figure 6.2. The entry radius is set to be the same for all the dies tested. The dies are arranged in rows from the smallest entry angle, 26^0 to the largest, 180^0. The exit radius is varied from the widest, 18 mm to the smallest, 3 mm. The dies are named using entry angle and exit radius. For example, in the first row, the dies with the same entry angle, 26^0 but with different exit radii, 18 mm, 14 mm and 11 mm are named as die 26^0a, 26^0b and 26^0c respectively.

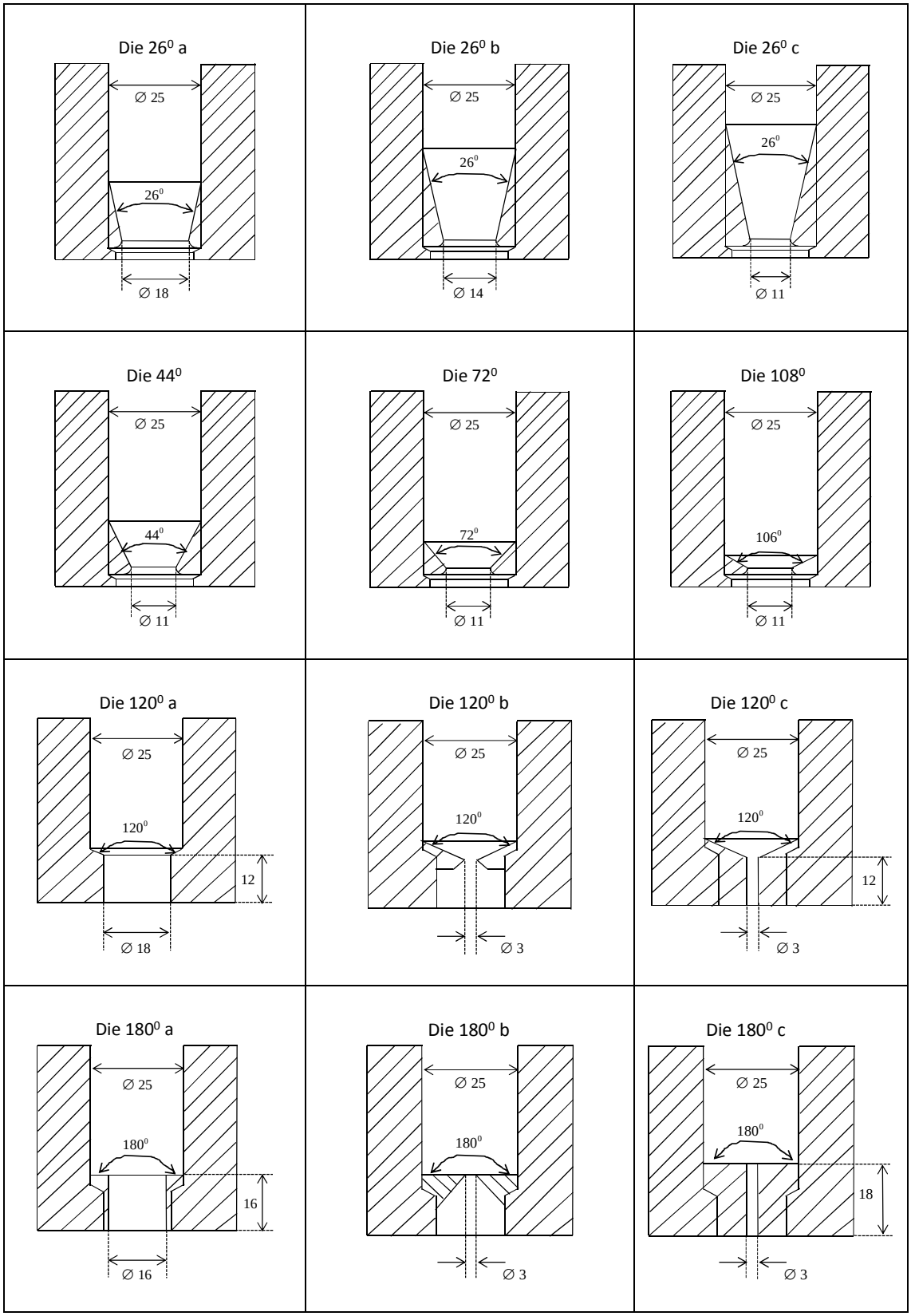

Figure 6.2. Dies used for wheat flour dough extrusion in previous work by Wanigasooriya [2006] and Lim [2007]. All units shown are in milimeter (mm).

A similar rule also applies to dies in rows three and four, except for dies 120^0c and 180^0c which have a similar exit radius to dies 120^0b and 180^0b respectively but a different die land length, as shown in Figure 6.2. The dies in the second row on the other hand are arranged with similar exit radius, 11 mm, but different entry angles, namely 44^0, 72^0 and 108^0. Finally, note that die 26^0a, 26^0b, 26^0c, 44^0, 72^0, 108^0, 120^0b, and 180^0b have a zero die land length.

The experiments were performed at 22^0C and 50 % relative humidity. Since the extrusion rig was set up vertically, steady state extrusion pressures were achieved by extruding the dough into Glycerol (density of 1.25 g/ml) to counteract the effect of gravity on the experimental results, as demonstrated by Wanigasooriya [2006].

An interesting phenomenon in the extrusion process is the formation of static zones. Static zones at the walls of the die are defined as stationary material which does not move into the die mouth. This has been observed by Benbow and Bridgwater [1993] who investigated the presence of static zones during extrusion using square entry die angles (i.e. 180^0) and large diameter reductions typically seen in the extrusion of pastes in industry. An illustration of the static zones is shown in Figure 6.3.

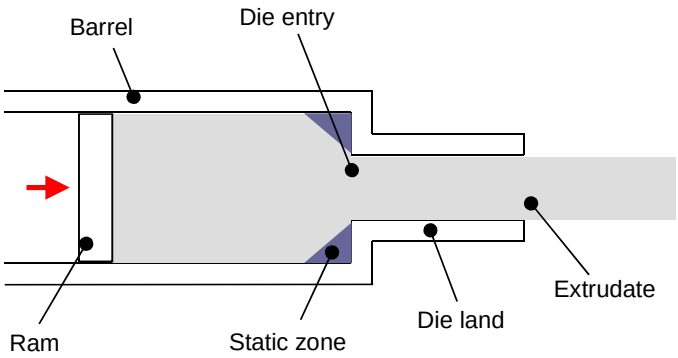

Figure 6.3. Illustration of static zones [Wanigasooriya 2006].

Experimental results using dies with a 26^0 angle and different exit radii are shown in Figure 6.4. Rate dependent behaviour is observed for both speeds tested (500 mm/min and 50 mm/min). The extrusion pressures reached steady state condition after approximately 40 mm ram displacement for all the 26^0 dies. It is worth noting that the initial rise in extrusion pressure is due to the dough being compressed by the ram until it is consolidated into the barrel and die, with a steady state reached thereafter [Wanigasooriya 2006]. It can be seen that decreasing the output radius of the dies resulted in higher extrusion pressures.

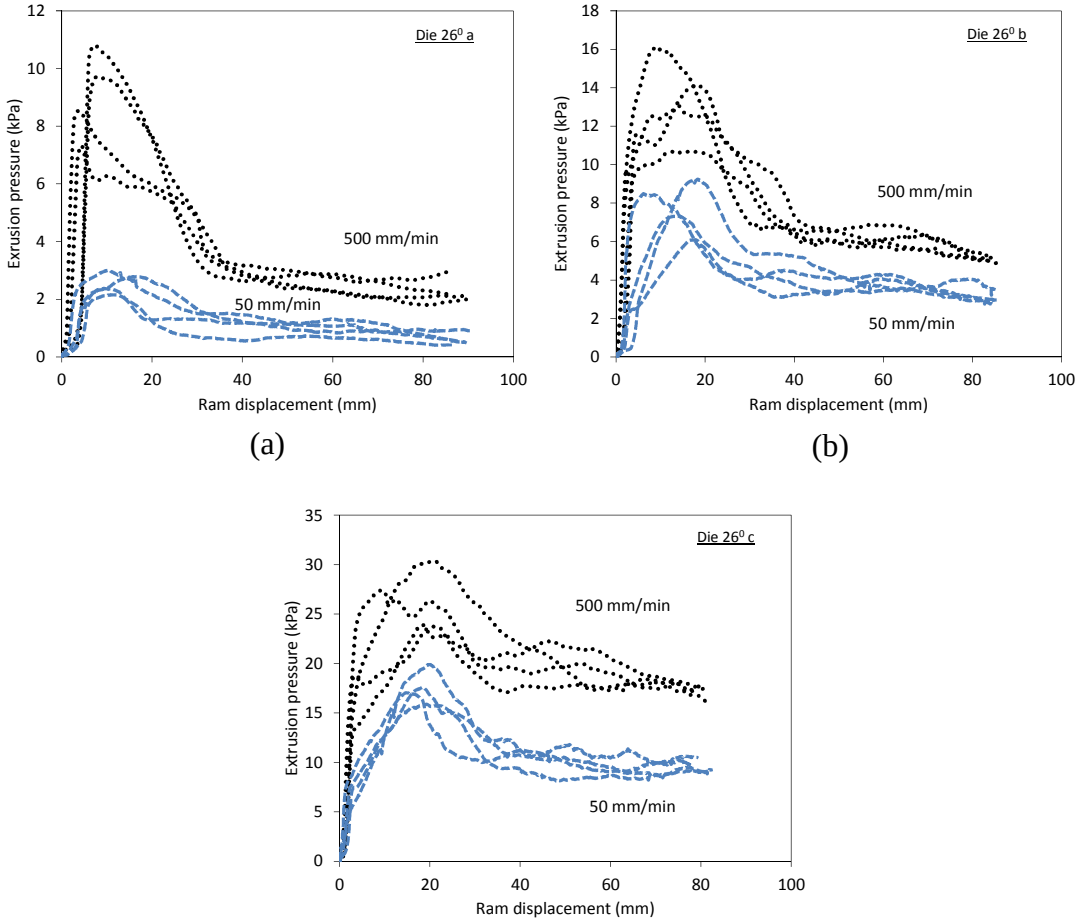

Figure 6.4. Experimental results performed by Wanigasooriya [2006] for dies with 26^0 entry angle and different exit radii, namely 18 mm, 14 mm and 11 mm for die 26^0a, 26^0b and 26^0c respectively.

Wanigasooriya [2006] investigated the formation of the static zones through deformation visualisation experiments using coloured (Supercook food colouring) layers of dough. These colours were obtained by brushing different food paints onto the barrel wall before dough was moulded into the barrel, as shown in Figure 6.5. No static zones were observed at the die wall for the dies with 26^0 angle. This can be seen from an example shown in Figure 6.5 for die 26^0c, where the various colours

along the barrel wall move into the die mouth. The static zones for other dies will be shown later in this section.

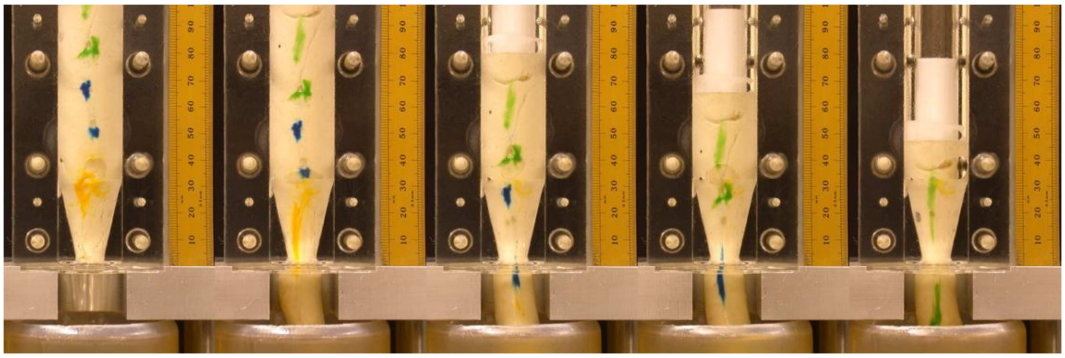

Figure 6.5. No static zones build up were observed for die 26^0c [Wanigasooriya 2006].

Experimental results for dies with entry angle of 44^0, 72^0 and 108^0 with the same entrance and exit radii are shown in Figure 6.6. These experiments were performed by Lim [2007].

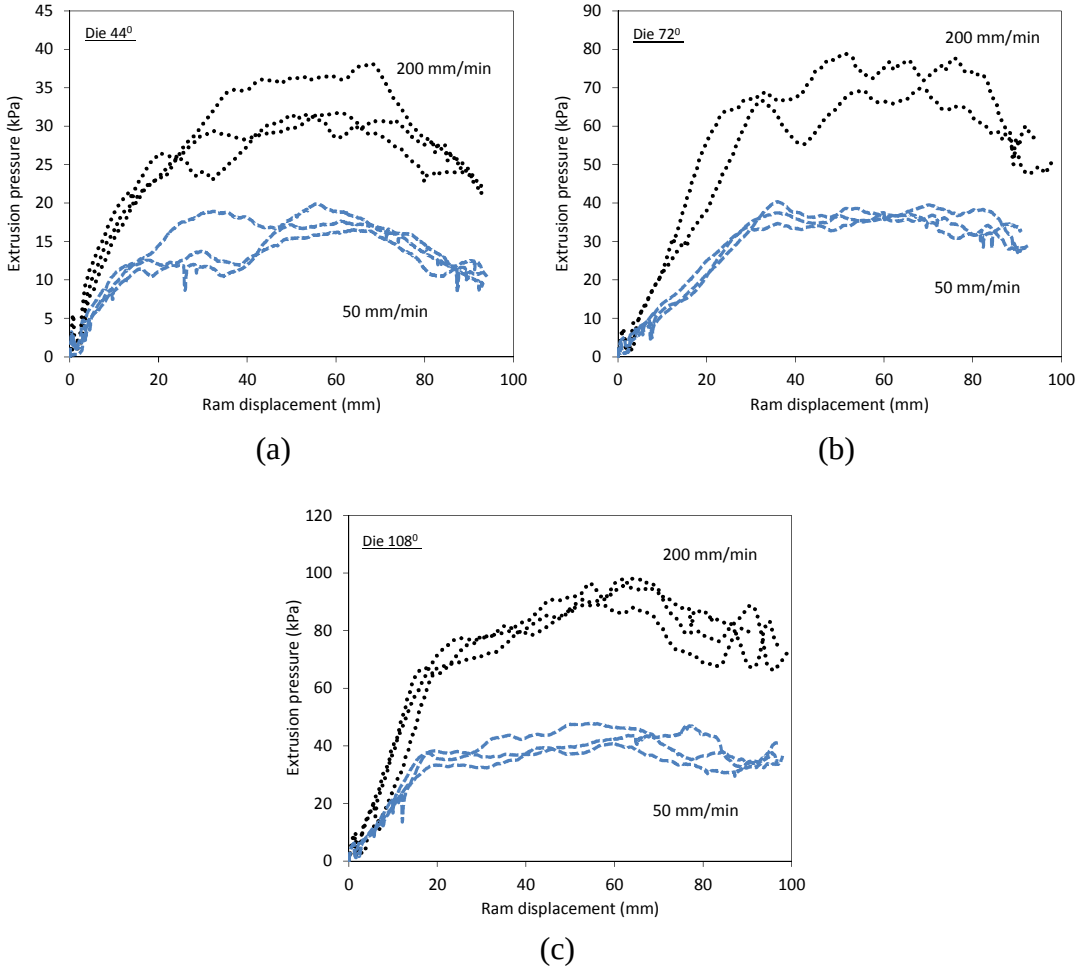

Figure 6.6. Experimental results performed by Lim [2007] for die 44^0, 72^0 and 108^0 with the same entrance and exit radii, 25 mm and 11 mm respectively.

No static zones were observed for die 44^0 [Lim 2007]. However, static zones occurred for die 72^0 at 200 mm/min and 50 mm/min. An example of the static zones is shown in Figure 6.7 for the test at 200 mm/min. This can be seen from the various colours along the barrel wall that do not move into the die mouth, which indicates the occurrence of static zones. Similar static zones were also reported for die 108^0 [Lim 2007] at 200 mm/min and 50 mm/min.

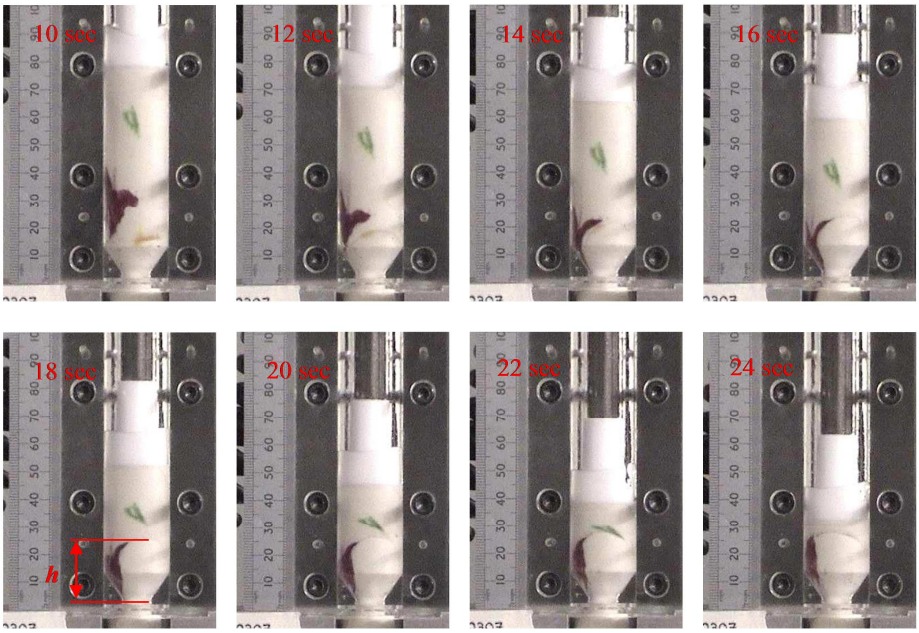

Figure 6.7. Image sequence of extrusion at 200 mm/min using die 72^0 entry angle demonstrating the formation of a static zone [Lim 2007].

Experimental results using dies with a 120^0 angle and different exit radii are shown in Figure 6.8. The experiments were performed by using a step speed rate increasing from 50 mm/min to 500 mm/min after a 40-50 mm ram displacement. It can be seen that except for die 120^0a, steady state extrusion pressures were obtained. However, the pressure for die 120^0a shown in Figure 6.8(a) is much lower than dies 120^0b and 120^0c, therefore pressure fluctuation for dies 120^0b and 120^0c are not as obvious as die 120^0a.

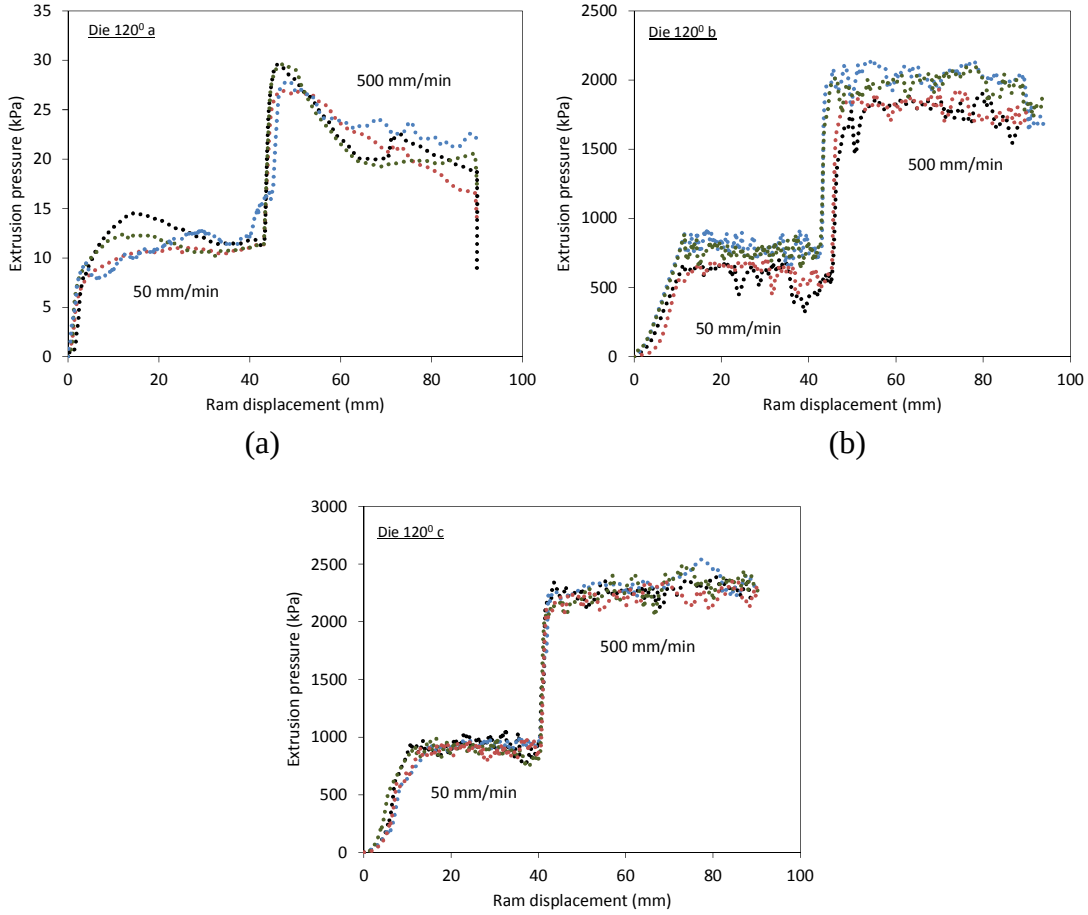

Figure 6.8. Experimental results performed by Wanigasooriya [2006] for dies with 120^0 entry angle and different exit radii, namely 18 mm and 3 mm for 120^0a and 120^0b respectively. Die 120^0c has a similar exit radius as die 120^0b but with different exit length, 12 mm as shown in Figure 6.2.

It should be noted that for die 120^0a, the tests are invalidated as dough was found to touch the rig, as shown in Figure 6.9 at test times of 35 seconds and above.

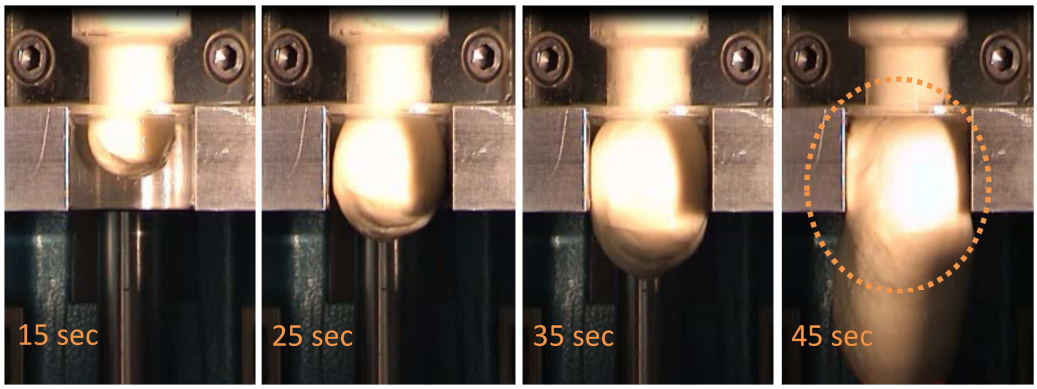

Figure 6.9. Image sequence of extrusion for die 120^0a , the dough was found to touch the rig at 45 seconds test time as highlighted.

Static zones were observed for all the dies with a 120^0 entry angle. An example is shown in Figure 6.10 for die 120^0c , where the various colours along the barrel wall do not move into the die mouth after 20 seconds [Wanigasooriya 2006].

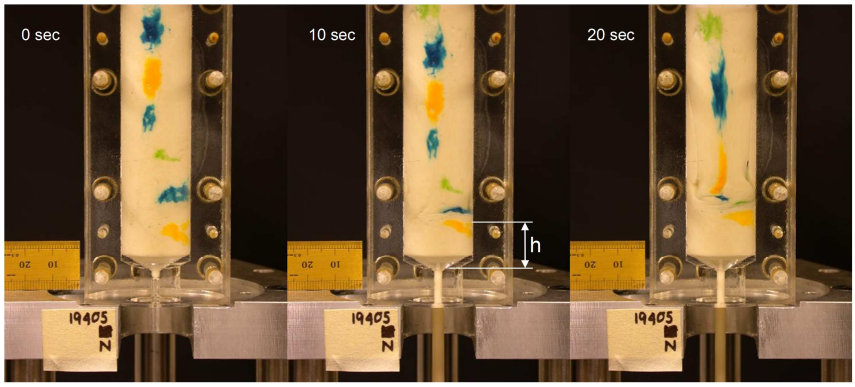

Figure 6.10. Formation of static zones on die 120^0c , with deformation visualisation using different colours within the barrel [Wanigasooriya 2006].

Finally, extrusion test results using dies with a 180^0 angle are shown in Figure 6.11. The experiments were also performed by using a step speed rate. It can be seen that except for die 180^0a , steady state extrusion pressures were obtained. The static zones were observed for all the dies with a 180^0 entry angle. The sudden pressure drop

observed for die 180^0a at 500 mm/min is similar to the pressure drop seen in Figure 6.8(a) (die 120^0a).

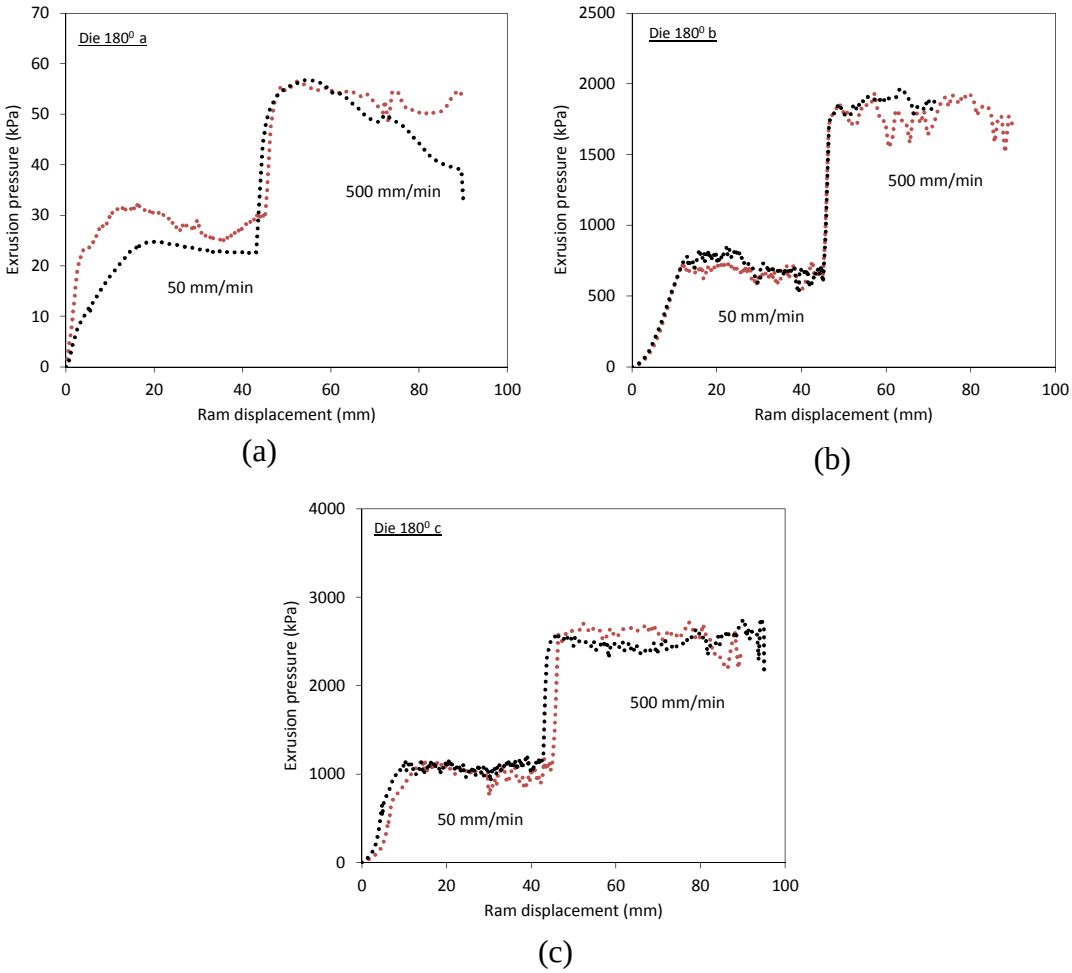

Figure 6.11. Experimental results performed by Wanigasooriya [2006] for dies with 180^0 angle and different exit radii, namely 16 mm and 3 mm for 180^0a and 180^0b respectively. Die 180^0c has a similar exit radius as die 180^0b but with a different die land length of 18 mm as shown in Figure 6.2.

6.3 Numerical Model

Numerical simulation of the dough extrusion was performed using the finite element (FE) software, Abaqus [Abaqus 2009]. A personal computer with Intel Core 2 processor and 4 MB SDRAM was used to perform the numerical simulation. It took approximately one hour or less to perform each extrusion simulation. For simplicity, a continuum material model is assumed for dough. In the previous numerical studies on dough extrusion by Wanigasooriya [2006] and Tow [2009], the visco-hyperelastic material model was used. The model has been shown to give a good approximation to the gluten behaviour in Section 5.3.3, which can then be used for micromechanical modelling.

The van der Waals strain energy function and the Prony series time-dependent function described in Section 3.3 were used. The model was calibrated using the dough test data under different loading conditions, namely uniaxial compression, uniaxial tension, simple shear and cyclic-compression, as shown in Figure 6.12.

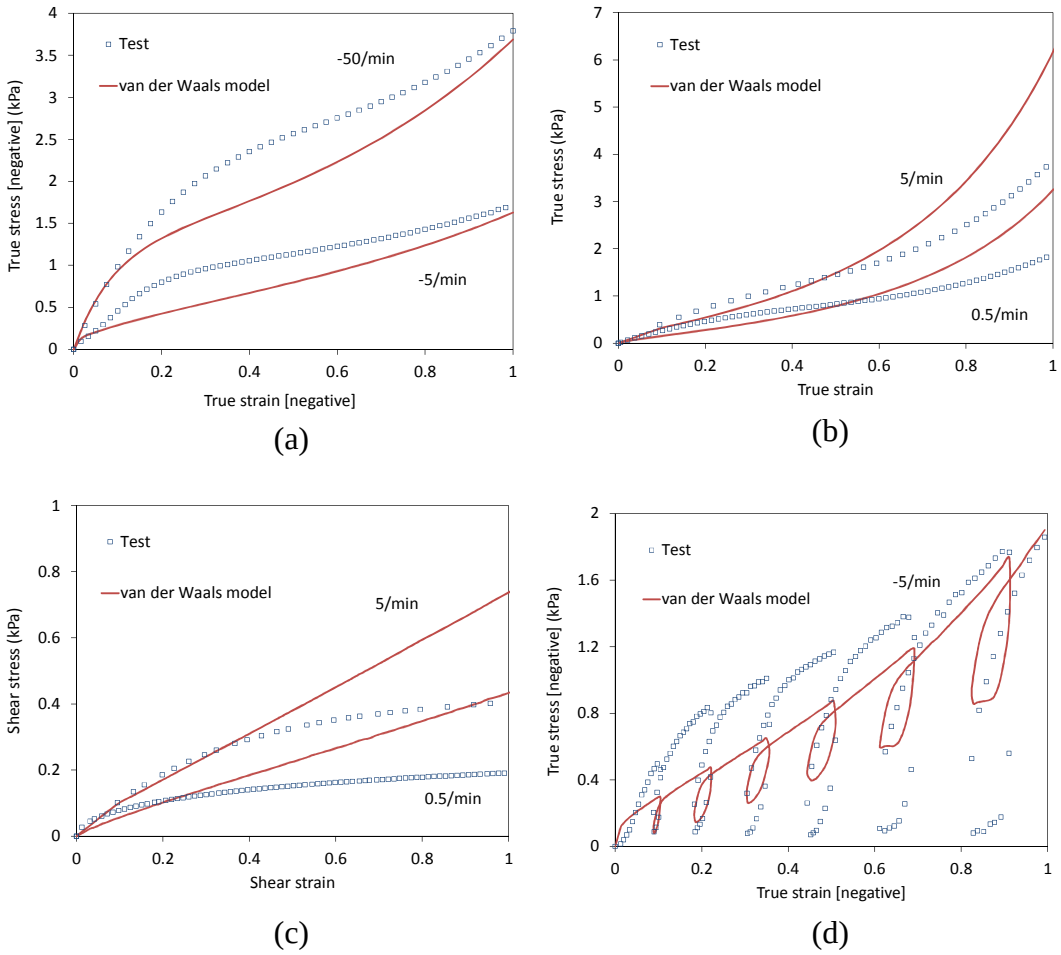

Figure 6.12. Dough test results and calibration of visco-hyperelastic (van der Waals) material model under: (a) uniaxial compression; (b) uniaxial tension; (c) simple shear; and (d) cyclic-compression. The model is described by Equations (3.63), (3.79), and (3.80) and calibrated using the least squares method (Table 6.1) [Goh *et al.* 2004].

The calibration was performed simultaneously using a least squares method [Goh *et al.* 2004; Charalambides *et al.* 2006]. A constraint was defined during the calibration procedure where the time dependent constants, g_i are set to be non-negative values. The calibrated parameters are shown in Table 6.1. Note that the values in Table 6.1 are unique, since it was fitted to different modes of deformation, namely uniaxial compression, uniaxial tension, simple shear and cyclic compression.

Table 6.1. Visco-hyperelastic model parameters for dough for the extrusion simulation.

Material	**Strain dependent constants**			**Time dependent constants**						
				i	1	2	3	4	5	∞
	μ (kPa)	λ_m	a	ξ_i (s)	0.1	1	10	100	1000	
Dough	5	6	0.1	g_i	0.85	0.05	0.04	0.03	0.02	0.01

The calibration results are shown in Figure 6.12. The model agrees reasonably well with the compression test data at different rates. However, the model fit to the uniaxial tension and simple shear overestimate the response at strains larger than 0.6 and 0.5 respectively. The model prediction does not capture the unloading-reloading response of the cyclic-compression loading. This is probably due to the viscoplastic behaviour of starch, which contributes to the behaviour of dough, as discussed in Section 5.3.3. However, the viscoplastic material model cannot be combined with the visco-hyperelastic model in Abaqus [Abaqus 2009; 2010]. Alternatively, a viscoplastic model can be used to model dough. Unfortunately, the viscoplastic model alone cannot capture the strain hardening behaviour under tension, which is caused by the rubberlike behaviour of gluten. Therefore the visco-hyperelastic model was used instead.

Before simulations of dough extrusion are performed, the dough experimental stress-strain data from this work (Figure 6.12) are compared to the experimental results

obtained by Wanigasooriya [2006] and Lim [2007]. This is conducted to ensure that the wheat flour used by Wanigasooriya [2006] and Lim [2007] in their extrusion tests has approximately the same mechanical behaviour as the wheat flour used in this work. The comparison to the experimental results by Wanigasooriya [2006] is shown in Figure 6.13. Approximately similar stress-strain curves are observed from uniaxial tension and uniaxial compression results, except for the tension test at 5/min. Note that shear rheometry and cyclic-compression tests were not performed by Wanigasooriya [2006] and Lim [2007].

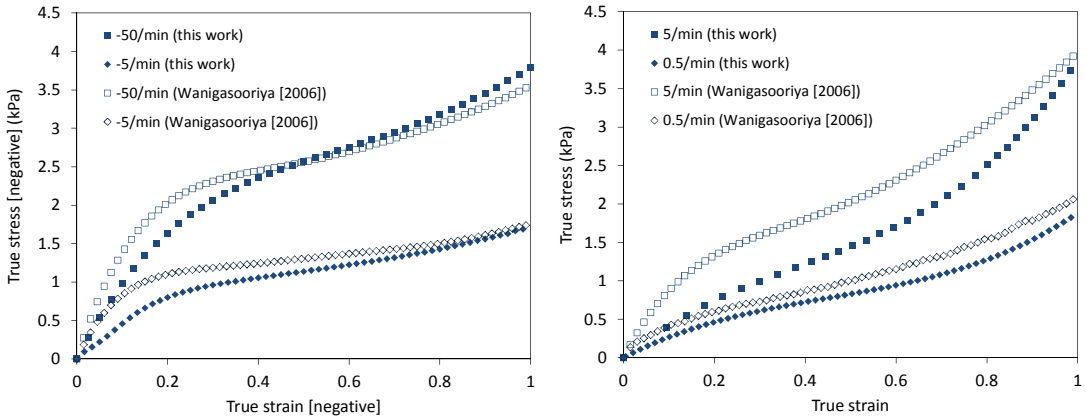

(a) (b)

Figure 6.13. Comparison between dough stress-strain data performed in this work and by Wanigasooriya [2006] for: (a) uniaxial compression; and (b) uniaxial tension.

Lim [2007] on the other hand performed only uniaxial compression tests at different strain rates (see Figure 6.14). Therefore, a direct comparison between the test results by Lim [2007] and those from this work cannot be made. However, the test data by Lim [2007] can be compared to the output of the calibrated material model using the parameters in Table 6.1. This is shown in Figure 6.14, where the rate dependent stress-strain curve in the model shows a correct pattern to the experimental data at different rates. Therefore, it was deemed appropriate to use the material parameters in

Table 6.1 to model extrusion and then compare numerical prediction to the extrusion experimental results by Wanigasooriya [2006] and Lim [2007]. This would avoid the need to perform new extrusion tests which would not be possible within the time scale of this work.

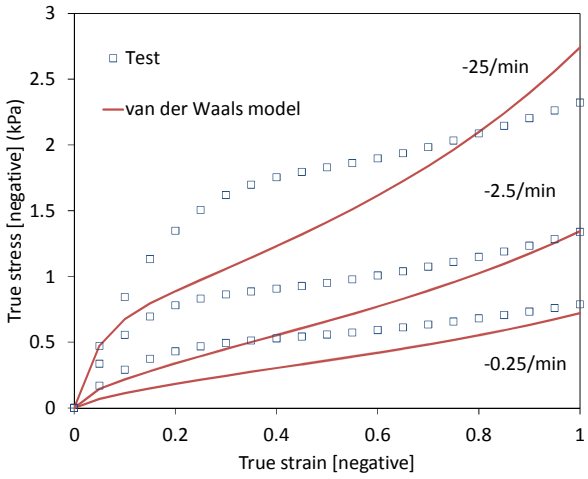

Figure 6.14. Comparison between output of calibrated visco-hyperelastic model and test results by Lim [2007] under uniaxial compression (material model parameters as in Table 6.1).

A finite element simulation of extrusion was performed in Abaqus/Explicit using axisymmetric elements. A schematic of the model is shown in Figure 6.15. The billet represents dough being forced through the barrel with dies at different angles and exit radii shown in Figure 6.2. The material model is assigned to the billet and the boundary conditions used in the model are as shown in Figure 6.15.

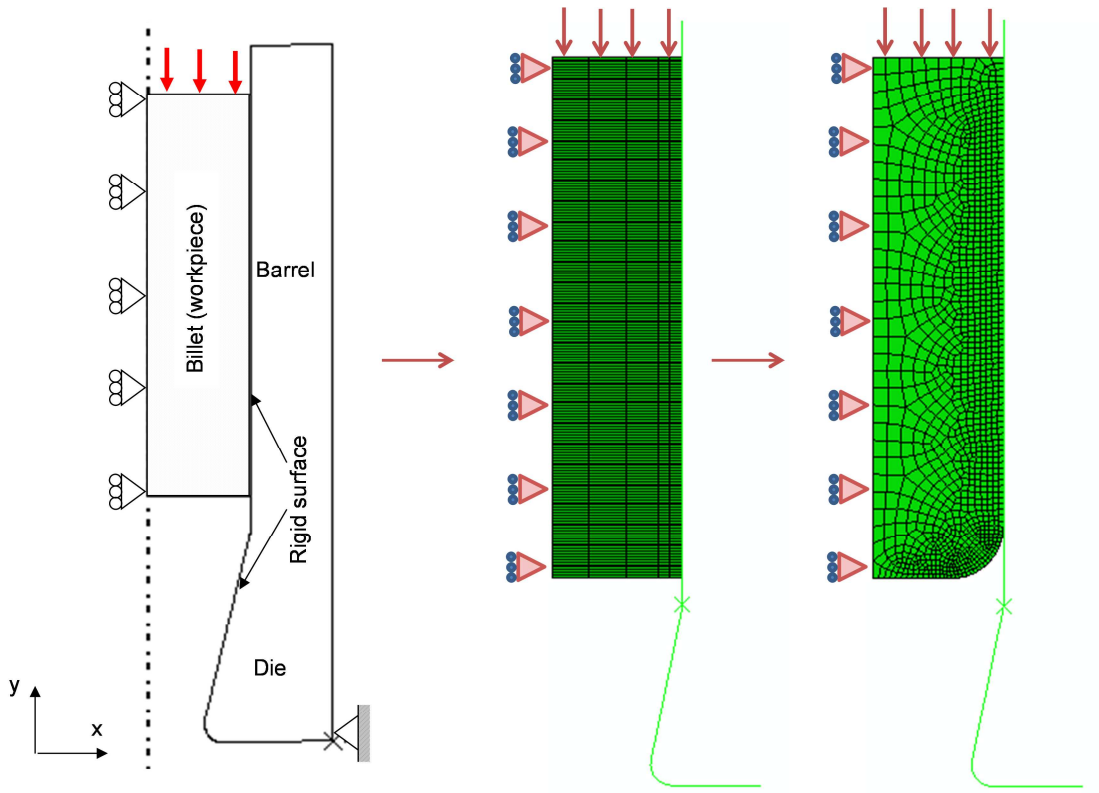

(a) (b) (c)

Figure 6.15. (a) Schematic of dough extrusion simulation and the type of mesh used: (b) structured mesh [Wanigasooriya 2006]; and (c) modified mesh used in this work.

It is worth noting that Wanigasooriya [2006] and Tow [2009] highlighted the issue of severe mesh distortion when the mesh in Figure 6.15(b) was used. This can be seen in the simulation results performed by Wanigasooriya [2007] and Tow [2009] in Figure 6.16, where the elements penetrate the corner near the entry to the die land, and the mesh boundary is no longer closely following the profile of the die. This unrealistic severe mesh distortion worsens as the analysis proceeds until a point is reached where the analysis prematurely terminates.

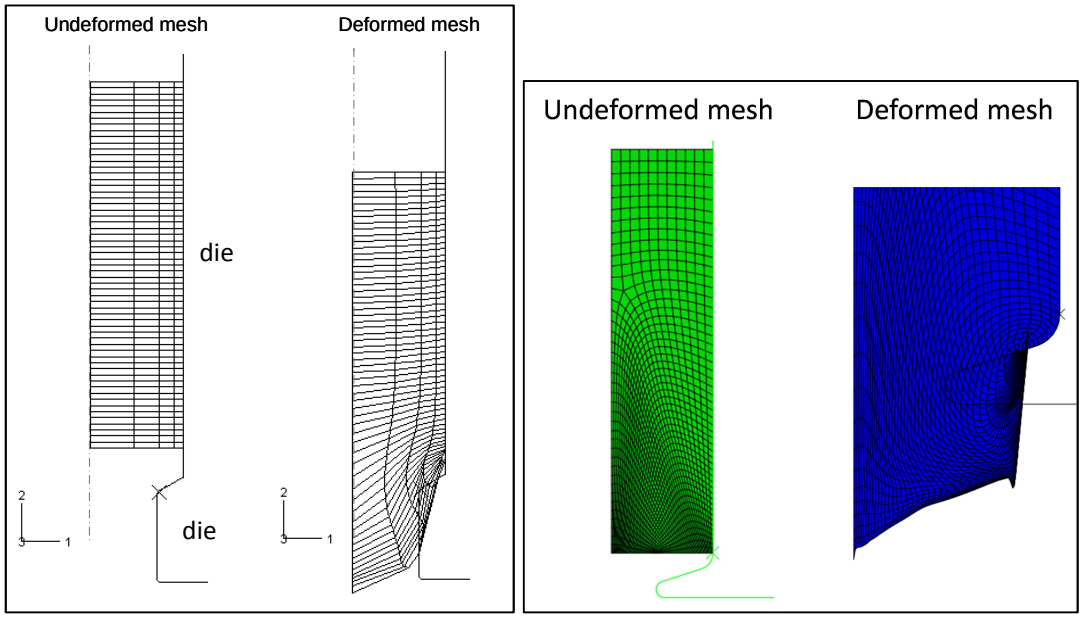

(a) (b)

Figure 6.16. Severe mesh distortion of the deformed mesh by (a) Wanigasooriya [2006]; and (b) Tow [2009].

Therefore, an improved extrusion model is proposed in this work, which consists of two parts. In the first part, a modified mesh is introduced, as shown in Figure 6.15(c). The mesh is refined at the die wall and the sharp end of the billet next to the die wall is smoothed to reduce the mesh distortion problem shown in Figure 6.16. The second part involves using the adaptive meshing option available in Abaqus [2009; 2010]. The adaptive meshing enables a high-quality mesh throughout the analysis, even when large deformations occur, by allowing the mesh to move independently with the material. This is possible due to the fact that the adaptive meshing combines the features of pure Lagrangian analysis (in which the mesh follows the material) and Eulerian analysis (in which the mesh is fixed spatially and the material flows through the mesh) [Abaqus 2009; 2010]. This type of adaptive meshing is often referred to as Arbitrary Lagrangian-Eulerian (ALE).

To investigate the effect of ALE on the extrusion model, a simulation was performed using a die with a 44^0 entry angle (see Figure 6.2). The material model in Table 6.1 and a frictionless contact between the billet and die wall were defined for the simulation. The following parameters are required to use the ALE option in Abaqus: frequency and remeshing sweep per increment. A default value of frequency = 10 and remeshing sweep per increment = 1 suggested for Abaqus/Explicit [Abaqus 2009; 2010] is used in this work. The results are shown in Figure 6.17. It can be seen that mesh distortion occurs at a 4.93 simulation time when the ALE meshing is not activated (Figure 6.17(a)). This then causes the simulation to terminate prematurely (Figure 6.17(c)). In contrast, smooth meshes are observed for the simulation with the ALE meshing (Figure 6.17(b)). The comparison results obtained with ALE and without ALE are shown in Figure 6.17(c).

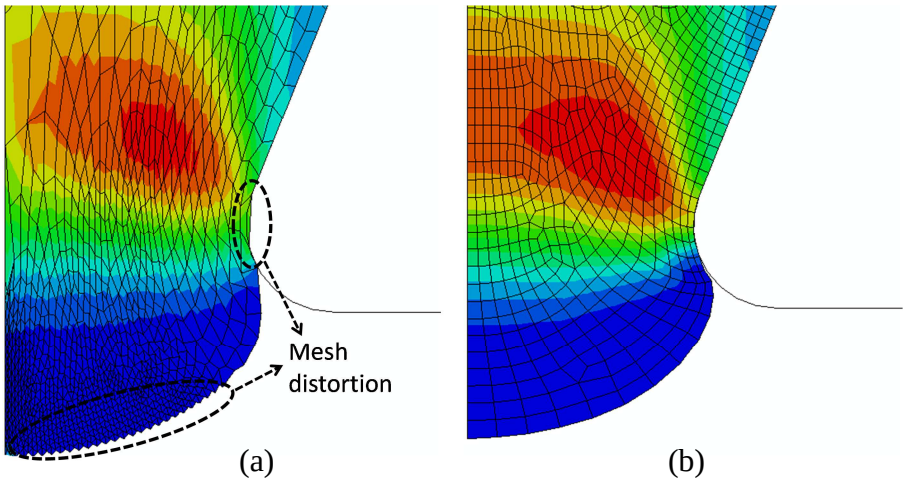

(a) (b)

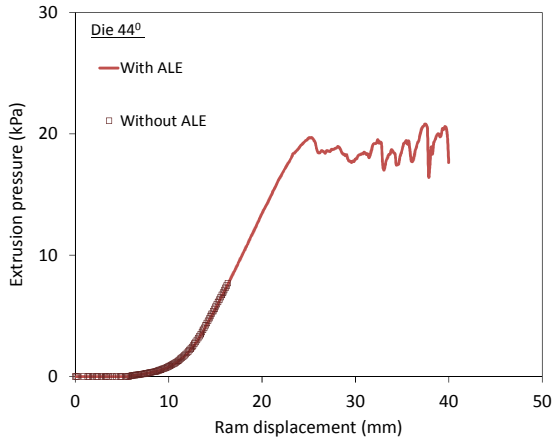

(c)

Figure 6.17. Comparison of simulation of die 44^0 (speed 500 mm/min) at 4.93 seconds for: (a) without ALE activated; and (b) with ALE activated. Note that the simulation terminated at 4.93 seconds for the model without ALE. (c) Comparison of results obtained with ALE and without ALE.

A mesh sensitivity study was performed by varying the number of elements in the extrusion model. The results are shown in Figure 6.18 for die 26^0a, 26^0b, 26^0c, 44^0, 72^0 and 108^0 at an extrusion speed of 500 mm/min. Note that the simulations for dies with higher entry angles (120^0 and 180^0) are not shown because the program aborted due to non-convergence problem before steady state results were reached.

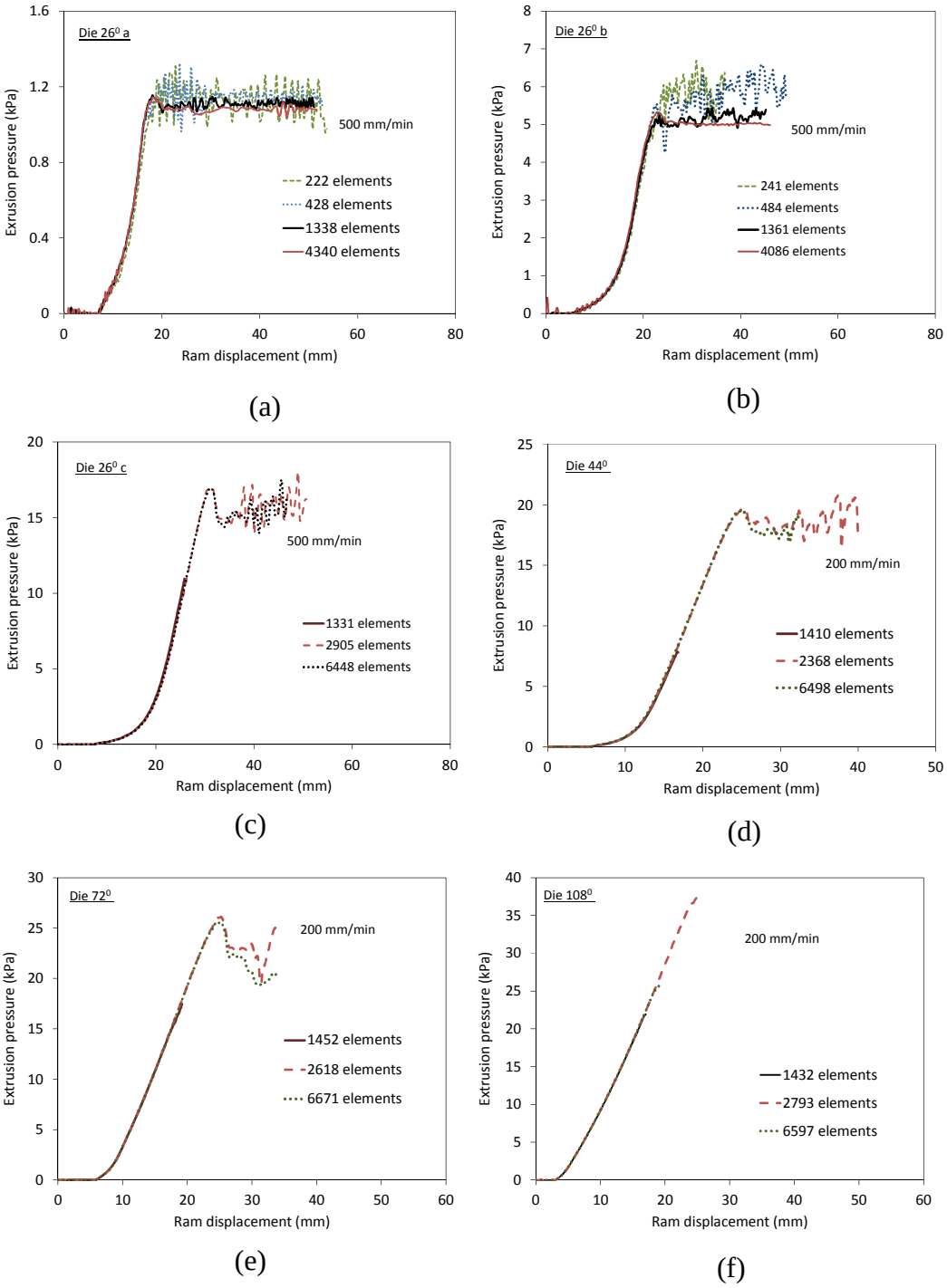

Figure 6.18. Mesh sensitivity simulation results using frictionless contact for different dies.

A frictionless contact between the billet and die wall was defined for the results in Figure 6.18. It can be seen that at least 1000-1500 elements are needed to perform the

extrusion simulation for dies 26^0a, 26^0b, and 26^0c, whereas at least 2000-3000 elements are needed for dies 44^0, 72^0, and 108^0, as shown in Figure 6.18. It is worth noting that as the die angle increases, it is more difficult to obtain steady state results. This can be seen from the results for die 108^0 in Figure 6.18(f), where the simulation was aborted before steady state was reached.

Images from the FE simulation using frictionless contact for dies 26^0a, 26^0b, 26^0c, 44^0, 72^0, and 108^0 are shown in Figures 6.19 to 6.22.

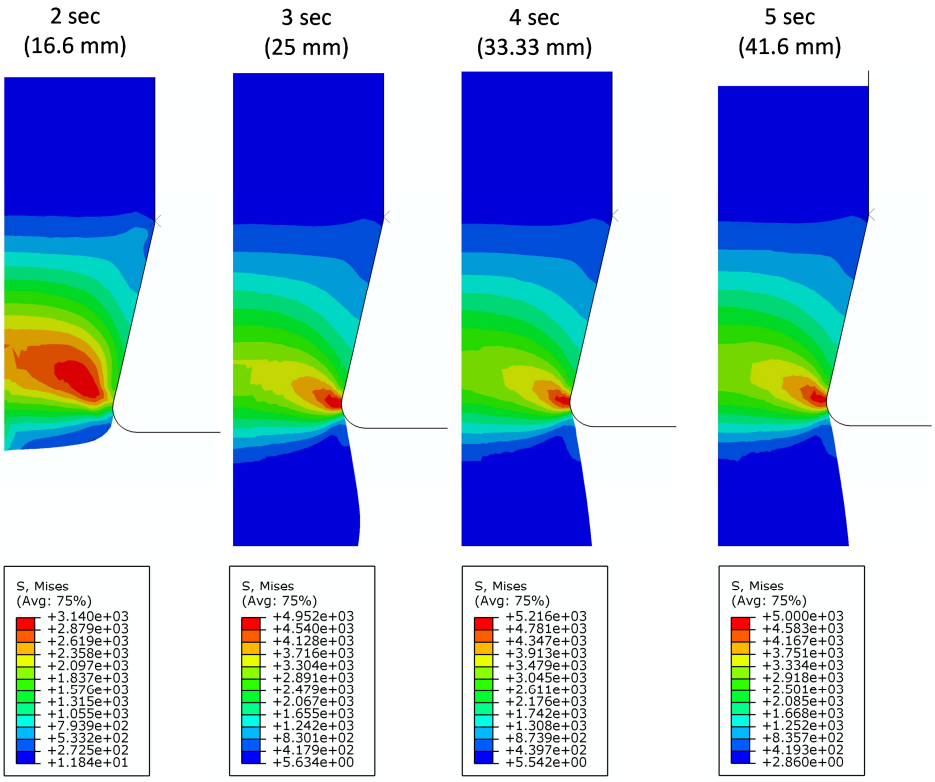

Figure 6.19. The von Mises contour plots for die 26^0a at 500 mm/min using frictionless contact. The scale shown is in Pascal (Pa).

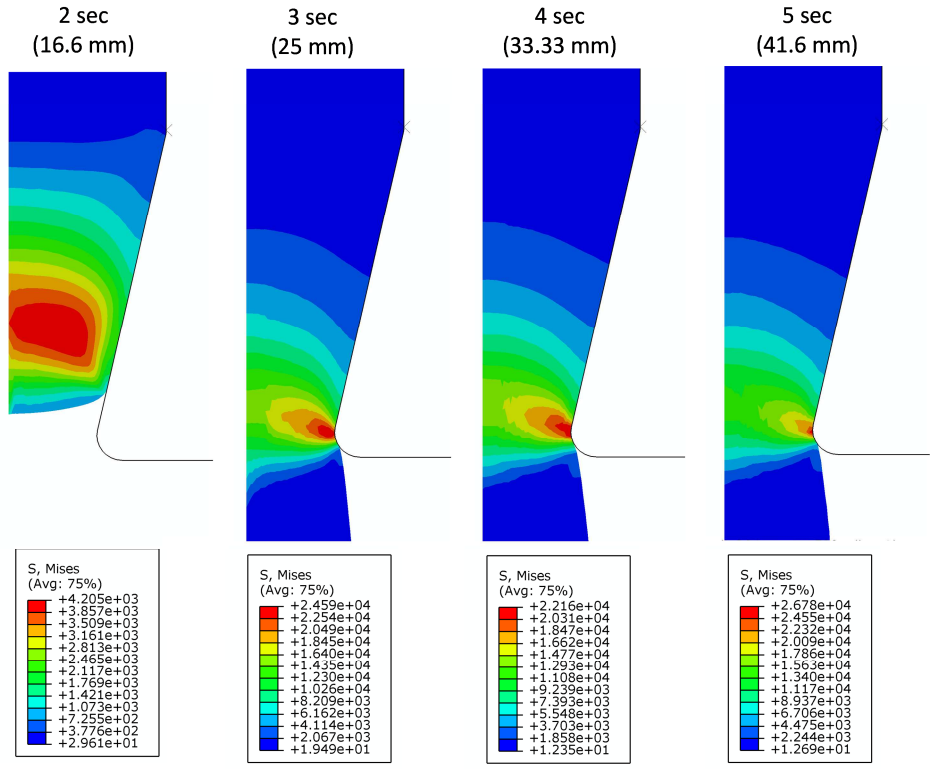

(a)

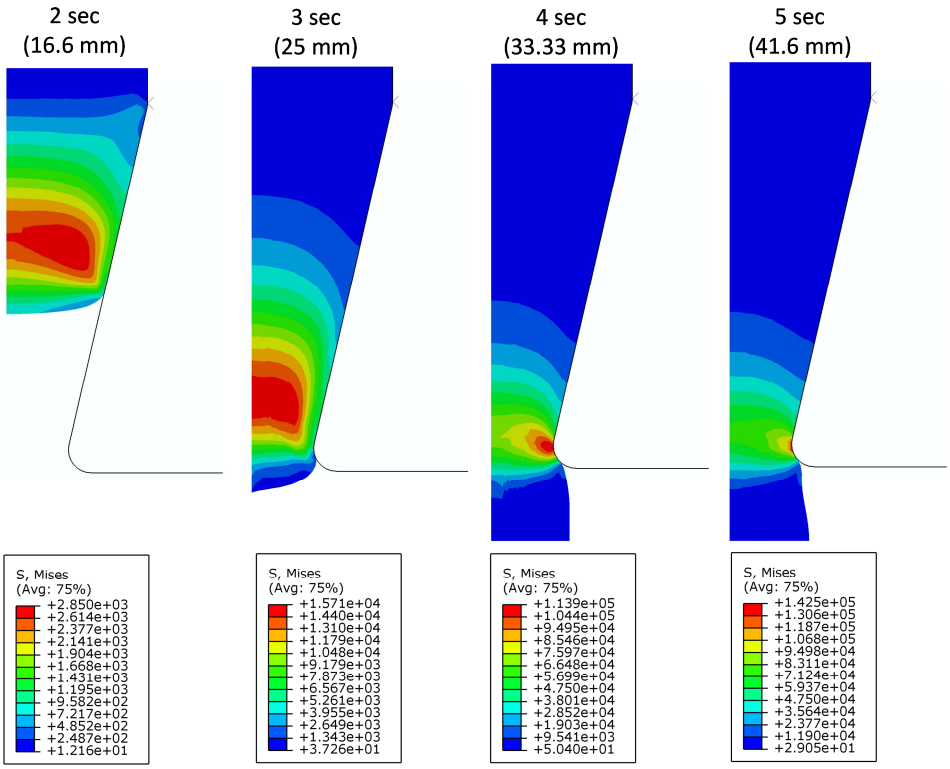

(b)

Figure 6.20. The von Mises contour plots for: (a) die 26^0b ; and (b) die 26^0c at 500 mm/min using frictionless contact. The scale shown is in Pascal (Pa).

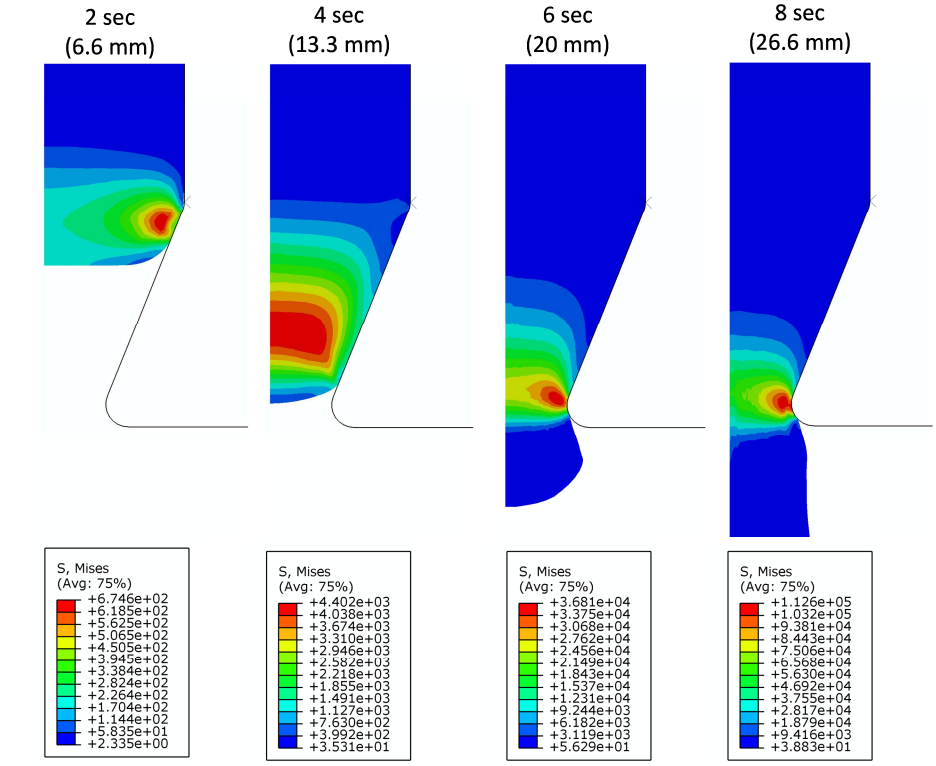

(a)

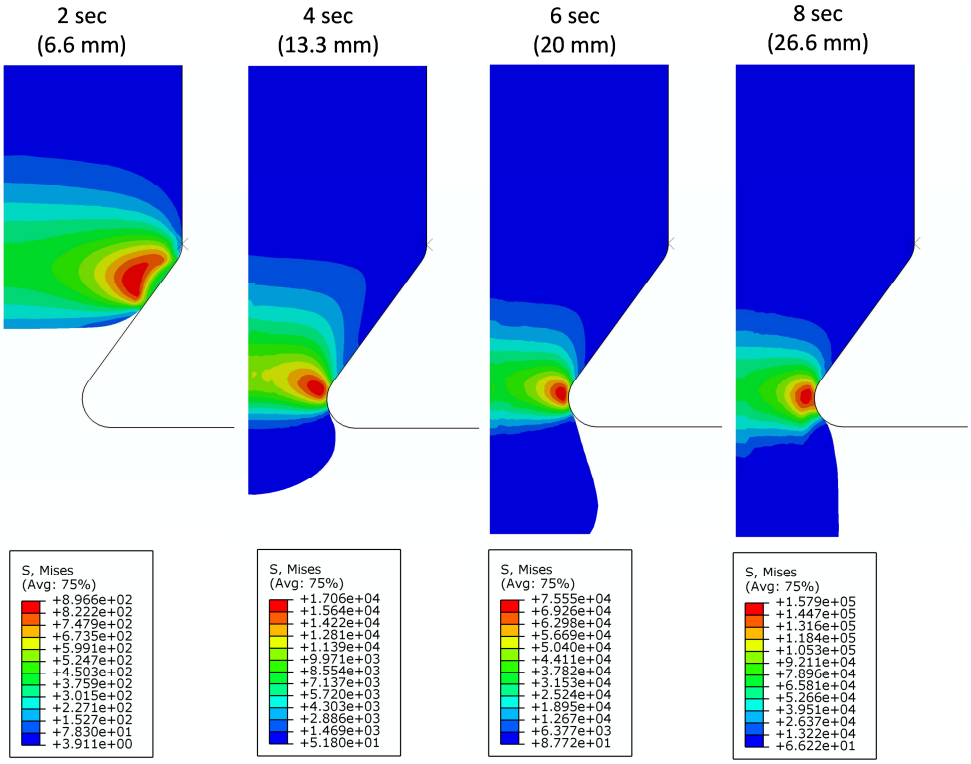

(b)

Figure 6.21. The von Mises contour plots for: (a) die 44^0 ; and (b) die 72^0 at 200 mm/min using frictionless contact. The scale shown is in Pascal (Pa).

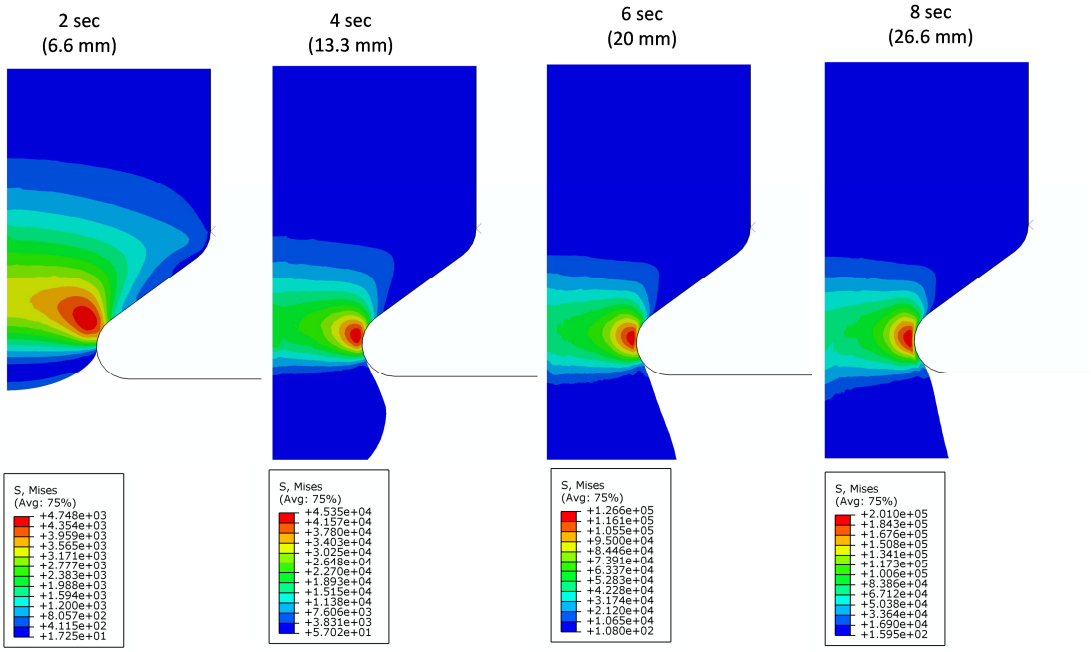

Figure 6.22. The von Mises contour plots for die 108^0 at 200 mm/min using frictionless contact. The scale shown is in Pascal (Pa).

The results in Figures 6.19 to 6.22 are shown as the von Mises stress contour plots. The von Mises stress is described as [Charalambides and Dean 1997]:

$$\sigma_{Mises} = \sqrt{\frac{1}{2}\left[(\sigma_1 - \sigma_2)^2 + (\sigma_2 - \sigma_3)^2 + (\sigma_3 - \sigma_1)^2\right]} \qquad (6.1)$$

where σ_1, σ_2, and σ_3 are the principal stresses. Notice that except for die 44^0, the von Mises contour plots show an increase in extrusion pressure when the entry angle is increased. The reason why the von Mises stress for die 44^0 is smaller than die 26^0c is because the test were performed at different speed (die 26^0c at 500 mm/min and die 44^0 at 200 mm/min).

The model fit to the extrusion test data at different rates using the frictionless condition is shown in Figure 6.23. It is observed that the model fit underestimates the extrusion test data for die 26^0a, 44^0, 72^0, and 108^0.

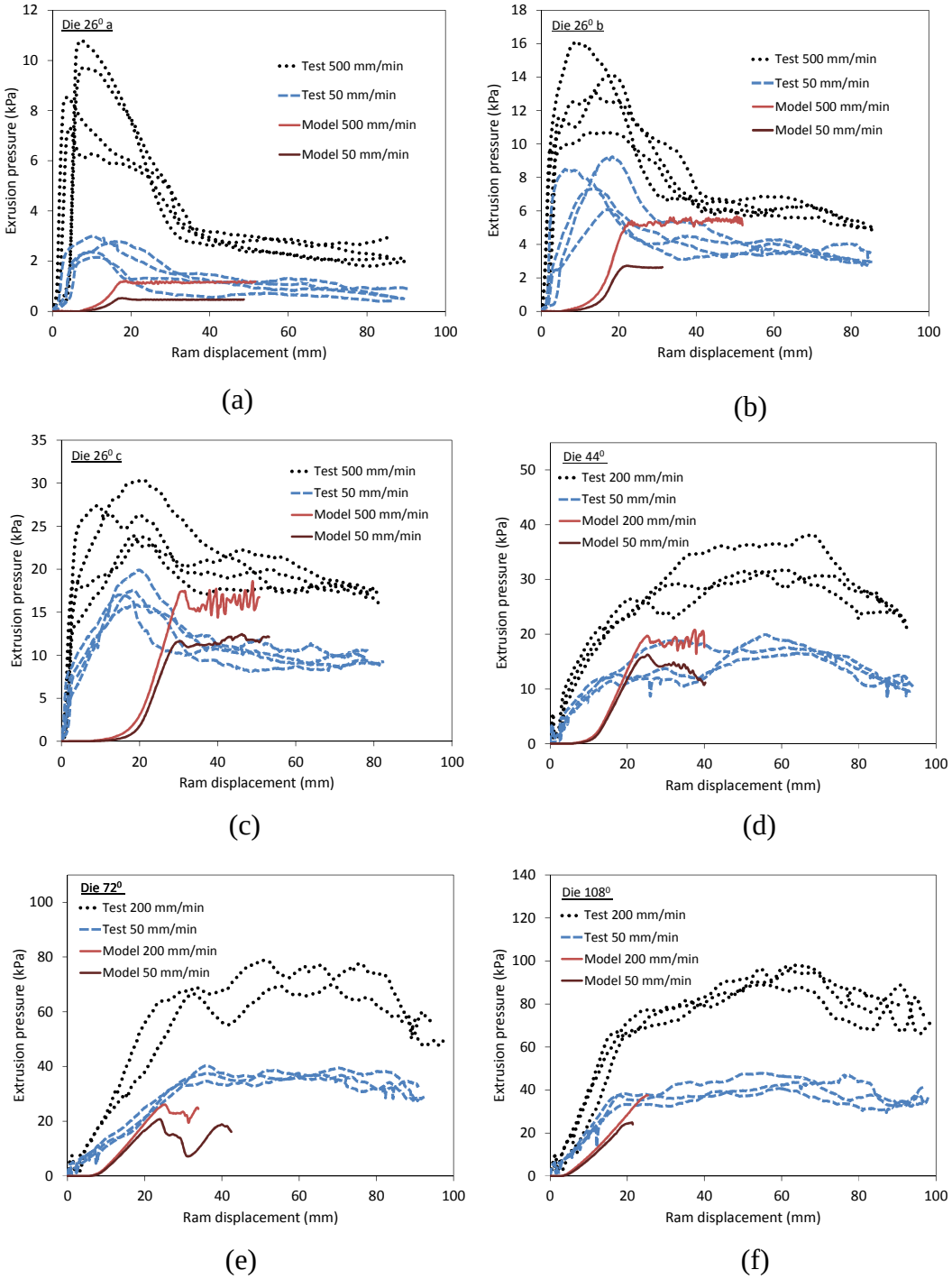

Figure 6.23. Comparison between experimental data and extrusion model using frictionless conditions at different rates.

The model fit can be improved by including a non-zero coefficient of friction between the die wall and the billet surface. This is performed using a Coulomb friction law available in Abaqus [2009; 2010]. An independent measurement of the friction during extrusion was obtained by Wanigasooriya [2006] by placing a known mass of dough on to one half of the lubricated (paraffin oil) extrusion unit. The extrusion unit was then attached onto a combination reversing protractor (see Figure 6.24(a)). The kinetic coefficient of friction was determined by allowing the dough sample to slide and subsequently altering the angle until no sliding occurred. The value of μ was calculated from $\mu = \tan\theta$, where θ is the angle at which the dough sample stopped sliding, as shown in Figure 6.24(b). Several dough samples of mass varying from 3 to 30 grams were used for the experiment, giving an average resting angle of ~5º and a coefficient of friction of $\mu = 0.09$.

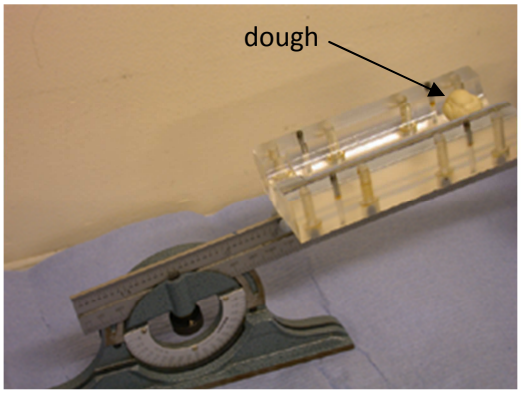

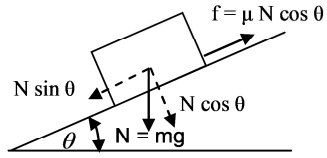

For sliding: $N\sin\theta = \mu N\cos\theta \Rightarrow \mu = \tan\theta$

(a) (b)

Figure 6.24. Experimental measurements of the kinetic coefficient of friction [Wanigasooriya 2006]: (a) experimental rig; and (b) free body diagram of friction on an inclined plane.

The comparison between the model and the extrusion test data at different rates corresponding to a coefficient of friction of $\mu = 0.09$ is shown in Figure 6.25.

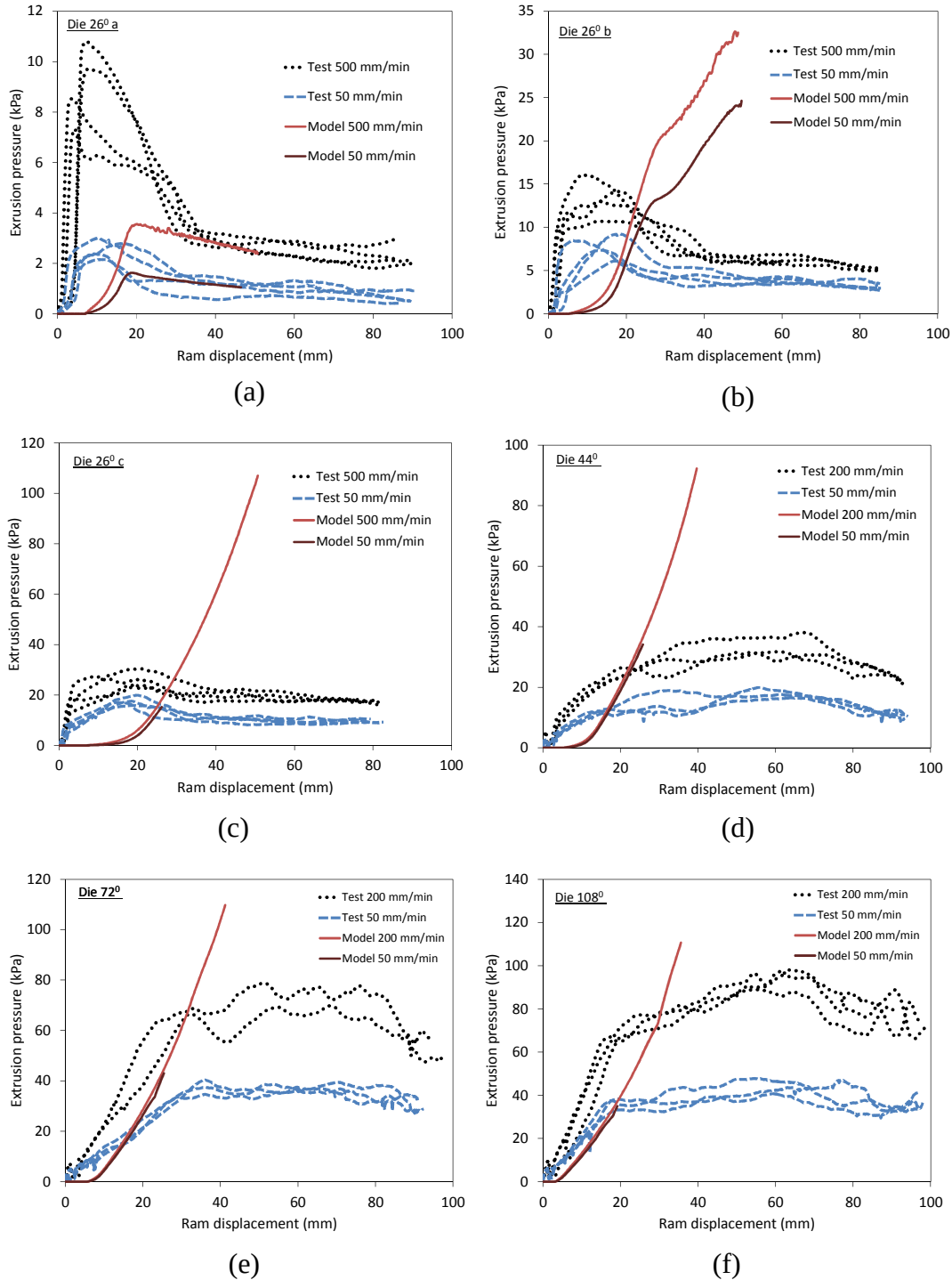

Figure 6.25. Extrusion model using coefficient of friction, $\mu = 0.09$.

It is observed that except for die 26^0a, the model fit extremely overestimates the response for all other dies. This is believed to be caused by slippage between the die wall and the billet surface during the experiments. Hicks and See [2010] studied

capillary extrusion of dough and highlighted the phemonenon of wall shear slip when dough is extruded. Since the working concept of capillary extrusion is similar to ram extrusion, the slippage between the die wall and billet is believed to occur in ram extrusion of dough.

To model the shear slip between the die wall and the billet surface, an improved contact interaction is proposed, which consists of a critical shear stress limit combined with the coefficient of friction obtained before. This function is available in Abaqus [Abaqus 2009; 2010], as shown in Figure 6.26. A critical shear stress limit, τ_{max}, is defined which allows a shear slip behaviour to be modelled at a specified value of coefficient of friction.

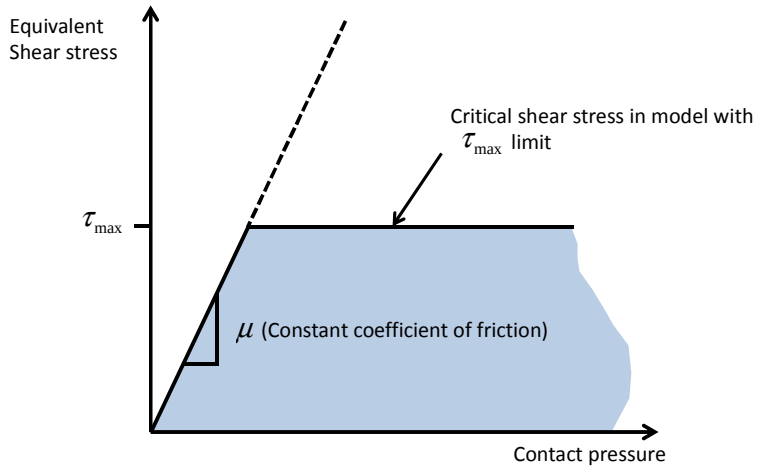

Figure 6.26. Slip regions for the friction model with a limit on the critical shear stress (reproduced from Abaqus [2010]). The critical shear stress, τ_{crit} is shown as the dotted line.

The critical shear stress limit in Figure 6.26 is described as follows. The Coulomb friction model relates the maximum allowable shear (frictional) stress across an

interface to the contact pressure between the contacting bodies. The contacting surfaces can carry shear stresses up to a certain magnitude across their interface before relative tangential motion can begin, which is also known as sliding. The Coulomb friction model defines this critical shear stress, τ_{crit}, at which sliding of the surfaces starts as functions of the contact pressure, p and coefficient of friction, μ:

$$\tau_{crit} = \mu p \tag{6.2}$$

The critical shear stress, τ_{crit} is shown as the dotted line in Figure 6.26. The critical shear stress limit, $\tau_{\max}$ is then introduced to limit the critical shear stress if the magnitude of the equivalent shear stress reaches $\tau_{\max}$, as shown in Figure 6.26.

The model fit to the extrusion test data using the coefficient of friction of $\mu = 0.09$ with different critical shear stress limit values are shown in Figure 6.27 at 500 mm/min and 200 mm/min. A similar comparison of the model to the test data at 50 mm/min is shown in Figure 6.28. The results for higher rate tests (500 mm/min and 200 mm/min) show that a higher die angle requires a higher $\tau_{\max}$ value. Dies with the same exit radius, i.e. dies with a 26^0 entry angle require a $\tau_{\max}$ value of 0.1-0.3 kPa, whereas die 44^0 requires 1 kPa, and dies 72^0 and 108^0 would require 3 kPa. On the other hand, the results for lower rate tests (50 mm/min) show that dies 26^0a, 26^0b, 26^0c, and 44^0 require a $\tau_{\max}$ value of 0.1-0.3 kPa, whereas dies 72^0 and 108^0 would require 1 kPa.

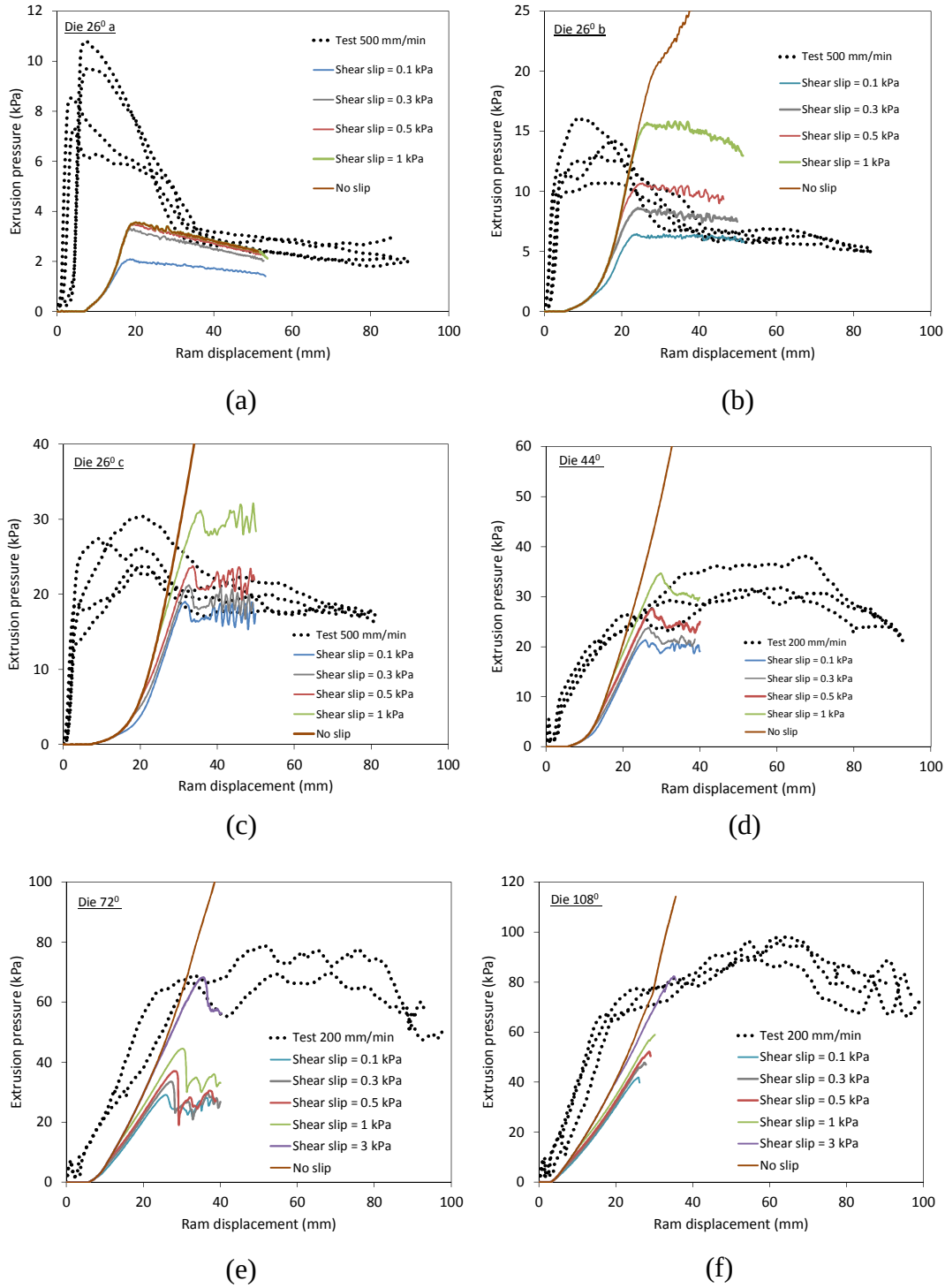

Figure 6.27. Extrusion model using coefficient of friction, $\mu = 0.09$ with different critical shear stress limit values at 500 mm/min and 200 mm/min.

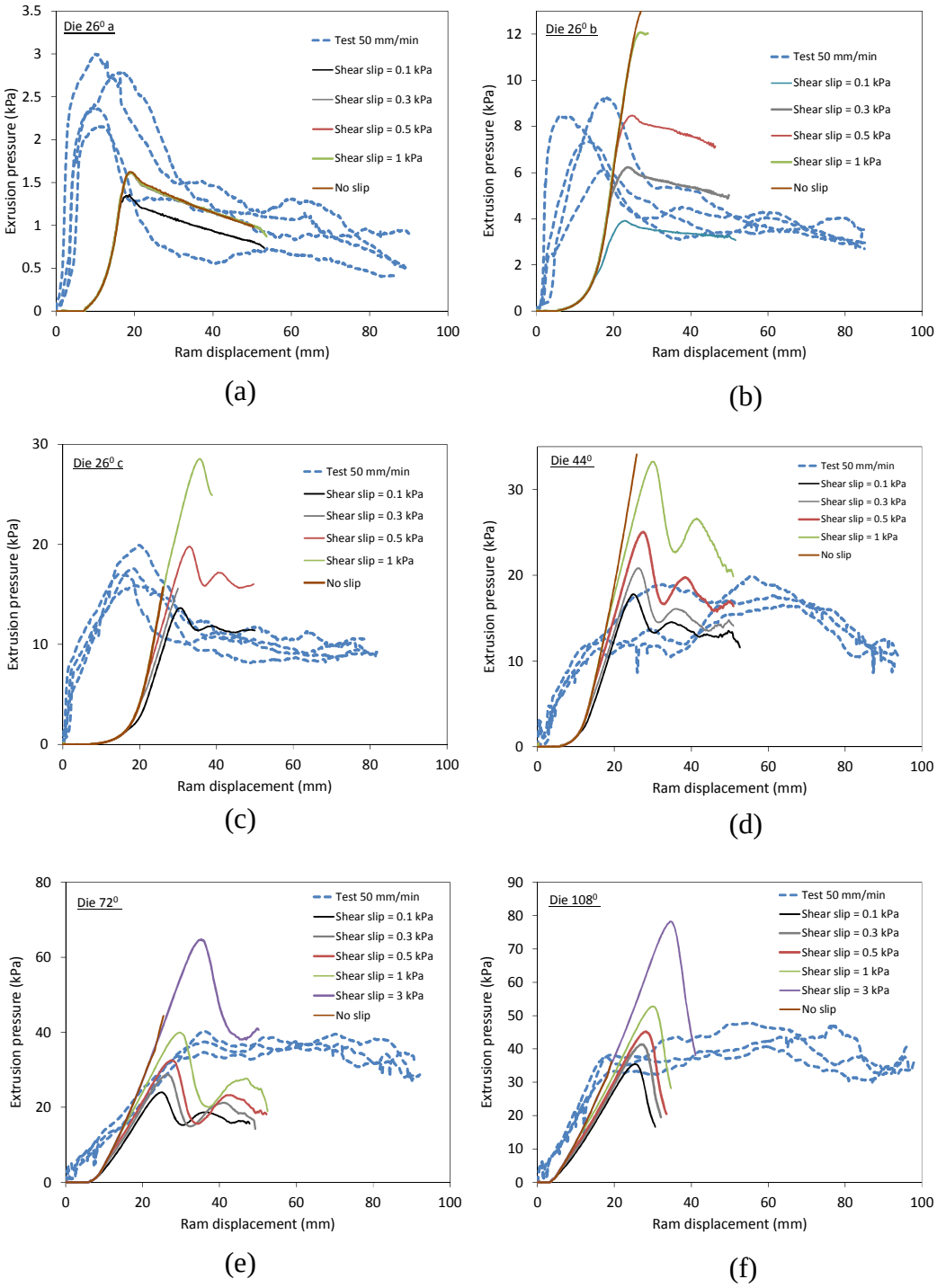

Figure 6.28. Extrusion model using coefficient of friction, $\mu = 0.09$ with different critical shear stress limit values at 50 mm/min.

It should be noted that pressure peaks are observed in the simulation results for dies 26^0c, 44^0, 72^0, and 108^0 in Figure 6.28. To investigate this, finite element images

(contour plots) at different simulation times (Figure 6.29(a)) are examined in Figure 6.29 for the die with 72^0 entry angle and a τ_{max} of 3 kPa (Figure 6.29(b)).

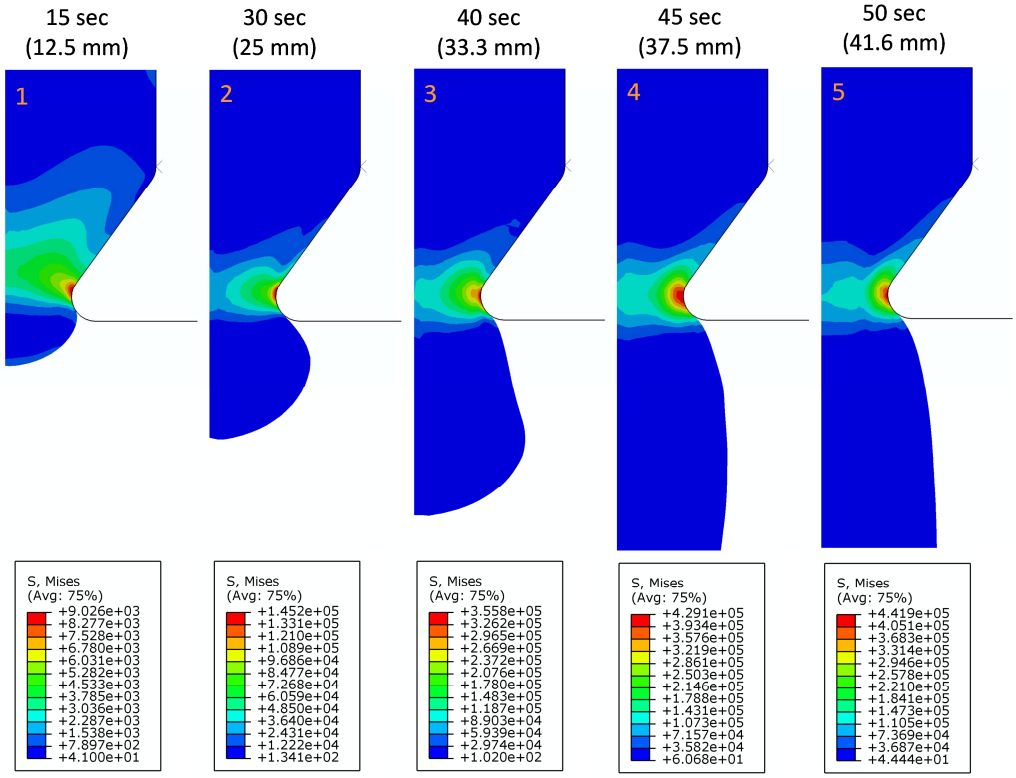

(a)

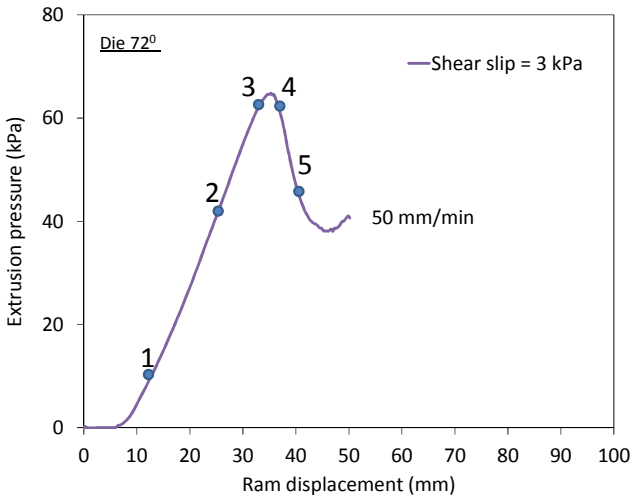

(b)

Figure 6.29. (a) The von Mises contour plots; and (b) extrusion pressure versus ram displacement. Both results are for die 72^0 with τ_{max} of 3 kPa. The scale shown is in Pascal (Pa).

It can be seen that the pressure peak starts at point 3 in Figure 6.29(b). When this is compared to point 3 in Figure 6.29(a), notice that a significant volume of material is forced through the die opening in a short time period of 5 seconds (from point 3 to 4). However, the experimental results in Figure 6.28(e) show no significant pressure peaks. The difference between experiment and model is confined to the initial transient response and does not affect the steady state results.

Finally, the maximum shear stress limit, τ_{max}, that fits the extrusion tests for different dies shown in Figures 6.27 and 6.28 was plotted against maximum principal strain rate. The maximum principal strain rate was obtained from the finite element simulation results for different dies. An example is shown in Figure 6.30 for die 26^0b extruded at 500 mm/min.

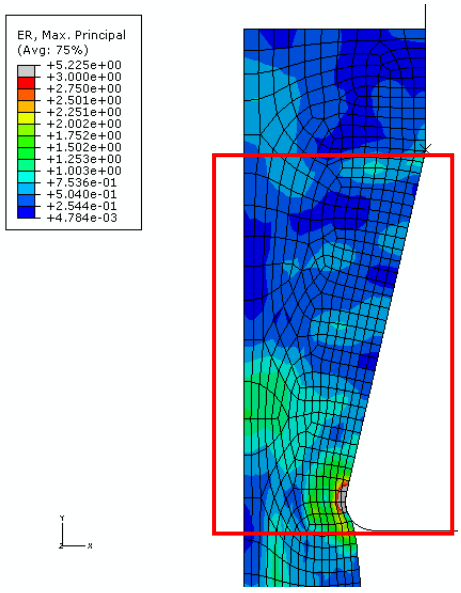

Figure 6.30. Contour plot of maximum principal strain rate for die 26^0b for simulation at 500 mm/min. The scale shown is in 1/s. The highlighted region is used to approximate the maximum principal strain rate.

The maximum principal strain rate in the highlighted region in Figure 6.30 was approximated from the percentage of colour in the contour plot corresponding to different strain rate, i.e. a value of 0.704/s is obtained from the sum of ~40 % of 0.504/s (blue in Figure 6.30), ~40 % of 0.7536/s (light blue) and ~20 % of 1.003/s (light green). A similar procedure was used for the other dies at different extrusion speed. The values are summarised in Table 6.2.

Table 6.2. The maximum shear stress limit, τ_{max}, and maximum principal strain rate for different dies.

Die	Extrusion rate (mm/min)	Maximum principal strain rate (1/s)	Analytical average strain rate (Equation 6.3) (1/s)	τ_{max} (kPa)
26^0a	50	0.063	0.048	0.3
26^0b	50	0.071	0.065	0.3
26^0c	50	0.136	0.083	0.1
44^0	50	0.198	0.145	0.3
72^0	50	0.237	0.261	1
108^0	50	0.664	0.494	1
44^0	200	0.741	0.580	1
72^0	200	0.804	1.043	3
108^0	200	1.920	1.974	3
26^0a	500	0.505	0.484	0.3
26^0b	500	0.704	0.649	0.1
26^0c	500	0.794	0.828	0.3

Wanigasooriya [2006] on the other hand suggested an average strain rate, $\bar{\dot{\varepsilon}}$, for the extrusion tests using the following analytical equation:

$$\bar{\dot{\varepsilon}} = \frac{6SD_b^2 \tan(\alpha)\ln(R)}{D_b^3 - D_a^3} \tag{6.3}$$

where S is the extrusion speed (mm/min), D_b and D_a are the entry and exit diameter of the die respectively and α is half of the entry angle. The remaining parameter, R is an extrusion ratio described through the following: $R = A_b / A_a$, where A_b is the cross-sectional area of the billet and A_a is the area of the extrudate at die exit. Details on the derivation of Equation (6.3) are provided in Wanigasooriya [2006]. The average strain rate calculated using Equation (6.3) for dies at different extrusion speed is shown in Table 6.2. The results show agreement with the maximum principal strain rate obtained from finite element results.

Finally, the results for $\tau_{\max}$ versus maximum principal strain rate are plotted in Figure 6.31(a). There is a large scatter in the data and no definite relationship can be concluded as a result. It is apparent that $\tau_{\max}$ increases with increasing maximum principal strain rate. $\tau_{\max}$ was also plotted against dies with different entry angles. The dies in Figure 6.31(b) are referred to as die 26^0a, 26^0b, 26^0c, 44^0, 72^0 and 108^0 for die 1 to 6 respectively. It can be seen that $\tau_{\max}$ increases with increasing die entry angle. It is apparent that more experiments would be needed to confirm these observations.

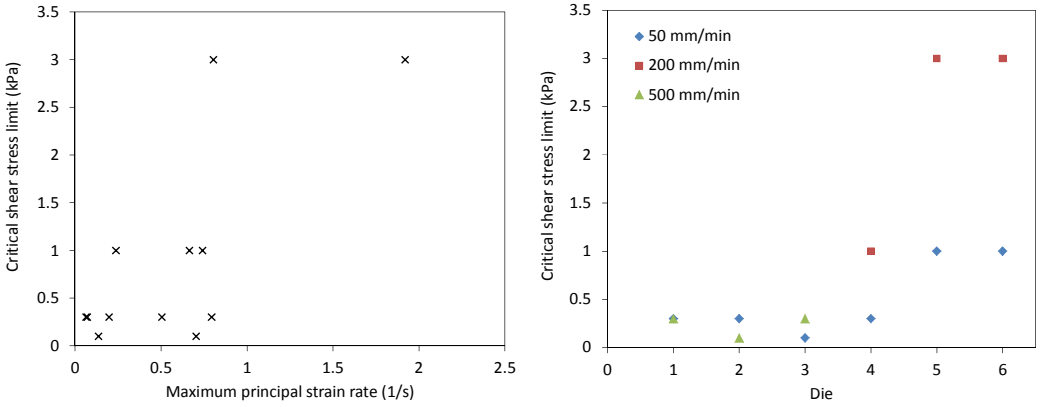

(a) (b)

Figure 6.31. (a) Critical shear stress limit versus maximum principal strain rate; and (b) critical shear stress limit versus die.

This section can be concluded as follows. The extrusion model proposed in this work has been shown to solve the mesh distortion problem highlighted by Wanigasooriya [2006] and Lim [2007]. This allows extrusion model of dough to be performed for dies 26^0a, 26^0b, 26^0c, 44^0, 72^0 and 108^0, as compared to only dies 26^0a, 26^0b and 26^0c by these researchers. However, the material model for dough needs to be improved in the future, i.e. by combining the visco-hyperelastic and viscoplastic material model. The model can then be used to simulate dough extrusion, where an accurate investigation can be performed on complex contact behaviour between the die wall and dough surface. A new experimental study for the dies shown in Figure 6.2 is also needed, since the experimental work by Wanigasooriya [2006] and Lim [2007] was performed using different flour than the one used in this thesis, as shown in Figures 6.13 and 6.14.

6.4 Conclusion

The experimental investigations on dough extrusion performed by Wanigasooriya [2006] and Lim [2007] were reviewed and discussed. Experiments with dies of different entry angles and exit radii were conducted. Numerical simulations of the extrusion were performed using Abaqus [2009]. Simulations were performed using dies with entry angles of 26^0, 44^0, 72^0 and 108^0. Previous simulations performed by Wanigasooriya [2006], Lim [2007] and Tow [2009] showed that large mesh distortion occurred when die entry angle was increased. Therefore, an improved extrusion model is proposed, which consists of a modified mesh and adaptive meshing option available in Abaqus [2009; 2010].

Simulations performed using a frictionless contact between the billet and die wall showed that the model underestimates the response at high entry angles. Therefore a frictional contact between the die wall and the billet surface was defined, where the kinetic coefficient of friction, μ of 0.09 was obtained from the experimental study by Wanigasooriya [2007]. When this value of μ was used in the model, the response was overestimated, i.e. the extrusion pressure was much higher than the experimentally measured values. To improve this, a critical shear stress limit, $\tau_{\max}$ was used in the model. The results show that higher die angles require higher $\tau_{\max}$ values. In addition, the results also show that $\tau_{\max}$ increases with increasing maximum principal strain rate, which suggest strain rate sensitivity of $\tau_{\max}$. This indicates complex contact behaviour between die wall and dough, which need to be investigated further in the future.

Chapter 7. Conclusion and Future Work

7.1 Introduction

This chapter provides a summary and suggested future work for the experimental and numerical work on wheat flour dough performed in this thesis. First, the experimental work in Chapter 4 is summarised and future experimental work is proposed. This is followed by the constitutive modelling of dough, where some possible future work on the model is discussed. Finally, the processing study is summarised and future work on the extrusion of dough is proposed.

7.2 Experimental Work

Experimental investigation was performed on dough, starch and gluten. The sample preparation involved mixing flour, water and salt to produce dough. The mixed dough was washed using water to separate the starch and gluten constituents. Dough, wet gluten and reconstituted wet starch were used for uniaxial tension, uniaxial compression, shear rheometry and Cryo-SEM tests. The experimental results showed that rate-dependent behaviour is observed from all the samples tested in uniaxial compression, uniaxial tension and shear tests. Cryo-SEM images show that starch is embedded in gluten matrix. The starch consists of large ellipsoidal-shaped and small circular-shaped fillers. No trace of starch was observed on the gluten matrix based on the Cryo-SEM images of washed gluten. A comparison of the test results showed that dough is stiffer than gluten in the Small Amplitude Oscillatory Shear (SAOS) tests. However, at large deformation tests, namely uniaxial tension and simple shear, the dough stress-strain curves cross over gluten curve at larger deformations. On the other hand, uniaxial compression test results showed that the stress-strain curve of

dough is always higher than gluten, indicating that possibly damage is not as significant under compression. This is supported by the Cryo-SEM observation of dough when compressed manually, where damage in terms of debonding is not apparent.

Future experimental work includes investigation on the cohesive behaviour of starch and gluten interface. This can be performed using Atomic Force Microscopy (AFM) or cohesive peel tests [Dobraszczyk 1997]. The cohesive properties obtained from the experiments, i.e. fracture energy values, can then be used for the micromechanical modelling of dough. Another very useful piece of experimental observation could be obtained through mechanical loading tests performed in-situ inside Environmental Scanning Electron Microscopy (E-SEM) [Donald 2003] to investigate the effect of microstructure of dough subjected to deformation under compression, tension and shear. This will provide information on the critical damage initiation stresses of the starch-gluten interface under different modes of deformation stated before.

7.3 Constitutive Modelling of Wheat Flour Dough

A micromechanics model for dough is proposed in Chapter 5. A starch volume fraction of 45 % was measured experimentally from Cryo-SEM images. A single-particle model was developed consisting of a single 2D cylindrical filler representing starch surrounded by gluten matrix. The interaction between the starch and gluten was defined using cohesive elements. The simple composite model agrees with the trends shown by the experimental data, indicating possible debonding of starch and gluten in dough under tension and shear. This argument was supported further by Cryo-SEM images of stretched dough as well as the apparent need for damage

functions when the Lodge constitutive model was used to represent the mechanical test data of dough. Good agreement is seen between single-particle and multi-particle models, as well as with 3D single-particle models with spherical and cylindrical geometries, indicating that the 2D single-particle model can be used to accurately represent the microstructure of dough.

Future constitutive modelling work on dough includes improvement of the micromechanics modelling by using a rate-dependent cohesive law for the gluten-starch interface. This has been performed numerically by Geiβler and Kaliske [2010] for polymeric materials. On the other hand, finite element modelling can be performed in 3D geometries using large ellipsolidal type A starch and smaller circular type B starch. Air bubbles in dough can then be included in the 3D model, since Chin and Campbell [2005] believe that air bubbles influence the mechanical behaviour of dough.

7.4 Processing Study of Wheat Flour Dough

The experimental work on dough extrusion performed by Wanigasooriya [2006] and Lim [2007] was summarised. Dies with different angles were used for the extrusion experiments. The entry radius is set to be the same for all the dies tested. The dies are arranged in rows from the smallest entry angle, 26^0 to the largest, 180^0. The exit radius is varied from the widest, 18 mm to the smallest, 3 mm. Rate dependent extrusion behaviour is observed. A numerical simulation of dough extrusion was performed using finite element (FE) software, Abaqus [Abaqus 2009]. An improved extrusion model is proposed, which consists of a modified mesh and an adaptive meshing option available in Abaqus [2009; 2010]. Simulations performed using a

frictionless contact between the billet and die wall showed that the model underestimates the tests result at high entry angle. The coefficient of friction, $\mu = 0.09$ between the billet and die wall was later used in the model to improve the prediction. However, the model was shown to overestimate the test data. To improve this, a critical shear stress limit combined with the coefficient of friction was used in the model. The results show that higher die angles require a higher critical shear stress limit values.

To improve the extrusion model of dough, a continuum material model which combines the viscoelastic and viscoplastic functions [Andriyana *et al.* 2010] is proposed. The model aim is to resemble the complex micromechanics model shown in Chapter 5. This model can then be used to investigate the complex contact behaviour of dough between the die wall and billet.

7.5 Final Words

It is hoped that this thesis will highlight the importance of studying food texture using solid mechanics approach. The complex mechanical behaviour of food materials, in particular dough shown in this thesis indicates that food cannot be treated as a simple material. Investigation on the food texture may assist food technologists and engineers to improve the quality of the food production line and reduce food wastage during processing.

References

AACC. 1976. Method 38-10. Gluten-Handwashing Method. In: Approved Methods of the American Association of Cereal Chemists, Vol. 1, seventh ed. AACC Inc. Minnesota, USA.

Abang Zaidel D. N., Chin N. L., Abdul-Rahman R. and Karim R. 2008. Rheological Characterisation of Gluten From Extensibility Measurement. Journal of Food Engineering, 86: 549-556.

Abaqus's User Manual ver. 6.8. 2009. Hibbitt Karlsson and Sorensen, Providence, USA.

Abaqus's User Manual ver. 6.9. 2010. Hibbitt Karlsson and Sorensen, Providence, USA.

Amemiya J. I. and Menjivar J. A. 1992. Comparison of Small and Large Deformation Measurements to Characterize the Rheology of Wheat Flour Doughs. Journal of Food Engineering, 16: 91-108.

Andriyana. A., Billon N. and Silva L. 2010. Mechanical Response of a Short Fiber-Reinforced Thermoplastic: Experimental Investigation and Continuum Mechanical Modeling. European Journal of Mechanics-A/Solids, 29(6): 1065-1077.

Aydin I., Biglari F. R., Briscoe B. J., Lawrence C. J. and Adams M. J. 2000. Physical and Numerical Modelling of Ram Extrusion of Paste Materials: Conical Die Entry Case. Computational Materials Science, 18: 141-155.

Barnes H. A. and Bell D. 2003. Controlled-Stress Rotational Rheometer: an Historical Review. Korea-Australia Rheology Journal, 15: 187-196.

BBC. 2010. www.bbc.co.uk/history/ancient/romans/daily_life_gallery_02.shtml. Accessed on 1 September 2010.

Benbow J. and Bridgwater J. 1993. Paste Flow and Extrusion. Clarendon Press, Oxford, UK.

Bergström J. S. and Boyce M. C. 1998. Constitutive Modelling of the Large Strain Time-Dependent Behavior of Elastomers. Journal of Mechanics and Physics of Solids, 46: 931-954.

Bergström J. S. and Boyce M. C. 2001. Constitutive Modelling of Time-Dependent and Cyclic Loading of Elastomers and Application to Soft Biological Tissues. Mechanics of Materials, 33: 523-530.

Blancher G., Morel M. H., Gastaldi E. and Cuq B. 2005. Determination of Surface Tension Properties of Wheat Endosperms, Wheat Flours and Wheat Glutens. Cereal Chemistry, 82(2): 158-165.

Bohm H. J. 2011. A Short Introduction to Basic Aspects of Continuum Mechanics. ILSB Report, Vienna University of Technology, Austria.

British Museum. 2010. www.britishmuseum.org. Accessed on 1 September 2010.

Camanho P. P. and Davila C. G. 2002. Mixed-Mode Decohesion Finite Elements for the Simulation of Delamination in Composite Materials. NASA/TM-2002-211737: 1-37.

Charalambides M. N. and Dean G. D. 1997. Constitutive Models and Their Data Requirements for Use in Finite Element Analysis of Adhesives under Impact Loading. NPL Report CMMT(A) 59.

Charalambides M. N., Wanigasooriya L., Williams J. G. and Chakrabarti S. 2002a. Biaxial Deformation of Dough Using the Bubble Inflation Technique I: Experimental. Rheologica Acta, 41: 532–540.

Charalambides M. N., Wanigasooriya L. and Williams J. G. 2002b. Biaxial Deformation of Dough using Bubble Inflation Technique II: Numerical Modelling. Rheolgica Acta, 41: 541–548.

Charalambides M. N., Goh S. M., Wanigasooriya L., Williams J. G. and Xiao W. 2005. Effect of Friction on Uniaxial Compression of Bread Dough. Journal of Material Science, 40: 3375–3381.

Charalambides M. N., Wanigasooria L., Williams J. G., Goh S. M. and Chakrabarti S. 2006. Large Deformation Extensional Rheology of Bread Dough. Rheologica Acta, 46: 239–248.

Chin N. L. and Campbell G. M. 2005. Dough Aeration and Rheology: Part 2. Effects of Flour Type, Mixing Speed and Total Work Input on Aeration and Rheology of Bread dough. Journal of the Science of Food and Agriculture, 85: 2194–2202.

Clemeur N., Rutgers R. P. G. and Debbaut B. 2003. On the Evaluation of Some Differential Formulations for the Pom-Pom Constitutive Model. Rheologica Acta, 42: 217-231.

Connelly R. K. and Valenti-Jordan J. 2008. Mixing Analysis of a Newtonian Fluid in a 3D Planetary Pin Mixer. Chemical Engineering Research and Design, 86: 1434-1440.

Diani J., Fayolle B. and Gilormini P. 2009. A Review on the Mullins Effect. European Polymer Journal, 45: 601-612.

Dienes J. K. 1979. On the Analysis of Rotation and Stress Rate in Deforming Bodies. Acta Mechanica, 32(4): 217-232.

Dobraszczyk B. J. 1997. The Rheological Basis of Dough Stickiness. Journal of Texture Studies, 28: 139-162.

Dobraszczyk B. J. and Morgenstern M. P. 2003. Rheology and Breadmaking Process. Journal of Cereal Science, 38: 229-245.

Dobraszczyk B. J. 2004. The Physics of Baking: Rheological and Polymer Molecular Structure-Function Relationship in Breadmaking. Journal of Non-Newtonian Fluid Mechanics, 124: 61-69.

Donald A. M. 2003. The Use of Environmental Scanning Electron Microscopy for Imaging Wet and Insulating Materials. Nature Materials, 2(8): 511-516.

Dorfmann A. and Ogden R. W. 2004. A Constitutive Model for the Mullins Effect with Permanent Set in Particle-Reinforced Rubber. International Journal of Solids and Structures, 41: 1855-1878.

Dunlap M. and Adaskaveg J. E. 1997. Introduction to the Scanning Electron Microscope: Theory, Practice and Procedures. User Manual, Facility for Advanced Instrumentation, University of California at Davis, USA.

Dus S. J. and Kokini J. L. 1990. Prediction of the Nonlinear Viscoelastic Properties of a Hard Wheat Flour Dough using the Bird-Carreau Constitutive Model. Journal of Rheology, 34(7): 1069-1084.

Edwards N. M., Mulvaney S. J., Scanlon M. G. and Dexter J. E. 2003. Role of Gluten and Its Components in Determining Durum Semolina Dough Viscoelastic Properties. Cereal Chemistry, 6: 755-763.

Eisele U., Heise B., Kilian H. G. and Pietralla M. 1981. A New Method of Characterizing Molecular Networks with the van der Waals Equation of State. Die Angewandte Makromolekulare Chemie, 100: 67-85.

Enderle H. F. and Kilian H. G. 1987. General Deformation Modes of a van der Waals Network. Progress in Colloid and Polymer Science, 75: 55-61.

Ewoldt R. H. 2009. Nonlinear Viscoelastic Materials: Bioinspired Applications and New Characterization Measures. PhD Thesis, Massachusetts Institute of Technology, USA.

Ferry J. D. 1980. Viscoelastic Properties of Polymers. 3rd Edition, John Wiley and Sons, New York, USA.

Figoni. P. 2011. How Baking Works: Exploring the Fundamentals of Baking Science. 3rd Edition, John Wiley and Sons, USA.

Freeman T. P., Shelton D. R., Bjerke J. M. and Skierkowski K. 1991. The Ultrastructure of Wheat Gluten: Variations Related to Sample Preparation. Cereal Chemistry, 68(5): 492-498.

Gabriele D., de Cindio B., and D'Antona P. 2001. A Weak Gel Model for Foods. Rheologica Acta, 40: 120-127.

Gamonpilas C., Charalambides M. N., Williams J. G., Dooling P. J. and Gibbon S. R. 2010. Predicting the Mechanical Behaviour of Starch Gels Through Inverse Analysis of Indentation Data. Applied Rheology, 20-33283: 1-9.

Geiβler G. and Kaliske M. 2010. Time-Dependent Cohesive Zone Modelling for Discrete Fracture Simulation. Engineering Fracture Mechanics, 77(1): 153-169.

Goesaert H., Brijs K., Veraverbeke W. S., Courtin C. M., Gebruers K. and Delcour J.A. 2005. Wheat Flour Constituents: How They Impact Bread Quality, and How to Impact Their Functionality. Trends in Food Science and Technology, 16: 12-30.

Goh S. M., Charalambides M. N. and Williams J. G. 2004. Determination of the Constitutive Constants of Non-Linear Viscoelastic Materials. Mechanics of Time-Dependent Materials, 8: 255–268.

Hagan, E. W. S. 2009. The Viscoelastic Properties of Latex Artist Paints. PhD Thesis, Mechanical Engineering Department, Imperial College London, UK.

Harito L. 2010. Rheological Properties of Foodstuffs. Undergraduate Project, Mechanical Engineering Department, Imperial College London, UK.

Haupt, B. J., Ennis J. and Sevick E. M. 1999. The Detachment of a Polymer Chain From a Weakly Adsorbing Surface Using an AFM Tip. Langmuir, 15: 3886-3892.

Hermansson A. M. and Svegmark K. 1996. Developments in the Understanding of Starch Functionality. Trends in Food Science and Technology, 7: 345-353.

Hicks C. I. and See H. 2010. The Rheological Characterisation of Bread Dough Using Capillary Rheometer. Rheologica Acta, 49: 719-732.

Holzapfel G. A. 2000. Nonlinear Solid Mechanics, a Continuum Approach for Engineering. John Wiley and Sons, UK.

Horgan C. O. and Murphy J. G. 2010. Simple Shearing of Incompressible and Slightly Compressible Isotropic Nonlinearly Elastic Materials. Journal of Elasticity, 98: 205-221.

James B. 2009. Advances in “Wet” Electron Technique and Their Application to the Study of Food Structure. Trends in Food Science and Technology, 20: 114-124.

Janmey P. A. and Schiwa M. 2008. Rheology. Current Biology, 18(15): R639-R641.

Kaliske M. and Rothert H. 1997. Formulation and Implementation of Three-Dimensional Viscoelasticity at Small and Finite Strains. Computational Mechanics, 19: 228-239.

Kaliske M., Nasdala L. and Rothert H. 2001. On Damage Modelling for Elastic and Viscoelastic Materials at Large Strain. Computers and Structures, 79: 2133-2141.

Kavanagh G. M. and Ross-Murphy S. B. 1998. Rheological Characterization of Polymer Gels. Progress in Polymer Science, 23: 533-562.

Keentok M. and Tanner R. I. 1982. Cone-Plate and Parallel Plate Rheometry of Some Polymer Solutions. Journal of Rheology, 26(3): 301-311.

Khan S. A. and Larson R. G. 1987. Comparison of Simple Constitutive Equations for Polymer Melts in Shear and Biaxial and Uniaxial Extensions. Journal of Rheology, 31(3): 207-234.

Kilian H. G. 1982. Thermo-Elasticity of Network. Colloid Polymer Science, 260: 895-910.

Kitoko M. and Xue S. C. 1999. Edge Fracture in Cone-Plate and Parallel Plate Flows. Rheologica Acta, 38: 321-348.

Klemuk S. A. and Titze I. R. 2009. Determining Motor Inertia of a Stress-Controlled Rheometer. Journal of Rheology, 53: 765-780.

Kontogiorgos V. and Goff H. D. 2006. Calorimetric and Microstructural Investigation of Frozen Hydrated Gluten. Food Biophysics, 1: 202-215.

Kontogiorgos V., Goff H. D. and Kasapis S. 2008. Effect of Aging and Ice-Structuring Proteins on the Physical Properties of Frozen Flour-Water Mixtures. Food Hydrocolloids, 22: 1135-1147.

Kouassi-Koffi J. D., Launay B., Davidou S., Kouame L. P. and Michon C. 2010. Lubricated Squeezing Flow of Thin Slabs of Wheat Flour Dough: Comparison of Results at Constant Plate Speed and Constant Extension Rates. Rheologica Acta, 49: 275-283.

Krueger R. 2006. Computational Fracture Mechanics for Composites: State of the Art and Challenges. NAFEMS Nordic Seminar: Prediction and Modelling of Failure using FEA, Copenhagen, Denmark.

Laun H. M. 2006. Industrial Rheology of Polymers. Lecture Notes, University of Dortmund, Germany.

Launay B. and Michon C. 2008. Biaxial Extension of Wheat Flour Doughs: Lubricated Squeezing Flow and Stress Relaxation Properties. Journal of Texture Studies, 39: 496-529.

Lefebvre J. 2009. Non-Linear, Time Dependent Shear Flow Behavior, and Shear Induces Effect in Wheat Flour Rheology. Journal of Cereal Science, 49: 262-271.

Lim Q. W. L. 2007. Extrusion of Wheat Flour Dough. Undergraduate Project, Mechanical Engineering Department, Imperial College London, UK.

Lodge A. S. 1964. Elastic Liquids. Academic Press, New York, USA.

Macosko C. W. 1994. Rheology Principles, Measurements, and Applications. Wiley VCH, Canada.

Martin P. J., Wilson D. I. and Bonnett P. E. 2004. Rheological Study of a Talc-Based Paste for Extrusion-Granulation. Journal of the European Ceramic Society, 24: 3155-3168.

Mascia S., Patel. M. J., Rough S. L., Martin P J. and Wilson D. I. 2006. Liquid Phase Migration in the Extrusion and Squeezing of Microcrystalline Cellulose Pastes. European journal of Pharmaceutical Sciences, 29: 22-34.

MATLAB ver. 7.8. 2009. The MathWorks Inc., Natick, USA.

McLeish T. C. B. and Larson R. G. 1998. Molecular Constitutive Equations for a Class of Branched Polymers: Pom-Pom Polymer. Journal of Rheology, 42(1): 81-110.

Meddad A. and Fisa B. 1997. A Model for Filler-Matrix Debonding in Glass-Bead Filled Viscoelastic Polymers. Journal of Applied Polymer Science, 65: 2013-2024.

Miehe C. 1995. Discontinuous and Continuous Damage Evolution in Ogden-Type Large-Strain Elastic Materials. European Journal of Mechanics A/Solids, 14: 697-720.

Migliori M. and Gabriele D. 2010. Effect of Pentosan Addition on Dough Rheological Properties. Food Research International, 43: 2315-2320.

Mishnaevsky Jr L. 2007. Computational Mesomechanics of Composites: Numerical Analysis of the Effect of Microstructures of Composites on Their Strength and Damage Resistance. John Wiley and Sons, Chichester, UK.

Mullins L. 1947. Effect of Stretching on Properties of Rubber. Journal of Rubber Research, 16: 275-289.

NABIM. 2011. NABIM Wheat Guide 2011. http://www.nabim.org.uk/content/1/34/wheat-varieties.html. Accessed on 10 November 2011.

National Physical Laboratory. 2011. What Do 'High Vacuum' and 'Low Vacuum' Mean? (FAQ - Pressure). http://www.npl.co.uk/reference/faqs/what-do-high-vacuum-and-low-vacuum-mean-(faq-pressure). Accessed on 1 April 2012.

Ng T. S. K., McKinley G. H. and Padmanabhan M. 2006. Linear to Non-Linear Rheology of Wheat Flour Dough. Applied Rheology, 16: 265-274.

Ng T. S. K. 2007. Linear to Nonlinear Rheology of Bread Dough and Its Constituents. PhD Thesis, Massachusetts Institute of Technology, USA.

Ng T. S. K. and McKinley G. H. 2008. Power Law Gels at Finite Strains: The Nonlinear Rheology of Gluten Gels. Journal of Rheology, 52(2): 419-449.

Ng T. S. K., McKinley G. H. and Ewoldt. R. H. 2011. Large Amplitude Oscillatory Shear Flow of Gluten Dough: A Model Power-Law Gel. Journal of Rheology, 55(3): 627-654.

Ogden R. W. and Roxburgh D. G. 1999. A Pseudo-Elastic Model for the Mullins Effect in Filled Rubber. Proceeding of the Royal Society A, 455: 2861-2877.

Pfluger L. 2009. Quality Traits Gluten Strength. http://maswheat.ucdavis.edu/protocols/gluten/index.htm. Accessed on 14 May 2009.

Phan-Thien N., Safari-Ardi M. and Morales-Patino A. 1997. Oscillatory and Simple Shear Flows of a Flour-Water Dough: a Constitutive Model. Rheologica Acta 36: 38-48.

Phan-Thien N. and Safari-Ardi M. 1998. Linear Viscoelastic Properties of Flour-Water Doughs at Different Water Concentrations. Journal of Non-Newtonian Fluid Mechanics, 74: 137-150.

Phan-Thien N., Newberry M. and Tanner R. I. 2000. Non-Linear Oscillatory Flow of a Solid-Like Viscoelastic Material. Journal of Non-Newtonian Fluid Mechanics, 92: 67-80.

Robards A. W and Sleytr U. B. 1985. Low temperature Methods in Biological Electron Microscopy. 1st Edition, Elsevier Science, Amsterdam, Netherlands.

Rondo. 2012. http://www.rondo-online.com/en/machine-overview/rondostar/. Accessed on 4 October 2012.

Rondodoge. 2010. www.rondodoge.com. Accessed on 1 September 2010.

Roman-Gutierrez A. D., Guilbert S. And Cuq B. 2002a. Frozen and Unfrozen Water Contents of Wheat Flours and Their Components. Cereal Chemistry, 79 (4): 471-475.

Roman-Gutierrez A. D., Guilbert S. and Cuq B. 2002b. Distribution of Water between Wheat Flour Components: A Dynamic Water Vapour Adsorption Study. Journal of Cereal Science, 36: 347-355.

Rough S. L., Bridgewater J. and Wilson D. I. 2000. Effects of Liquid Phase Migration on Extrusion of Microcrystalline Cellulose Pastes. International Journal of Pharmaceutics, 204: 117-126.

Rubio P. and Wagner M. H. 2000. LDPE Melt Rheology and the Pom-Pom Model. Journal of Non-Newtonian Fluid Mechanics, 92: 245-259.

Schofield R. K. and Scott Blair G. W. 1932. The Relationship Between Viscosity, Elasticity and Plastic Strength of Soft Materials as Illustrated By Some Mechanical Properties of Flour Doughs. I. Proceeding of Royal Society (London), A138:707.

Schofield R. K. and Scott Blair G.W. 1933a. The Relationship Between Viscosity, Elasticity and Plastic Strength of Soft Materials as Illustrated By Some Mechanical Properties of Flour Doughs. II. Proceeding of Royal Society (London), A139:557.

Schofield R. K. and Scott Blair G.W. 1933b. The Relationship Between Viscosity, Elasticity and Plastic Strength of Soft Materials as Illustrated By Some Mechanical Properties of Flour Doughs. III. Proceeding of Royal Society (London), A141:72.

Schofield R. K. and Scott Blair G.W. 1937. The Relationship Between Viscosity, Elasticity and Plastic Strength of Soft Materials as Illustrated By Some Mechanical Properties of Flour Doughs. IV. Proceeding of Royal Society (London), A160:87.

Singh H. and MacRitchie F. 2001. Application of Polymer Science to Properties of Gluten. Journal of Cereal Science, 33: 231-243.

Smith M. E. and Finke E. H. 1972. Critical Point Drying of Soft Biological Material for the Scanning Electron Microscopy. Investigative Ophthalmology, 11(3): 123-132.

Song K., Davila C. G. and Rose C. A. 2008. Guidelines and Parameter Selection for the Simulation of Progressive Delamination. Abaqus User's Conference, Newport, Rhode Island, 1-15.

Stapountzi O. A. 2008. Stiffness and Fracture Properties of Alumina Trihydrate Filled Poly (Methyl Methacrylate) Composites. PhD Thesis, Mechanical Engineering Department, Imperial College London, UK.

Stapountzi O. A., Charalambides M. N. and Williams J. G. 2009. Micromechanical Models for Stiffness Prediction of Alumina Trihydrate (ATH) Reinforced Poly

(Methyl Methacrylate) (PMMA): Effect of Filler Volume Fraction and Temperature. Composites Science and Technology, 69: 2015-2023.

Stauffer C. E. 2007. Technology in Breadmaking. 2nd Edition, Springer, USA.

Steffe J. F. 1996. Rheological Method in Food Process Engineering. 2nd Edition, Freeman Press, USA.

Swilinski E. L., Kolster P. and van Vliet T. 2004. Large-Deformation Properties of Wheat Dough in Uni- and Biaxial Extension. Part 1. Flour Dough. Rheologica Acta, 43: 306-320.

Tanner R. I., Dai S. C. and Qi F. 2007. Bread Dough Rheology and Recoil: 2. Recoil and Relaxation. Journal of Non-Newtonian Fluid Mechanics, 143: 107-119.

Tanner R. I., Dai S. C. and Qi F. 2008. Bread Dough Rheology and Recoil: 1. Rheology. Journal of Non-Newtonian Fluid Mechanics, 148: 33-40.

Tanner R. I., Qi F. and Dai S. 2011a. Bread Dough Rheology: an Improved Damage Function Model. Rheologica Acta, 50: 75-86.

Tanner R. I., Uthayakumaran S., Qi F. and Dai S. 2011b. A Suspension Model of the Linear Viscoelasticity of Gluten Doughs. Journal of Cereal Science, 54(2): 224-228.

Tarleton E., Charalambides M. N. and Leppard C. 2012. Image-Based Modelling of Binary Composites. Computational Material Science, http://dx.doi.org/10.1016/ j.commatsci.2012.02.046.

Tester R. F. and Morrison W.R. 1990. Swelling and Gelatinization of Cereal Starches. I. Effect of Amylopetin, Amylose and Lipids. Cereal Chemistry, 67(6): 551-557.

Toh P. J. 2000. Mechanical Tensile Properties of Bread Dough. Undergraduate Project, Mechanical Engineering Department, Imperial College London, UK.

Tow M. R. 2009. Extrusion of Soft Solids. Undergraduate Project, Mechanical Engineering Department, Imperial College London, UK.

Touregypt. 2010. Bread in Ancient Egypt. www.touregypt.net/featurestories/bread.htm. Accessed on 1 September 2010.

Treloar L. R. G. 1975. The Physics of Rubber Elasticity. Clarendon Press, Oxford, UK.

Underwood E. E. 1970. Quantitative Stereology. Addison-Wesley Publishing Company, New York, USA.

USDA. 2011. U.S. Wheat Classes. http://www.ers.usda.gov/briefing/wheat/background.htm. Accessed on 10 November 2011.

Uthayakumaran S., Newberry M., Phan-Thien N. and Tanner R. 2002. Small and Large Strain Rheology of Wheat Gluten. Rheologica Acta, 41: 162-172.

Vader D. and Wyss H. 2012. Introduction to Rheology, Weitzlab Group Meeting Tutorial. http://weitzlab.seas.harvard.edu/links/tutorials/introductiontorheology2. Accessed on 27 April 2012.

Vilgis T. A. 1992. Neutron Scattering From a Deformed “van der Waals Chain”-Quasi Gaussian Approximation. Colloid Polymer Science, 270: 431-436.

Wanigasooriya L. 2006. Mechanical Characterisation and Ram Extrusion of Wheat Flour Dough. PhD Thesis, Mechanical Engineering Department, Imperial College London, UK.

Wang C., Dai S. and Tanner R. I. 2006. On the Compressibility of Bread Dough. Korea-Australia Rheology Journal, 18(3): 127-131.

Ward I. M. 1971. Mechanical Properties of Solid Polymers. 2nd Edition, Wiley-Interscience Publication, UK.

Williams J. G. 1980. Stress Analysis of Polymers. John Wiley, London, UK.

Winter H. H. and Chambon F. 1986. Analysis of Linear Viscoelasticity of a Cross-Linking Polymer at the Gel Point. Journal of Rheology, 30: 367-382.

Winter H. H. and Mours M. 1997. Rheology of Polymers Near Liquid-Solid Transitions. Advances in Polymer Science, 134: 165-234.

Wolfram. 2010. Wolfram Alpha, Computational Knowledge Engine. http://www.wolframalpha.com/. Accessed on 1 April 2011.

Xiao W. 2005. An Experimental and Numerical Study of the Rolling Process of Wheat Flour Dough. PhD Thesis, Mechanical Engineering Department, Imperial College London, UK.

Xiao W., Charalambides M. N and Williams J. G. 2007. Sheeting of Wheat Flour Dough. International Journal of Food Science and Technology, 42: 699-707.

Yi J. and Kerr W. L. 2009. Combined Effects of Freezing Rate, Storage Temperature and Time on Bread Dough and Baking Properties. LWT- Food Science and Technology, 42: 1474-1483.

Zheng H., Morgenstern M. P., Campanella O. H. and Larsen N.G. 2000. Rheological Properties of Dough During Mechanical Dough Development. Journal of Cereal Science, 32: 293-306.

Zounis S., Quail K. J., Wootton M. and Dickson M. R. 2002. Effect of Final Dough Temperature on the Microstructure of Frozen Bread Dough. Journal of Cereal Science, 36: 135-146.

Appendix A: Derivation of Equation (3.33)

From Equation (3.32):

$$\frac{\sigma}{n\dot{\varepsilon}^{n}G(1)} = h = \int_{0}^{\varepsilon} z^{-(n+1)}\left(e^{2z} - e^{-z}\right)dz + \frac{1}{n}\varepsilon^{-n}\left(e^{2\varepsilon} - e^{-\varepsilon}\right). \tag{A1}$$

The integral in Equation (A1) can be separated into two parts:

$$\int_{0}^{\varepsilon} z^{-(n+1)}\left(e^{2z} - e^{-z}\right)dz = \int_{0}^{\varepsilon} z^{-(n+1)}\left(e^{2z}\right)dz - \int_{0}^{\varepsilon} z^{-(n+1)}\left(e^{-z}\right)dz. \tag{A2}$$

Using the variable substitution of $2z = -t$, and $2dz = -dt$, the first integral in Equation (A2) can be rearranged as:

$$\int_{0}^{\varepsilon} z^{-(n+1)}\left(e^{2z}\right)dz = \int_{0}^{-2\varepsilon}\left(\frac{-t}{2}\right)^{-(n+1)} e^{-t}\left(\frac{-dt}{2}\right) \tag{A3}$$

Notice that the limit of the integral has changed to 0 to -2ε. Reversing the limit in the integral in Equation (A3) and rearranging yields:

$$\frac{1}{2}\left(-\frac{1}{2}\right)^{-(n+1)} \int_{-2\varepsilon}^{0} (t)^{-(n+1)} e^{-t}dt. \tag{A4}$$

Equation (A4) is re-written as:

$$\begin{aligned} &\frac{1}{2}\left(-\frac{1}{2}\right)^{-(n+1)} \int_{-2\varepsilon}^{0} (t)^{-(n+1)} e^{-t}dt \\ &= \frac{1}{2}\left(-\frac{1}{2}\right)^{-(n+1)}\left[\int_{-2\varepsilon}^{\infty} (t)^{-(n+1)} e^{-t}dt - \int_{0}^{\infty} (t)^{-(n+1)} e^{-t}dt\right] \end{aligned} \tag{A5}$$

where the limits of the integrals on the right of Equation (A5) can be represented in Figure A1:

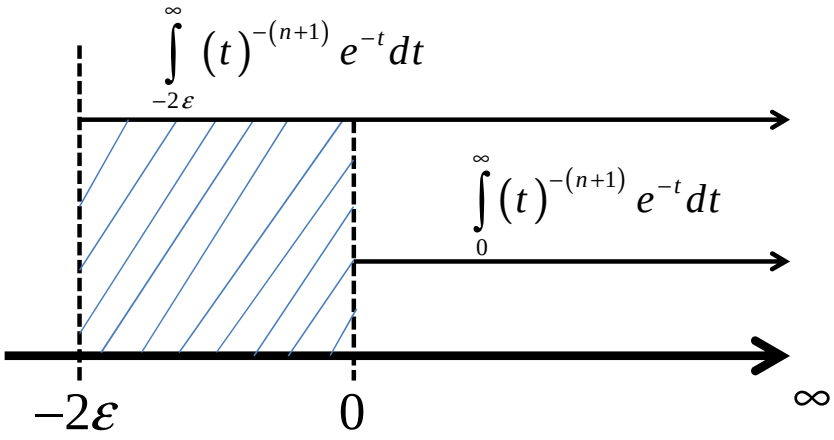

Figure A1. Limit of integral for Equation (A5).

Now, definition for the Gamma function, $\Gamma(a)$, is:

$$\int_0^{\infty} t^{a-1} e^{-t} dt = \left[\Gamma(a)\right] \tag{A6}$$

whereas the incomplete Gamma function, $\Gamma(a,s)$, is defined as:

$$\int_s^{\infty} t^{a-1} e^{-t} dt = \left[\Gamma(a,s)\right]. \tag{A7}$$

Therefore the integrals in Equation (A5) can be written as:

$$\begin{aligned} &\frac{1}{2}\left(-\frac{1}{2}\right)^{-(n+1)}\left[\int_{-2\varepsilon}^{\infty} (t)^{-(n+1)} e^{-t} dt - \int_0^{\infty} (t)^{-(n+1)} e^{-t} dt\right] \\ &= \frac{1}{2}\left(-\frac{1}{2}\right)^{-(n+1)}\left[\Gamma(-n,-2\varepsilon) - \Gamma(-n)\right] \end{aligned} \tag{A8}$$

which is equivalent to the first part of the integral in Equation (A2):

$$\int_0^{\varepsilon} z^{-(n+1)}\left(e^{2z}\right)dz = \frac{1}{2}\left(-\frac{1}{2}\right)^{-(n+1)}\left[\Gamma\left(-n,-2\varepsilon\right)-\Gamma\left(-n\right)\right] \tag{A9}$$

Similarly, the second integral in Equation (A2) can be represented as follows:

$$\int_0^{\varepsilon} z^{-(n+1)}\left(e^{-z}\right)dz = \int_0^{\infty} z^{-(n+1)}\left(e^{-z}\right)dz - \int_{\varepsilon}^{\infty} z^{-(n+1)}\left(e^{-z}\right)dz \tag{A10}$$

where the limits of the integral in Equation (A10) are illustrated in Figure A2:

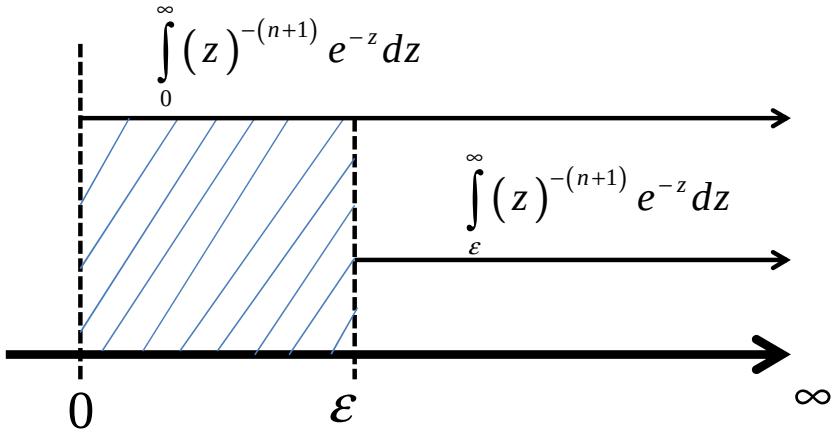

Figure A2: Limit of integral for Equation (A10).

Using the definition of $\Gamma\left(a\right)$ and $\Gamma\left(a,s\right)$ in Equations (A6) and (A7) respectively, Equation (A8) can be written as:

$$\int_0^{\varepsilon} z^{-(n+1)}\left(e^{-z}\right)dz = \left[\Gamma\left(-n\right)-\Gamma\left(-n,\varepsilon\right)\right]. \tag{A11}$$

Equations (A9) and (A11) are substituted in Equation (A2) to give:

$$\int_0^{\varepsilon} z^{-(n+1)}\left(e^{2z}\right)dz - \int_0^{\varepsilon} z^{-(n+1)}\left(e^{-z}\right)dz$$
$$= \frac{1}{2}\left(-\frac{1}{2}\right)^{-(n+1)}\left[\Gamma(-n,-2\varepsilon)-\Gamma(-n)\right]-\left[\Gamma(-n)-\Gamma(-n,\varepsilon)\right]. \quad \text{(A12)}$$

Equation (A12) is finally included in Equation (A1) to yield:

$$h = \left\{\left(\frac{1}{2}\right)\left(-\frac{1}{2}\right)^{-n-1}\left[\Gamma(-n,-2\varepsilon)-\Gamma(-n)\right]-\left[\Gamma(-n)-\Gamma(-n,\varepsilon)\right]\right\}$$
$$+\frac{1}{n}\varepsilon^{-n}\left(e^{2\varepsilon}-e^{-\varepsilon}\right). \quad \text{(A13)}$$

This is identical to Equation (3.33).

Appendix B: Plane Stress, Plane strain, Generalised Plane Strain and Axisymmetric Elements in Abaqus

For 2D modelling in Abaqus, the following elements are available, namely plane stress, plane strain, generalised plane strain and axisymmetric elements. Illustration of the elements is shown in Figure B1.

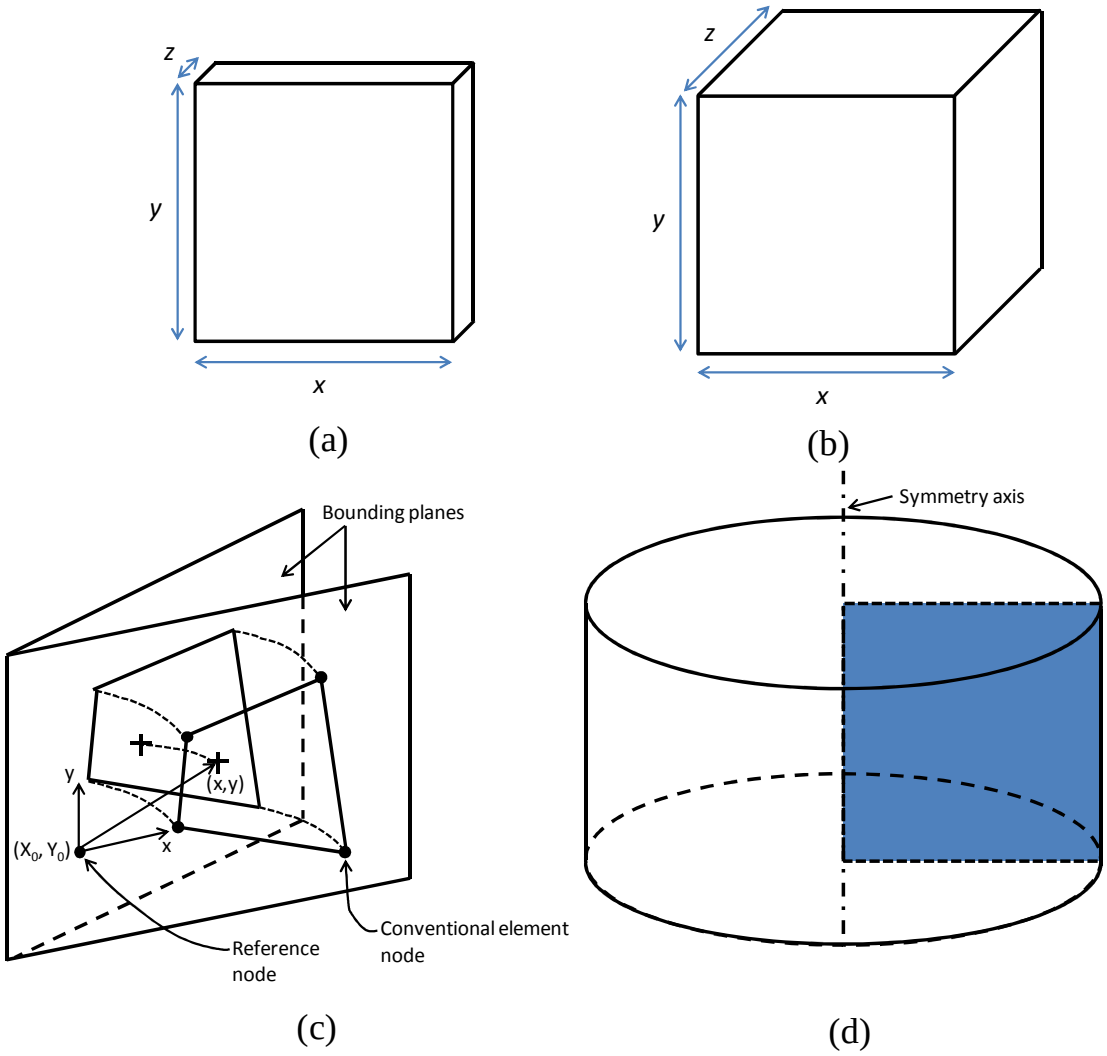

Figure B1. (a) Plane stress element; (b) plane strain element; (c) generalised plane strain element [Abaqus 2010]; and (d) axisymmetric element.

The plane stress element assumes a very small thickness, such that the thickness of the element, z in Figure B1(a) is much smaller than the height, y and length, x. This would then lead to the stress in the thickness direction being zero.

In contrast, the plane strain element assumes a very thick element, such that the thickness of the element, z in Figure B1(b) is much larger than the height, y and length, x. Therefore this implies that the strain in the thickness direction is zero.

The generalised plane strain element assumes the element lies between two bounding planes, which may move as rigid bodies with respect to each other [Abaqus 2009]. The relative motion of the two planes causes a direct strain in the thickness direction only, as shown by the dotted lines connecting the two planes in Figure B1(c).

Finally, the axisymmetric element is generated by revolving a plane cross-section about an axis (symmetry axis in Figure B1(d)). This corresponds to a body whose geometry is axisymmetric and subjected to axially symmetric loading conditions.

Appendix C: Dough Mixer Movement

The mixer used in this work is manufactured by National Manufacturing Co. It was used in previous studies on dough by Xiao [2005] and Wanigasooriya [2006]. The mixer movement consists of four planetary pins on the head revolving around two stationary pins at the bottom of the mixing bowl. The mixer has the capability of recording torque and speed during mixing to a computer.

The pin configuration and movement is shown in Figure C1. The pin movement was recorded by marking the tip of the pins at an angle of rotation. The mark on the pins was then copied to a piece of paper. This procedure is repeated at different angle of rotation until a complete rotation cycle is obtained, as shown in Figure C1.

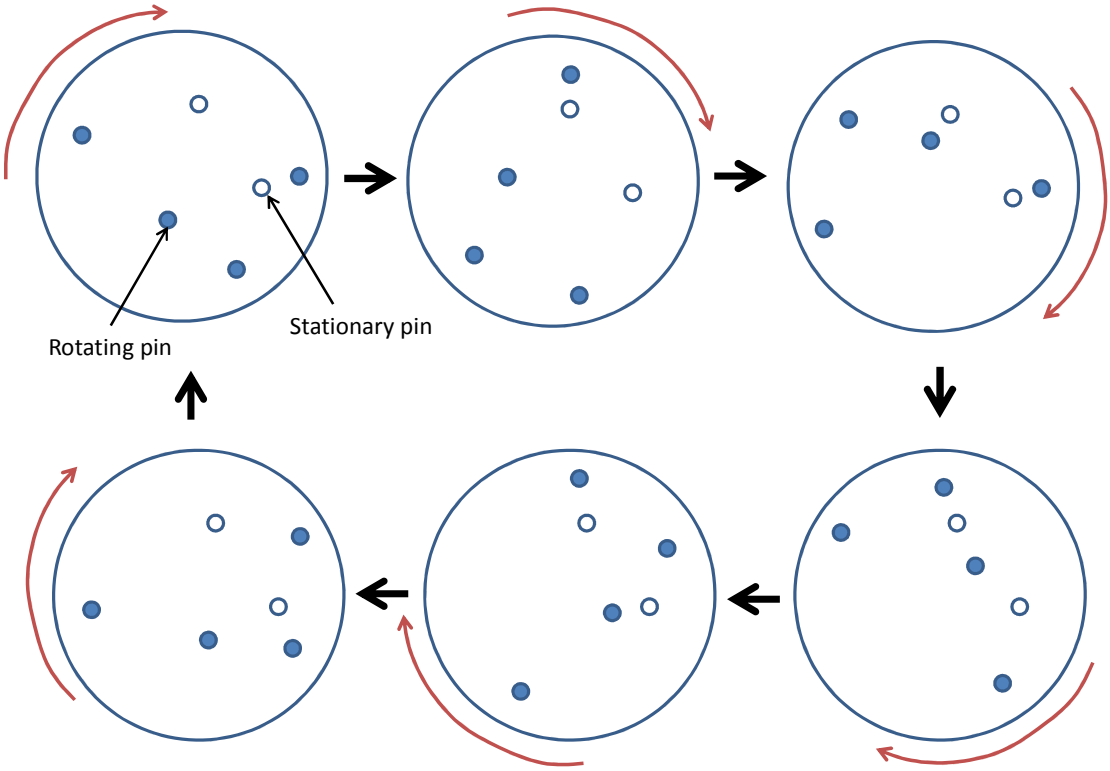

Figure C1. Top view of the pin movement inside the mixing bowl of the mixer.

The pin movement in Figure C1 is illustrated from a top view, where the filled circles are top pins attached to the revolving head, while the unfilled circles are bottom stationary pins at the bottom of the mixing bowl. It can be seen that the pin configuration is not symmetric. The reason for this is to provide a uniform distribution of flour and water when mixed inside the bowl. This has been shown by Connelly and Valenti-Jordan [2008], who investigated the distribution of Newtonian corn syrup fluid inside a planetary pin mixer using Computational Fluid Dynamic (CFD) analysis. The pin configuration is shown in Figure C2.

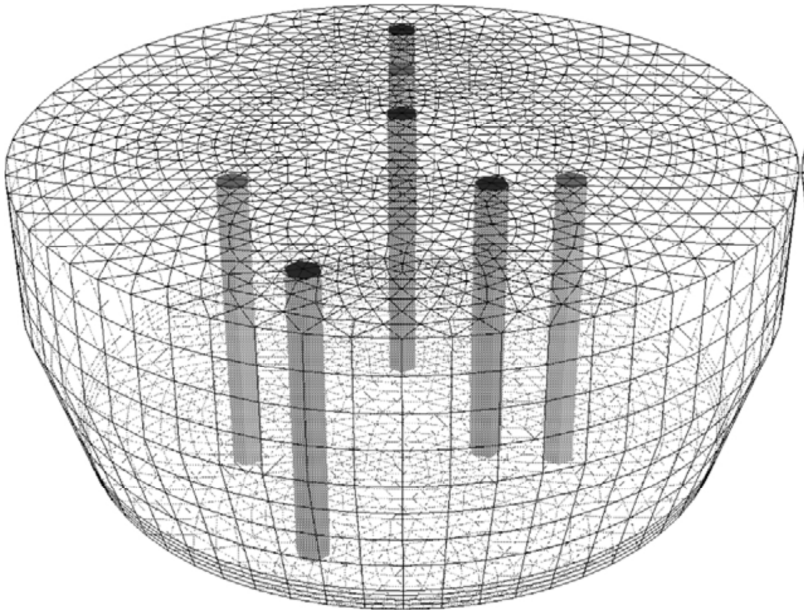

Figure C2. Configuration of the pins in the CFD study of mixer by Connelly and Valenti-Jordan [2008], where the dark circles are top pins attached to revolving head, while the grey circles are bottom stationary pins at the bottom of the bowl.

The CFD analysis showed that the stretch distribution of the mixed material inside the bowl is approximately uniform, except at the wall of the bowl, as shown in Figure C3. They suggested that the best pin configuration is the one that provides the highest increase in the amount of stretch to the material when mixed.

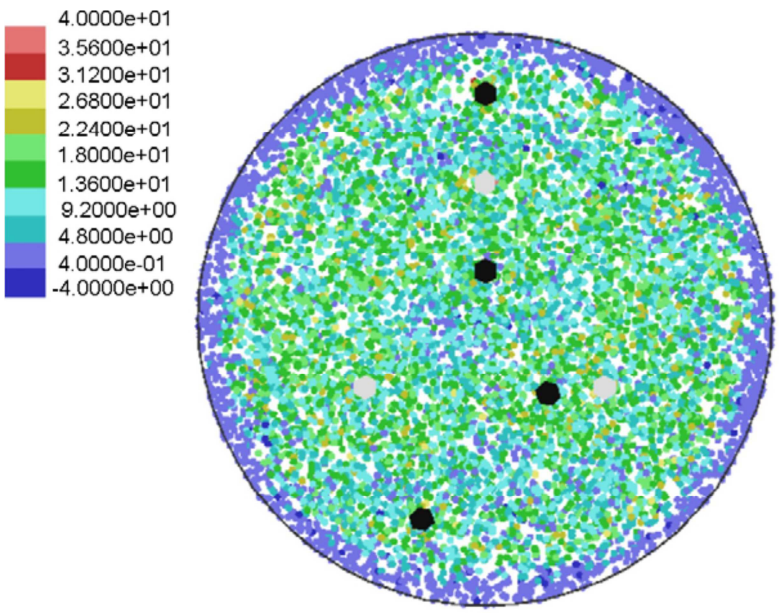

Figure C3. Stretch distribution results obtained using CFD by Connelly and Valenti-Jordan [2008]. Note that the scale is shown in mm.

However, further work is needed to investigate the mixing behaviour in the vertical direction, for example the mixing distribution close to the floor of the bowl, as well as the performance of individual pins inside the mixing bowl. This is because different mixer manufacturers have different pin configuration, for example the pin configuration in this work (Figure C1), is different than the one used by Connelly and Valenti-Jordan [2008] (Figure C2). CFD studies also need to be performed on dough samples, since dough is a soft solid material, which is different than the Newtonian fluid investigated by Connelly and Valenti-Jordan [2008].